Report No. CCEER 20-07

REGIONAL-SCALE SEISMIC RISK TO REINFORCED CONCRETE BUILDINGS BASED ON PHYSICS-BASED EARTHQUAKE GROUND MOTION SIMULATIONS

Maha Kenawy
and
David McCallen

U.S. Department of Energy Contract number 17-SC-20-SC

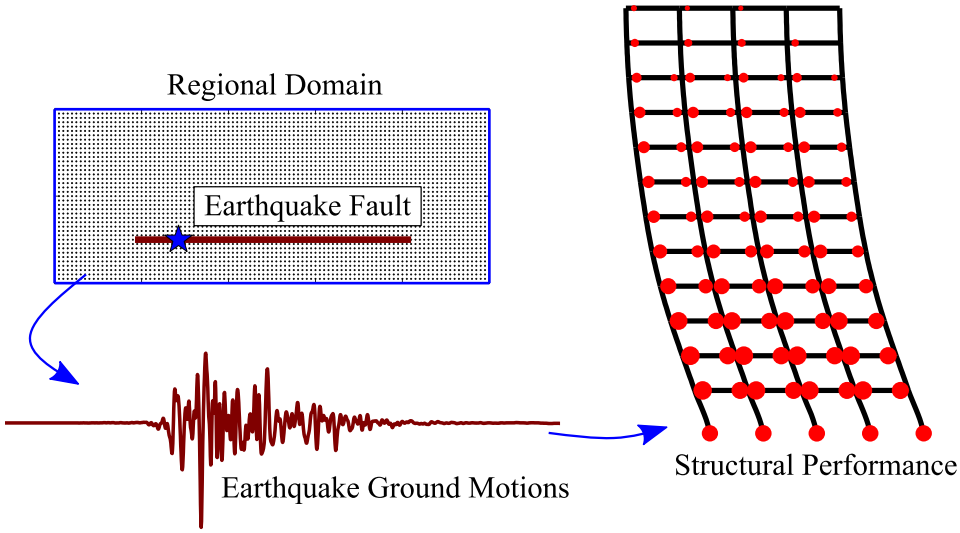

Center for Civil Engineering Earthquake Research

University of Nevada, Reno
Department of Civil and Environmental Engineering, MS 258
1664 N. Virginia St.
Reno, NV 89557

September 2020

Abstract

This document reports the development and findings of a computational study which examines the regional-scale variability of seismic risk to reinforced concrete (RC) buildings using physics-based earthquake simulations. The development of the structural simulation models is presented first, followed by a description of the study components, and discussion of its findings as they relate to the seismic risk to RC buildings. Finally, the implications of the study findings on the performance and design of RC buildings near active earthquake faults are summarized, and the study limitations are reported. This report is divided into three parts:

In part I, the simulation framework for RC moment frames is described. The framework rests upon the theory of lumped plasticity (LP) models, which is described in the first chapter. The second chapter outlines a program, the RC Structural Model Generator, which calibrates the LP component parameters and generates structural analysis scripts of RC frames with any number of stories/bays. The program is intergated into a regional-scale workflow to allow for expedient simulation of the nonlinear response of RC buildings to earthquake ground motions over large computational domains. The program performance is assessed using several static and dynamic verification problems that are described in the following chapter.

In part II, broadband physics-based earthquake simulations are utilized to characterize the regional-scale risk to modern RC buildings using the workflow described in part I. Dense datasets of high-resolution simulated ground motions were generated using kinematic fault rupture models with varying rupture characteristics to represent shallow crustal earthquakes, and resolved up to frequencies of 5 Hz. Over forty thousand nonlinear time history simulations of modern short- and mid-rise RC special moment frame buildings were conducted. The spatial variability of the structural risk within a single earthquake scenario and between different rupture scenarios was examined, and the impact of the geologic and rupture characteristics on the structural response quantities was characterized. In addition, the relationship between the structural demands near the fault and the stiffness and ductility characteristics of the buildings was investigated. The study reveals that the structural demands on RC buildings due to a M7 strike-slip earthquake may vary by a factor of up to 8.0 at very short distances from the fault, and the dispersion in the demands is found to depend on the frequency content of the buildings. The interstory drift and member rotation demands are substantially impacted by important features of the geological structure and the characteristics of the rupture scenarios, particularly the presence of localized high-slip regions along the fault plane. Flexible buildings exhibit higher sensitivity to the presence of strong velocity pulses near the fault, as compared to stiffer buildings. Comparison of the characteristics of the simulated ground motions against real earthquake records suggests that the simulated motions, particularly using the hybrid rupture scenarios, may offer reasonable risk estimates for low-frequency structures, and conservative estimates for high-frequency structures.

Part III of this report presents some computational and theoretical supplements to the study, including the software tool which was created to aid the design of modern RC moment frame buildings.

Acknowledgements

The work reported in this document was supported by the Exascale Computing Project (ECP), Project Number: 17-SC-20-SC, a collaborative effort of two U.S. Department of Energy organizations - the Office of Science and the National Nuclear Security Administration. The earthquake simulations utilized in this study were created by Arben Pitarka, Ph.D. (Lawrence Livermore National Laboratory), and the structural system simulations were performed using the computing tools of the National Energy Research Scientific Computing Center. The author is also thankful to Houjun Tang, Ph.D. (Lawrence Berkeley National Laboratory) for his help with creating the regional simulations workflow, and to Sashi Kunnath, Ph.D. (University of California, Davis) for the fruitful discussions on the modeling approaches of reinforced concrete structures.

Contents

List of Figures

List of Tables

Part I

Simulation Models of Reinforced Concrete Frames

Chapter 1

RC Structural Component Modeling

1.1 Beam-spring assembly modeling concepts

The behavior of reinforced concrete (RC) structural members is simulated by lumped or concentrated plasticity (LP) models. These models represent a computationally-inexpensive idealization of the nonlinear behavior of structural components. The model consists of a linear elastic beam element connected in series with two (or one) nonlinear springs at the member ends. The beam element is assumed to remain elastic during the entire analysis, whereas the nonlinear response of the member is represented by a nonlinear constitutive relationship for the end springs. This modeling approach implies the following:

- The nonlinear response history of the structural component (or the end-springs) cannot be directly calibrated from a mechanics-based approach. Rather, it is calibrated based on comparisons against physical observations. This implies that these calibrations have a limited range of applicability, which corresponds to the range of available component laboratory test data. This aspect represents one of the major drawbacks of the lumped plasticity approach.

- The stiffness properties of the structural component are based upon the in-series stiffness of the beam element and the end springs in the model. This implies that the stiffnesses of both components of the model (the beam element and the springs) need to be scaled to produce the correct stiffness for the structural member.

- The commonly used LP element model is incapable of directly predicting the effects of the interaction between the bending moment and the axial load on the structural memebers during the analysis.

The concept and use of LP models in nonlinear structural analysis date back to the 1960s. A description of two types of LP models which employ bilinear hysteretic moment-rotation relationships, and their use in the dynamic analysis of a 20-story structural frame can be found in [Giberson, 1967]. Chen [1982] and Powell and Chen [1986] presented a formulation for a plasticity-based 3D generalized plastic hinge element, which accounts for the interaction between axial, torsional and biaxial bending effects in the member, and Dides and De la Llera [2005] conduct a comparative

study between the different types of concentrated plasticity models and their use in the dynamic analysis of structures.

In the following decades, more sophisticated constitutive relationships of the beam hinges were developed to incorporate the degradation in strength (or post-capping behavior), and the degradation in strength and stiffness under cyclic loading conditions. Examples of these models include those by Kunnath et al. [1991], Sivaselvan and Reinhorn [2000] and Song and Pincheira [2000] - see Lignos [2008] for a comprehensive review of deterioration models. These models became increasingly necessary for seismic analysis and design, particularly with the advent of performance-based seismic engineering methodologies, and the emphasis on predicting extreme limit states of structures- including structural collapse. The key challenge in using lumped plasticity models is calibrating the hysteretic properties of the member nonlinear hinges, which determine the nonlinear behavior of the structural component, including the deterioration in strength and stiffness under complex loading conditions. Several studies have proposed methodologies to arrive at estimates of the hysteretic hinge properties. One of the most widely used deteriorating hysteretic hinge models is the Ibarra-Medina-Krawinkler (IMK) model which is described in Ibarra and Krawinkler [2005] and Ibarra et al. [2005], along with its calibration for steel, plywood and reinforced concrete components. This model was further refined by Lignos [2008], and calibrated for steel sections, to enable the prediction of sidesway collapse of steel frames. The calibration process yields prediction equations, which were developed systematically based on statistical regression approaches using a large number of experimental test data. A similar calibration approach was proposed for reinforced concrete components in Haselton [2008], which calibrated the so called 'peak-oriented' version of the IMK model to 255 reinforced concrete column tests. Then, using statistical regression, equations which relate the column design parameters to the column element model parameters were developed. The prediction equations developed in Haselton [2008] were echoed in the PEER-ATC 72-1 report [PEER/ATC, 2010], and were later refined in Haselton et al. [2016]. The equations in the latter publication were used to predict the properties of the LP models in the numerical study described herein.

1.2 Stiffness scaling of the beam-spring assembly

The LP component models consist of an elastic beam element connected in series with nonlinear springs at one or both ends (depending on the boundary conditions), as shown in figure 1.1. The properties of the structural member as a whole are, therefore, the aggregate of the properties of both beam and spring components. In other words, the use of LP models requires the following steps:

1. Estimating the properties of the structural members, which involves determining a moment-rotation relationship for the member, and includes the strength and stiffness deterioration properties. The estimation of the member properties is the subject of the following section.

2. Computing the properties of the beam element and nonlinear springs which correspond to the properties of the structural member. This procedure is the subject of this this section.

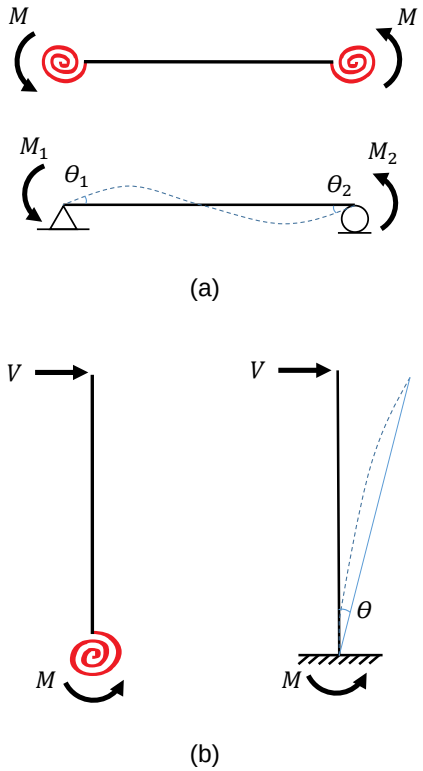

Figure 1.1: Illustration of the beam-spring assembly in the lumped plasticity model.

The properties of the beam and spring elements are used as input to the numerical analysis model.

1.2.1 Stiffness properties of the beam-spring assembly

The stiffness of the structural member is equivalent to the in-series stiffness of the beam-spring assembly. This means that the rotation at one end of the member (see figure 1.1) is equal to the sum of the rotation of the beam element and the rotation of the nonlinear spring:

$$\theta_{mem} = \theta_{ele} + \theta_{spr} \tag{1.1}$$

where all the properties with the subscript 'mem' belong to the entire assembly, and the subscripts 'ele' and 'spr' refer to the properties which belong to the beam element and the nonlinear spring, respectively. Utilizing the small-displacement moment-rotation relationship $M = K\theta$, equation (1.1) becomes:

$$\frac{M}{K_{mem}} = \frac{M}{K_{ele}} + \frac{M}{K_{spr}} \tag{1.2}$$

where M is the moment at the end of the member, and K is the stiffness. Equation (1.2) can be reduced to:

$$\frac{1}{K_{mem}} = \frac{1}{K_{ele}} + \frac{1}{K_{spr}} \tag{1.3}$$

which yields the stiffness of the assembly in terms of the stiffness of its constituents. There are multiple ways one can assign stiffnesses to the assembly components:

- Assigning the entire member stiffness to the spring, i.e. $K_{spr} = K_{mem}$ and $K_{ele} = \infty$. Ibarra and Krawinkler [2005] point out this option is not desirable because it would force all the deformations into nonlinear springs. Consequently, the member stiffness becomes independent of the moment gradient in the beam element, and the effects of the moment gradient and its changes during the analysis will not be accounted for in the simulation models. This approach may also result in spurious damping forces in the analysis, depending on the underlying damping formulation in the model.

- Assigning the entire member stiffness to the beam element, i.e. $K_{ele} = K_{mem}$ and $K_{spr} = \infty$. This option is problematic because having an infinite spring stiffness precludes the evolution of member stiffness in the strain-hardening and post-capping regions, which is conventionally expressed as a fraction of the initial spring stiffness in the LP model.

- Assigning the spring stiffness as a multiple of the beam element stiffness, i.e. $K_{spr} = nK_{ele}$, such that $n >> 1$ [Ibarra and Krawinkler, 2005]. This option is the currently accepted approach for LP models, because it avoids or minimizes the problems associated with the other options. Using equation (1.3), the spring and element stiffnesses can be expressed in terms of the member stiffness:

$$K_{spr} = nK_{ele} = (n+1)K_{mem} \tag{1.4}$$

$$K_{ele} = \frac{n+1}{n} K_{mem} \tag{1.5}$$

  A value of $n = 10$ was deemed appropriate [Ibarra and Krawinkler, 2005] for permitting the use of a nonlinear backbone relationship for the springs, accounting for the element moment gradient effects, and avoiding some of the potential damping issues associated with infinite stiffness.

1.2.2 Scaling of other member properties

Because the stiffnesses of the spring and element are modified in the LP analysis models (refer to equations (1.4) and (1.5)), other member properties associated with the stiffness properties have to be modified as well to reproduce the correct moment-rotation relationship for the member. These properties are outlined in the following paragraphs:

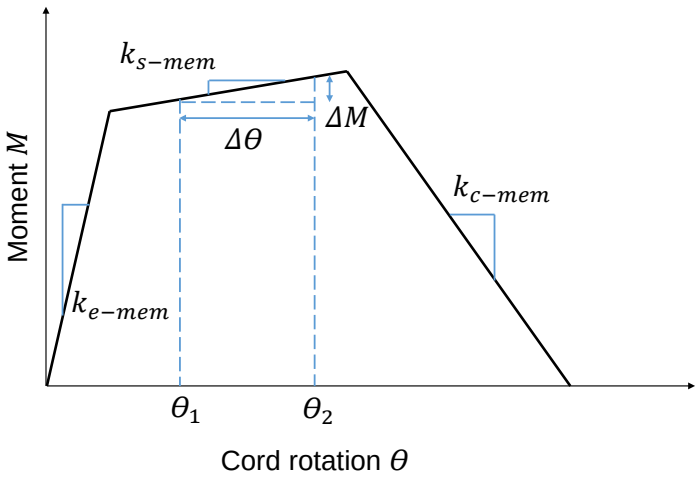

Figure 1.2: Hardening and post-capping member stiffness in the moment-rotation backbone relationship in a structural member

Strain-hardening coefficient α : The strain hardening coefficient α is defined as the ratio between the hardening stiffness of the member K_{s-mem} and the initial elastic stiffness of the member K_{e-mem}, i.e.:

$$K_{s-mem} = \alpha K_{e-mem} \tag{1.6}$$

Similarly, the ratio between the hardening stiffness of the spring K_{s-spr} and the initial elastic stiffness of the spring K_{e-spr} can be expressed as:

$$K_{s-spr} = \alpha_{spr} K_{e-spr} \tag{1.7}$$

Because of the stiffness scaling described in the preceding subsection, the ratio between the elastic and hardening stiffness of the spring α_{spr} is not equal to α, and has to be derived. Referring to figure 1.2, the difference in the member cord rotation between two points in the hardening range $\Delta\theta$ can be expressed as follows:

$$\Delta\theta_{mem} = \Delta\theta_{ele} + \Delta\theta_{spr} \tag{1.8}$$

Using the moment-rotation relationship $\Delta M = K\Delta\theta$, where K is the tangent stiffness, equation (1.8) can be rewritten as:

$$\frac{\Delta M}{K_{s-mem}} = \frac{\Delta M}{K_{ele}} + \frac{\Delta M}{K_{s-spr}} \tag{1.9}$$

where the tangent stiffness of the beam element is K_{ele} because the element remains elastic throughout the analysis. Substituting equations (1.6) and (1.7), the following relationship is obtained:

$$\frac{1}{\alpha K_{mem}} = \frac{1}{K_{ele}} + \frac{1}{\alpha_{spr} K_{spr}} \tag{1.10}$$

The desired relationship between α_{spr} and α can be obtained by substituting equations (1.4) and (1.5) into equation (1.10):

$$\alpha_{spr} = \frac{\alpha}{1 + n\,(1 - \alpha)} \tag{1.11}$$

This relationship permits computing the value of α_{spr}, which is used as input in the numerical model, after determining the ratio α for the structural member, using the prediction equation presented later in this chapter.

Post-capping stiffness coefficient α_c : This parameter expresses the ratio between the post-capping member stiffness and initial member stiffness $\alpha_c = \frac{K_{c-mem}}{K_{mem}}$. A similar derivation can be applied in the post-capping region of the moment-rotation relationship, leading to a similar relationship between the spring post-capping stiffness coefficient α_{c-spr} and the member post-capping stiffness coefficient α_c:

$$\alpha_{c-spr} = \frac{\alpha_c}{1 + n\,(1 - \alpha_c)} \tag{1.12}$$

However, the implementation of the LP model in the structural analysis platform Opensees [McKenna et al., 2000] (the IMK material model) does not require specification of the post-capping stiffness coefficient directly. Rather, the post-capping slope is determined indirectly through specifying the post-capping rotation capacity, as described in the following section. Therefore, computing the spring post-capping stiffness coefficient is unnecessary in the context of this analysis.

Damping coefficient β : Rayleigh Damping is the most common damping formulation for structural analysis applications, in which stiffness- and mass-proportional damping coefficients are introduced into the simulation model to account for damping effects in the structure, such that the damping matrix is expressed as follows:

$$\mathbf{C} = \beta_1 \mathbf{M} + \beta_2 \mathbf{K} \tag{1.13}$$

where $\mathbf{M}$ is the mass matrix of the structure, $\mathbf{K}$, in this case, is the initial structural stiffness (rather than the tangent stiffness), and β_1 and β_2 are the mass-proportional and stiffness-proportional damping coefficients, respectively. Using a Rayleigh damping formulation, the damping in the LP model is assigned as follows:

- Because the structure's mass is lumped at the nodes, the mass-proportional damping is assigned to the model nodes only.

- To avoid the numerical problems and spurious damping forces associated with the change in the spring stiffness during the analysis [Ibarra and Krawinkler, 2005, Chopra and McKenna, 2016], the stiffness-proportional damping is assigned to the beam elements only (but not the springs), which have constant elastic stiffness throughout the analysis. This approach also avoids using a non-constant damping matrix which results from tangent-stiffness proportional damping, generates a hysteretic force-velocity relationship (for which there is no physical basis), and may lead to negative damping when the tangent stiffness becomes negative.

It is worth noting that Opensees has the capability to assign damping to specific regions of the model, rather than the entire model, using the 'region' command. The reader is referred to the Opensees command manual for a detailed description of the command. Because β_2 is a stiffness-proportional damping coefficient applied to the beam elements only, the coefficient value in the simulation model must be modified to reflect the correct damping coefficient for the beam elements (as opposed to the damping coefficient for the entire structural member). Based on the stiffness relationship in equation (1.5), the modified damping coefficient can be trivially determined as:

$$\beta_{2-ele} = \frac{n+1}{n}\beta_{2-mem} \tag{1.14}$$

1.3 Estimation of the moment-rotation relationship for RC components

The prediction of the properties of the LP hinge model is the process of determining the appropriate nonlinear moment-rotation relationship of the structural component. This relationship is typically represented as a multi-linear moment-rotation diagram, which includes a pre-yield elastic range, a post-yield hardening range, and a post-peak or post-capping (negative) stiffness range. In addition, recent available prediction equations include predictions of the cycle-to-cycle strength degradation (degradation in strength during cyclic loading), and degradation of the unloading and reloading stiffness based on some dissipation energy measures, as detailed in the references cited above.

After determining the component M-θ relationship, the properties of the constituents of the structural member model (the elastic beam element and the inelastic spring) can be determined as described earlier. These properties can then be used to create a numerical model of the assembly using structural analysis codes, in this case using OpenSees. An overview of these steps is provided in the following subsections.

The following paragraphs, along with figure 1.3 describe the parameters of the component moment-rotation relationship, which are the targets of the IMK model calibration process. Various forms of the same parameters have been presented in different studies. In this document, the parameter definitions and the prediction equations used to estimate them are described first, then corresponding input parameters to the Opensees material model are discussed. It is noted that three different types of the IMK model exist: bilinear, peak-oriented, and pinching [Ibarra et al., 2005].

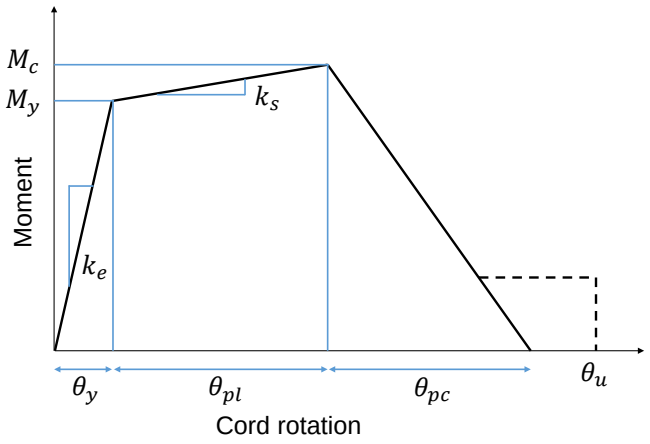

Figure 1.3: Parameters of the backbone of the IMK hysteretic material model.

In the numerical models developed herein, the peak-oriented IMK model is used, because it has been previously calibrated for RC components.

Yield moment capacity M_y : the yield moment capacity of the model can be represented by the nominal flexural strength of the RC beam-column, and determined using the standard rectangular compressive stress block analysis of the member's cross section (ACI 318-11) in combination with the expected (rather than nominal) steel and concrete material strengths. An alternative method of estimating the flexural yield strength is using the empirical equation developed in Panagiotakos and Fardis [2001]. Following the suggestions of Haselton et al. [2016], the former method is used to estimate M_y, although both methods were explored in this study and provide very close estimates in most cases. The section analysis approach is preferred because it is grounded in structural mechanics theories, albeit with a simple representation of the stress distribution over the cross section.

Initial elastic stiffness K_e : this parameter is not estimated directly using the prediction equations, because the member stiffness depends on the member length and boundary conditions. Instead, the flexural rigidity EI_e is estimated (as a fraction of the gross section flexural stiffness EI_g) using the prediction equation proposed in Haselton et al. [2016]:

$$\frac{EI_e}{EI_g} = 0.30\left(0.1 + \frac{P}{A_g f'_c}\right)^{0.8}\left(\frac{L}{h}\right)^{0.72} \qquad where\ 0.2 \leq \frac{EI_e}{EI_g} \leq 0.6 \tag{1.15}$$

where P is the axial load on the member, A_g is the gross cross-sectional area, f'_c is the nominal compressive strength of the concrete, and $\frac{L}{h}$ is the ratio of the member length to its cross-sectional depth. The initial elastic stiffness of the member is computed as $\frac{3EI_e}{L}$ for a member in single

curvature (such as a cantilever member), and as $\frac{6EI_e}{L}$ for a member in double curvature (such as beams and columns in typical moment frames). It is noted that the yield stiffness EI_e is a measure of the secant stiffness to the yield point, and is primarily intended for analyses in the nonlinear range (large displacement demands). Another measure of the initial stiffness EI_{40} provides an estimate of the secant stiffness up to 40% of the yield load, and is intended for analyses at low deformation demands. Therefore, it provides a better estimate of the initial stiffness. Haselton et al. [2016] point out that the value of the initial stiffness was not seen to have a significant impact on the structural response in the nonlinear range and up to collapse. The initial stiffness EI_{40} can be estimated using the following equation:

$$\frac{EI_{40}}{EI_g} = 0.77\left(0.1 + \frac{P}{A_g f'_c}\right)^{0.8}\left(\frac{L}{h}\right)^{0.43} \qquad where\ 0.35 \leq \frac{EI_{40}}{EI_g} \leq 0.8 \tag{1.16}$$

Yield rotation capacity θ_y : this parameter describes the ratio between the yield moment and the initial stiffness $\frac{M_y}{K_e}$.

Plastic rotation capacity θ_{pl} : this parameter is defined as the rotation capacity at the capping point, minus the the yield rotation capacity, and is estimated using the prediction equation in Haselton et al. [2016]:

$$\theta_{pl} = 0.12\,(1 + 0.55a_{sl})\,(0.16)^{v}(0.02 + 40\rho_{sh})^{0.43}(0.54)^{0.01c_{units}f'_c}(0.66)^{0.1s_n}(2.27)^{10.0\rho} \tag{1.17}$$

where a_{sl} is a parameter which indicates whether or not bond-slip is possible in the structural member, and is either equal to 1 or 0, v is the axial load ratio on the component, ρ_{sh} is the transverse reinforcement ratio, which is equal to the transverse reinforcement area A_{sh} over the area encompassed by the spacing of the transverse reinforcement s and the section width b. c_{units} is a units conversion ratio equal to 1.0 when f'_c is in MPa, and 6.9 when it is in ksi. s_n is a slendness ratio of the reinforcing steel bars, which is equal to the ratio of transverse reinforcement spacing s over the longitudinal bar diameter d_b. Finally, ρ is the longitudinal reinforcement ratio $\frac{A_s}{bh}$ where h is the total section depth. The experimental data used to develop equation (1.17) is limited to columns with symmertic steel reinforcement. To determine the plastic rotation capacity for sections with unsymmetric tension and compression reinforcement, the following correction was proposed by Fardis and Biskinis [2003] and echoed in Haselton et al. [2016] to account for the unsymmetry in the reinforcement:

$$\theta_{pl(non-symmetric)} = \left(\frac{max\left(0.01, \frac{\rho' f_y}{f'_c}\right)}{max\left(0.01, \frac{\rho f_y}{f'_c}\right)}\right)^{0.225} \theta_{pl(symmetric)} \tag{1.18}$$

where ρ' and ρ are the compression and tension reinforcement ratios in the section, respectively. Equation (1.18) is used in this study to compute the plastic rotation capacity of all beam and column sections.

Maximum moment capacity M_c : this parameter represents the value of the moment at the capping point. The maximum moment capacity is not estimated directly, but rather, the ratio of the maximum to yield moment capacity $\frac{M_c}{M_y}$ is computed by the prediction equations. Haselton et al. [2016] recommend the constant relationship:

$$\frac{Mc}{My} = 1.13 \tag{1.19}$$

It is noted that a different prediction equation for the maximum moment capacity ratio was proposed in Haselton [2008]; however, the same authors later recommended the use of the constant relationship, which seemed to produce satisfactory results. In this study, we found that using equation (1.19) provided reasonable estimates, whereas the relationship in Haselton [2008] tended to overestimate the capacity occasionally.

Post-capping rotation capacity θ_{pc} : the post-capping rotation capacity is defined as the rotation beyond the capping point until complete loss of the component moment-carrying capacity. This parameter is estimated using the following equation [Haselton et al., 2016]:

$$\theta_{pc} = 0.76\ (0.031)^{v}(0.02 + 40\rho_{sh})^{1.02} \qquad \leq 0.10 \tag{1.20}$$

It is noted that there is a large uncertainty in predicting the post-capping rotation capacity, due to the sparsity of observational data in the post-peak region of the behavior of RC components. Consequently, only 15 tests with clear post-capping behavior were available for calibrating the post-capping rotation [Haselton et al., 2016]. Therefore, a large scatter is associated with this prediction equation, and the upper bound of 0.10 is imposed as a practical limit, because of the lack of data for components subjected to sufficiently large deformations.

Cyclic deterioration parameter λ : this parameter controls the rate of cyclic deterioration in the model. The modified IMK model [Lignos and Krawinkler, 2010] permits the use of different cyclic deterioration parameters to control the following forms of cyclic deterioration: 1) pre-capping strength deterioration, 2) post-capping strength deterioration, 3) accelerated reloading stiffness deterioration, and 4) the unloading stiffness deterioration. As suggested in Haselton [2008], the pre- and post-capping strength deterioration is assumed to be the same (although this assumption remains difficult to verify due to the lack of observations on cyclic strength deterioration in the post-peak region). In addition, both modes of stiffness degradation are not considered. However, this assumption does not eliminate the stiffness deterioration from the model entirely, because the peak-oriented IMK model induces some stiffness deterioration by default. The preceding assumptions reduce the strength deterioration to a single parameter estimated using the following equation ([Haselton et al., 2016]):

$$\lambda = (30)\ (0.3)^{v} \tag{1.21}$$

The cyclic energy dissipation capacity is then determined as $E_t = \lambda M_y \theta_{pl}$. Another alternative approach to determining the cyclic energy dissipation capacity uses the yield rotation capacity,

instead of the plastic rotation capacity: $E_t = \gamma M_y \theta_y$, and the parameter γ, which is equivalent to the parameter λ, is determined using the following equation:

$$\gamma = (170.7)\ (0.27)^{v} (0.10)^{\frac{s}{d}} \tag{1.22}$$

where d is the section depth. It is unclear which approach should be used to determine the cyclic energy dissipation capacity. Haselton et al. [2016] stated that using γ and the yield rotation capacity seems to have less prediction uncertainty; however, the use of λ and the plastic rotation capacity was preferred, because the dissipation capacity is expected to be correlated with the associated plastic rotation capacity (rather than the yield capacity). In this study, both approaches were used and their estimates were compared to experimental test results. The parameter λ seemed to provide more reasonable estimates of the member response to laboratory-controlled cyclic loading.

Rate of strength deterioration c : each deterioration mode is associated with an exponent term c, which describes the rate of change of the deterioration with accumulation of damage. As suggested in Haselton [2008], the four rate parameters are consolidated into one parameter c, and that parameter is assumed to be equal to 1, in order to reduce the complexity of the calibration procedure.

1.4 Description of the component analysis model

An Opensees tcl-based analysis code for RC cantilever columns was created to benchmark the performance of the previously detailed calibration process against available test data. A MATLAB-based [MATLAB, 2020] driver program was created to perform the following tasks:

- Read the component geometric and material properties from an Excel sheet; including the member and section dimensions, concrete and steel material properties, longitudinal and transverse reinforcement ratios, and the axial load on the member.
- Use the component properties and the prediction equations described in the previous section to determine the moment-rotation constitutive relationship for the member, including the backbone curve and the cyclic deterioration parameters.
- Write the member properties and analysis parameters to the Tcl-based simulation file, call Opensees to run a static pushover analysis and a quasi-static cyclic loading analysis, and plot the load-deformation response history for each run.

A flowchart of the MATLAB-based analysis program is shown in figure 1.4.

The lumped-plasticity component analysis model for a RC member in the Opensees environment consists of the following two components:

- *An elastic beam element*: in Opensees, this element is known as *elasticBeamColumn*, and requires the definition of the member cross sectional area, elastic modulus and second moment of area, in addition to a geometric transformation type (Linear, PDelta or Corotational). Note that the entire member consists of one elastic finite element.

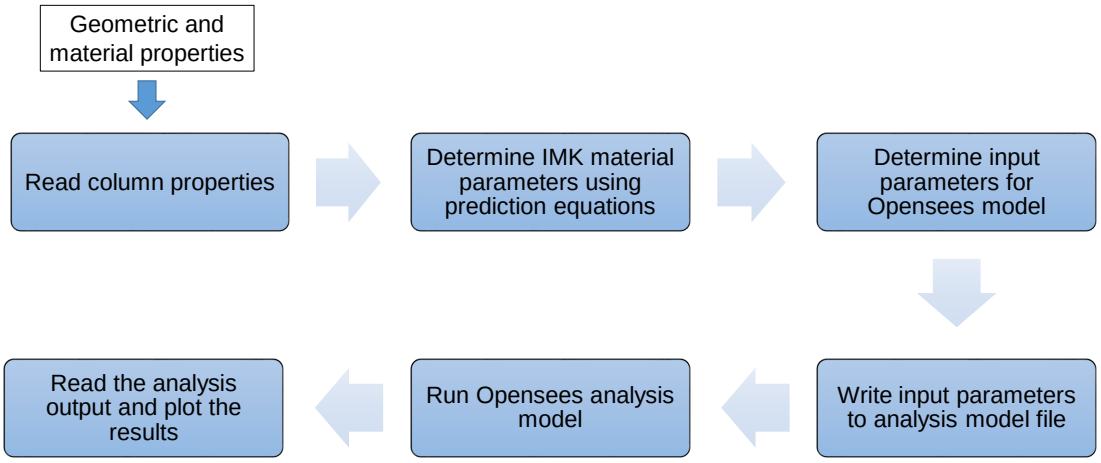

Figure 1.4: Flowchart of the MATLAB-based script driving the analysis of RC components using the Lumped Plasticity modeling approach.

- *A rotational spring model*: this model consists of a zero-length element connecting the bottom node of the beam/column member and a secondary coincident node (the fixed base node, in this case). This element is assigned a constitutive model in one direction only: rotation about the z-axis. The assigned constitutive model is the peak-oriented Ibarra-Medina-Krawinkler model *ModIMKPeakOriented*. Although the prediction equations described in the previous section are targeted towards predicting the parameters of the IMK model, some parameter adjustments are required, as outlined next.

Beam element parameters

Based on the stiffness scaling described in section 1.2, the moment of inertia of the beam element is modified to enforce the stiffness scaling as follows:

$$I_{ele} = \frac{n+1}{n} I_{mem} \tag{1.23}$$

where I_{mem} is the moment of inertia based on the structural member properties, and $n = 10$ in this model. The elastic modulus of concrete is used to approximate the elastic modulus of the element.

Spring IMK model parameters

Several of the member parameters described in the previous sections require additional adjustments to yield the appropriate input parameters for the structural analysis in Opensees. The necessary additional computations conducted in this study, if any, are outlined in the following paragraphs:

- The elastic stiffness of the spring is computed using equation (1.4) based on the elastic stiffness of the member (or the element). For the case of a cantilever member (refer to Appendix A), the elastic stiffness of the spring can be computed as:

$$K_{e-spr} = (n+1)\, K_{e-mem} = (n+1)\, \frac{3EI_{mem}}{L} \tag{1.24}$$

or

$$K_{e-spr} = nK_{e-ele} = n\frac{3EI_{ele}}{L} \tag{1.25}$$

- The yield rotational capacity is computed as:

$$\theta_y = \frac{M_y}{K_{e-mem}} \tag{1.26}$$

- The strain-hardening ratio of the spring is computed as follows:

$$\alpha_{spr} = \frac{\alpha_{mem}}{1 + n\,(1 - \alpha_{mem})} \tag{1.27}$$

where α_{mem} is the strain hardening ratio of the member, and is computed as:

$$\alpha_{mem} = \frac{K_{s-mem}}{K_{e-mem}} \tag{1.28}$$

and K_{s-mem} can be computed based on the parameters determined previously as:

$$K_{s-mem} = \frac{\theta_y}{\theta_p}\left(\frac{M_c}{M_y} - 1\right) K_{e-mem} \tag{1.29}$$

- The cyclic degradation parameter for basic strength deterioration, denoted as λ_S, required for the IMK model in Opensees is computed based on either of the cyclic degradation parameters in equation (1.21) or (1.22). For a cyclic degradation parameter based on the plastic rotation capacity, λ_S is computed as:

$$\lambda_S = \lambda\theta_p \tag{1.30}$$

For a cyclic degradation parameter based on the yield rotation capacity, λ_S can be computed as:

$$\lambda_S = \gamma\theta_y \tag{1.31}$$

In this study, equation (1.30) is used to compute the basic strength cyclic deterioration parameter λ_S. The cyclic energy dissipation capacity is internally computed in Opensees as:

$$E_t = \lambda_S M_y \tag{1.32}$$

- The cyclic degradation parameter for post-capping strength deterioration λ_C is assumed to be equal to λ_S. There are not enough experimental test data in the post-capping region to support the calibration of a different prediction equation for this type of cyclic degradation. As mentioned previously, other types of cyclic degradation (relating to the stiffness deterioration) are disabled in this study by setting the corresponding parameters λ_A and λ_K equal to zero.

- All cyclic deterioration exponent rate parameters are set equal to 1.0.

- The yield moment capacity, plastic rotation capacity, post-capping rotation capacity of the spring are the same as those predicted for the member in previous sections. The ultimate rotation capacity is the value of the rotation beyond which all the moment resisting capacity of the spring is lost. This value is assumed to be larger than (or equal to) the sum of the yield, plastic and post-capping rotation capacities, in order to avoid numerical convergence issues.

- A residual moment capacity between 1% and 10% is assumed in the simulation models (before reaching the ultimate rotation capacity), and symmetric response is assumed for both positive and negative loading directions (the parameter D in Opensees is set equal to 1.0).

Chapter 2

Reinforced Concrete Moment Frame System Modeling

This chapter describes the computational infrastructure which was created to generate the structural simulation models of RC moment frames, and integrated into a regional-scale workflow for expedient simulation of large numbers of buildings subjected to earthquake ground motions.

2.1 Overview of the computational framework

The computational framework was created using both MATLAB-based and tcl-based scripts which generate the structural model, perform the analysis by calling Opensees within MATLAB, and post-process the analysis output files. The framework, which is described schematically in figure 2.1, consists of the following components:

- A MATLAB-based main driver program which calls the necessary scripts to create the building model, run the analysis and post-process the analysis output data.
- A skeletal tcl-based RC moment frame template script which describes a "building skeleton" that can be customized to generate moment frames of any height, number of floors and bays, and member geometric and material properties.
- The Structural Model Generator (SMG), which is a MATLAB-based program that takes in the building and member information, and generates tcl-based input files which supply the structure's geometric, material and loading parameters to the skeletal template script.
- Multiple tcl-based analysis scripts, which are called depending on the specified type of analysis (pushover, cyclic, free vibration and nonlinear time history) to apply the loading and perform the analysis on the structural model, in addition to scripts which drive multiple runs for nonlinear time history simulations using multiple earthquake ground acceleration records.

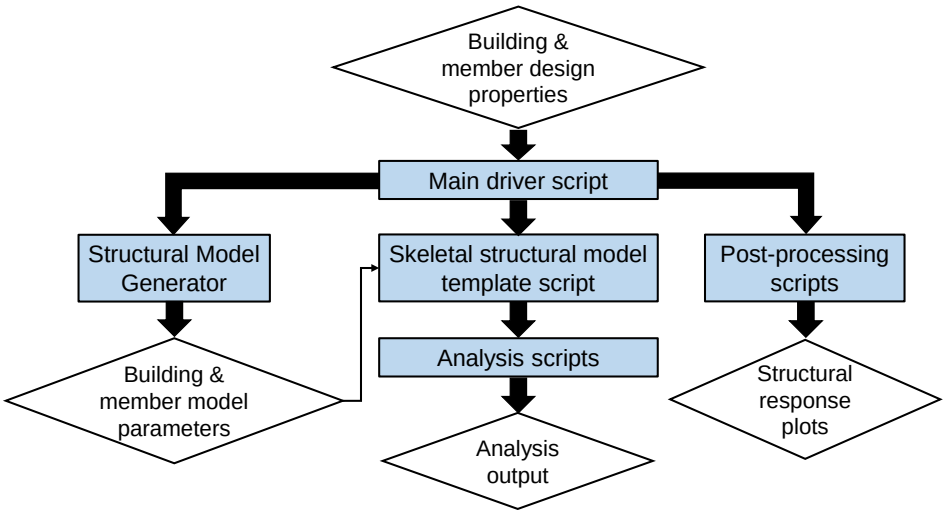

Figure 2.1: Computational workflow for the analysis of RC buildings.

The scripts used in the analysis are available at https://github.com/mmkenawy/Regional_RC_Simulations (last accessed in December, 2020).

2.2 Description of the RC moment frame simulation models

2.2.1 The Structural Model Generator tool

The main analysis script of the RC moment frame is a skeletal piece of code that parametrically generates information for each building story in a loop that depends on a set of initial data that dictates the number of stories/bays and other story information. To generate the necessary input data for this script, a MATLAB-based program, SMG, was created. The script takes as input the following:

- **Frame design parameters**: the script has the ability to accommodate a different first story height, but has otherwise uniform story heights and bay widths. A sample of the building information input sheet is presented in figure 2.2. In addition to the standard geometric building information, the input must include the following information:
  - Whether IMK model prediction equations should be used or not. If the prediction equations are not used, the input is expected to be the IMK model parameters required by the Opensees analysis model.
  - Whether or not an additional P-Delta column is to be added to the model (if the frame supports other gravity frames, for example).
  - The column and beam section assignments, which specifies the floors at which the column/beam section properties change.

Number of stories	Nstory	6
Number of bays	Nbay	5
Height of the first floor column	Hcol1	240
height of the typical column	Hcol2	156
bay width	Lbeam	288
thickness of the slab	tslab	8
whether or not the building uses IMK calibration	useIMKCalibration	1
Add a Pdelta column with additional load?	PDeltaCol	0
floors at which column section assignment begins	colassign	1,2,3,6
floors at which beam section assignment begins	beamassign	1,2,3,6
Liver load per area (from ASCE 7)	LL per area	0.0004525
Density of Reinforced Concrete	Weight per unit volumne	8.68E-05
Gravitational acceleration	g	386.2
Units (1 for N,mm and 2 for Kips, in)	units	2

Figure 2.2: Sample input of a moment frame building information for the SMG program.

  - The live load per unit area of the building, which can be determined based on the occupancy category as specified in ASCE 7-16.
  - The density of the reinforced concrete material, and gravitational acceleration in the units consistent with the other input parameters, in addition to a units specification parameter (1 for N, mm units, and 2 for kips, in units).

- **Beam and column section design information** including section dimensions, and longitudinal and transverse reinforcement. A sample input sheet for a column member is shown in figure 2.3.

The SMG then performs the following tasks:

- Reads and enforces the input geometric information and section assignments.
- Computes the member loads on all beams and columns.
- Computes the lumped plasticity model parameters of all beam-column elements and nonlinear hinges using the IMK model prediction equations described in the previous chapter.
- Writes the computed building and member geometric, constitutive and loading parameters into tcl-based files, which act as input into the building skeletal script.

Figure 2.4 shows a high-level flowchart of SMG, which also corresponds to the names of the functions that are executed when SMG is called within the analysis. The SMG program scripts are available at https://github.com/mmkenawy/Regional_RC_Simulations. It is noted that the program allows for either of the following options:

Strength of unconfined concrete	f_c	4
unconfined concrete strain at maximum stress	e_co	0.003
unconfined concrete strain at zero	e_zero_ucc	0.01
yield stress of longitudinal steel	fyl	66.8
hardening ratio of longitudinal steel	bst_tangent	0.01
elastic modulus of steel	Est	29000
yield stress of transverse steel	fyh	66.8
width of column section	b	30
depth of column section	h	30
clear cover	ccover	1.295
transverse steel bar diameter	phi_t	0.5
number of shear legs of transverse steel	legs	4
spacing of transverse steel	s	5
longitudinal steel bar diameter	phi_l	1.41
longitudinal steel volumetric ratio	rho_l	0.0379
number of longitudinal steel bars per dimension	nx	6
total number of longitudinal steel bars	ntotal	20
column length	L	240
configuration of transverse reinforcement	config	1

Figure 2.3: Sample input of the properties of a structural member for the SMG program.

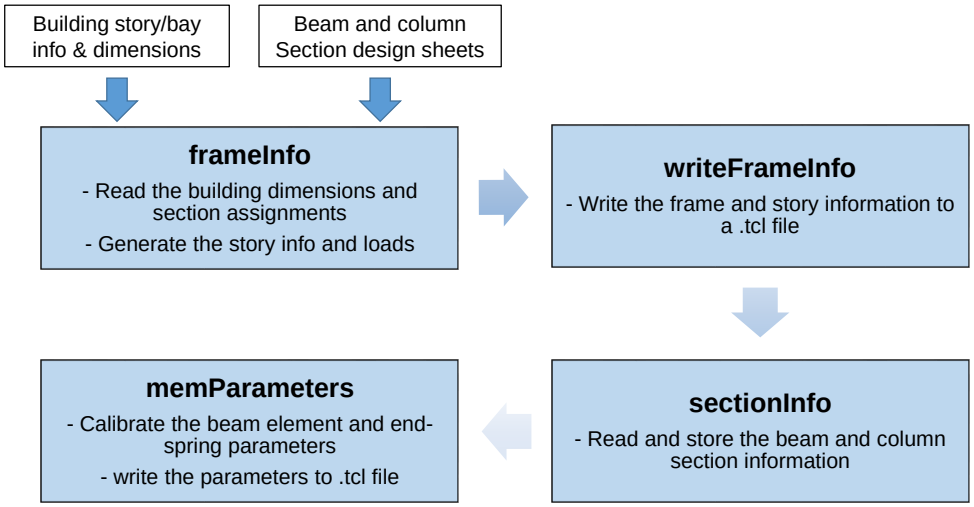

Figure 2.4: Flowchart for the Structural Model Generator program.

Elastic modulus of member	E_ele	29000
Cross-sectional area of the member	A_ele	38.5
Moment of inertia of the member	I_mem	4020
Yield moment capacity	My	20350
Ratio between maximum moment and yield moment	McMy	1.05
Cyclic strength degradation	LS	1000
post-peak cyclic strength degradation	LC	1000
plastic rotation capacity	theta_pl	0.025
post-capping rotation capacity	theta_pc	0.3
Residual moment capacity	Res	0.4
ultimate rotation capacity	theta_u	0.4

Figure 2.5: Sample input for lumped-plasticity parameters of a structural member for the SMG program.

- Option 1: Use IMK prediction equations described in the previous chapter. In this case, the member input sheets take the form shown in figure 2.3. This option corresponds to *useIMKCalibration = 1* in the building input sheet.
- Option 2: Skip using the prediction equations, and input the computed IMK model parameters directly. In this case, the member input sheets take the form in figure 2.5. This option corresponds to *useIMKCalibration = 0* in the building input sheet.

2.2.2 Moment frame model properties

The generated moment frames are two-dimensional structural models with equal-width bays and equal-height floors, except for the first floor which can have a different height. The following are some of the important aspects of the RC moment frames created using the SMG:

Beam and column nonlinear springs

At every beam-column intersection node, and at the base of the column members, additional nodes are defined for creating the nonlinear springs. The rotational spring is created by defining a zero-length element connecting the two coincident nodes. Rotation about the z-axis is the only assigned DOF to the zero-length element, and the IMK material model discussed in the previous chapter is the constitutive model assigned to this rotational DOF.

Boundary conditions

The generated frames are assumed to have a fixed-base condition, therefore neglecting the rotational flexibility of the footings, and potential soil-structure interaction effects. In future iterations,

it is planned to incorporate the effects of the rotational flexibility of grade beams and the soil beneath the structure by adding rotational springs at the base of the first floor column members. In addition, a rigid diaphragm assumption is enforced by creating an equal-DOF constraint on the nodes of each individual level of the frame.

Gravity loading

It is initially assumed that the frame supports only its own weight and tributary load for the purposes of both gravity and seismic loading analyses. This assumption implies that the frame is part of a building in which the lateral loads are resisted by all frames. The gravity load on the frame is computed based on the input slab thickness, density of reinforced concrete, member section dimensions, building geometry and specified live load per ASCE 7-16. These loads are applied as distributed loads to all beam and column members in the model. In addition, the SMG has the capability to add a 'P-Delta column' to the model to incorporate additional loads supported by the modeled frame for the purpose of seismic loading. This feature can be added by turning the P-Delta column switch on, thereby assuming that the modeled lateral load-resisting frame supports other gravity frames.

2.3 Regional simulation framework

The structural analysis infrastructure presented in the previous sections was integrated into a regional-scale simulations framework. The overarching framework loops over a number of ground motion acceleration records and applies them to a given 2D structural frame model, either sequentially (on a single computer) or in parallel (on a parallel computing machine). The workflows described in this chapter enable running thousands of nonlinear time history simulations in parallel using the National Energy Research Scientific Computing Center (NERSC) CORI machine.

The logic of the workflow described in this section is shown in figure 2.6. For performing simulations on a local single-memory computer, a MATLAB based interface is used for handling the user-input and post-processing operations, and the simulations are conducted via the Opensees command line. The following tasks are performed within the framework:

- Convert the ground motion acceleration time history files to be read by the structural models. It is noted that the ground motion records in this study are synthetic records which have been generated as output of the software SW4 (Seismic Waves, fourth order) [Sjögreen and Petersson, 2012] by Arben Pitarka (Lawrence Livermore National Laboratory (LLNL)) using three-dimensional high resolution simulations of fault rupture scenarios.

- Process the user input for the analysis, which consists of the building name (among the available library of RC buildings), the ground motion set (among the available ground motion simulations sets) and the ground motion acceleration component of choice (either fault-normal or fault-parallel).

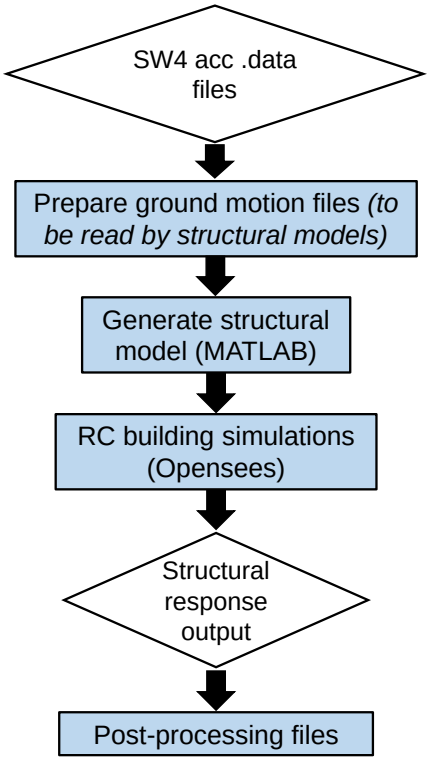

Figure 2.6: Workflow for running a large number of nonlinear time history simulations.

- Generate the structural model based on the supplied building data, loop over the ground motion records, apply each record as a time-series excitation to the Opensees building model, and generate output information consisting primarily of interstory drifts.
- Run a post-processing program which extracts the maximum drifts from the output files, and creates several types of plots to facilitate viewing and analyzing the data.

The post-processing script for the multiple-analysis framework focuses on comparing the response of a certain structure to different ground motions, with the purpose of developing insight on the variability of structural risk over a particular region. The structural response quantities of interest in this case are the total building drift ratios and the interstory drift ratios. The post-processing program is used to produce a variety of plots for each simulation set, including 2D map representations of interstory drifts over a region, variation of the drifts along the parallel or normal distance to the fault, and correlation plots between structural demands and ground motion intensity measures.

To run thousands of simulations in a reasonable time period, the preceding workflow was adapted to execute on parallel-memory computers. The CORI machine at NERSC was utilized to run structural simulations in parallel on a large number of computer nodes. To enable efficient creation and submission of computing jobs on CORI, Python [Van Rossum and Drake Jr, 1995] and shell scripts were created to automate the generation the simulation models, and initiation of the simulations remotely. The Task Farmer capability on CORI was utilized to distribute the simulations over thousands of CPU cores. The components of this workflow, and detailed instructions on its usage are available at https://github.com/mmkenawy/Regional_RC_Simulations (last accessed in December, 2020).

Chapter 3

Verification of the Reinforced Concrete Building Analysis Framework

The components of the RC building analysis workflow were subjected to an incremental verification process. The major components of the verification study are summarized in figure 3.1, and the following subsections discuss some of the verification problems and their results. The study consists of the following components:

1. Verification of the IMK model prediction equations [Haselton et al., 2016], which predict the parameters of the modified Ibarra-Medina-Krawinkler peak-oriented deterioration model for RC structural components.

2. Verification of the lumped plasticity component analysis model, with focus on assessing the ability of the LP models to reproduce the response of RC columns to quasi-static cyclic loading, by comparing the simulated response against available experimental test data (it is worth noting that the available test data is a subset of the database used to calibrate the model by Haselton et al. [2016]; therefore, the comparison in this study does not serve to generate any additional validation of the model, but merely verifies that the model implementation is correct). In addition, the predictions of the LP component models are compared with the predictions of distributed plasticity models, and conclusions are drawn regarding the performance of each type of modeling approach. The results of these comparisons are summarized in section 3.1 of this chapter.

3. Verification of the RC moment frame analysis scripts, with focus on testing the performance of the analysis program created for simulating the response of RC moment frames to different types of loading. In this part of the study, the parametric SMG program was used to simulate different RC moment frame buildings (a two-story, a six-story and a ten-story frame), and perform different types of analyses on each building model (static pushover, eigenvalue analysis, dynamic free vibration, dynamic pushover analysis and dynamic nonlinear time history analysis). The output of all analyses was compared against theoretical calculations in some of the simpler analysis cases, or against the output of independently-created simula-

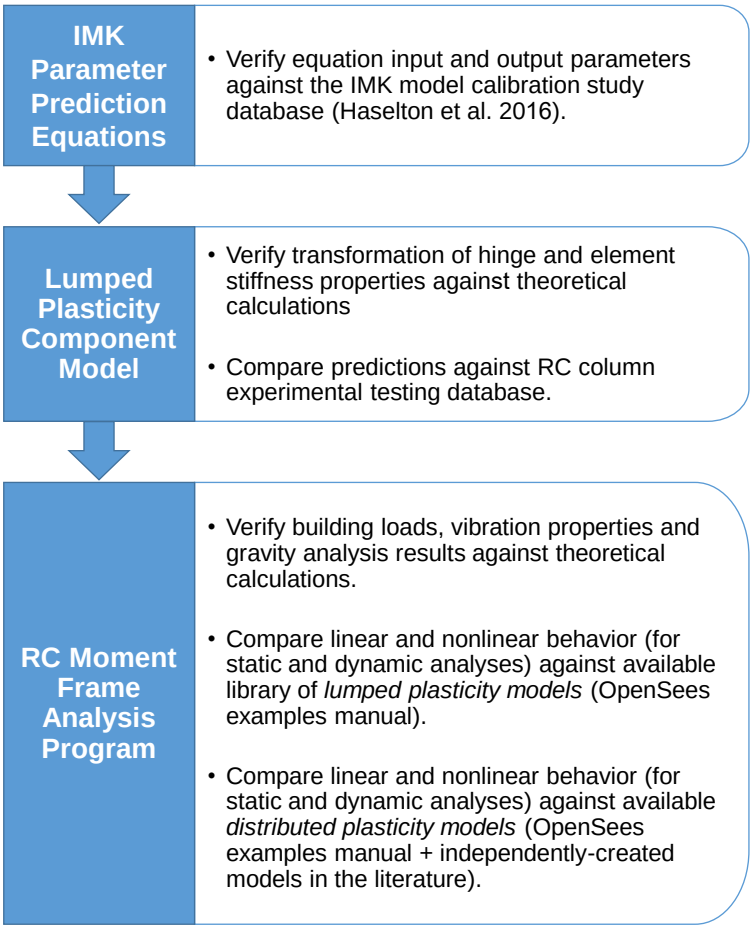

Figure 3.1: Description of the verification study conducted on the RC lumped plasticity analysis framework.

tion models that are available in the OpenSees examples manual or in the literature. Sample results of these comparisons are presented in sections 3.2 through 3.4 of this chapter.

3.1 Reinforced Concrete lumped-plasticity component model verification

3.1.1 Comparison against experimental test data

The performance of the IMK parameter-prediction equations and analysis scripts described in the previous chapters was assessed against a database of experimental observations; this database includes 24 RC columns that were tested in the laboratory under constant axial load and reversed

quasi-static cyclic loading. The columns from the experimental database are shown in table 3.1, which lists the relevant geometric and loading parameters of each specimen. The predicted response (by the equations) of a representative sample of the column specimens is overlaid on the observed specimen response in figures 3.2 through 3.15. The primary observation for all specimens is that the prediction equations tend to perform reasonably well, and produce satisfactory agreement with the experimental data if the component does not experience significant strength loss (in-cycle degradation or cycle-to-cycle degradation). In cases where significant degradation is present, the simulation model tends to produce poor predictions of the load-deformation response in the later stages of the inelastic component behavior.

Table 3.1: Properties of the benchmark column specimens

Specimen #	Reference	Length L (mm)	Section Depth d (mm)	Axial Load Ratio $\eta = \frac{P}{f_c A_g}$	Unconfined Concrete Strength f_c (MPa)	Transverse Reinf. Ratio ρ_t	Longitudinal Reinf. Ratio ρ_l	Bond-Slip Parameter a_{sl}
1	Ang et al. [1981], No. 3	1600	400	0.38	23.6	0.028	0.015	0
2	Ang et al. [1981], No. 4	1600	400	0.21	25.0	0.022	0.015	0
3	Atalay and Penzien [1975], No. 11	1676	305	0.28	31.0	0.015	0.016	0
4	Atalay and Penzien [1975], No. 10	1676	305	0.27	32.4	0.009	0.016	0
5	Atalay and Penzien [1975], No. 6S1	1676	305	0.18	31.8	0.009	0.016	0
6	Gill et al. [1979], No. 1	1200	550	0.26	23.1	0.015	0.018	0
7	Gill et al. [1979], No. 3	1200	550	0.42	21.4	0.018	0.018	0
8	Kanda et al. [1988], 85STC-1	750	250	0.11	27.9	0.011	0.016	1
9	Kono and Watanabe [2000], D1N60	625	242	0.66	37.6	0.015	0.024	1
10	Kono and Watanabe [2000], D1N30	625	242	0.33	37.6	0.015	0.024	1
11	Saatcioglu and Grira [1999], BG-1	1645	350	0.43	34.0	0.010	0.020	1
12	Saatcioglu and Grira [1999], BG-2	1645	350	0.43	34.0	0.020	0.020	1
13	Saatcioglu and Grira [1999], BG-3	1645	350	0.20	34.0	0.020	0.020	1
14	Saatcioglu and Grira [1999], BG-4	1645	350	0.46	34.0	0.013	0.029	1
15	Saatcioglu and Grira [1999], BG-8	1645	350	0.23	34.0	0.013	0.029	1
16	Soesianawati et al. [1986], No. 1	1600	400	0.10	46.5	0.009	0.015	0
17	Soesianawati et al. [1986], No. 2	1600	400	0.30	44.0	0.012	0.015	0
18	Soesianawati et al. [1986], No. 3	1600	400	0.30	44.0	0.008	0.015	0
19	Soesianawati et al. [1986], No. 4	1600	400	0.30	40.0	0.006	0.015	0
20	Tanaka and Park [1990], No. 1	1600	400	0.20	25.6	0.026	0.016	0
21	Tanaka and Park [1990], No. 7	1650	550	0.30	32.1	0.021	0.013	1
22	Watson and Park [1989], No. 5	1600	400	0.50	41.0	0.014	0.015	0
23	Watson and Park [1989], No. 9	1600	400	0.70	40.0	0.048	0.015	0
24	Zahn et al. [1985], No. 7	1600	400	0.22	28.3	0.016	0.015	0

3.1.2 Comparison against distributed plasticity models

The ability of the calibrated IMK component models to capture the capacity of RC components is compared against the distributed plasticity (DP) modeling approach. It is noted that, the comparison is only valid in the early stages of a nonlinear analysis, because the distributed plasticity approach is susceptible to mesh sensitivity issues in the later stages, and is therefore not appropriate for use as a reference.

An example of such a comparison is provided in figure 3.16a for a typical RC column, from which the following observations can be made:

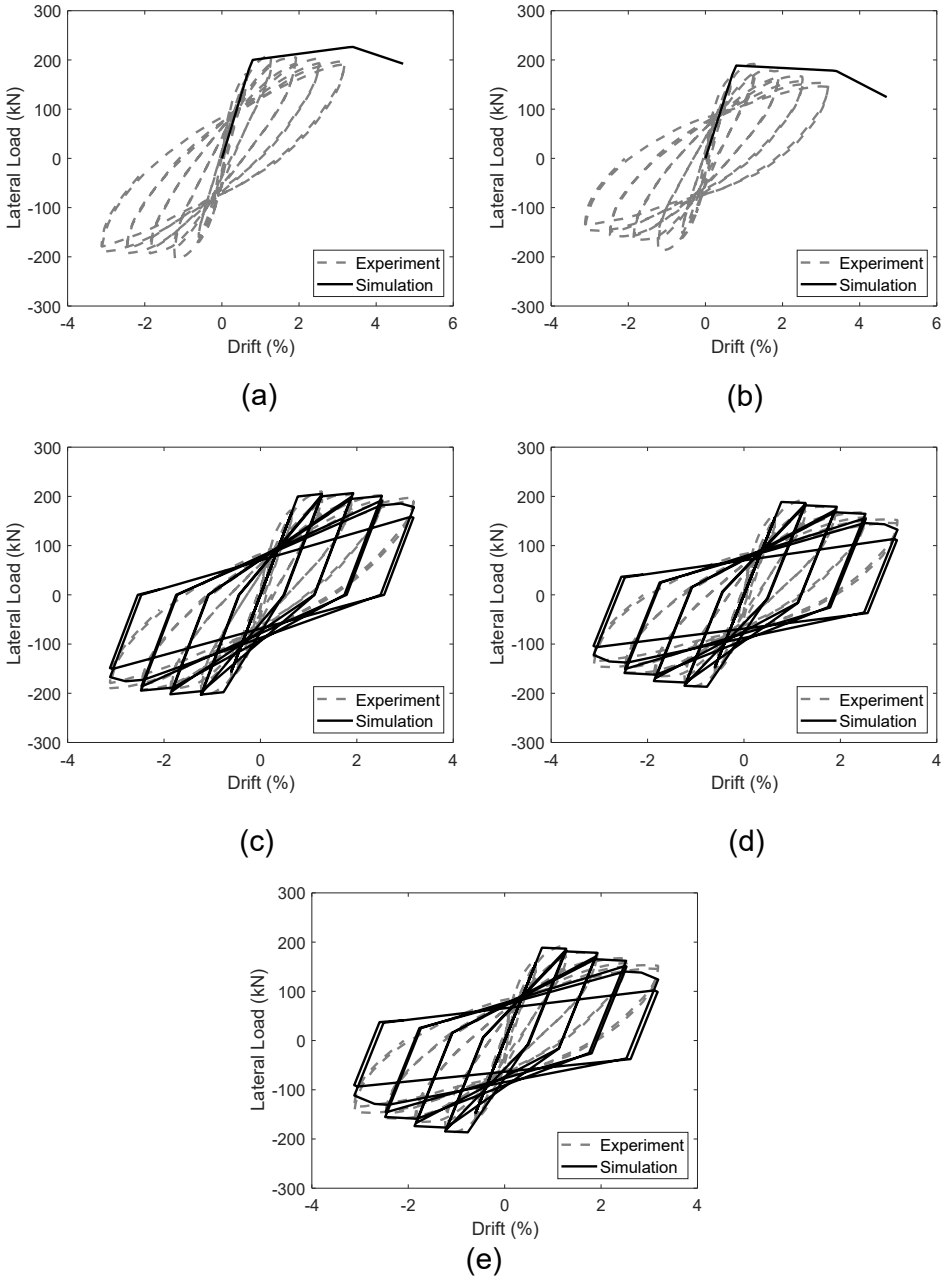

Figure 3.2: Simulated and observed member response for specimen Ang et al. [1981], No. 3: a) backbone monotonic response without P-Delta effects; b) backbone monotonic response with P-Delta effects; c) quasi-static cyclic response without P-Delta effects; d) quasi-static cyclic response with P-Delta effects - using a plastic rotation capacity-based cyclic degradation; e) d) quasi-static cyclic response with P-Delta effects - using a yield rotation capacity-based cyclic degradation.

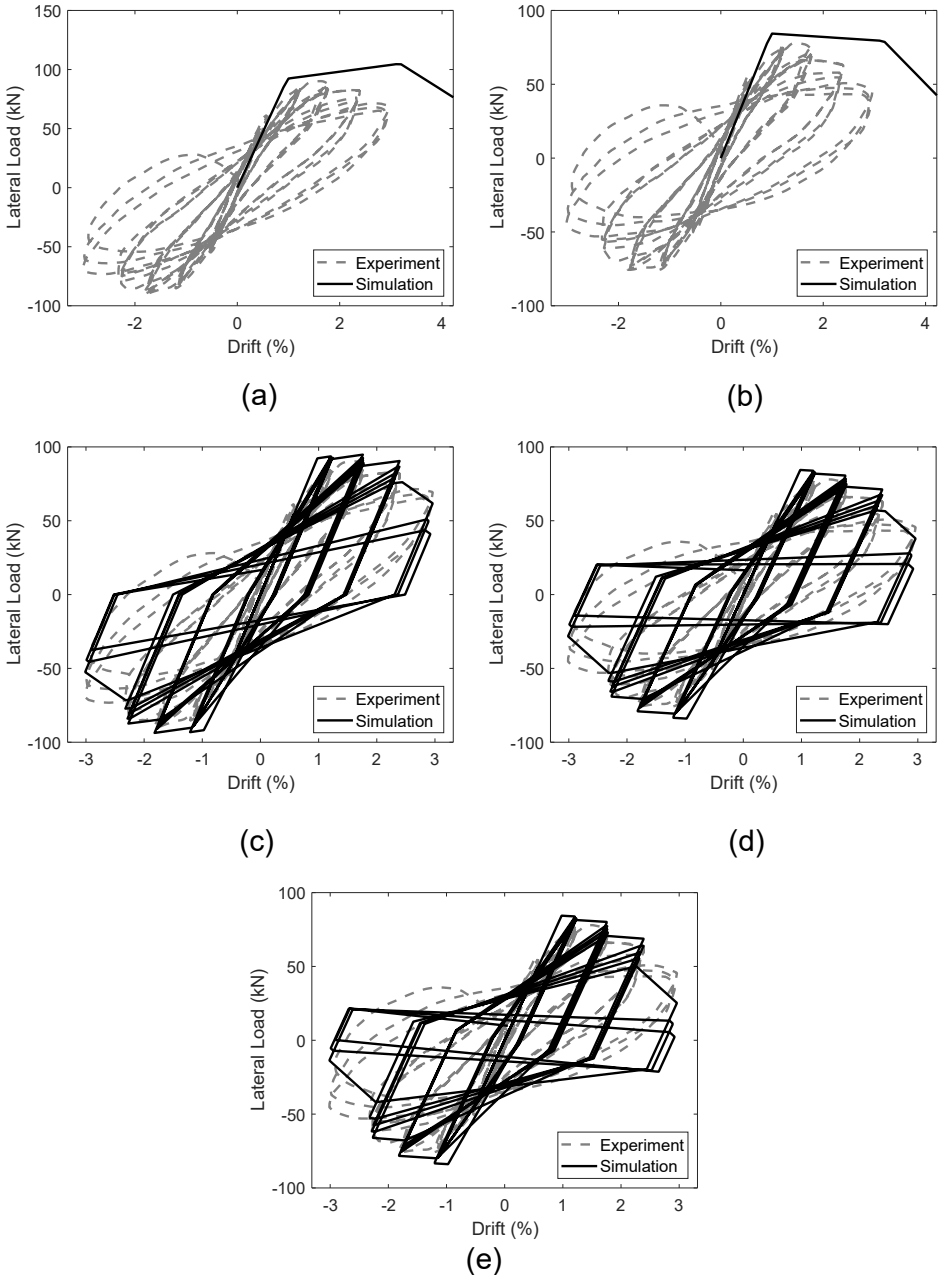

Figure 3.3: Simulated and observed member response for specimen Atalay and Penzien [1975], No. 10: a) backbone monotonic response without P-Delta effects; b) backbone monotonic response with P-Delta effects; c) quasi-static cyclic response without P-Delta effects; d) quasi-static cyclic response with P-Delta effects - using a plastic rotation capacity-based cyclic degradation; e) d) quasi-static cyclic response with P-Delta effects - using a yield rotation capacity-based cyclic degradation.

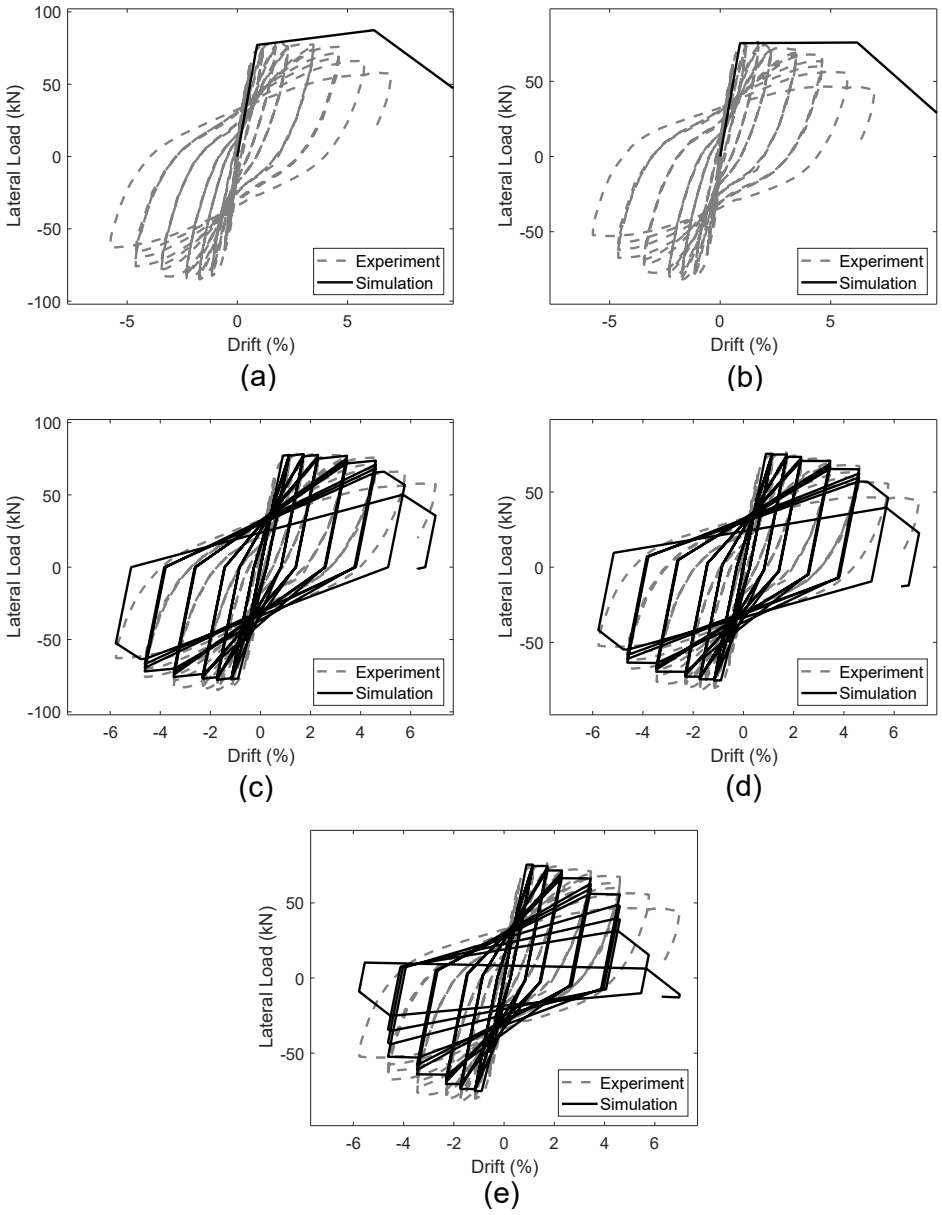

Figure 3.4: Simulated and observed member response for specimen Kanda et al. [1988], 85STC-1: a) backbone monotonic response without P-Delta effects; b) backbone monotonic response with P-Delta effects; c) quasi-static cyclic response without P-Delta effects; d) quasi-static cyclic response with P-Delta effects - using a plastic rotation capacity-based cyclic degradation; e) d) quasi-static cyclic response with P-Delta effects - using a yield rotation capacity-based cyclic degradation.

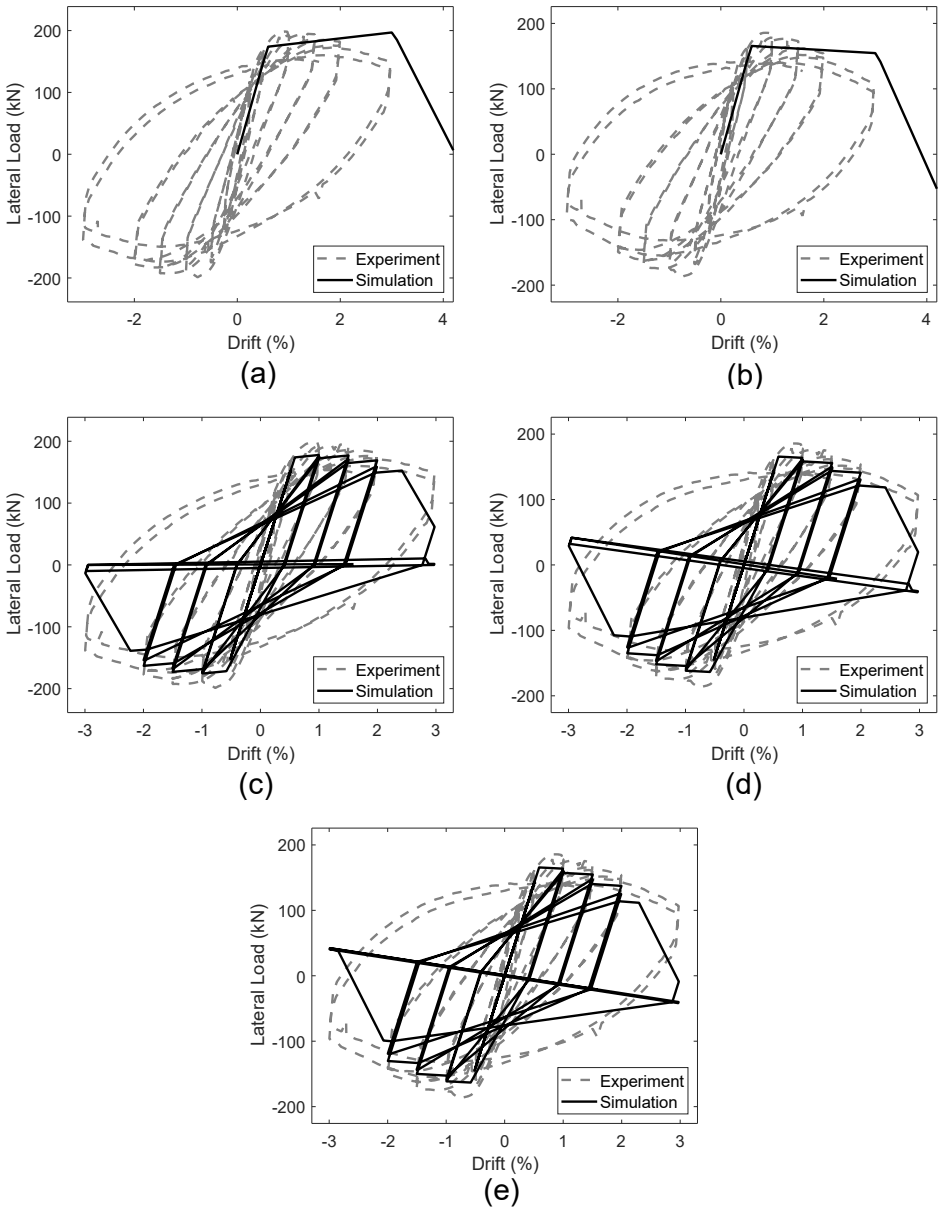

Figure 3.5: Simulated and observed member response for specimen Kono and Watanabe [2000], D1N60: a) backbone monotonic response without P-Delta effects; b) backbone monotonic response with P-Delta effects; c) quasi-static cyclic response without P-Delta effects; d) quasi-static cyclic response with P-Delta effects - using a plastic rotation capacity-based cyclic degradation; e) d) quasi-static cyclic response with P-Delta effects - using a yield rotation capacity-based cyclic degradation.

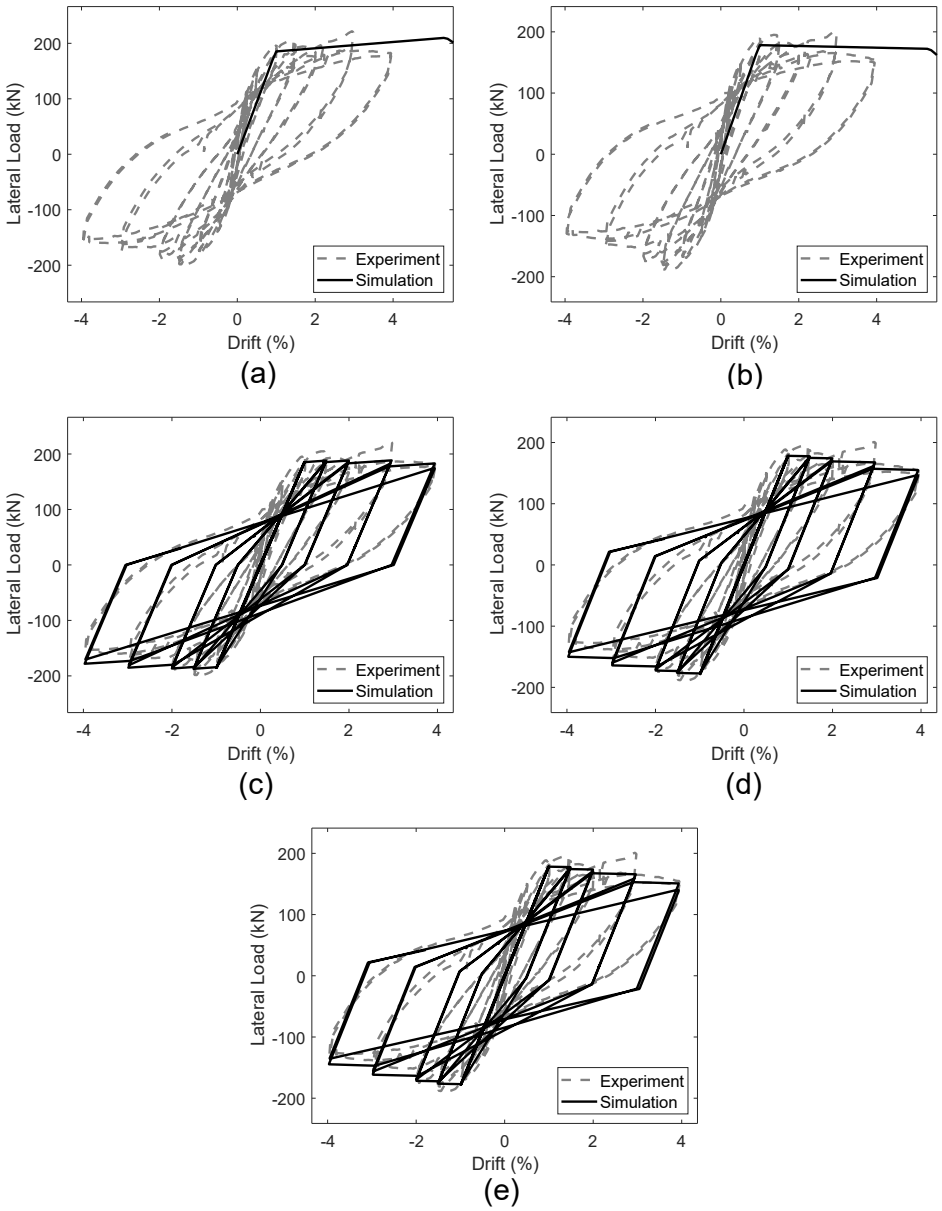

Figure 3.6: Simulated and observed member response for specimen Kono and Watanabe [2000], D1N30: a) backbone monotonic response without P-Delta effects; b) backbone monotonic response with P-Delta effects; c) quasi-static cyclic response without P-Delta effects; d) quasi-static cyclic response with P-Delta effects - using a plastic rotation capacity-based cyclic degradation; e) d) quasi-static cyclic response with P-Delta effects - using a yield rotation capacity-based cyclic degradation.

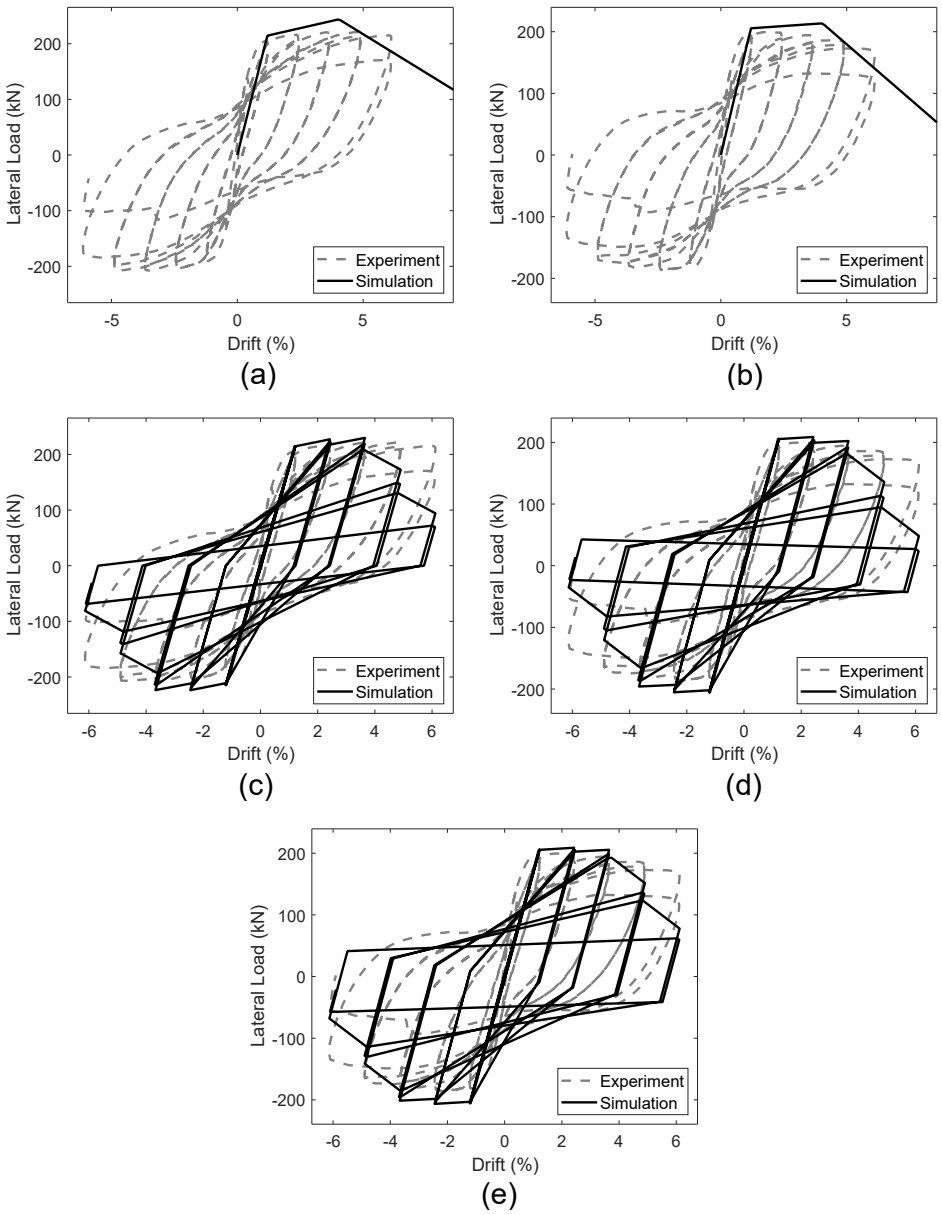

Figure 3.7: Simulated and observed member response for specimen Soesianawati et al. [1986], No. 1: a) backbone monotonic response without P-Delta effects; b) backbone monotonic response with P-Delta effects; c) quasi-static cyclic response without P-Delta effects; d) quasi-static cyclic response with P-Delta effects - using a plastic rotation capacity-based cyclic degradation; e) d) quasi-static cyclic response with P-Delta effects - using a yield rotation capacity-based cyclic degradation.

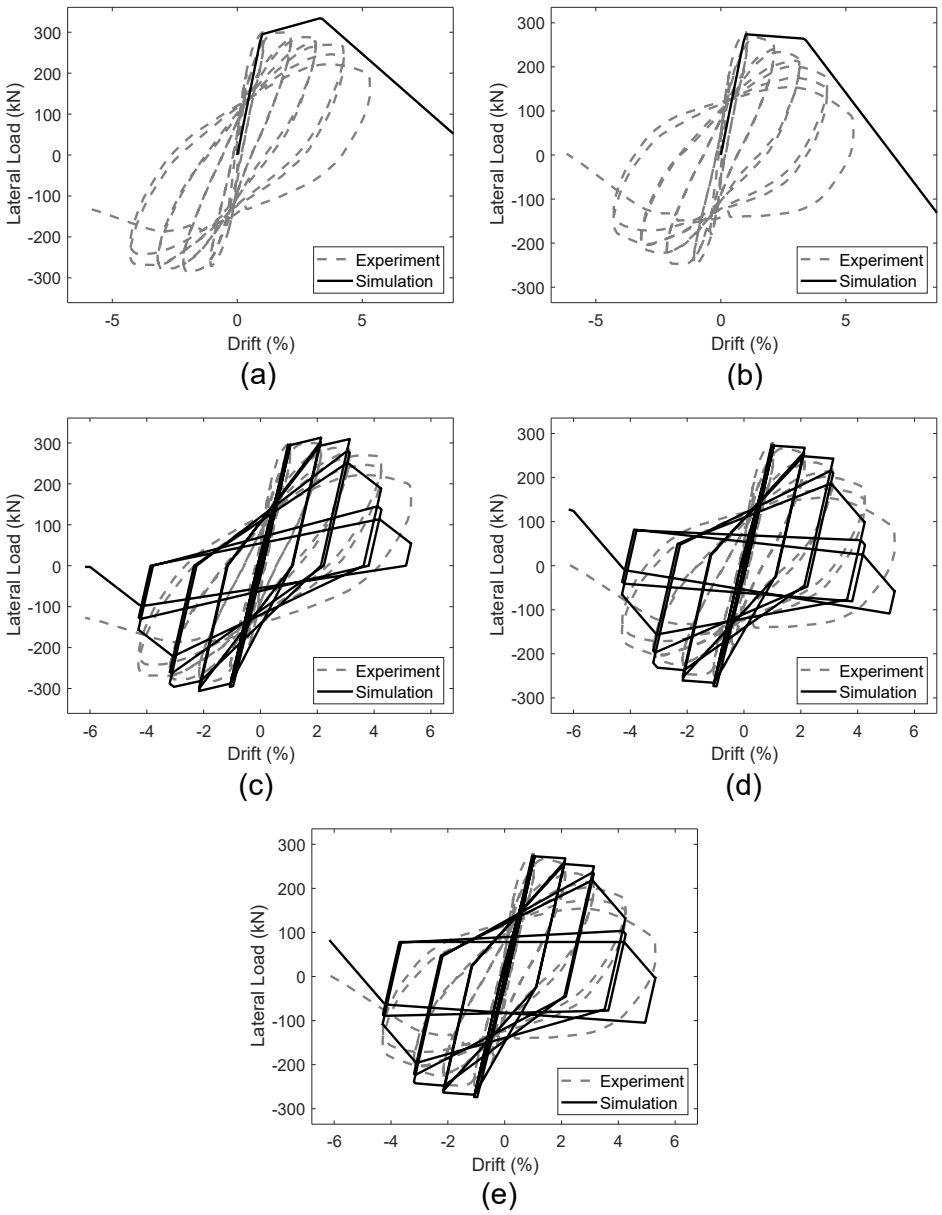

Figure 3.8: Simulated and observed member response for specimen Soesianawati et al. [1986], No. 2: a) backbone monotonic response without P-Delta effects; b) backbone monotonic response with P-Delta effects; c) quasi-static cyclic response without P-Delta effects; d) quasi-static cyclic response with P-Delta effects - using a plastic rotation capacity-based cyclic degradation; e) d) quasi-static cyclic response with P-Delta effects - using a yield rotation capacity-based cyclic degradation.

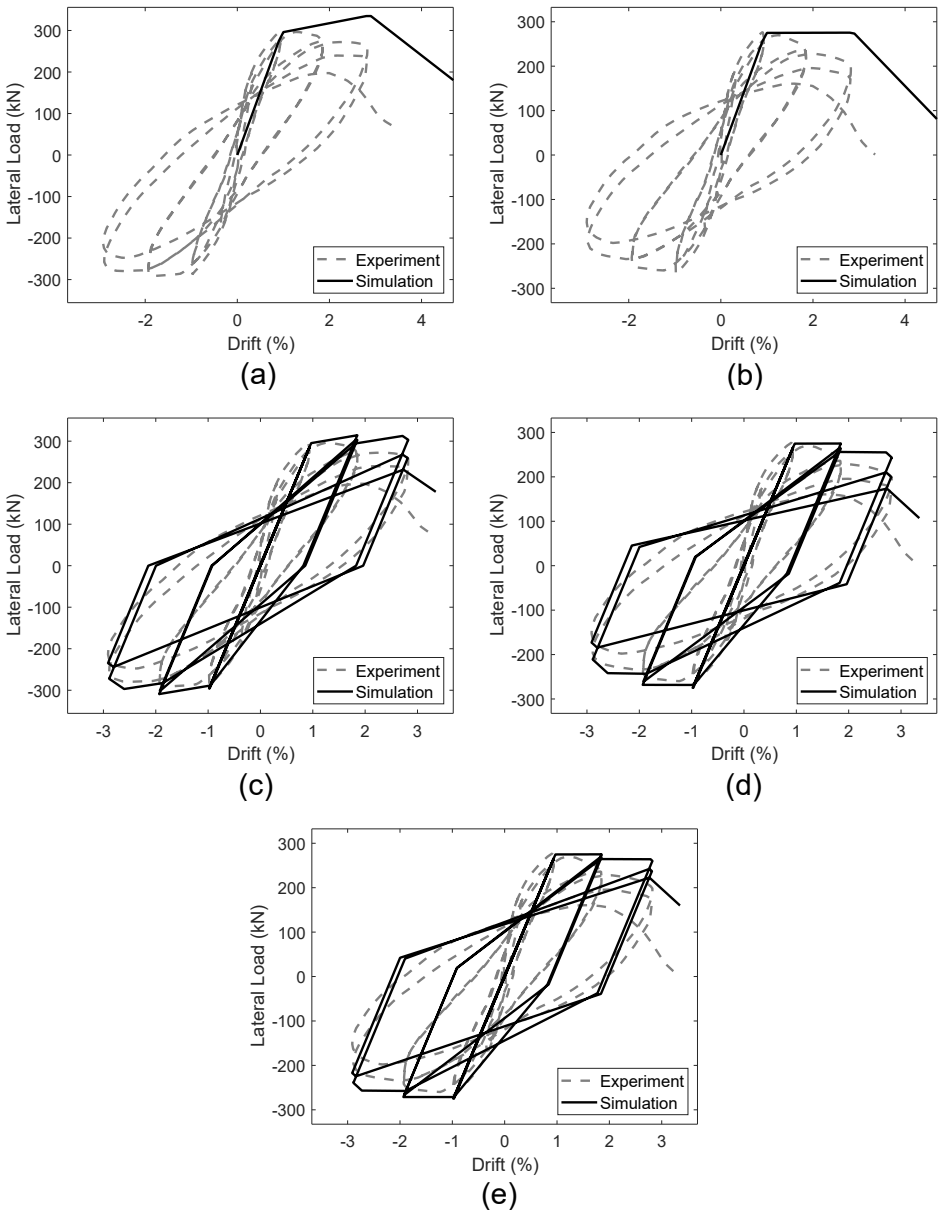

Figure 3.9: Simulated and observed member response for specimen Soesianawati et al. [1986], No. 3: a) backbone monotonic response without P-Delta effects; b) backbone monotonic response with P-Delta effects; c) quasi-static cyclic response without P-Delta effects; d) quasi-static cyclic response with P-Delta effects - using a plastic rotation capacity-based cyclic degradation; e) d) quasi-static cyclic response with P-Delta effects - using a yield rotation capacity-based cyclic degradation.

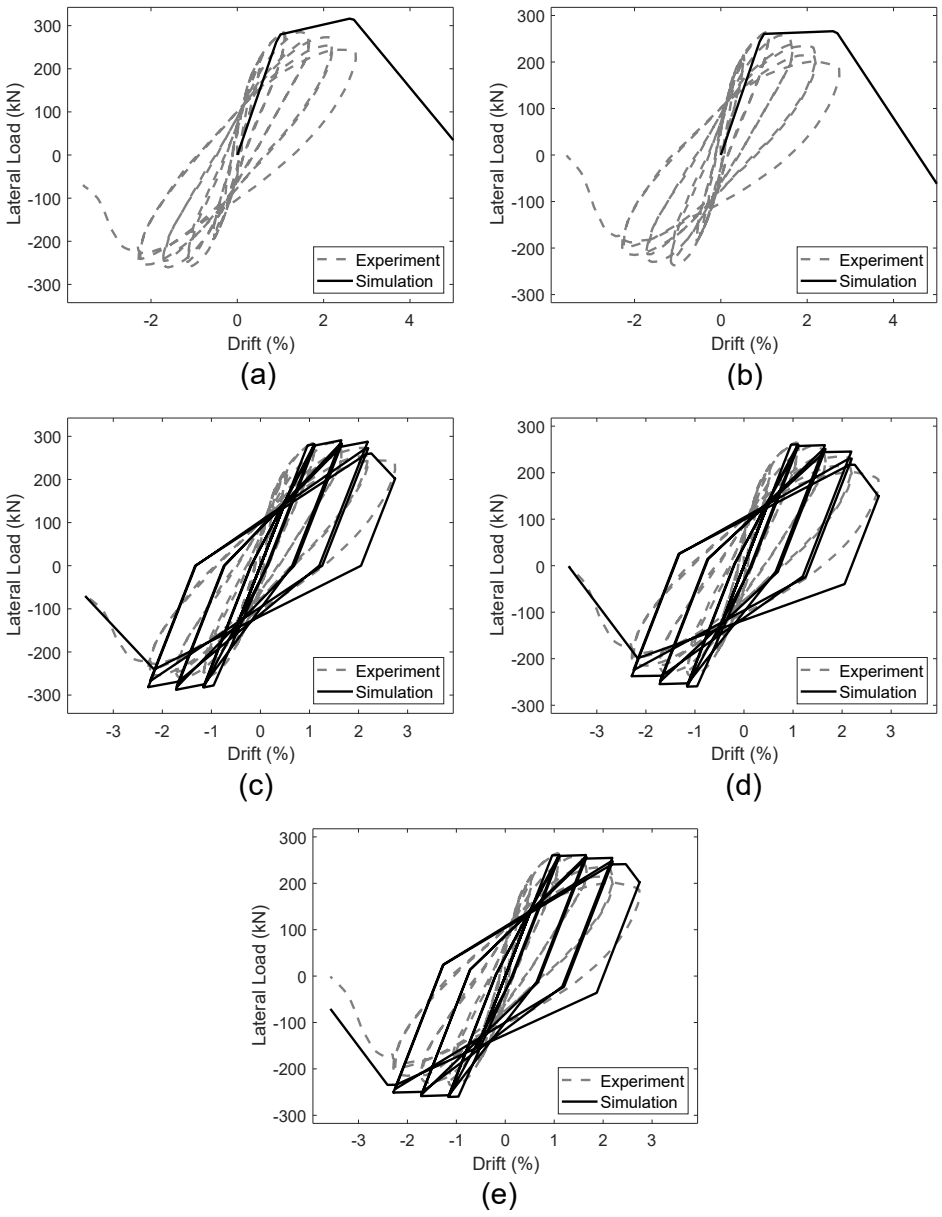

Figure 3.10: Simulated and observed member response for specimen Soesianawati et al. [1986], No. 4: a) backbone monotonic response without P-Delta effects; b) backbone monotonic response with P-Delta effects; c) quasi-static cyclic response without P-Delta effects; d) quasi-static cyclic response with P-Delta effects - using a plastic rotation capacity-based cyclic degradation; e) d) quasi-static cyclic response with P-Delta effects - using a yield rotation capacity-based cyclic degradation.

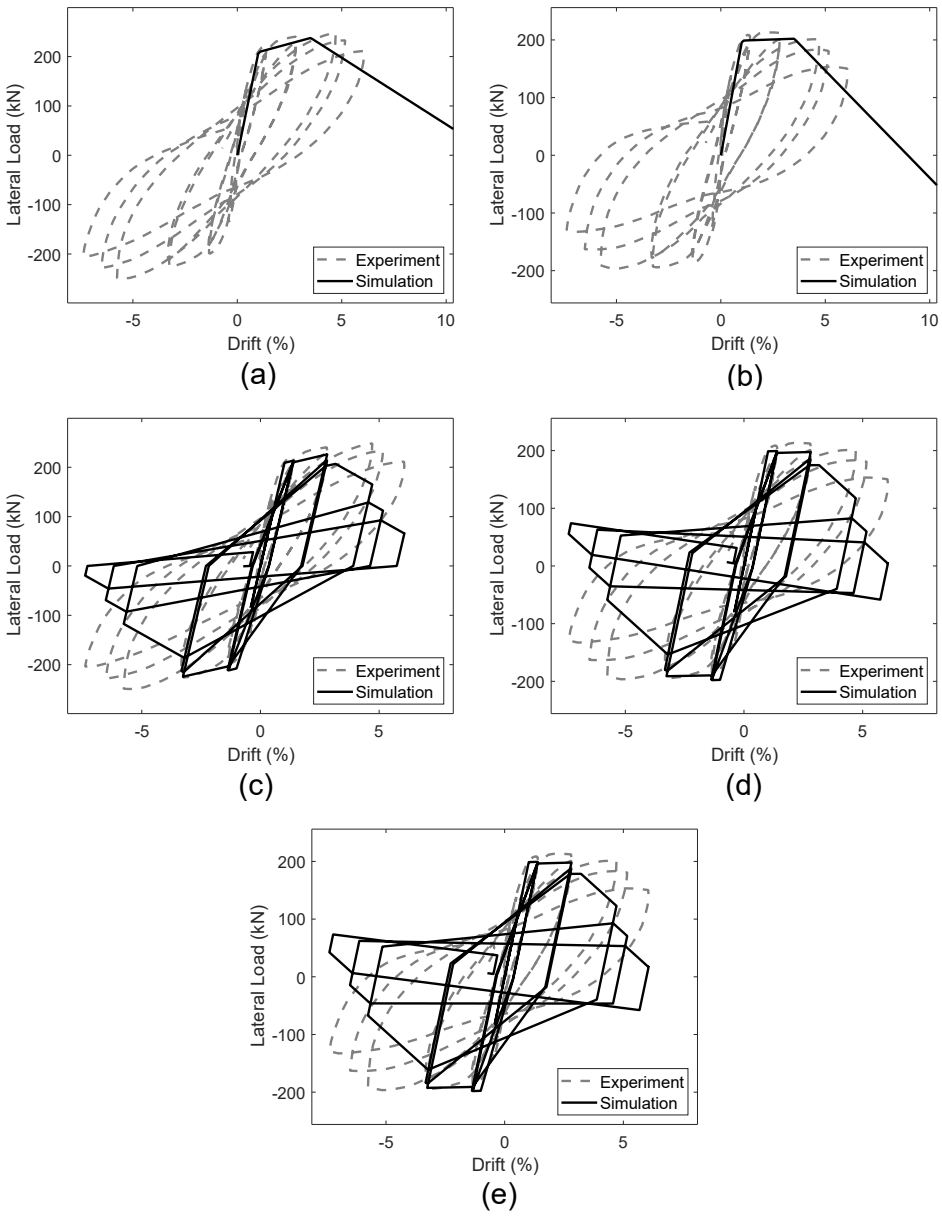

Figure 3.11: Simulated and observed member response for specimen Zahn et al. [1985], No. 7: a) backbone monotonic response without P-Delta effects; b) backbone monotonic response with P-Delta effects; c) quasi-static cyclic response without P-Delta effects; d) quasi-static cyclic response with P-Delta effects - using a plastic rotation capacity-based cyclic degradation; e) d) quasi-static cyclic response with P-Delta effects - using a yield rotation capacity-based cyclic degradation.

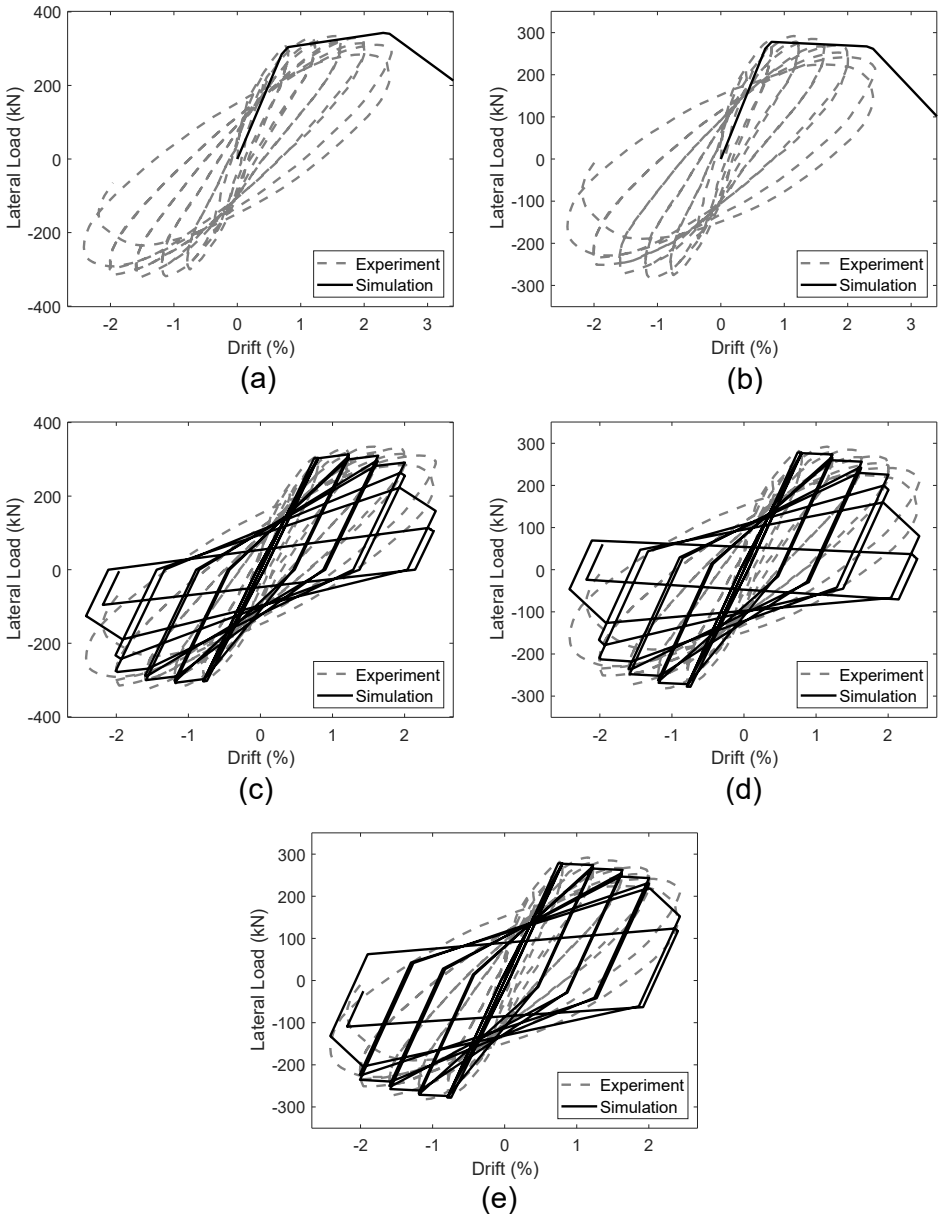

Figure 3.12: Simulated and observed member response for specimen Watson and Park [1989], No. 5: a) backbone monotonic response without P-Delta effects; b) backbone monotonic response with P-Delta effects; c) quasi-static cyclic response without P-Delta effects; d) quasi-static cyclic response with P-Delta effects - using a plastic rotation capacity-based cyclic degradation; e) d) quasi-static cyclic response with P-Delta effects - using a yield rotation capacity-based cyclic degradation.

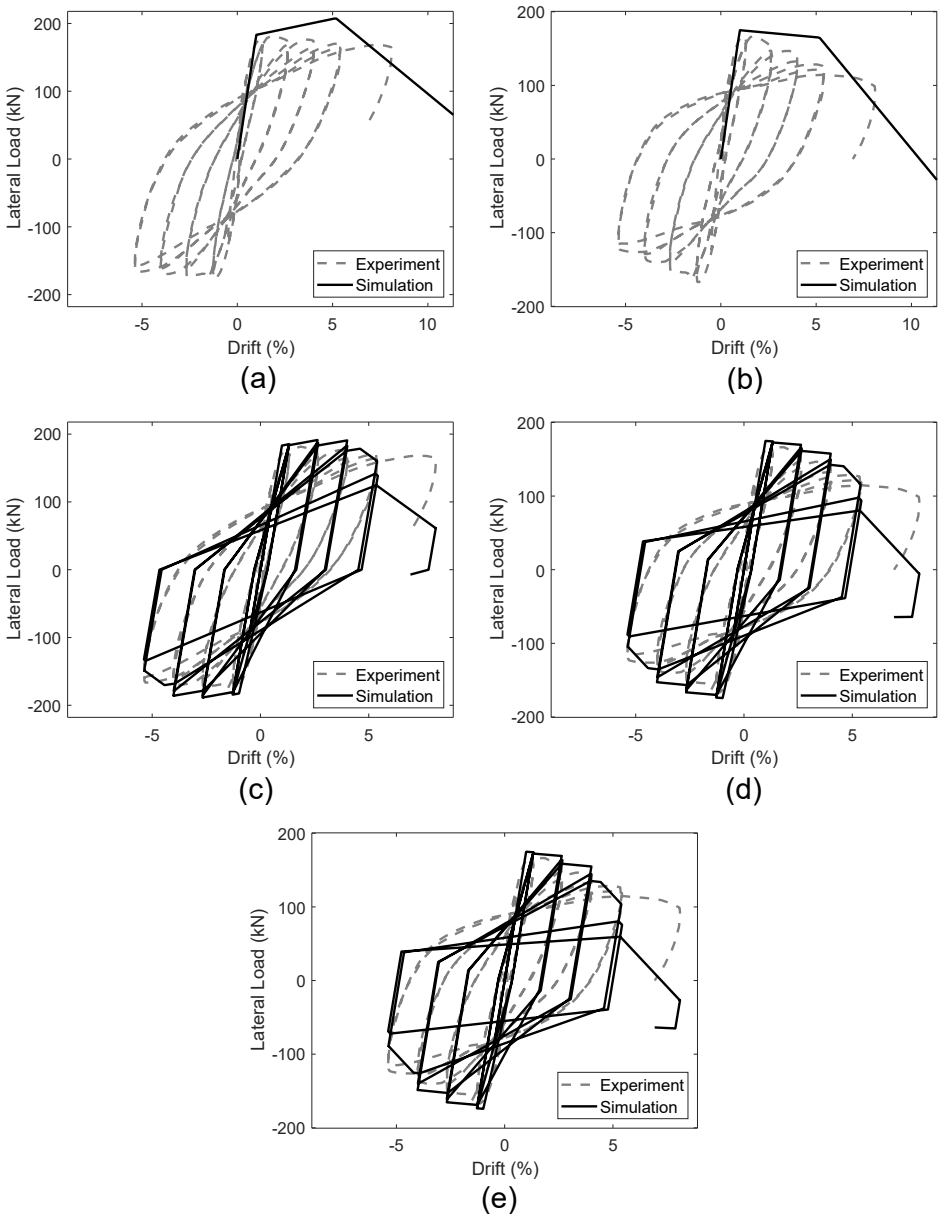

Figure 3.13: Simulated and observed member response for specimen Tanaka and Park [1990], No. 1: a) backbone monotonic response without P-Delta effects; b) backbone monotonic response with P-Delta effects; c) quasi-static cyclic response without P-Delta effects; d) quasi-static cyclic response with P-Delta effects - using a plastic rotation capacity-based cyclic degradation; e) d) quasi-static cyclic response with P-Delta effects - using a yield rotation capacity-based cyclic degradation.

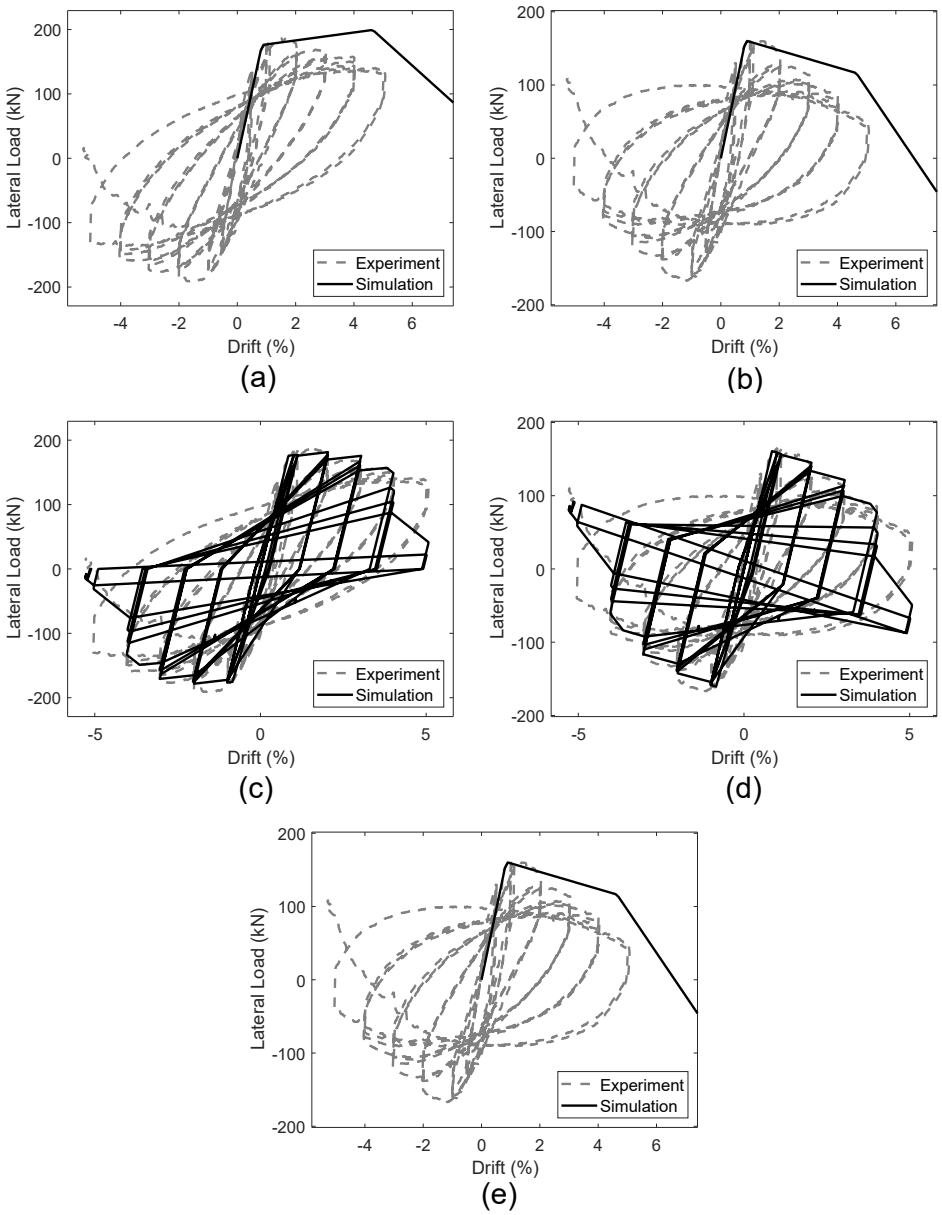

Figure 3.14: Simulated and observed member response for specimen Saatcioglu and Grira [1999], BG-2: a) backbone monotonic response without P-Delta effects; b) backbone monotonic response with P-Delta effects; c) quasi-static cyclic response without P-Delta effects; d) quasi-static cyclic response with P-Delta effects - using a plastic rotation capacity-based cyclic degradation; e) d) quasi-static cyclic response with P-Delta effects - using a yield rotation capacity-based cyclic degradation.

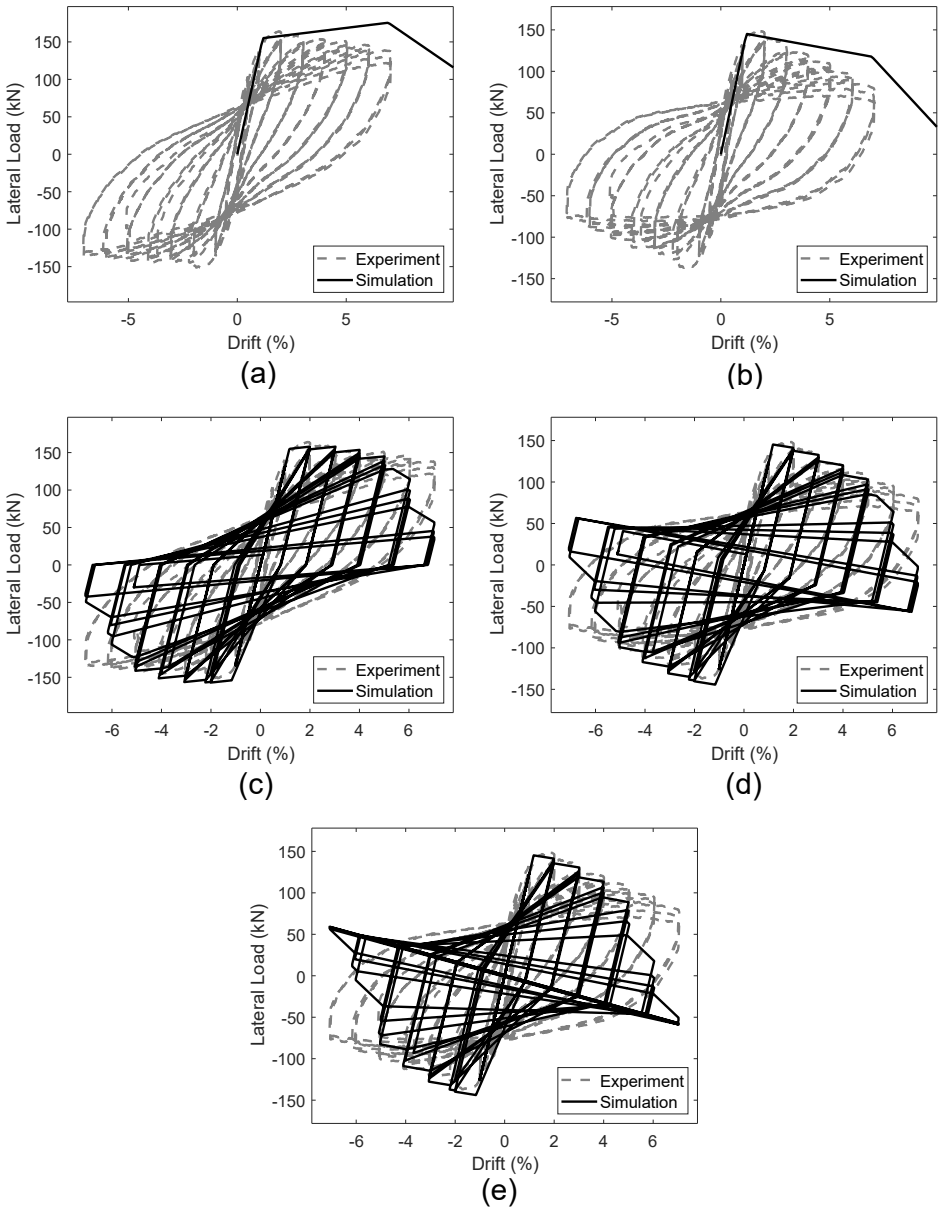

Figure 3.15: Simulated and observed member response for specimen Saatcioglu and Grira [1999], BG-3: a) backbone monotonic response without P-Delta effects; b) backbone monotonic response with P-Delta effects; c) quasi-static cyclic response without P-Delta effects; d) quasi-static cyclic response with P-Delta effects - using a plastic rotation capacity-based cyclic degradation; e) d) quasi-static cyclic response with P-Delta effects - using a yield rotation capacity-based cyclic degradation.

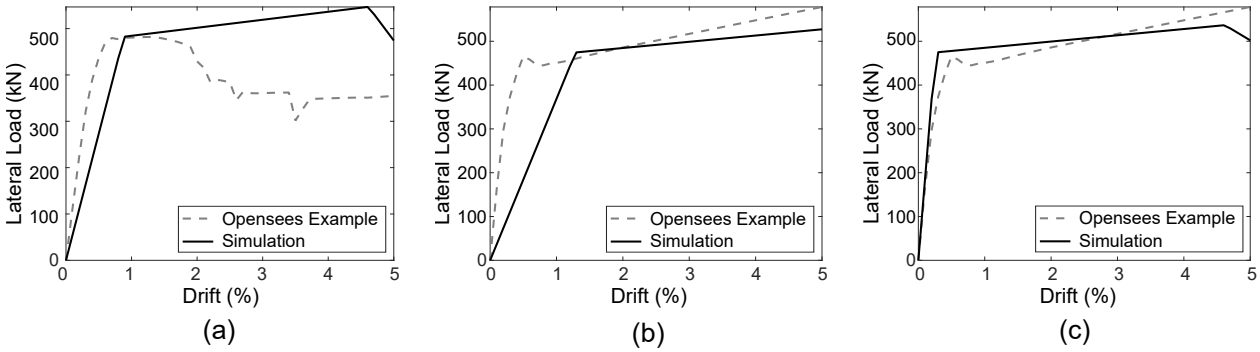

Figure 3.16: Comparison between the lumped-plasticity (simulation) and distributed-plasticity (Opensees example) approaches: A) pushover analysis of a RC column; b) pushover analysis of a RC beam (with zero axial load); c) pushover analysis of a RC beam the initial gross flexural stiffness EI_g.

- The initial stiffness of the column as predicted by the LP model is significantly lower than that predicted by the DP approach. This is an expected result because the LP calibration equations predict a secant stiffness to the yield point of the component, which is limited to being between 0.2 and 0.6 of the gross flexural rigidity of the section EI_g, whereas the utilized DP model employs EI_g directly (it is noted that, for the purposes of design and performance assessment, the flexural stiffness of the DP model should also be reduced in accordance with ACI 318 provisions). The lower initial stiffness predicted by the LP approach is intended to also account for additional nonlinear deformation mechanisms such shear and bond-slip deformations, which are not considered in the DP model.

- There is excellent agreement between the yield force predicted by both the LP and the DP approaches. It is noted that, as recommended in Haselton et al. [2016], the expected material properties are used to determine the section yield moment in the LP calibration process.

- There is a significant disagreement in the ductility capacity and softening response of the component as predicted by both approaches. Again, this result is due to the presence of spurious localization and mesh sensitivity issues in the DP approach. Experimental tests would be an appropriate reference for comparison in this stage of the behavior, as opposed to DP models.

Similar results are obtained for a beam component (with no axial load) in a pushover analysis. However, the post-yield stiffness predicted by the LP model is consistent with that predicted by the DP model, which is due to the absence of axial loads that may accelerate the component deterioration. Figure 3.16b shows the lateral load-displacement response predicted by both the LP and DP approaches for the beam member. In addition, figure 3.16c shows excellent agreement between both approaches if the initial gross stiffness is used in the LP model, rather than the secant yield stiffness.

3.2 Eigenvalue analysis of moment frames

3.2.1 One-story frame

An eigenvalue analysis of a single-story portal frame with arbitrary mass and stiffness properties was conducted using the created modeling framework. The fundamental period of the frame was verified against the theoretically-determined fundamental period of a frame with a single lateral degree of freedom (SDOF). The analytical calculation starts with the stiffness matrix of a portal frame (see figure 3.17a) considering only one lateral transitional DOF (u) and two rotational DOFs (θ_1, θ_2), which can be written as follows:

$$\mathbf{K} = \begin{bmatrix} \frac{24EI_c}{H^3} & \frac{6EI_c}{H^2} & \frac{6EI_c}{H^2} \\ \frac{6EI_c}{H^2} & \frac{4EI_c}{H} + \frac{4EI_b}{L} & \frac{2EI_b}{L} \\ \frac{6EI_c}{H^2} & \frac{2EI_b}{L} & \frac{4EI_c}{H} + \frac{4EI_b}{L} \end{bmatrix} \tag{3.1}$$

where E is the elastic modulus of the frame material, I_c and I_b are the second moment of area of the cross-sections of the column and beam, respectively, H is the story height, and L is the bay width. Using static condensation, the rotational DOFs can be eliminated, and the lateral stiffness of the SDOF frame becomes:

$$K_{cond.} = \frac{12\rho + 1}{12\rho + 4} \frac{24EI_c}{H^3} \tag{3.2}$$

where ρ is equal to:

$$\rho = \frac{EI_b/L}{2EI_c/H} \tag{3.3}$$

Equation (3.2) was used to compute the lateral stiffness of the frame, and the frame natural circular frequency and fundamental period were computed using the relations $\omega = \sqrt{\frac{K_{cond}}{m}}$ and $T = \frac{2\pi}{\omega}$, respectively, where m is the mass of the frame, which was assumed to be lumped at the beam level.

3.2.2 Two-story frame

The predicted first and second vibration mode periods of a two-story moment frame were compared against the corresponding periods computed using an Opensees frame example script, and against the analytical vibration periods of a simplified two-DOF frame with lumped masses. The model geometry and material parameters are based on the Opensees example, which can be found on this page: http://opensees.berkeley.edu/wiki/index.php/Pushover_Analysis_of_2-Story_Moment_Frame.

To analytically determine the natural frequencies of a two-story frame, the frame is assumed to have only two lateral translation DOFs (one at each floor level), and the mass of the frame is

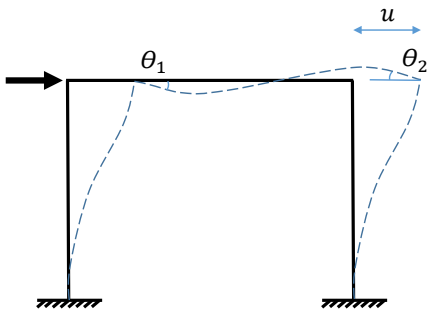

(a)

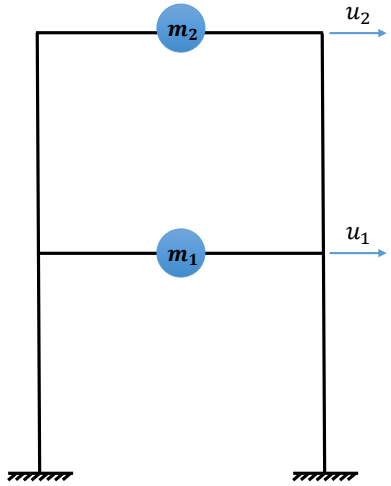

(b)

Figure 3.17: Moment frames used for the eigenvalue analysis: a) a fixed-based portal frame with a single lateral translational, and two rotational DOFs; b) A fixed-base two-story frame with two lateral translational DOFs.

lumped at each beam level (m_1, m_2), as shown in figure 3.17, and the individual lateral stiffnesses of each floor are k_1 and k_2. The frame may be represented by two springs with stiffnesses k_1 and k_2 connected in series, where spring 1 is fixed at one end. The stiffness matrix of the assembly can then expressed as:

$$\mathbf{k} = \begin{bmatrix} k_1 + k_2 & -k_2 \\ \\ -k_2 & k_2 \end{bmatrix} \tag{3.4}$$

where each of k_1 and k_2 can be computed using equation (3.2). The equation of motion of the undamped system can be expressed as:

$$\begin{bmatrix} m_1 & 0 \\ \\ 0 & m_2 \end{bmatrix} \begin{bmatrix} \ddot{u}_1 \\ \\ \ddot{u}_2 \end{bmatrix} + \begin{bmatrix} k_1 + k_2 & -k_2 \\ \\ -k_2 & k_2 \end{bmatrix} \begin{bmatrix} u_1 \\ \\ u_2 \end{bmatrix} = \begin{bmatrix} 0 \\ \\ 0 \end{bmatrix} \tag{3.5}$$

or

$$\mathbf{m}\ \ddot{\mathbf{u}}(t) + \mathbf{k}\ \mathbf{u}(t) = \mathbf{0} \tag{3.6}$$

in which $\mathbf{u}(t)$ is assumed to take the form:

$$\mathbf{u}(t) = \begin{bmatrix} u_1 \\ \\ u_2 \end{bmatrix} = \begin{bmatrix} u_{o1} \\ \\ u_{o2} \end{bmatrix} \sin \omega_n t \tag{3.7}$$

where u_{o1} ans u_{o2} are constants. From equation 3.7, the characteristic equation of the eigenvalue problem for the system can be derived:

$$\left|\mathbf{k} - \omega_n^2 \mathbf{m}\right| = 0 \tag{3.8}$$

and solved for natural frequencies ω_1 and ω_2. The predicted natural periods of the system by the three approaches are shown in table 3.2.

Table 3.2: 1st and 2nd mode periods of a two-story frame predicted by several methods

Simulation	$T_1(s)$	$T_2(s)$
SMG program	0.826	0.212
Opensees example	0.826	0.223
Theoretical calculations	0.765	0.223

It is observed that the predicted periods by the SMG program are almost identical to those predicted by the Opensees example, which verifies the ability of the SMG program to correctly compute the mass and stiffness properties of the system. The analytically determined periods (with simplifying assumptions regarding the DOFs and system masses) are very close to the predicted periods by the simulation models, lending more confidence to the SMG program calculations.

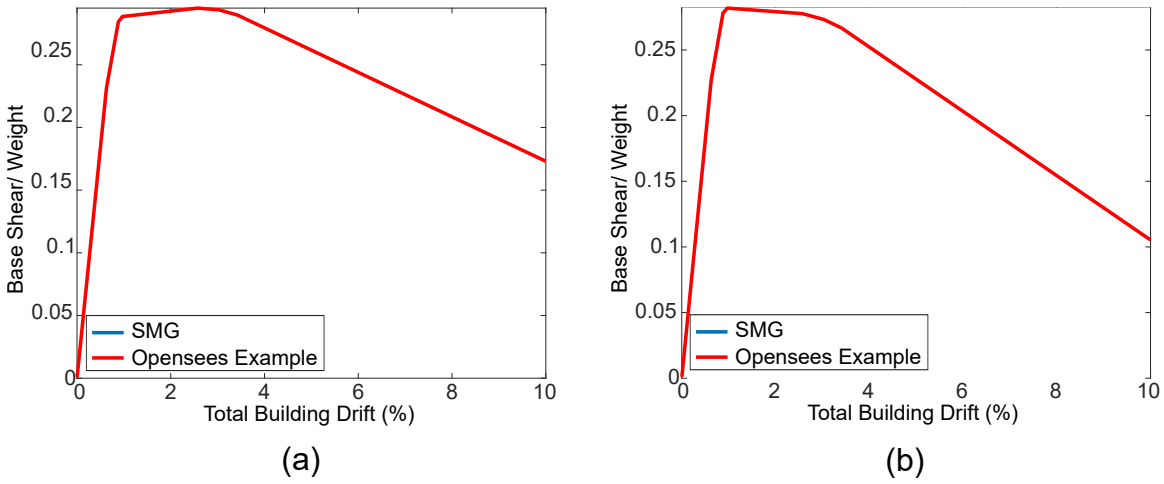

Figure 3.18: Pushover analysis results of a two-story steel moment frame example: (a) without a P-Delta column; (b) with a P-Delta column.

3.3 Static pushover analysis of moment frames

The results of static nonlinear simulations of several moment frames were compared against the results of available Opensees example models, and models created independently by other researchers. The following subsections summarize some of the relevant verification problems and results.

3.3.1 Two-story moment frame

Two-story moment frame - *without P-Delta column*

The reference structure was obtained through the Opensees examples manual at: http://opensees.berkeley.edu/wiki/index.php/Pushover_Analysis_of_2-Story_Moment_Frame. The structure is a two-story steel frame. The frame model was created using the SMG, and the results of a pushover analysis were compared against the corresponding results of the example. The example script adopts the same lumped plasticity modeling approach. Therefore, the results of both simulations were expected to be identical. The analysis excluded the additional P-Delta column (which was part of the original example) from both models. The normalized base shear vs. the lateral displacement at the top of the frame are plotted for both models in figure 3.18a. The plot shows that the pushover curves predicted by both models are identical.

Two-story moment frame - *with P-Delta column*

The same two-story frame was simulated using the SMG program, and adjusted to incorporate an additional P-Delta column, which carries additional gravity loads. The normalized base shear vs. the normalized lateral displacement at the top of the frame is plotted for both the SMG simulation

and corresponding example in figure 3.18b. As expected, the predicted building base shear vs. drift response is identical for both the SMG program and the reference example.

3.3.2 Six-story RC moment frame

In this set of simulations, the predictions of the lumped plasticity model created using the SMG program were compared against the predictions of a distributed plasticity model of the same structure. The goal of this study was to examine the differences between both approaches in simulating an RC moment frame system, and generally assess the performance of the LP model. The reference simulation model is a six-story RC moment frame created independently by Sashi Kunnath (University of California, Davis) using a distributed plasticity approach; particularly, a fiber-discretized force-based element formulation. Therefore, the comparisons in this section provide insight on the predictions of the calibrated IMK deterioration model for the lumped-plasticity springs, and those of the fiber-discretized model with uniaxial concrete and steel material properties. In each case, the frame model was statically subjected to lateral displacements using a displacement-control scheme up to a 10% drift ratio (or until convergence was not possible to achieve). figure 3.19a shows the pushover load-displacement curve of the frame as predicted by both approaches. The following observations can be made from this analysis:

- The simulation model created using the DP elements has a somewhat higher initial stiffness than the lumped-plasticity-based model. This is to be expected because the LP model calibration provides a secant stiffness that is between 20% and 60% of the initial gross stiffness. This conclusion can be verified by conducting a LP model analysis with the initial gross stiffness (instead of the secant stiffness). The initial stiffness of the structure from such an analysis is almost identical to that of the DP model, as shown in figure 3.19b. However, the post-yield stiffness is overestimated because this stiffness is computed as a fraction of the initial stiffness.

- The post-peak region of response predicted by the lumped plasticity model exhibits significant strength deterioration. This behavior is in accordance with the calibration of the IMK model with a post-peak negative stiffness of the member nonlinear springs to simulate such degradation. On the other hand, no clear post-peak degradation is observed in the DP model. This is due to the fact that DP models are incapable of capturing strength degradation effects properly (typically modeled as constitutive softening). In the case of this moment frame, inspection of fiber stress-strain histories at multiple locations across multiple cross sections of beams and columns reveals the following:

  - the concrete material appears to soften rather rapidly at the fiber locations of critical sections (e.g., the base of the column), and neighboring sections start to experience unloading. This effect is a result of the spurious mesh sensitivity of the numerical solution in the presence of constitutive softening. Such mesh sensitivity can be further scrutinized by changing the number of integration points (IPs) per element in the distributed plasticity model. Figure 3.19c shows the results of a parametric mesh sensitivity study with 2, 4 and 6 IPs per element.

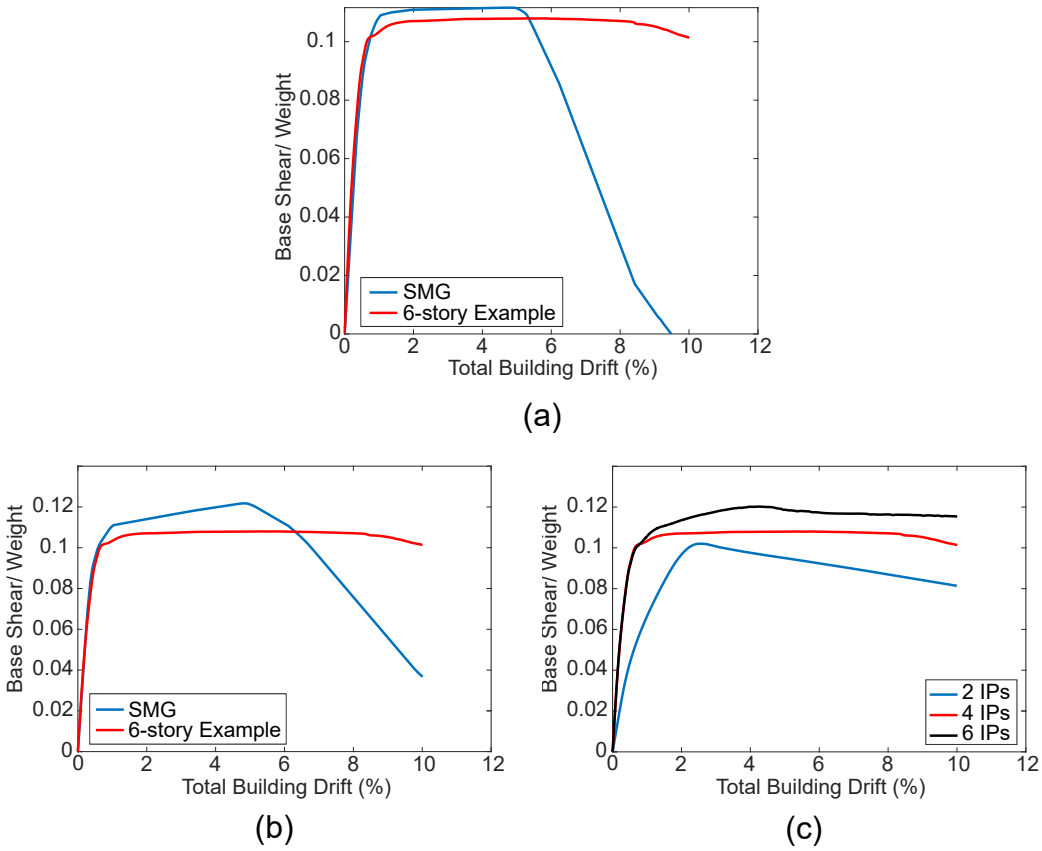

Figure 3.19: Pushover analysis predictions of a distributed-plasticity six-story RC moment frame example: (a) with secant stiffness EI_e of the LP model; (b) with initial gross stiffness EI_g of the LP model; (c) using multiple mesh sizes of the distributed plasticity model.

– the response of the steel material (whose behavior is described by a kinematic hardening behavior with no softening) seems to control the building response, particularly at large drifts after the concrete material loses most of its load carrying capacity. Therefore, no material degradation is captured at large drifts because the model does not account for rebar degradation effects including buckling and fracture. The slight degradation observed in the model, therefore, is mostly due to P-Delta effects.

3.3.3 Ten-story RC moment frame

The generic DP RC moment frame provided in the Opensees examples manual (http://opensees.berkeley.edu/wiki/index.php/OpenSees_Example_6._generic_2D_Frame,_N-story_N-bay,_Reinforced-Concrete_Section_%26_Steel_W-Section) was used as a reference for comparison against a 10-story, 3-bay RC moment frame building simulated by the SMG program using identical structural member properties. The static pushover analysis results using both the LP model and DP Opensees example are shown in figure 3.20a and figure 3.20b, in which the LP model employs the secant stiffness EI_e and the stiffness calibrated at 40% of the yield force EI_{40}, respectively. These simulations were conducted with a linear transformation (P-Delta effects are not included). Figure 3.20c shows a similar comparison of the predicted response after including P-Delta effects. The following observations can be made based on the these plots:

- *In the elastic range of response*, there is a significant difference between the initial stiffness predicted by both modeling approaches, because the LP model initial stiffness is limited to 60% of the initial gross stiffness by design, as previously pointed out. The difference between the LP and DP model initial stiffness is reduced when the EI_{40} stiffness is used in the LP model (which can take a maximum value of 80% the gross stiffness).

- *In the hardening range of response*, the predictions of both the LP and the DP model agree remarkably well in the simulations conducted without P-Delta effects. In the simulation which uses a P-Delta transformation, there is a small difference in the predicted maximum base shear between both models.

- *In the post-capping range of response*, as previously noted, there is a significant difference in the predictions of the LP and DP models. This difference is by design, and mainly due to the inability of the DP model to properly capture strength degradation effects in the model. This issue makes it difficult to judge the performance of the LP model in the post-peak range. Ideally, a comparison against experimental observations would provide more insight. However, experimental observations of RC moment frame tests are rather sparse in the literature. Even for single columns, observations in the post-capping range of behavior are just as sparse, and the prediction equations for the LP component models are intended to provide a conservative estimate in the post-capping range.

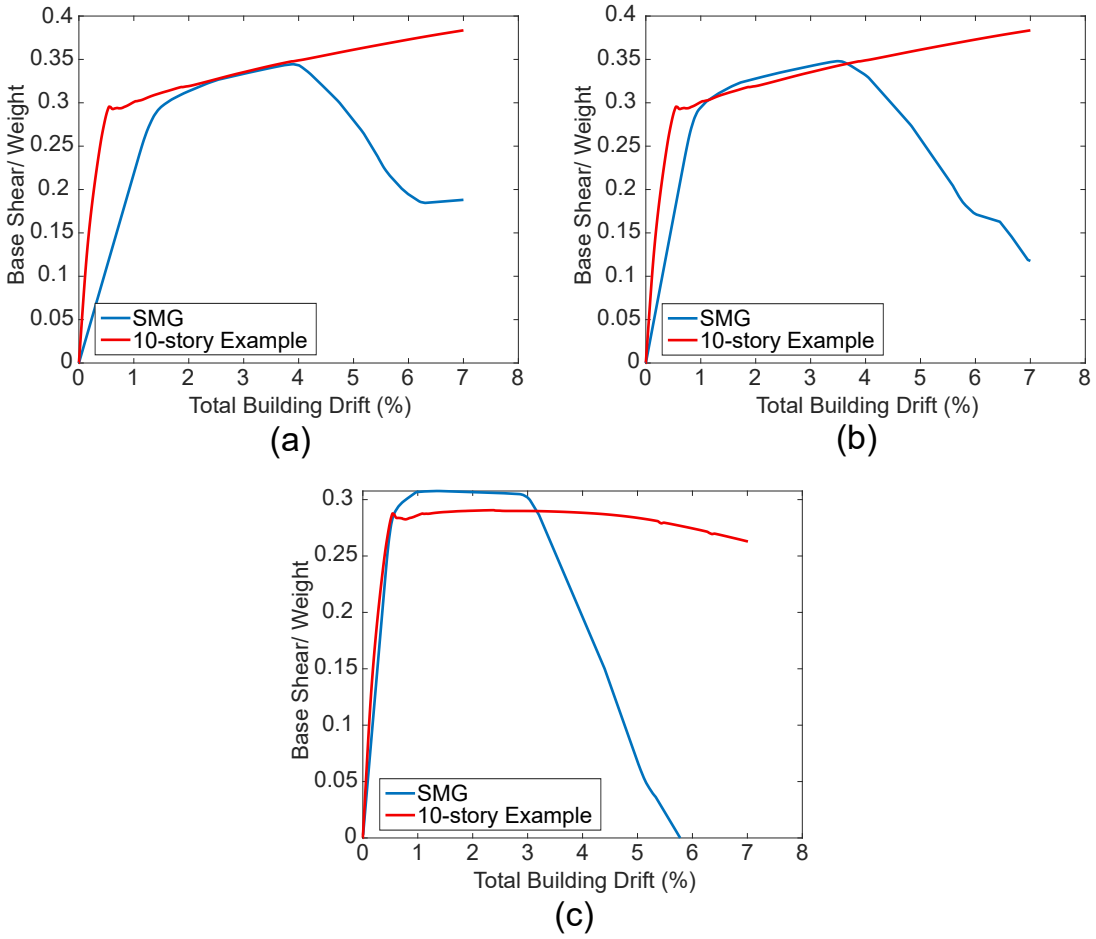

Figure 3.20: Pushover analysis predictions by the LP model of a distributed-plasticity ten-story RC moment frame example: (a) using the secant stiffness EI_e and without PDelta effects; (b) using the EI_{40} stiffness and without PDelta effects; (c) using the EI_{40} stiffness and with PDelta effects.

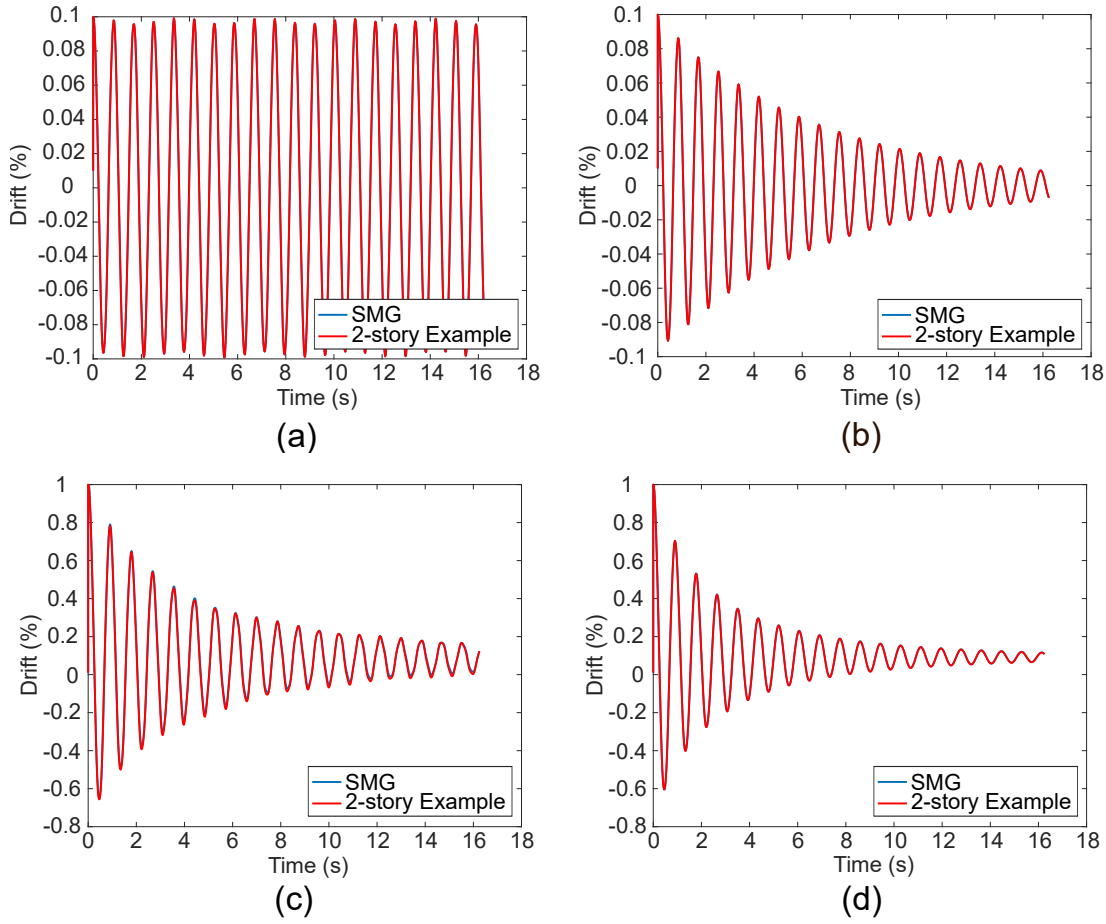

Figure 3.21: Free vibration of a two story steel moment frame: (a) undamped - in the elastic range; (b) damped - in the elastic range; (c) undamped - in the inelastic range; (d) damped - in the inelastic range.

3.4 Dynamic analysis of RC moment frames

A series of dynamic simulations were conducted using the SMG program and compared against available example problems. The results of these simulations are summarized in the following subsections.

3.4.1 Free vibration of a two-story steel moment frame

Figure 3.21 shows the results of the SMG and reference example in a free vibration analysis of the same two-story moment frame analyzed previously. A lateral force was initially applied statically to the frame, then the static force was removed and the building was allowed to vibrate. A P-Delta transformation was used for the model columns, and a 2% Rayleigh damping ratio was assigned in a subset of the simulations.

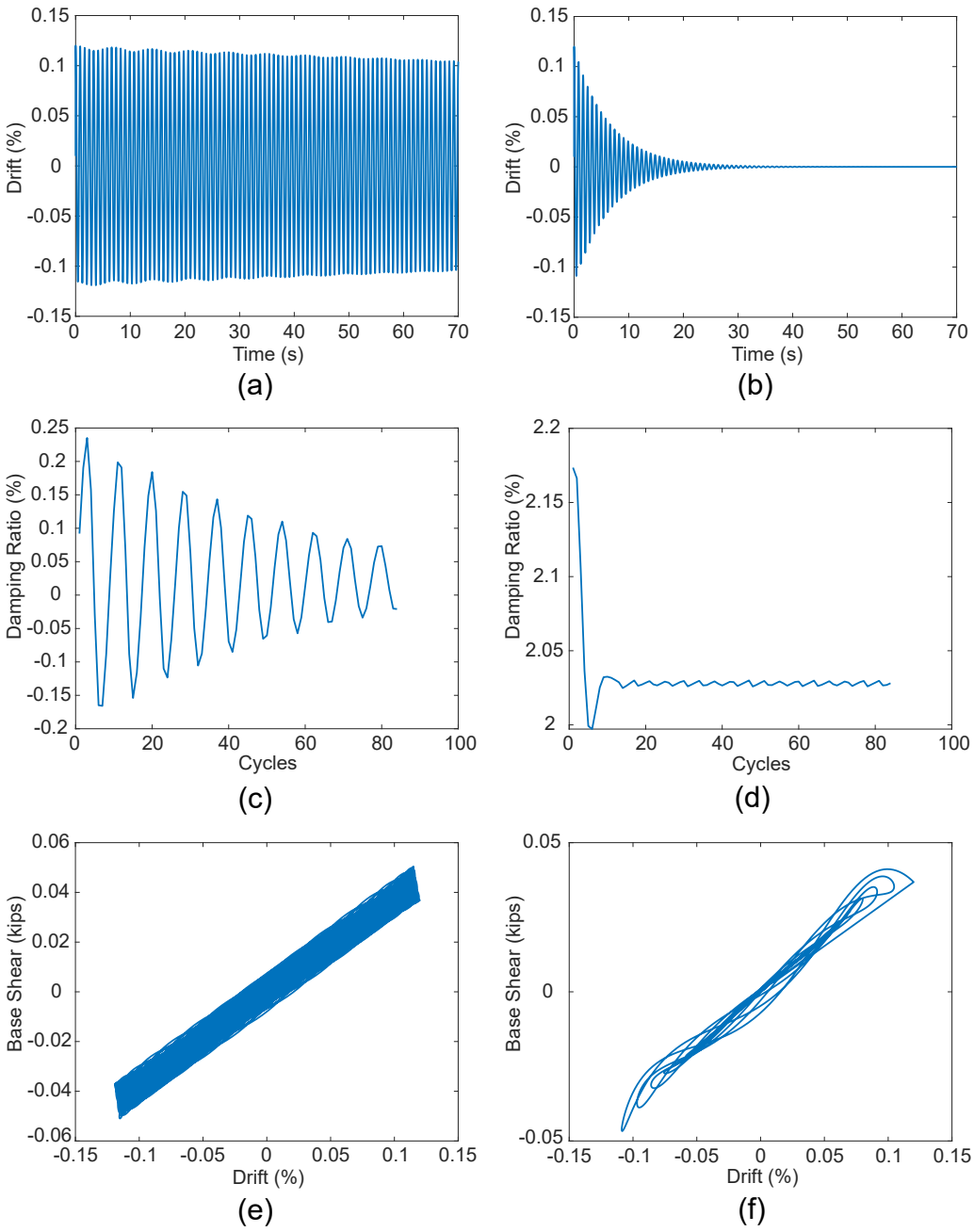

Figure 3.22: Free vibration of a two-story moment frame in the elastic range: (a) undamped drift time history; (b) damped drift time history; (c) damping ratio in the undamped system; (d) damping ratio in the damped system; (e) base shear vs. drift for the undamped system; (e) base shear vs. drift for the damped system.

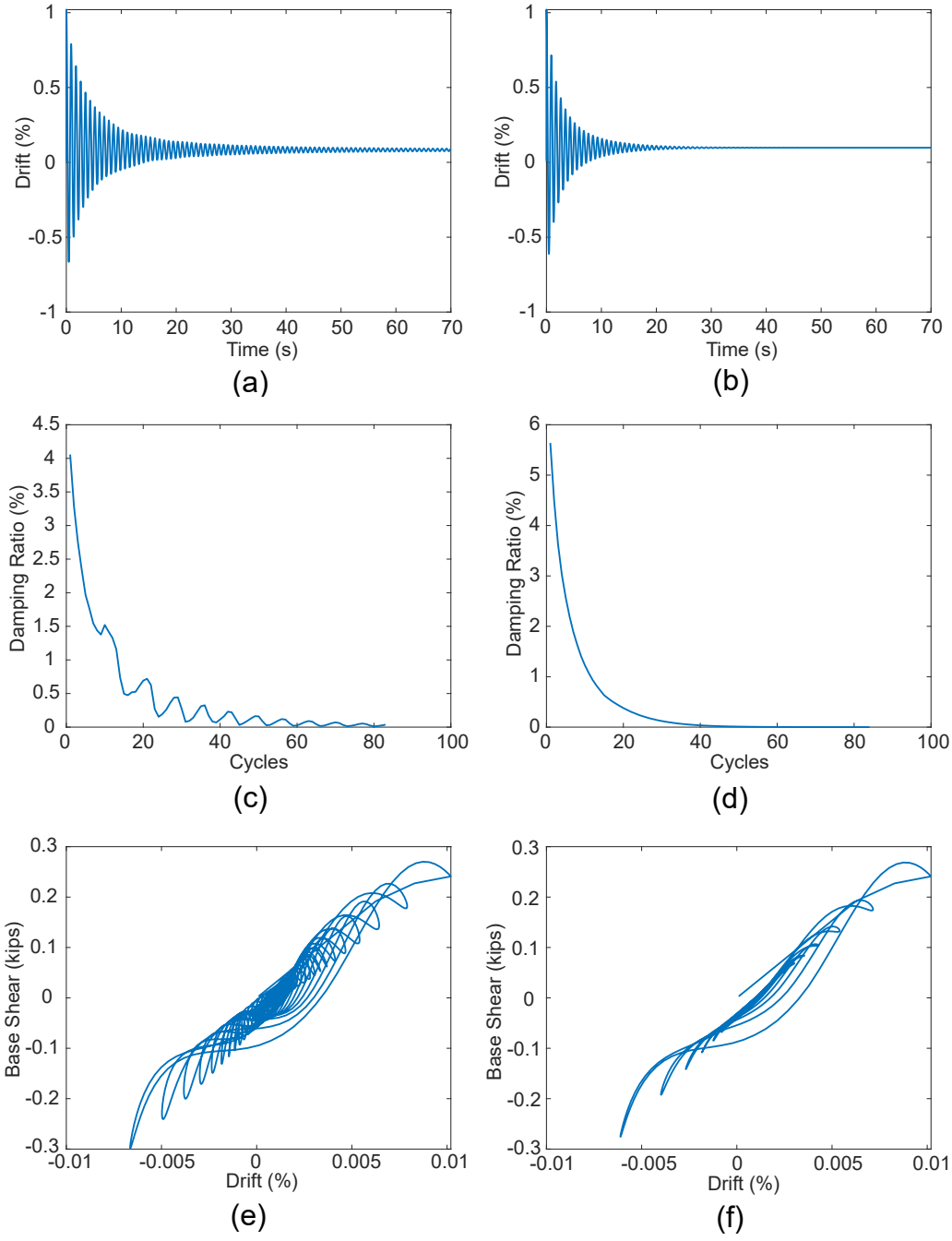

Figure 3.23: Free vibration of a two-story moment frame in the inelastic range: (a) undamped drift time history; (b) damped drift time history; (c) damping ratio in the undamped system; (d) damping ratio in the damped system; (e) base shear vs. drift for the undamped system; (e) base shear vs. drift for the damped system.

The drift history predicted by the SMG program and the reference example is plotted in figure 3.21 for four different analysis cases: subplots a and c represent the response of an undamped system after the building was initially pushed to 0.1% and 1% drift ratio before being allowed to vibrate, respectively, whereas subplots b and d show the response of the damped system to the same initial conditions. The plots reveal the following:

- Subplots a and b represent the response of the system in the elastic range of behavior. Subplot a shows an undamped response, in which the amplitude of the free vibration primarily remains constant, whereas subplot b shows the damped response in which the amplitude is reduced exponentially at the assigned Rayleigh damping rate.
- Subplots c and d represent the response of the system in the inelastic range of behavior, where additional energy dissipation occurs due to the hysteretic response of the material model in the inelastic region. This leads to a reduction in the amplitude of the motion in the undamped system, and accelerates this reduction in the damped system.
- The predictions of both the SMG program and the reference example are identical for all analysis cases.

To further investigate the numerical damping in the SMG simulation model, additional simulations of the same system (but with linear geometric transformation) were conducted for a much longer time frame (70 seconds). The damping was calculated between each two cycles in the system's vibratory motion and plotted for the entire analysis history. The damping ratio was calculated using the basic logarithmic decrement relationship:

$$\zeta = \frac{1}{2\pi j} \ln \frac{u_i}{u_{i+j}} \tag{3.9}$$

where ζ is the damping ratio, u_i is the amplitude of the displacement at cycle i, and u_{i+j} is the amplitude of the displacement at cycle $i+j$. In addition, the system base shear was plotted against the drift ratio, to provide insight on the degree of inelasticity in the system. These results are plotted in figures 3.22 and 3.23 in the primarily elastic and inelastic ranges of behavior, respectively. The results show a small amount of numerical damping in the undamped system pushed to 0.1% drift, which indicates some inelasticity (figure 3.22c). The numerical damping value starts at 0.2% damping ratio, and drops as the vibration continues. This numerical damping is also present in the damped system in figure 3.22d along with the applied 2% Rayleigh damping.

For the inelastic system in figure 3.23, the damping is relatively high at the start of the analysis (about 4% for the undamped system, and 5.8% for the damped system). Then, the damping ratio drops to zero as the system dissipates all its energy through hysteretic behavior in the structural components, which is evident in the reduction in the system base shear with each cycle in subplots e and f of the same figure. It is finally noted that the damping ratio of the Rayleigh damped system shows less oscillatory behavior as it drops throughout out the analysis (figure 3.23d) as opposed to the numerical damping oscillations noted in the damping time history of the undamped system (figure 3.23c).

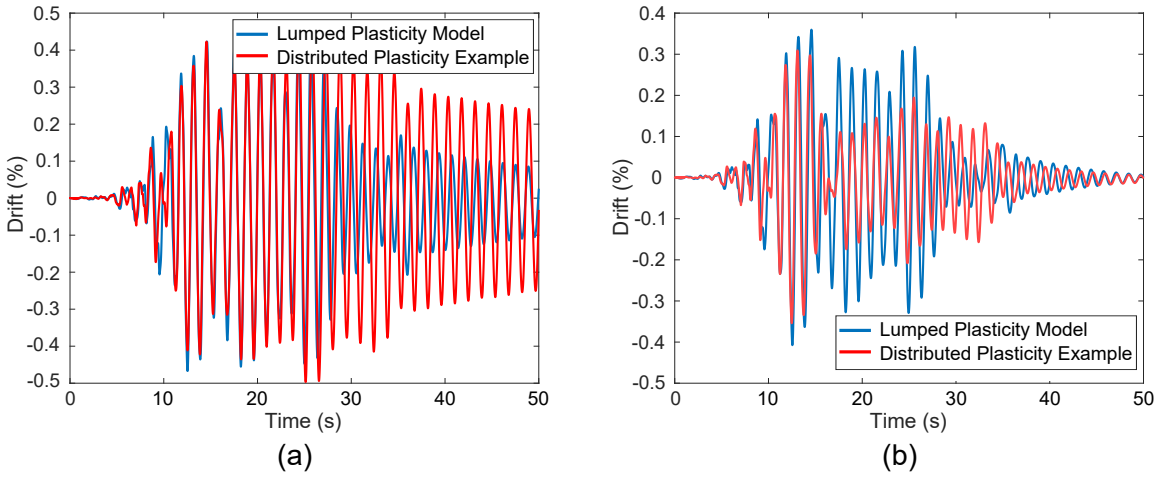

Figure 3.24: Building drift time history for a ten-story RC moment frame using the LP and DP modeling approaches: (a) for an undamped system; (b) for a damped system.

3.4.2 Nonlinear time history analysis of a ten-story RC moment frame

Another set of simulations was performed to compare the ability of the LP models generated by the SMG and the independently-created DP model to simulate the response of a 10-story RC moment frame to an earthquake excitation. It is noted that the total time of the applied ground motion is 39 seconds, and the analysis is conducted for 50 seconds, thus allowing 11 seconds of free vibration.

The results of the first pair of simulations, which represent the undamped system, are shown in figure 3.24a. The plot shows reasonable agreement between both approaches at the beginning of the analysis (up to about 25 seconds). In the later phase of the response, there is a large difference in the predicted drifts between both approaches. This difference is the result of the incorporated strength degradation in the LP model, which leads to additional energy dissipation in the dynamic analysis. Interestingly, a different trend is observed in the results of the second pair of simulations in figure 3.24b, which overlay the predicted drift time history by each approach for a system with 2% Rayleigh damping with coefficients in the first and third vibration modes. Whereas the drift time history is similar at the beginning of the analysis, the response of the DP model exhibits higher energy dissipation (and lower displacements) in the time window between 15 and 25 seconds. This trend suggests that the common methods of applying the damping in both modeling approaches may not produce equivalent results. In the DP model, the stiffness damping is applied to the tangent stiffness; specifically, the committed stiffness from the previous analysis time step. Therefore, the damping varies during the analysis. In the LP model, the stiffness damping is applied to the column and beam elements, which remain elastic throughout the analysis; i.e., the damping ratio is constant. Toward the end of the loading time history, both approaches exhibit similar free vibration displacement amplitudes, which are quickly damped by the applied viscous damping model.

The following set of simulations were intended to examine the effect of the LP model stiffness and damping on the dynamic response of the building. Figure 3.25 shows the drift time history

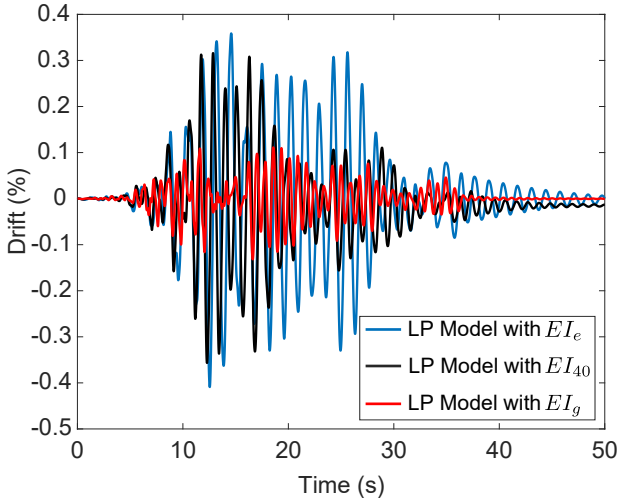

Figure 3.25: Building drift time history of a ten-story RC moment frame (with damping) predicted using the secant stiffness EI_e, the initial gross stiffness EI_g, and the secant stiffness EI_{40} of the LP model.

predicted by a LP model which uses the secant stiffness EI_e, the EI_{40} stiffness, and the initial gross stiffness EI_g. The results reveal much lower displacement amplitudes when the stiffness EI_{40} or EI_g is used. This reduction in the displacement amplitude is likely the result of both the increased stiffness and stiffness-proportional damping in the model.

3.4.3 Nonlinear time history analysis of a six-story RC moment frame

Nonlinear time history simulations were performed on the six-story RC moment frame model introduced previously, and compared against its DP counterpart. Figure 3.26 displays the drift time history of both the LP and DP models with Rayleigh Damping in the first and sixth modes, with the damping ratios $\zeta_1 = 0.05$ and $\zeta_6 = 0.1$. The utilized Rayleigh damping model included both mass and stiffness proportional damping coefficients, and was applied in the manner described in chapter 1.

Figure 3.26 demonstrates the surprising agreement between the results of the LP and DP modeling approaches. This agreement suggests that only minor to no degradation effects are present in the LP model. In other words, the structure remains within the hardening inelasticity region for the entire analysis, leading to similar predictions by the LP and DP models. The same agreement is retained when a different type of damping is used in the model, namely modal damping, in which the damping matrix is defined as a superposition of modal damping matrices [Chopra and McKenna, 2016]. This agreement is demonstrated in figure 3.27a, which shows the results of both the DP and LP model with 5% modal damping ratio. However, it is seen that the predicted response by the DP model exhibits a substantially different response when the damping ratio for both models is 2%, as shown in figure 3.27b. This result suggests a higher sensitivity of the DP model to the damping

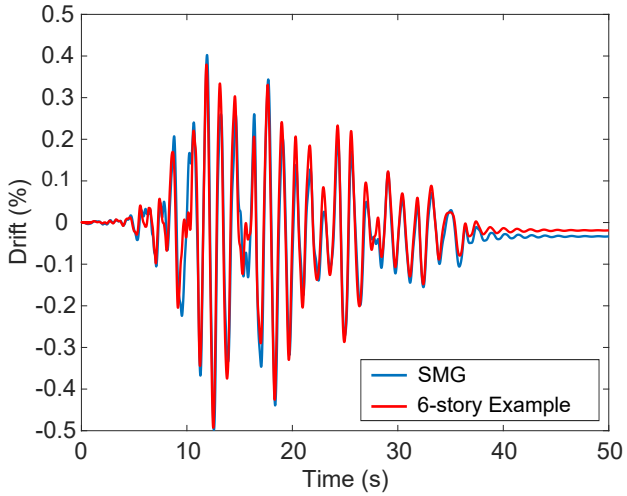

Figure 3.26: Building drift history of a six-story RC moment frame with Rayleigh damping using 5% and 10% damping in the first and sixth modes, respectively.

ratio, compared to the LP model.

Damping sensitivity of the lumped plasticity model

To further examine the sensitivity of the LP model to the type and magnitude of the damping, several additional simulations were conducted and the following five damping cases were compared:

1. Rayleigh model with damping ratios of $\zeta_1 = 0.05$ in the first mode, and $\zeta_6 = 0.1$ in the sixth mode.

2. Rayleigh model with damping in the first and sixth mode with equal damping ratios of $\zeta_1 = \zeta_6 = 0.02$.

3. Rayleigh model with damping in the first and third mode with equal damping ratios of $\zeta_1 = \zeta_6 = 0.02$..

4. Modal damping [Chopra and McKenna, 2016] in the first three modes: damping ratios in all three modes of $\zeta = 0.02$.

5. Modal damping [Chopra and McKenna, 2016] in the first three modes: damping ratios in all three modes of $\zeta = 0.05$.

The drift time history for each case is shown in figure 3.28. The results indicate that the LP model is not highly sensitive to the damping ratios, and exhibits no sensitivity to the type of damping.

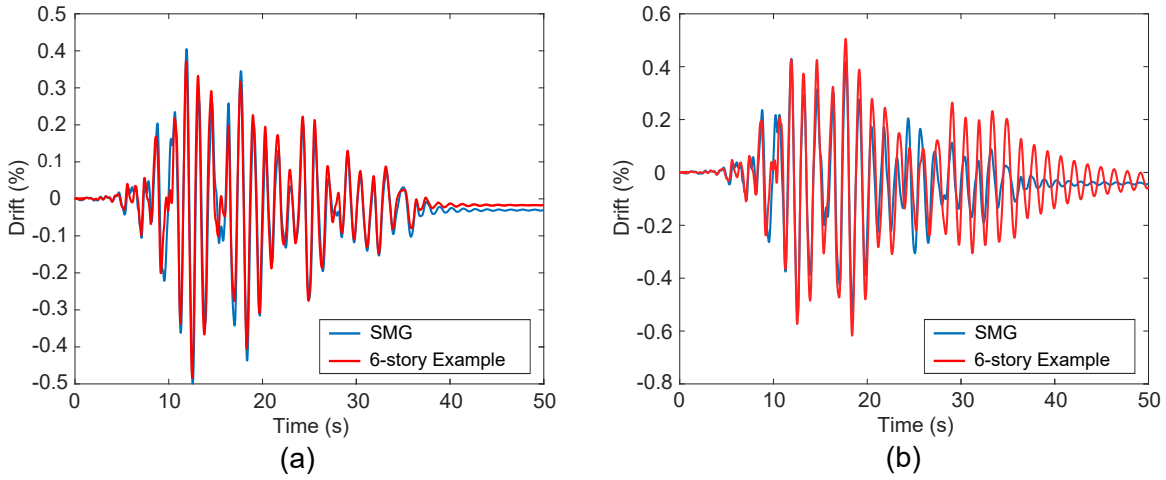

Figure 3.27: Building drift history of a six-story RC moment frame with: (a) 5% modal damping ratio; (b) 2% modal damping ratio.

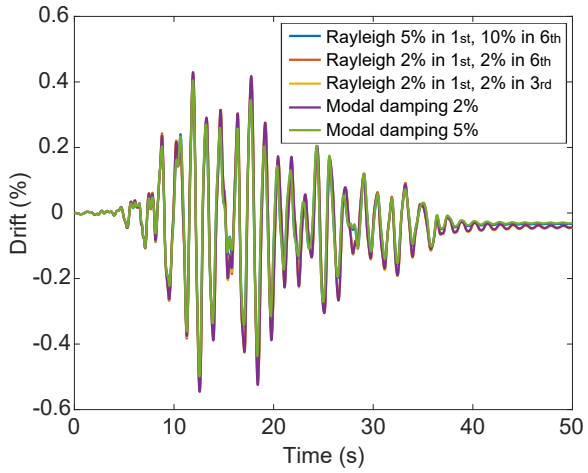

Figure 3.28: Sensitivity of the lumped plasticity six-story RC moment frame model response to the damping type and ratio.

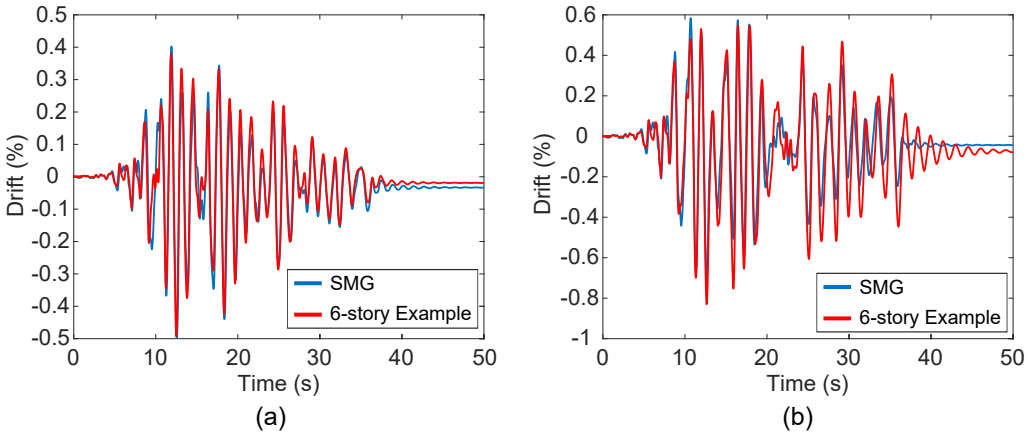

Figure 3.29: Building drift history of a six-story RC moment frame subjected to: (a) the unscaled ground motion record; (b) the same ground motion record scaled by a factor of 1.5.

Effect of ground motion intensity

To examine the impact of strength degradation in the LP frame model on the predicted response, another pair of simulations was conducted with a higher ground motion intensity. The previously used ground motion record was scaled by a factor of 2.0. Simulations with 5% and 10% Rayleigh Damping in the first and sixth modes, respectively, were repeated with the scaled ground motions, and the drift time history was recorded. The results due to the scaled and unscaled intensity levels are shown in figures 3.29a and b. Whereas the response of both the LP and DP models to a low intensity ground motion is very similar, significant disagreement exists in the response to the higher intensity ground motion. As described previously, the reason for this disagreement is the difference between the LP and DP model behavior as the system deformations become significant. In particular, the LP model experiences substantial strength degradation and energy dissipation in the post-capping range of behavior, as opposed to the DP model which does not capture the degradation effects properly.

Chapter 4

Part I Summary and Conclusions

Part I of this report described the details of using the lumped plasticity (LP) modeling approach to simulate the behavior of reinforced concrete (RC) moment frame systems of any number of floors/bays using a MATLAB-based program, and the structural analysis platform Opensees. The theory of the LP approach was discussed first, followed by a description of the numerical implementation of a set of prediction equations for determining the properties of RC structural component models. These equations, developed by Haselton [2008] and refined in Haselton et al. [2016], predict the member strength, ductility capacity and deterioration based on the member dimensions, reinforcement and axial load. RC system models created using the LP approach consist of elastic frame elements and nonlinear springs at the member ends; the constitutive relations of the springs are intended to cumulatively represent all sources of material-related nonlinearities in the system. Because of the design of the LP models, application of the damping effects in dynamic analyses requires special approaches to avoid spurious forces and potential convergence issues. Several sensitivity studies were conducted to assess the LP model's sensitivity to the damping model type and ratios.

A computational workflow was created for parametrically generating LP RC moment frame models of any regular geometric configuration, and for running different types of static and dynamic simulations. An incremental verification study was conducted, in which the predictions of the component and system models were compared against the results of available datasets and models in the literature under static and dynamic loading conditions. The structural analysis models were then integrated into a regional simulation workflow, which enables running thousands of nonlinear time history simulations on parallel-memory computing machines. In Part II of this report, this workflow is used to examine the variability of structural risk to RC buildings over a large spatial domain. The main conclusions of part I of this study are:

- The process of determining the parameters of each RC component based on the available prediction equations, and generating a moment frame model with a given number of floors/bays and member properties is fully automated using the Structural Model Generator Program (SMG) developed in this study. This program significantly accelerates the generation and calibration of structural simulation models for Opensees.

- The prediction equations used in this study for determining the RC component model parameters perform reasonably well when compared to experimental test data in the early- to mid-range of structural component behavior. In the later phases of the component response to cyclic loading, however, the prediction equations tend to produce poor predictions of the component strength degradation. This poor performance is primarily due to the sparsity of experimental test data in the post-capping range of behavior. The prediction equations seem to consistently predict conservative estimates of the member deterioration rate.

- The reasonable agreement between the predictions of the LP models created in this study and existing distributed plasticity models (DP) in the literature in the pre-peak region increases confidence in the LP modeling approach and the underlying prediction equations. The large difference between both approaches in the post-peak region reaffirms the established deficiencies in the ability of DP models to capture strength degradation. These deficiencies result from the loss of ellipticity of the governing differential equations, which leads to spurious localization of the softening deformations in the finite element solution, and mesh-dependent global system response. Therefore, the DP model is not an appropriate reference for comparison in the post-peak region. Several approaches have recently been developed to "regularize" the performance of the DP models in the presence of softening [Kenawy et al., 2020], and will be considered in future studies.

- The damping sensitivity analysis conducted in this study reveals that the adopted damping approach yields LP simulation models that are not as sensitive to the damping ratio as DP models. The primary reason for that is the constant stiffness-damping assigned to the elastic elements of the model only. It is, however, noted that application of damping in the LP models is somewhat cumbersome, and requires assigning certain damping components to specific regions of the domain. In addition, it is far more susceptible to the presence of spurious damping forces, than the DP modeling approach. These are all motivations for moving toward the use of DP models in collapse assessment studies.

- Due to the sparsity of experimental test data on RC moment frame systems, the predicted system performance, particularly in the post-peak region, is difficult to validate. At this stage, even the predictions of the post-peak behavior of individual RC components primarily represent conservative estimates. More experimental tests conducted to large deformations are needed to validate the near-collapse performance of both RC components and systems.

- A multiple-simulations framework was developed for a single computer and is appropriate for running a relatively small number of nonlinear time history simulations in a reasonable time period (for example, a run with a hundred ground motion records would be completed in a few hours). However, as the number of ground motion records (or regional domain size) increases, using a parallel computing machine becomes necessary.

- The multiple-simulations framework developed for a parallel computing platform takes advantage of the computational infrastructure available through NERSC. The framework is

capable of running thousands of nonlinear time history simulations in parallel on the CORI machine in about the same time it takes to run a single simulation.

The effects of member joint deformations were not considered in this study. These effects will be explored in future studies by enhancing the structural models to incorporate joint rigidity and shear deformation effects. In addition, all structural frames were assumed to be fixed at the base, and the foundation flexibility and potential soil-structure interaction effects were not modeled. Future iterations of the structural models will include additional springs at the base of the columns to indirectly account for the flexibility of the foundations and grade beams on the deformations of the building frames.

Part II

Variability of Seismic Risk to Reinforced Concrete Buildings Based on Physics-Based Earthquake Simulations

Chapter 5

Introduction and Background

5.1 Characterizing seismic hazard and risk near active faults

Characterizing the complex variability of risk to engineered structures near active earthquake faults is a challenging problem hindered by the sparsity of observed earthquake ground motion data in the near-fault region. Ground motions near rupturing faults (within about 15 km) exhibit unique characteristics that are different from shaking recorded at long distances. These near-fault ground motions can contain large velocity pulses which result from propagation of the fault rupture front at a speed close to the local shear wave velocity. When the rupture propagates toward a site in a strike-slip faulting mechanism, the site may experience the release of all the seismic energy in one large pulse at the beginning of the shaking, which can cause severe damage to structures. This effect is known as forward directivity, and has been observed near rupturing faults as early as the 1966 Parkfield, CA earthquake [Housner and Trifunac, 1967], and the 1971 San Fernardo, CA earthquake during which extensive damage to buildings was attributed to the poorly-understood effects of pulse-like ground motions, particularly on flexible structures [Bertero et al., 1978]. The strength and deformation demands imposed on structures located near earthquake faults began to receive significant attention from engineers following the observed structural damage in the 1992 Landers, 1994 Northridge and 1995 Kobe earthquakes [Hall et al., 1995]. This research attention was necessitated by the fact that code provisions were historically developed based on recorded far-field ground motions, but progress was stymied by the limited number of available near-fault records.

In response to the observations of large near-source motions and structural damage, building code provisions began to recognize near-fault effects. The 1997 Uniform Building Code [ubc, 1997] contained a set of near-source amplification factors for standard design spectra for sites located near active faults. These factors, however, were deemed inadequate in providing consistent protection of structures, because they did not consider the unique physical response characteristics of near-fault ground motions [Alavi and Krawinkler, 2004]. ASCE 7-16 [ASCE, 2017], one of the key standards adopted for building design in the U.S., establishes more restrictive design criteria for near-fault sites, and requires consideration of near-fault motion characteristics in selection and scaling of ground motion records for nonlinear response history analysis. In most engineering ap-

plications, selection of earthquake ground motions is performed with the aide of empirically-based ground motion prediction equations (GMPEs) which predict selected ground motion intensity parameters as a function of earthquake magnitude, distance, faulting, and path and site parameters. To account for forward directivity effects in engineering analysis, Somerville et al. [1997] and Abrahamson [2000] developed modification factors to GMPEs based on empirical analysis of available near-fault data and characterization of fault-site geometry. Further refined near-field directivity amplification models were developed by Somerville [2005] and Tothong et al. [2007], and incorporated into probabilistic seismic hazard analysis [Tothong et al., 2007, Shahi and Baker, 2011]. Because GMPEs are calibrated using observations of past earthquakes, they can be deficient in predicting rare events (e.g., large magnitudes at short distances). Moreover, near-source ground motion is known to be substantially affected by source parameters; for example, the hypocenter location, rupture velocity, slip distribution over the fault, seismic wave propagation, coupling of source radiation with geologic structure such as the amplification of waves by sedimentary basins. These are aspects that are difficult to account for in empirical models. Therefore, GMPEs contain large epistemic uncertainty, and do not capture the variability seen at short fault distances. Because the response of engineered structures in the near-fault region is influenced heavily by the nature of the ground motion, these deficiencies are at odds with performance-based seismic design, which necessitates a detailed quantitative understanding of the response of structures to the expected ground shaking.

In recent years, physics-based numerical simulation of earthquake ground motions has steadily emerged as an alternative to the use of empirical ground motion equations. Physics-based simulation methods of earthquake fault rupture date back to the 1970s and 1980s (see Douglas and Aochi [2008] and Burks [2014] for comprehensive reviews of ground motion simulation approaches). The use of simulated ground motions to analyze the response of structures to earthquake events has been the subject of several studies [Bielak et al., 2003, Taborda and Bielak, 2011, Jayaram and Shome, 2012, Burks et al., 2015, Marafi et al., 2019, Bijelić et al., 2019b]. As the confidence in using synthetic ground motions in engineering applications has increased, more studies have focused on exploring the structural demands imposed by simulated near-fault ground motion during large earthquakes and at short distances [Bijelić et al., 2019a]. The majority of studies in the literature utilize a hybrid simulation approach combining deterministic simulation at low frequencies, and a stochastic simulation approach at the higher frequencies. Validation studies have demonstrated that the hybrid simulation approaches carry realistic features that are important for computing the response of different types of structures [Galasso et al., 2013, Baker et al., 2014, Burks et al., 2015, Bijelić et al., 2019b]. However, such approaches do not include the effects of wave propagation in 3D earth models across a broad frequency band, and may misrepresent the spectral correlation properties of ground motions at higher frequencies, which are important for structural risk assessments [Bayless and Abrahamson, 2018, Rodgers et al., 2019a].

Three-dimensional deterministic ground motion simulations are an attractive methodology to understand the site-specific variation of earthquake hazard because they can take into account the fault geometry and the physics of wave propagation. These methods have evolved rapidly in recent years due to advances in understanding of earthquake rupture processes, computational model sophistication, and computing technologies. Deterministic simulations have the potential

to provide a wealth of high resolution ground motion datasets; however, they require a substantial computational effort to cover large regional domains with the discretization granularity required to simulate frequencies of engineering interest. Such computationally intensive simulations are becoming more feasible owing to the tremendous strides in high-performance computing (HPC) tools in recent years. This study utilizes a fully deterministic broadband (0-5 Hz) physics-based three-dimensional ground motion simulations to characterize the regional-scale variation of risk to RC buildings subjected to shallow crustal earthquakes.

5.2 Response of structures to near-fault ground motions

As the number of available near-fault ground motion recordings increased, many researchers attempted to study their effects on elastic and inelastic structures [Alavi and Krawinkler, 2000, 2004, Chopra and Chintanapakdee, 2001, Iwan et al., 2000, Liao et al., 2001, Malhotra, 1999, Mavroeidis et al., 2004]. Many studies employed idealized single-degree-of-freedom and multiple-degrees-of-freedom oscillators with elastic or elastoplastic constitutive relationships to draw conclusions about the unique characteristics of near-fault ground motions and the anticipated response of engineered structures. Most studies focused on the following two response aspects: (1) correlation between ground motion spectral parameters, and the strength and ductility demands on structures of varying fundamental periods of vibration, and (2) the relationship between the first-mode period of the structure, and the properties of velocity pulses in near-fault ground motions, particularly the amplitude and duration of the pulse. In recent years, a few studies (e.g., Champion and Liel [2012]) used more sophisticated structural models, and attempted to quantify extreme structural limit states (e.g., the risk of structural collapse) at near-fault sites. Relevant findings from previous studies may be summarized as follows:

- Structures located in the forward directivity path of a seismic event may be exposed to ground motions containing large two-sided velocity pulses (known as pulse-like motions) which can induce higher displacement and strength demands, as compared to ground motions that do not contain velocity pulses (non-pulse motions), particularly for flexible buildings [Alavi and Krawinkler, 2004, MacRae et al., 2001, Iwan et al., 2000, Malhotra, 1999]. In a strike-slip earthquake, these velocity pulses are typically observed in the ground motion component normal to the fault.

- The inelastic response of structures (including the probability of collapse) at near-fault sites subjected to pulse-like motions is strongly influenced by the ratio of the period of the largest ground motion velocity pulse T_p and the effective building period [Mavroeidis et al., 2004, Alavi and Krawinkler, 2004]. In the case of ductile structures, this effective period is likely an elongated first-mode period [Champion and Liel, 2012], because yielding of the structure leads to increasing the effective vibration periods. If the pulse period coincides with higher mode periods (which is likely for relatively flexible buildings), the analysis suggests that the building may experience a traveling wave over the entire height leading to large demands and early yielding in the upper stories [Alavi and Krawinkler, 2004]. On the other hand,

for structures responding elastically, the highest demands in the near-fault region may be experienced when the building first-mode period coincides with the period of the ground motion pulse.

- After their importance for structural performance assessment was established, several methods have been proposed to characterize the waveforms and period of near-fault ground motion pulses [NIST, 2011]; some rely upon qualitative manual classifications [Bray and Rodriguez-Marek, 2004] whereas others establish quantitative and automated methodologies to extract relatively large pulses, and classify the available set of ground motion recordings as either pulse-like or nonpulse [Shahi and Baker, 2011, 2014]. It is believed that accurate characterization of near-fault ground motion pulse characteristics will further advance our understanding and quantification of the relationship between near-fault ground motions and performance of structural systems.

- Analysis of the response spectra of pulse-like ground motions showed that they tend to have larger ratios of peak ground velocity (PGV) to peak ground acceleration (PGA) compared to non-pulse motions. This observation translates to wider acceleration-sensitive region in the elastic response spectrum of pulse-like motions and higher spectral accelerations at longer periods [Malhotra, 1999, Chopra and Chintanapakdee, 2001]. This change in the spectral shape provided an explanation for the increased structural demands on flexible buildings, because multiple modes of vibrations for such buildings may fall within the acceleration sensitive region and be excited by near-fault motions.

- The pseudo spectral acceleration at the fundamental period of the structure $SA(T_1)$, a standard-practice ground motion intensity measure, was deemed inappropriate for expressing the intensity of near-fault ground motions [Luco and Cornell, 2007]. In addition to $SA(T_1)$ being generally inefficient for long-period buildings because it does not reflect the contributions of higher modes, these modes may become even more significant at near-fault sites. Luco and Cornell [2007] showed that, for near-fault pulse-like ground motions with a pulse period near the second-mode of the structure, $SA(T_1)$ can be particularly deficient. Studies have also shown that the inelastic displacements due to near-fault ground motions can be substantially larger than elastic displacements [Chopra and Chintanapakdee, 2001, Alavi and Krawinkler, 2004]. Therefore, ground motion intensity measures containing information about inelasticity (e.g., inelastic spectral displacement) and/or higher-mode frequency content were proposed as suitable alternatives for both near-fault and far-field ground motions [Tothong and Cornell, 2008].

- The peak ground velocity (PGV) was suggested as a potentially stable measure of the severity of a near-fault ground motion pulse [Alavi and Krawinkler, 2000, Malhotra, 1999].

Most of the preceding conclusions relied upon analysis of the available limited set of observed near-fault ground motions, although some utilize simple mathematical models or equivalent idealized pulses [Alavi and Krawinkler, 2004]. Because the response of structures at near-fault sites

significantly depends on the nature of the ground motions, it remains difficult to quantify the site-specific spatial variability of structural demands in the near-fault region, or the precise relationships between the relevant geophysical parameters and structural performance using the available records. It is also noted that, with a few exceptions, most of the aforementioned studies on recorded near-fault ground motions employed simplified structural models that are not capable of capturing extreme structural limit states, which may be observed at near-fault sites. Recent studies [Champion and Liel, 2012] suggest that using more realistic structural models that are capable of capturing the deterioration of structural components may yield important findings on the expected structural performance levels, and aid the integration of near-fault risk in performance-based design practices.

5.3 Study objectives

The study presented in part II of this report utilizes broadband physics-based three-dimensional ground motion simulations to characterize the regional-scale variation of risk to low- and mid-rise modern RC buildings subjected to shallow crustal earthquakes. The ground motion simulations were generated as part of an application development under the U.S. Department of Energy Exascale Computing Project [Johansen et al., 2017, Mccallen et al., 2020], and utilize HPC to span a 100 km x 40 km regional domain and resolve frequencies up to 5 Hz. The structural models of the building frames are capable of simulating the expected nonlinear response, including strength and stiffness degradation, of reinforced concrete frames up to collapse. The objectives of this study are:

- to characterize the spatial variability of structural demands (e.g., maximum interstory drift ratio) imposed on modern, ductile RC moment frame buildings using thousands of ground motion stations over a regional computational domain, particularly at locations impacted by strong forward directivity effects;
- to develop new insights into the relationships between geophysical parameters (fault rupture characteristics and geological structure) and the structural response of RC buildings;
- to study the relationship between the imposed structural demands on RC buildings in the forward directivity region and the frequency content of ground motions characterized by large velocity pulses, particularly for long-period buildings which are expected to exhibit higher sensitivity to the presence of strong pulses; and
- to interrogate the correlations between the simulated ground motion intensity measures (e.g., peak ground velocities) and induced structural demands at near-fault sites.

The following chapter describe the characteristics of the archetype reinforced concrete buildings designed for this study, in addition to the properties of the numerical structural models, ground motions simulations and underlying fault rupture scenarios. The remainder of part II lays out the results of thousands of nonlinear structural response history simulations, and reports important

findings on the regional-scale spatial variability of structural risk, significance of forward directivity effects on buildings, and impact of geophysical characteristics on the structural demands near the fault.

Chapter 6

Archetype Reinforced Concrete Buildings and Simulation Models

6.1 Characteristics of the RC buildings

Two archetype RC buildings were designed for seismic category E: a three-story building and a twelve-story building. The building frames were designed as special moment resisting frames following the seismic provisions of ASCE 7-16 [ASCE, 2017] and the RC provisions in ACI 318-14 [aci, 2014]. The seismic design is based on the risk-targeted maps for a Berkeley, California site with site class C, which was decided based on the shear wave velocity profile in the computational domain: the average shear-wave velocity in the top 30 meters ranges between 380 m/s for basin soils to 500 m/s for rock. The intensity of the ground motions simulated in this study are expected to be representative of the ground shaking at that geographical location. The maximum considered earthquake spectral response acceleration at short periods and at a period of one second, respectively, are $S_s = 2.154$ and $S_1 = 0.83$. These designs are representative of a high-hazard, near-fault seismic region. Both buildings have square floor plans: 80 by 80 square feet for the 12-story building, and 96 by 96 square feet for the 3-story building. The buildings were designed to resist the seismic forces using all interior and exterior frames in each orthogonal direction (which are identical in each direction), and both were designed using normal-strength concrete and steel materials. The geometry, seismic response coefficient, and computed first-mode period for each building, are listed in table 6.1.

The structural design process was semi-automated using Jupyter Notebooks [Kluyver et al., 2016], which are web-based interactive computational environments capable of combining text, figures and python-based script. The created Jupyter Notebooks do not conduct any structural analysis directly or eliminate the role of engineering judgment. Instead, the design notebook represents a workflow for the structural design of a regular RC moment frame building, including references to ASCE 7-16 tables and relevant sections, in addition to automated computations of necessary parameters and checks; for example, computing and checking the base shear requirements, computing the vertical distribution of the equivalent lateral force method, computing the structural member demand envelopes based on external analysis, and interactively designing and

Table 6.1: Design properties of the RC buildings.

Building	**12-story**	**3-story**
Number of bays	4	4
Bay width (ft)	20	24
Typical story height (ft)	13	13
First floor story height (ft)	18	18
Beam dimensions (inch)	20 X 30	22 X 32
Column dimensions (inch)	30 X 30	28 X 28
Seismic base shear coefficient	0.0758	0.1435
First-mode period (s)	2.23	0.75

checking the adequacy of beam and column reinforcement. The workflow of the design notebook is based in part on the design examples of the NEHRP 2015 Provisions [FEMA, 2016], and the accompanying structural analysis for design purposes was performed using the software SAP2000 [CSI, 2003]. The design notebook is an interactive template that can be customized to design buildings of different geometric properties. A sample notebook created for the design of the 12-story building is provided in appendix B.

6.2 Description of the Simulation Models

Two-dimensional structural simulation models of representative frames for the 3-story and 12-story buildings were created using the structural analysis platform OpenSees [McKenna et al., 2000]. The beams and columns were simulated using the lumped plasticity modeling approach, which was described in part I of this report. Each structural member is modeled using a linear elastic element connected in series with nonlinear springs at each end to cumulatively simulate the nonlinear effects due to strength and stiffness degradation of concrete and steel, steel rebar buckling and fracture, and bond slip between steel rebar and the surrounding concrete. The modified IMK material model [Ibarra and Krawinkler, 2005] with peak-oriented hysteretic response is used to represent the constitutive behavior of the nonlinear springs, which incorporates large member deformations, strength and stiffness deterioration, and additional deterioration due to load cycling. The key parameters of the IMK model were described in chapter 1 of this report.

The equations presented in Haselton et al. [2016] were used to relate the column design parameters (cross-sectional dimensions, reinforcement details, material properties, and axial load ratios) to the IMK parameters (initial stiffness, plastic and post-capping deformation capacities, cyclic deterioration parameters). Based on the Haselton equations, the plastic rotation capacities of the RC members in this study ranged between 0.042 and 0.069 (measured in radians), and the post-capping rotation capacity ranged between 0.082 to 0.1, where 0.1 is a conservative upper limit imposed due to the lack of experimental test data in the post-capping region [Haselton, 2008]. The cyclic deterioration parameter λ ranged from 21.7 to 30.0 (note that this parameter matches the

definition of the λ parameter in Haselton et al. [2016]). A residual load carrying capacity of 10% was assigned to all structural members to avoid convergence issues. The initial member stiffness is assumed to be represented by the secant stiffness through 40% of the yield capacity, as defined in Haselton [2008], and the hardening ratio M_c/M_y of all members was assumed to be 1.13, which is the value recommended based on regression analysis of hundreds of RC column tests. The lumped plasticity modeling approach was selected for this study because it is (1) computationally efficient, making it appropriate for running thousands of simulations; and (2) capable of including multiple nonlinear phenomena and simulating the nonlinear dynamic response of RC buildings from damage initiation to the onset of sidesway collapse. In particular, this modeling approach can rigorously represent the post-capping (negative stiffness) portion of the response of the RC components, which is critical for characterizing the building performance and assessing extreme limit states. Other novel nonlinear RC component models (e.g., nonlocal fiber-section models by Kenawy et al. [2020]) will be considered in future studies.

In addition to simulating inelastic component behavior, geometric nonlinearity effects are considered in the model by using a corotational geometric transformation. All models were assumed to have a fixed-base boundary condition; therefore, soil flexibility and potential soil structure interaction effects are disregarded. Rayleigh damping corresponding to 5% of the critical damping ratio is applied in the first and third modes of both building models. Both simulation models were subjected to earthquake ground motion acceleration time series in a nonlinear time-history analysis framework with a Newmark integration scheme, and the building maximum displacement and all interstory drifts were recorded at each time step of the analysis. The dynamic analysis of the buildings was conducted in a set of parallel simulations using the NERSC CORI machine at Lawrence Berkeley National Laboratory (LBNL), and the computational workflow described in the preceding chapters.

6.3 Description of the Earthquake Ground Motions

The ground motion acceleration time series employed in this study were generated by Arben Pitarka (LLNL) using the finite difference code SW4 (Seismic Waves, fourth order) developed at LLNL [Sjögreen and Petersson, 2012, Petersson and Sjögreen, 2015]. SW4 was developed for simulation of seismic waves using 3D earth models on distributed-memory parallel computers, and includes anelastic attenuation, mesh refinement capabilities and representation of ground surface topography. This type of simulations can capture important site and path effects, such as focusing and scattering of seismic waves and motion amplification by sedimentary basins. The simulated earthquake scenarios in this study utilize HPC machines in LLNL and LBNL, and resolve the ground motion frequency content up to 5 Hz.

The kinematic earthquake rupture modeling technique of Graves and Pitarka was used to simulate the fault rupture processes [Graves and Pitarka, 2016, Pitarka et al., 2019]. This technique has been validated and tested in simulations of recorded earthquakes [Graves and Pitarka, 2018, Pitarka et al., 2019]. A magnitude 7.0 strike-slip earthquake was simulated with a fault length of 62.6 km, and fault width of 16 km. The rupture velocity was set to 80% of the local shear wave

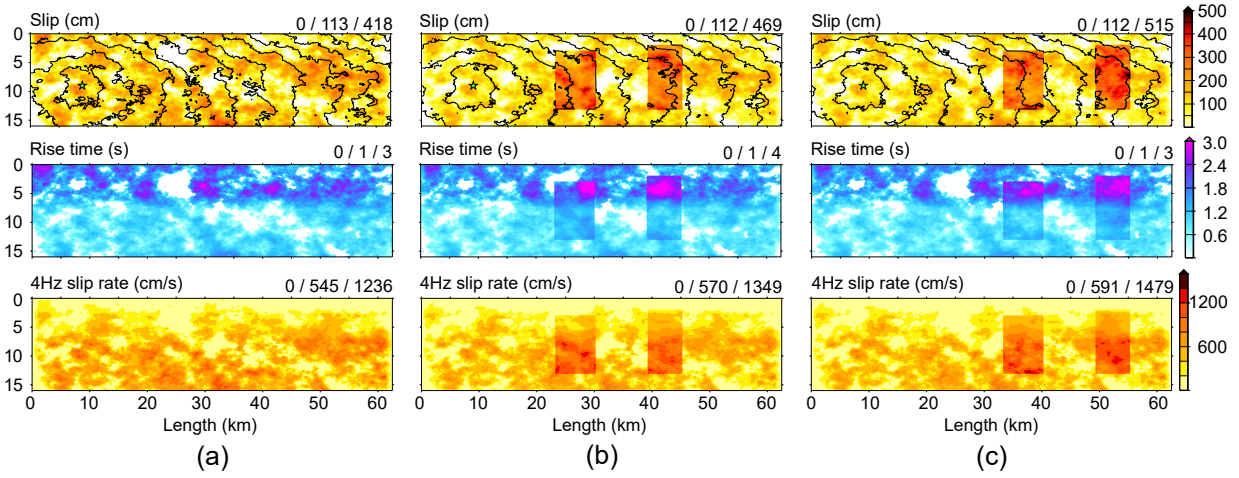

Figure 6.1: Rupture models used in ground motion simulations of M7 scenario earthquakes on a vertical strike-slip fault. The first row shows the slip distributions, the second row shows the rise time, and third row shows the peak slip rate computed after low-pass filtering the source time function at 4 Hz. The triplet of numbers at the upper right of each panel indicate the minimum, average and maximum values of the parameter being displayed. Isochrones plotted on the slip distribution indicate rupture front at 2 s time intervals: (a) rupture scenario A; (b) rupture scenario B; (c) rupture scenario B (generated by Arben Pitarka, LLNL).

velocity, which is consistent with observed rupture velocity values found for shallow crustal earthquakes. The depth to the top of the fault was set to 0.2 km and the dip angle was 90 degrees. The synthetic ground motions used in this study were computed using the kinematic rupture models shown in figure 6.1, and referred to as scenarios A, B and C. These models are representative of fault rupture of common shallow crustal earthquakes with a predominantly strike-slip mechanism. The three selected rupture scenarios have different slip distribution characteristics, and are capable of producing directivity effects with various strengths. Scenario A utilizes a fully stochastic distribution of slip over the entire domain (and is referred to as the stochastic scenario), and scenarios B and C contain distinct patches of large slip (250-500 cm) at different locations over the domain as shown in figure 6.1b and c (and are referred to as the hybrid rupture scenarios). Based on observations from previous earthquakes, near-fault ground motions can be significantly influenced by the slip distribution on the fault. Ruptures with localized areas of shallow large slip can result in ground motions with increased amplitude for sites near these slip patches (e.g., the 2016 Kumamoto, Japan earthquake) [Pitarka et al., 2019]. This very localized ground motion amplification can result in a significant increase in the structural demands. The inclusion of rupture scenarios with distinct large-slip patches is thus an important consideration in structural demand simulations. Further details about the rupture model can be found in Graves and Pitarka [2016], and validations of the generated ground motions are available in Pitarka et al. [2019], Rodgers et al. [2019b], and Rodgers et al. [2019a].

The computational domain in this study spans 100 km by 40 km by 30 km, and incorporates

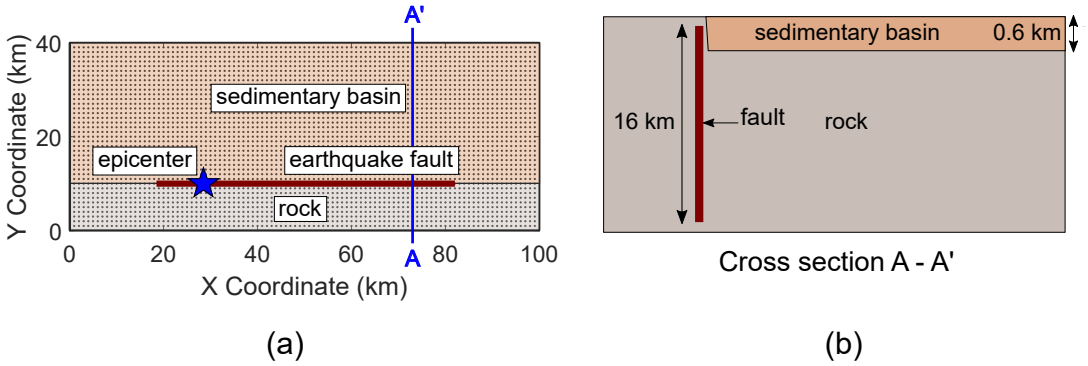

Figure 6.2: (a) a plane view of the computational domain showing the earthquake fault, the location of the epicenter, and relevant geologic features. Ground motion stations at the surface are represented by black dots; (b) an elevation view showing the sedimentary basin soil.

three-dimensional geological features. The minimal grid spacing used in the simulations is 8 m. The area north of the fault contains a shallow sedimentary basin (600 m deep), and that south of the fault is rock soils, as shown in the map and elevation view plotted in figure 6.2. These conditions allow for studying amplification effects in the near-fault area due to sedimentary basins. The location of the epicenter is marked with a star in the same figure. The surface of the domain contains 3,861 stations - spaced at one-kilometer intervals - at which three ground motion acceleration history components are generated from each rupture scenario: a horizontal FN component, a horizontal FP component, and a vertical component. Each two-dimensional building model is assumed to be replicated at all 3,861 stations, and is subjected to the FN and FP horizontal components separately. Three M7.0 scenarios were generated and the resulting ground motions were applied to both buildings. A total of 46,332 nonlinear building response history simulations were conducted for this study, including the FN and FP ground motion acceleration components of the three scenarios applied to both the 3-story and 12-story buildings. Representative results from all simulations are presented and discussed in the following chapters.

Chapter 7

Characteristics of the Simulated Earthquake Ground Motions

In this chapter, the spatial variation of the intensity of the ground motions generated in this study is examined, and the limitations of commonly-used intensity measures (IMs) in predicting the demands on flexible structures and/or structures with significant nonlinear behavior are discussed. First, the ability of the earthquake simulations to represent the seismic hazard near earthquake faults is demonstrated by comparing the characteristics of the simulated ground motions to the available body of real near-fault earthquake records. Then, the relationship between structural demands and ground motion IMs is studied for all the simulated rupture scenarios. The following ground motion measures are considered:

- The pseudo spectral acceleration at the fundamental vibration period of the structure $SA(T_1)$, which is one of the most commonly used measures, and is most correlated with structures whose response is primarily elastic and dominated by first-mode response.
- The peak ground velocity of the ground motion record (PGV), which was seen to correlate with structural response [Sehhati et al., 2011], particularly in the near-fault region where large velocity pulses dominate the ground motion record and impose large structural demands.
- A ductility-dependent ground motion intensity measure SA_{eff} combining the effect of the spectral acceleration at the fundamental period, and that of the ground motion spectral shape using a measure of the spectral shape over a period range related to the structure's ductility [Marafi et al., 2016, 2019].

7.1 Spectral characteristics of the simulated and recorded ground motions

Before describing the important aspects of the structural risk due to the simulated ground motions in this study, it is instructive to examine the features of the acceleration response spectra of the

different scenarios against the backdrop of recorded earthquake data. Such a comparison was performed against two datasets of near-fault earthquake data:

- Dataset 1 is a group of recorded earthquake records obtained from a database compiled by Baker et al. [2011], which includes ground motions with strong velocity pulses within approximately a 10-kilometer closest distance. The dataset consists of only 38 records from seven different earthquakes with moment magnitudes ranging between 6.53 and 7.62, with an average of 7.11, and spans a wide range of V_{s-30} with an average value 404 m/s. The database was originally compiled to contain ground motions with strong velocity pulses, and was rotated to FN and FP orientations. This dataset was deemed appropriate for comparison against the 4,728 simulated ground motions within a 10-kilometer closest distance to the fault which result from a magnitude 7.0 pure strike-slip rupture, and have an average V_{s-30} of 436 m/s. Because of the availability of the FN and FP components, this dataset enables the exploration of the differences between FN and FP components of the simulated and recorded ground motions.

- Dataset 2 is a group of 41 near-fault records containing only motions generated by a strike-slip earthquake mechanism, and within approximately 10 km closest distance to the causative fault. This dataset was obtained from the PEER NGA West database and has similar characteristics to dataset 1: an average magnitude of 7.0 (with magnitudes ranging between 6.53 and 7.9) and an average V_{s-30} of 424 m/s. The two main differences are: (1) only strike-slip earthquakes are included, and (2) no attention was paid to the pulse characteristics of this set; therefore, it includes ground motions with and without strong velocity pulses. The primary issue with this dataset is the inability to directly compare the characteristics of individual ground motion components, since the available records represent arbitrary sensor orientations. This dataset is referred to as the near-fault strike-slip (NFSS) set.

It must be acknowledged that the comparison against both sets of observational data has several limitations: (1) the small number of available data may not represent the full extent of the expected variability of ground motions at short distances; (2) the recorded ground motions are from earthquakes in different regions, with varying magnitudes and site conditions, whereas the simulated ground motions are generated by three scenarios with the same magnitude and site conditions; (3) The records from dataset 1 are caused by a variety of rupture mechanisms and may be associated with certain approximations in estimating the fault orientation; and (4) Other characteristics of the rupture process that may cause significant differences between the simulated and the recorded datasets are not considered in this study, including the depth to the top-of-rupture and the dip angle. Nonetheless, the comparison against the available records benchmarks the ability of the simulated motions to reasonably represent the characteristics of real ground motions over a broad range of frequencies, contextualizes the findings of this study with respect to structural risk estimates, and provides important insight to support the development of new rupture simulations.

Figure 7.1a through d show an orientation-independent measure of the maximum-direction spectral acceleration of the ground motions, or rotD100 [Boore, 2010] overlaid on top of dataset 1. Subplots a, b and c show the median response spectrum, in addition to the 2.5 and 97.5 percentile

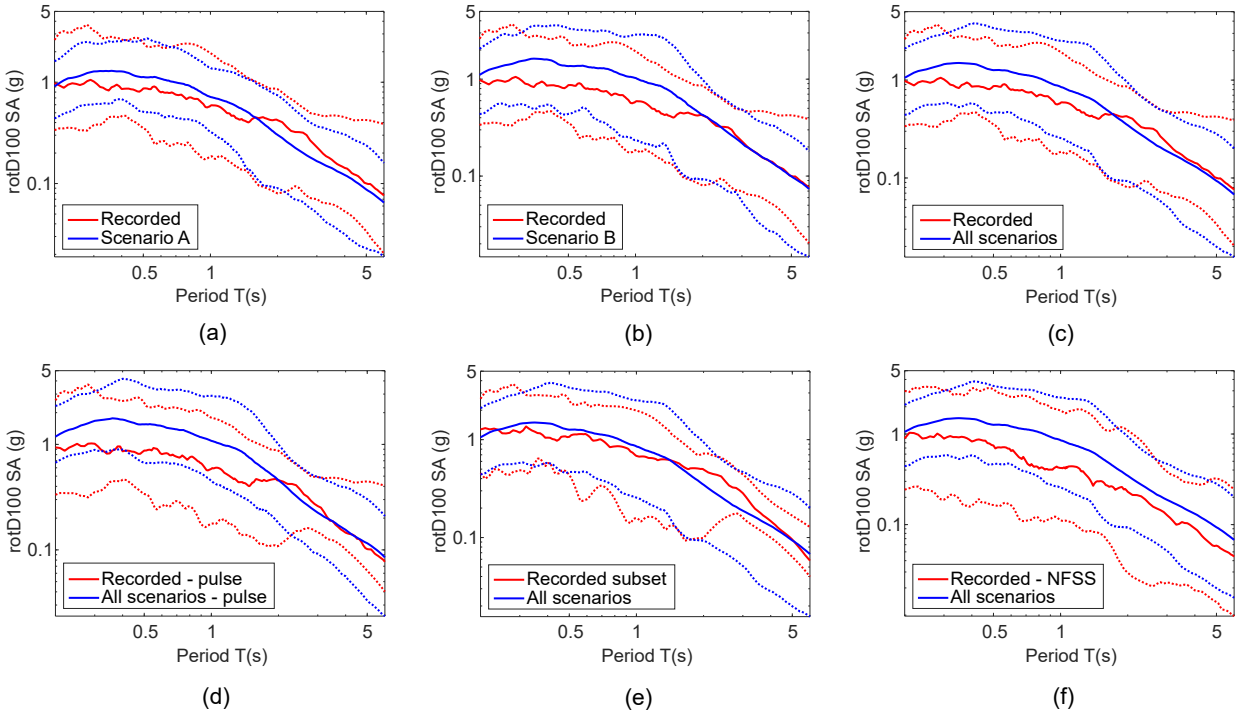

Figure 7.1: Maximum direction orientation-independent median, 2.5 and 97.5 percentile acceleration response spectra of the several simulated and recorded ground motion datasets: (a) for scenario A and recorded dataset 1; (b) for scenario B and recorded dataset 1; (c) for all simulated scenarios and recorded dataset 1; (d) for pulse-like motions only in all simulated scenarios and recorded dataset 1; (e) for all simulated scenarios and recorded dataset 1 subset without the ground motions of the Chi-Chi, Taiwan earthquake; (d) for all simulated scenarios and recorded dataset 2.

spectra for all the ground motions within a 10 kilometer closest distance to the fault in scenario A, scenario B and all scenarios, respectively. The median and percentile spectra of the records of scenario A (stochastic) agree reasonably well with the records of dataset 1 over a broad frequency band. The simulated ground motions have, however, consistently higher median spectral accelerations in the short period range (up to a period of about 1.7 seconds) than the real recorded motions. Scenario A motions also have slightly lower median spectral accelerations in the mid to long period range, meaning that this scenario would potentially underestimate the seismic risk for long-period structures. The hybrid rupture scenarios (B and C), generally have higher spectral accelerations over most periods than the stochastic scenario. This aspect improves the agreement between the simulated and real ground motions in the long-period range, as seen in figure 7.1b for scenario B. The median and 2.5 and 97.5 percentile spectra of all three scenarios exhibit better agreement with the available records of dataset 1, particularly in the long-period range.

To examine the pulse characteristics of the ground motions simulated in this study, two automated and objective classification algorithms were employed [Baker, 2008, Shahi and Baker, 2014], the characteristics of which will be discussed in later sections. In all three rupture scenarios, the algorithm classified about 20% of the simulated motions within a 10 km closest distance to be pulse-like (although the actually number is likely higher and may depend on the characteristics of the classification algorithm). Comparing the pulse-like motions from all scenarios against the pulse type motions of dataset 1 (33 records out of 38) reinforces the finding that the simulated ground motions have overall higher spectral intensity in the short-period range that may vary by up to a factor of 2.0 (figure 7.1d). Close examination of the individual ground motion spectral components reveals that most of the difference between the simulated and recorded motions is in the FN component, and suggests that the simulated ground motions tend to have more short-period pulses than the recorded motions. It is noteworthy that dataset 1 is dominated by 16 records from a single earthquake: Chi-Chi, Taiwan, which has been studied in the literature and is believed to have unusually low short-period spectral accelerations in the near-field [Somerville, 2003]. Comparison of the simulated scenarios against a subset of dataset 1 which does not include the records from the Chi-Chi earthquake (figure 7.1e) yields better agreement between the synthetic and real records in the short-mid period range. Finally, the synthetic motions are seen to mostly lie within the 2.5 and 97.5 percentiles of the ground motions of dataset 2, as shown in figure 7.1f, despite have a significantly higher median spectrum, particularly in the short-period range. It is also noted that simulated ground motions generally have less dispersion than both datasets of recorded motions. This is an expected result because of the uniformity of the site conditions, earthquake magnitude and focal mechanism producing the synthetic motions. The results of the comparison against the recorded datasets indicate that the structural demands predicted by the stochastic scenario would provide reasonable estimates for short-period structures, and may underestimate the risk for long-period structures. The rupture scenarios with localized slip regions may offer more appropriate risk estimates for long-period structures, and somewhat conservative estimates for short-period structures.

The results reported in this document focus primarily on the relative differences in the predicted structural demands over the domain. However, preliminary interpretation of the structural risk in an absolute sense necessitates an understanding of the relative intensity of the simulated ground mo-

tions compared to the risk-targeted maximum considered earthquake (MCE_R) design spectrum for the site selected in this study. Such a comparison is shown in figure 7.2 for the maximum-direction response spectra of the simulated ground motions within a 10 kilometer closest distance to the fault. The comparison demonstrates that the simulated scenarios generate relatively high intensity ground motions at most periods than the MCE_R spectrum. However, the 84th percentile spectrum of the simulated near-fault motions is in reasonable agreement with the MCE_R response spectrum, which represents a bounded minimum of the probabilistic and 84th percentile deterministic MCE ground motion intensities at the site. This agreement implies that the structural risk due to the simulated ground motions within 10 km of the fault is commensurate with the risk associated with the MCE_R spectrum at the selected building site, yet several locations at very short distances may experience severe shaking intensity and structural demands. It is important to emphasize that the same building design is replicated everywhere in the domain; therefore, the design characteristics at each unique distance from the fault do not represent the expected code standards at that location. The uniformity of the building design over the domain allows for studying the relative differences in the structural demands due to the source, path and site effects.

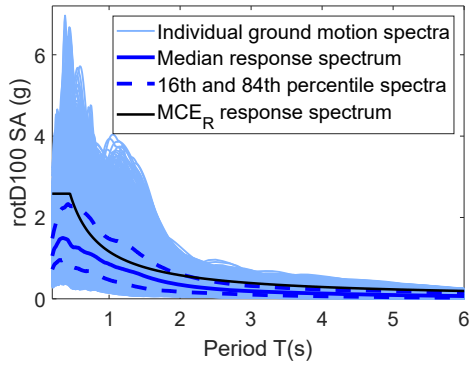

Figure 7.2: Maximum-direction orientation-independent acceleration response spectra of the simulated ground motions in all scenarios within a 10 km closet distance to the fault, along with the risk-targeted Maximum Considered Earthquake response spectrum for the buildings based on ASCE 7-16 ground motion parameter maps for 5% critical damping.

7.2 Correlation between structural demands and intensity measures of simulated and recorded ground motions

Comparing the response of structures to simulated ground motions against their response to real records is an important step toward establishing the use of simulated earthquake ground motions in engineering risk assessments. Such a comparison was conducted in this study using the available, relatively small dataset of records: dataset 1 compiled by Baker et al. [2011]. This dataset was selected because the ground motion FN and FP components are available; therefore, the FN and FP

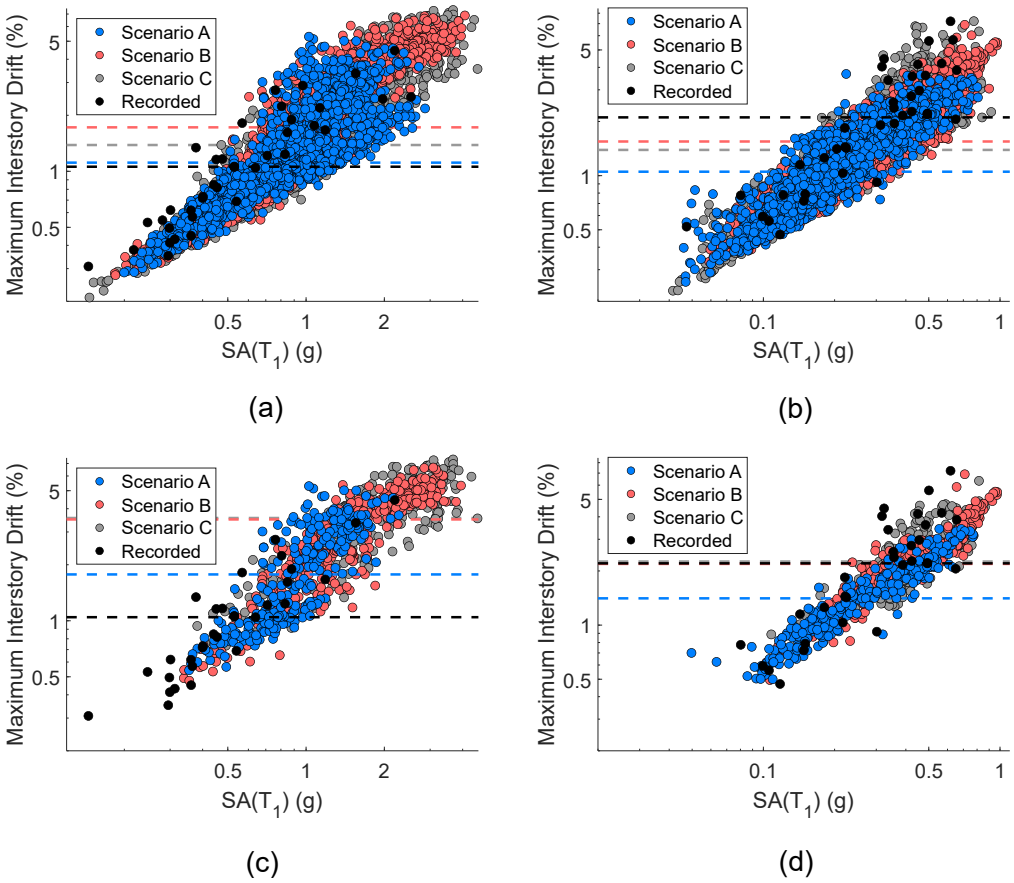

Figure 7.3: Correlation between the maximum interstory drift demands and spectral accelerations at the first-mode period of the building for all three rupture scenarios and recorded dataset 1: (a) for the 3-story building; (b) for the 12-story building; (c) for the 3-story building due to pulse-like motions only; (d) for the 12-story building due to pulse-like motions only.

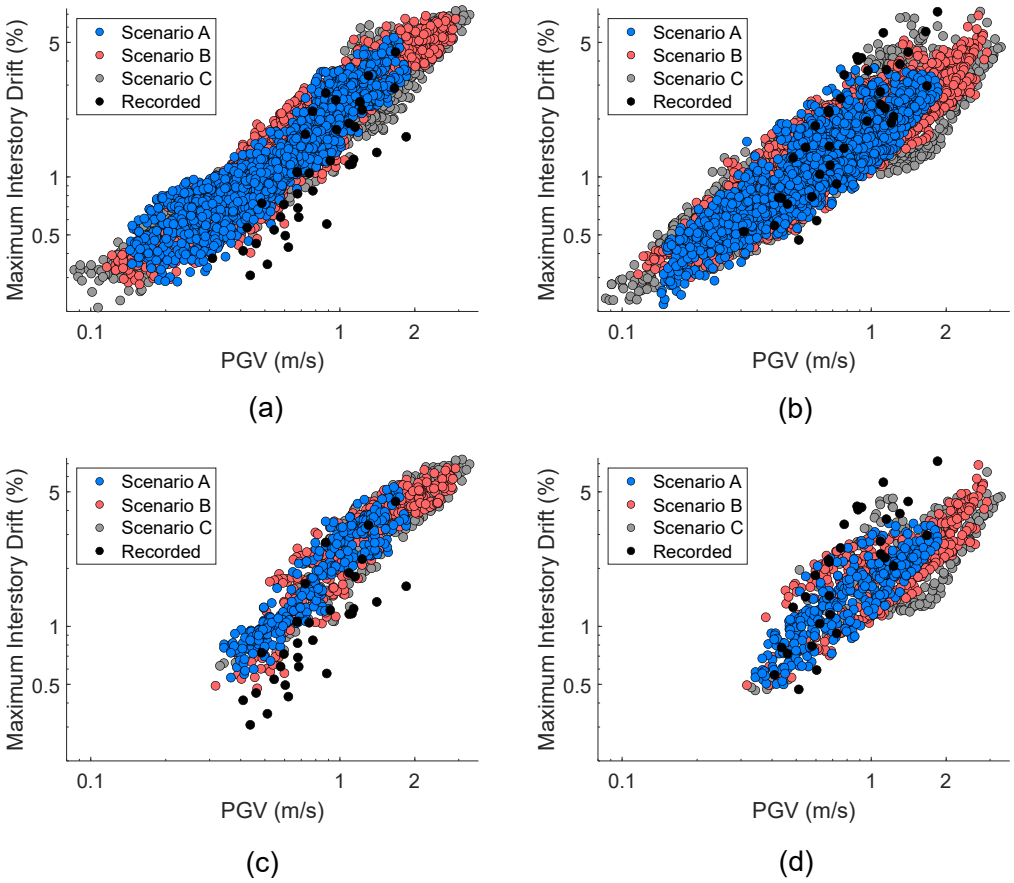

Figure 7.4: Correlation between the maximum interstory drift demands and peak ground velocities in all three rupture scenarios and recorded dataset 1: (a) for the 3-story building; (b) for the 12-story building; (c) for the 3-story building due to pulse-like motions only; (d) for the 12-story building due to pulse-like motions only.

components of the simulated datasets can be directly compared to the components of the recorded ground motions. Such consistency is particularly important at short distances because near-fault ground motions are known to be polarized, with the FN component intensity usually much higher than the FP component.

The maximum structural demands, in terms of the maximum interstory drift ratio (MIDR), on the 3-story and 12-story buildings are plotted against common ground motion intensity measures ($SA(T_1)$ and PGV) in figures 7.3 and 7.4, respectively, due to the FN component of simulated and recorded ground motions approximately within a 10 km closest distance to the fault. In both figures, subplots a and b display the results of the entire group of ground motions, whereas subplots c and d display similar results for the pulse-like ground motions only (specifically, ground motions classified to have a strong velocity pulse in their FN component). The median demands of each dataset are also marked in figure 7.3. The trends of the structural demands induced by scenarios A, B and C in both structures are generally consistent with those induced by the recorded motions. The median MIDR demand on the 3-story building due to scenario A is almost identical to that due to the recorded dataset. However, the hybrid rupture scenarios B and C, which are associated with higher short-period spectral content, lead to more significant structural demands on the 3-story building as compared to the demands induced by the recorded real motions. The opposite trend is evident in the response of the 12-story building, such that the MIDR median due to the recorded motions is higher than the medians of all ground motion simulations, which suggests potential deficiencies of the simulations in the long-period range. As expected, the demands induced by scenarios B and C are closer to those of the recorded motions (with a 27% differences), whereas the median demand of scenario A is about 50% less than that of the available records.

Similar conclusions can be made regarding the consistency of the structural response to the pulse-like simulated and recorded motions, which are plotted separately in figure 7.3c and d. The detected pulse type motions, in general, seem to be associated with a wide range of spectral accelerations, although fewer pulse motions are detected at relatively low SA values. For the 3-story building in particular, several pulse-like motions are detected in dataset 1 with $SA(T_1)$ below 0.35 g, whereas no simulated pulse-like motions are detected. In part, this could be due to the fact that the recorded ground motions generally contain longer period pulses as compared to the simulated motions. The differences between the median demands on the 3-story building due to the simulated and recorded motions are further amplified in the pulse-like subset of data, such that the demands imposed by all the simulated scenarios are significantly higher than those imposed by the recorded ground motions. On the other hand, the agreement between the demands imposed on the 12-story building by the hybrid rupture scenarios and recorded motions is improved for the pulse-like subset, such that the median demands of the pulse subsets of scenario B, C and recorded dataset 1 are identical (figure 7.3d).

The correlation between the PGV and structural demands in figure 7.4 demonstrates important differences between the frequency content of the simulated and recorded motions. In particular, many real records in figure 7.4a and c impose lower structural demands on the 3-story building than simulated motions with similar PGV values. Examining the ground motion waveforms reveals that the velocity pulses of the recorded motions, on average, have lower frequency content than the simulated motions (particularly those from the hybrid ruptures). The pulse frequency content of

each ground motion set is assessed via the mean period of the velocity pulses of the pulse-like records. The mean pulse period for all simulated scenarios (and considering pulses detected in all orientations) is 2.9 seconds, whereas that of the recorded motions is 5.7 seconds. The difference indicates that the recorded motions have significantly longer period energy than the simulated motions. This difference is apparent in the median velocity spectra for the FN components of all datasets in figure 7.5a, in which the distinctive "peaks" are expected to reflect the pulse frequency content of each dataset. All simulated scenarios have higher spectral energy in the short-mid period range (up to a period of about 2 seconds) than the recorded dataset, and scenarios B and C have significantly higher energy than scenario A. In addition, the spectra for scenarios B and C contain a distinctive peak near a period of 1.5 seconds, whereas the spectrum of the recorded motions peaks at a much longer period of about 3 seconds. Scenario A, on the other hand, has a similar energy content to the recorded motions, although it does not possess a prominent peak, which suggests the presence of pulses with a broad range of frequencies. The substantial differences between the ground motion sets are only seen in the FN component, whereas the FP components of the simulated and recorded sets are found to be rather similar (figure 7.5b). Several factors are likely behind the differences in the pulse frequency content between the simulated and recorded motions; most notably the geometry and distribution of the rupture asperities along the fault. These differences, however, decrease significantly at longer periods. Consequently, the response of the 12-story building to the simulated ground motions is consistent with its response to the recorded dataset (figure 7.4b and d), despite the presence of significant ground velocities in the hybrid rupture scenarios (upwards of 200 cm/s) that are not seen in the real records. In general, the comparison against the available records suggests that the structural demands predicted by the stochastic scenario may underestimate the risk for long-period structures. The rupture scenarios with localized slip regions may offer more appropriate risk estimates for long-period structures, and somewhat conservative estimates for short-period structures. It is worth noting that the impact of pulse-like motions on the structural demands strongly depends on the relationship between the effective structural period and the frequency content of the largest velocity pulse [Champion and Liel, 2012]; this topic is discussed in detail in chapter 9.

7.3 Spatial variability of the intensity of simulated ground motions

From the point of view of structural risk assessment, it is of interest to examine the correlation of structural demands with the spatially varying characteristics of ground motions, and to determine which intensity measures better correlate with structural response. In particular, estimates of the structural risk would be improved if the structural response depends only on the ground motion IMs (and not the fault distance or other parameters). Investigations of the efficiency of ground motion IMs in predicting structural demands are particularly feasible for earthquake simulations, which generate highly dense and regionally well-distributed ground motion datasets. Figure 7.6 shows 2D map plots of $SA(T_1)$ for the 3-story building and PGV from the FN components of scenarios A and B, along with maps of the maximum interstory drifts, and figure 7.7 shows similar data for the

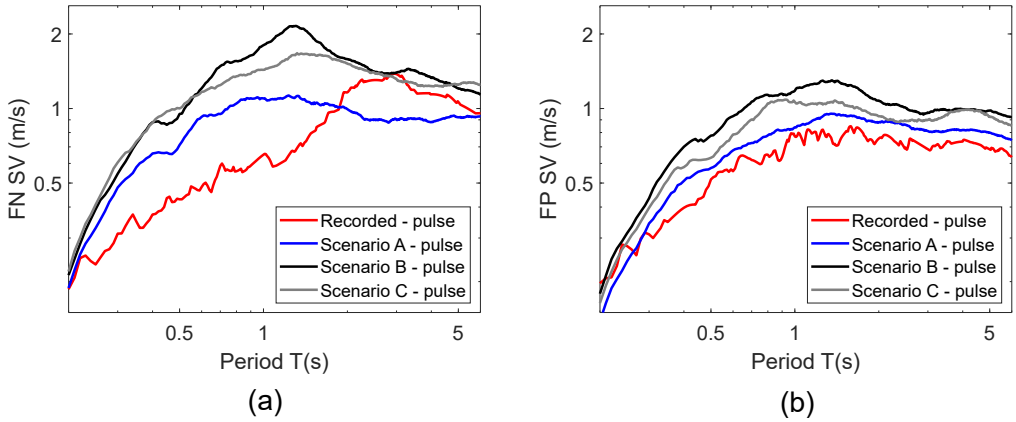

Figure 7.5: Median velocity response spectra for all simulated ground motion sets and the recorded dataset 1: (a) FN component; (b) FP component.

12-story building with different color scales. In addition, figure 7.8a and b show plots of the MIDR demands on both buildings against a normalized $SA(T_1)$ over the entire domain for all scenarios. The spectral accelerations are normalized by the base shear coefficient for each building γ listed in table 6.1, in order to enable the comparison between the demands on the two different buildings. A linear regression model is also shown in each subplot. In addition, the normal distance to the fault is indicated as a third parameter using the color-coding of the data points. Similar plots of the MIDR are shown in figure 7.8c and d against the PGV over the entire computational domain and for all scenarios.

The color map plots of figures 7.6 and 7.7 visually demonstrate the general agreement between $SA_(T_1)$ and the structural demand trends over the entire computational domain. The trends in figure 7.8a reveal a strong linear correlation between the 3-story MIDR and $SA_(T_1)$ for small SA values (up to about 0.3 g), which correspond mostly to locations that are between 20 and 30 km away from the fault. As the distance to the fault decreases, the ground motion intensity increases, inciting more nonlinear response in the 3-story building, and leading to a large dispersion in the MIDR-SA relationship. For example, at $SA_(T_1) = 2.0g$, the MIDR varies by a factor of 4.1. It is worth noting that the apparent reduction in the dispersion at the highest SA values (larger than 3.0 g) is likely due to the limited number of data points at such high values, because the highest spectral accelerations are only encountered in very localized regions near or at the fault.

In contrast to the 3-story building, the dispersion in the correlation between SA and MIDR for the 12-story building (figure 7.8b) is significant over the entire range of spectral accelerations, because the 12-story building is likely to be sensitive to a wider range of frequencies, which is not accounted for in the parameter $SA(T_1)$. The analysis also indicates that the 12-story building generally experiences less yielding and period elongation, compared to the 3-story building. Therefore, the dispersion in the correlation between $SA(T_1)$ and the 12-story MIDR is relatively uniform over the entire range of spectral accelerations. Unlike the 3-story building observations, figure 7.8b also reveals a larger scatter in the distribution of spectral acceleration values with respect to fault

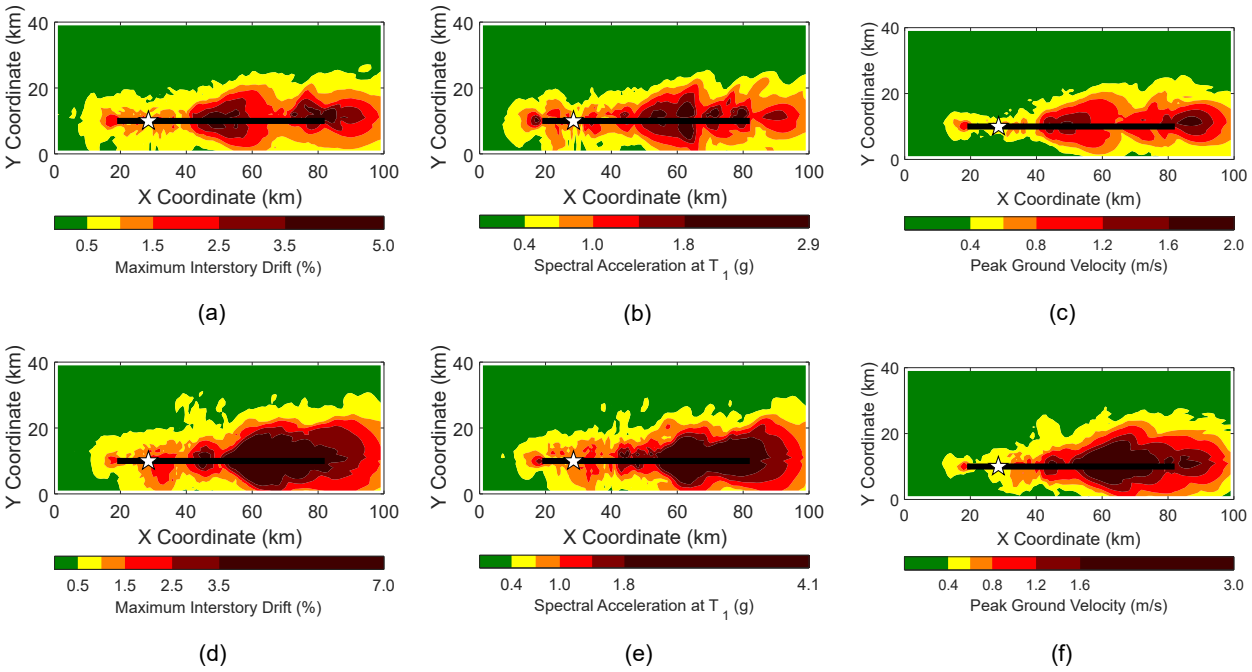

Figure 7.6: ground motion intensity and structural demand maps for the 3-story building: (a) interstory drift map - scenario A; (b) $SA(T_1)$ map - scenario A; (c) PGV map - scenario A; (d) interstory drift map - scenario B; (e) $SA(T_1)$ map - scenario B; (f) PGV map - scenario B.

normal distance. For example, relatively low spectral accelerations can be encountered at sites that are as close as a few kilometers or as far as 29 km away from the fault. This is further demonstrated by the attenuation plot in figure 7.9 which shows the variation of the spectral accelerations $SA(T_1)$ for both the 3-story and 12-story buildings with respect to the fault normal distance, along with the median values and multiplicative standard deviation of the normal distribution of $log(SA)$ at each given distance. To enable the comparison at the different fundamental periods, the spectral accelerations in each subplot are normalized by the median $SA(T_1)$ for all ground motion records at T_1. The figure shows that $SA(T_1)$ for the short-period building varies significantly with respect to normal distance from the fault (the median value varies by a factor of 9.0 over a distance of 29 km). At the same time, the dispersion in the $SA(T_1)$ values is higher at short distances from the fault, then drops significantly at longer distances. The higher dispersion in the near-fault region may be attributed to directivity effects amplifying the ground motion intensity in locations in the direction of the rupture propagation, whereas locations in the near-fault backward directivity region experience relatively lower intensities. In contrast, $SA(T_1)$ for the long-period building does not vary as significantly with distance (the median value varies by a factor of 4.0 over a 29 km distance) due to the slower attenuation of low-frequency waves. However, the dispersion is relatively high over the entire domain, and does not significantly decrease at longer distances. For example, at 29 km, the coefficient of variation of $log(SA(T_1))$, which is a measure of the data dispersion, is 0.63 for the 12-story building, compared to a value of 0.41 for the 3-story building.

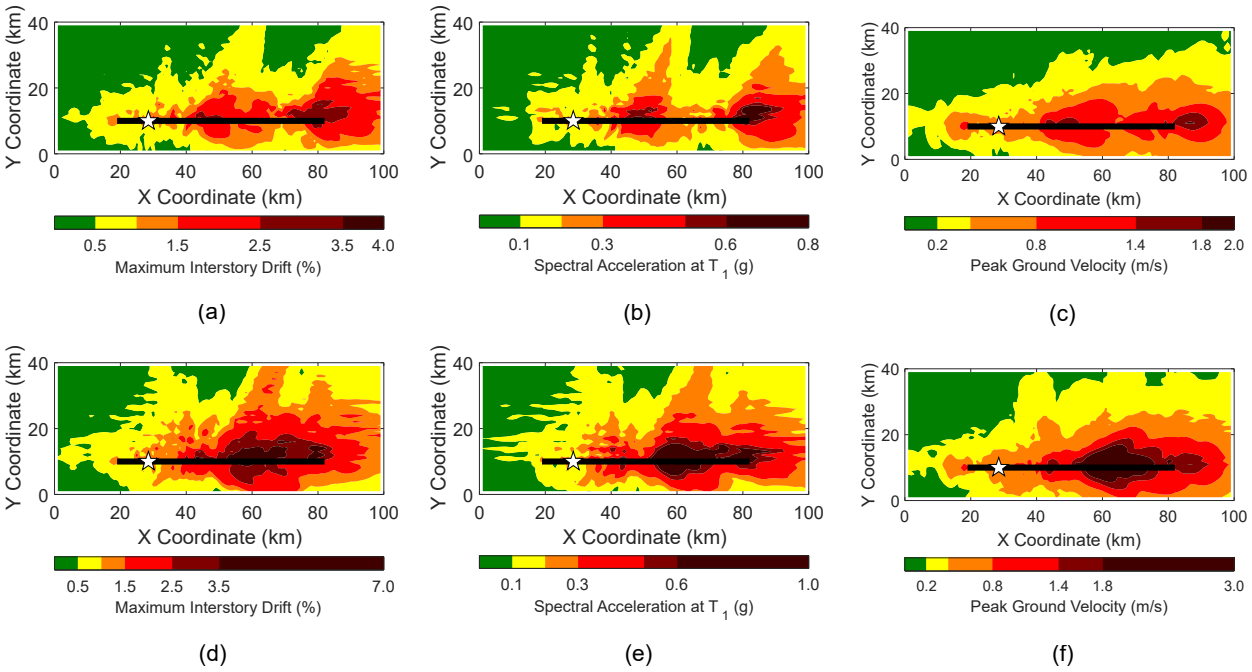

Figure 7.7: ground motion intensity and structural demand maps for the 12-story building: (a) interstory drift map - scenario A; (b) $SA(T_1)$ map - scenario A; (c) PGV map - scenario A; (d) interstory drift map - scenario B; (e) $SA(T_1)$ map - scenario B; (f) PGV map - scenario B.

Somewhat similar trends are observed for the relationship between the PGV and building structural demands. While the PGV is not directly associated with the building dynamic properties, it is a common measure of the to the amplitude of ground motion velocity pulses. Therefore, the PGV is anticipated to correlate with building response particularly in the near-field, where ground motions dominated by large velocity pulses are far more likely. The map plots of the PGV in figures 7.6 and 7.7 demonstrate the general correlation between the PGV and MIDR demands over the entire domain for both buildings. The regions of maximum structural demands - which differ between different scenarios but primarily span the region between 20 and 60 km away from the rupture source and within 10 km normal to the fault - coincide with the largest ground velocities (between 160 and 300 cm/s). Relatively low ground velocities (up to 40 cm/s) are experienced in most locations in the domain beyond 10 km away from the fault, in addition to most locations in the backward directivity region. This PGV value corresponds to essentially elastic response of the 3-story (up to 0.5% MIDR), and limited plastic response in the 12-story building (up to 1% MIDR). Despite the general agreement between the PGV and maximum structural demands in the near-field, the scatter plots of figure 7.8c and d, highlight the larger dispersion in the MIDR associated with a given PGV value, particularly in the far-field region. For the 3-story building, a linear regression model between the logarithms of $SA(T_1)$ and MIDR in the far-field region (beyond 10 km away from the fault) is associated with an error variance of 0.014, as compared to a variance of 0.083 for the logarithm of the PGV. A similar trend exists for the 12-story building. In the near-

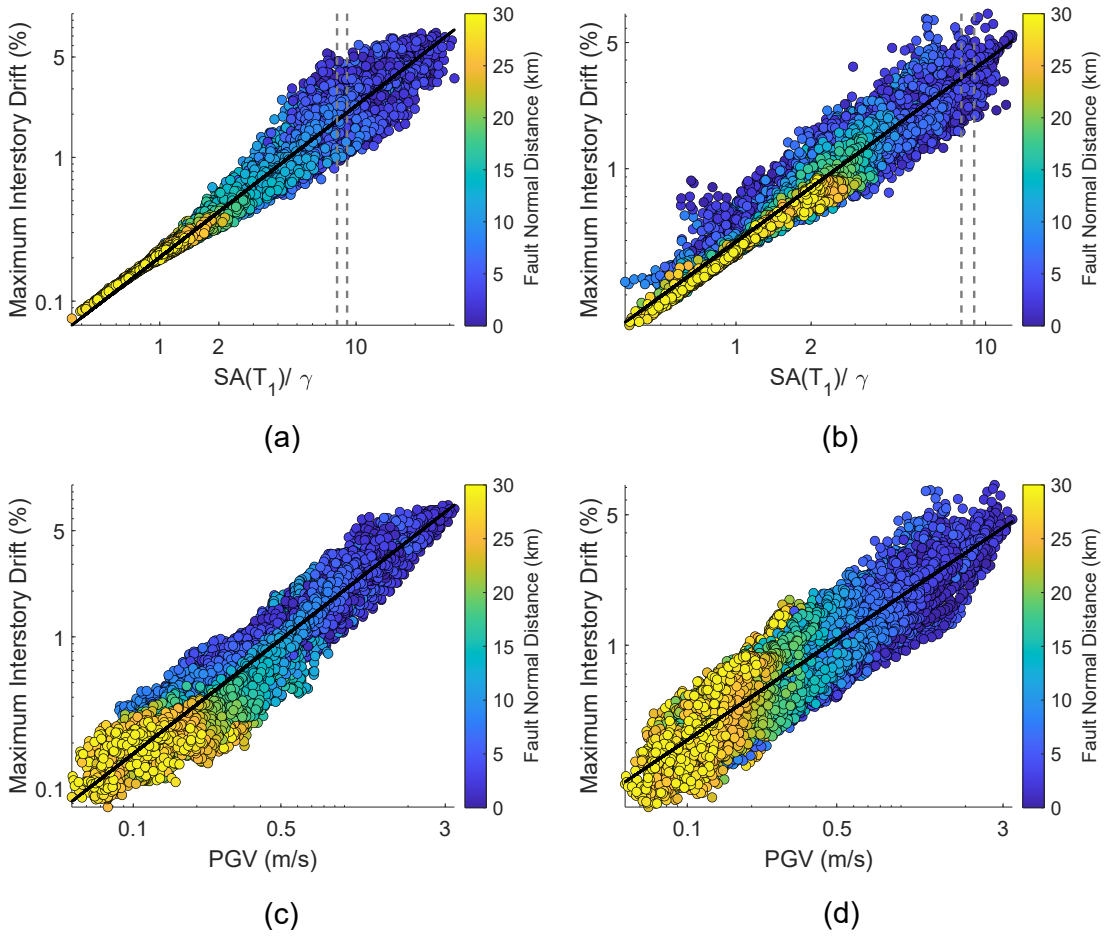

Figure 7.8: Correlation between the ground motion intensity and the maximum interstory drift color-coded by the normal distance from the fault: (a) $SA(T_1)/\lambda$ for the 3-story building; (b) $SA(T_1)/\lambda$ for the 12-story building; (c) PGV for the 3-story building; (d) PGV for the 12-story building.

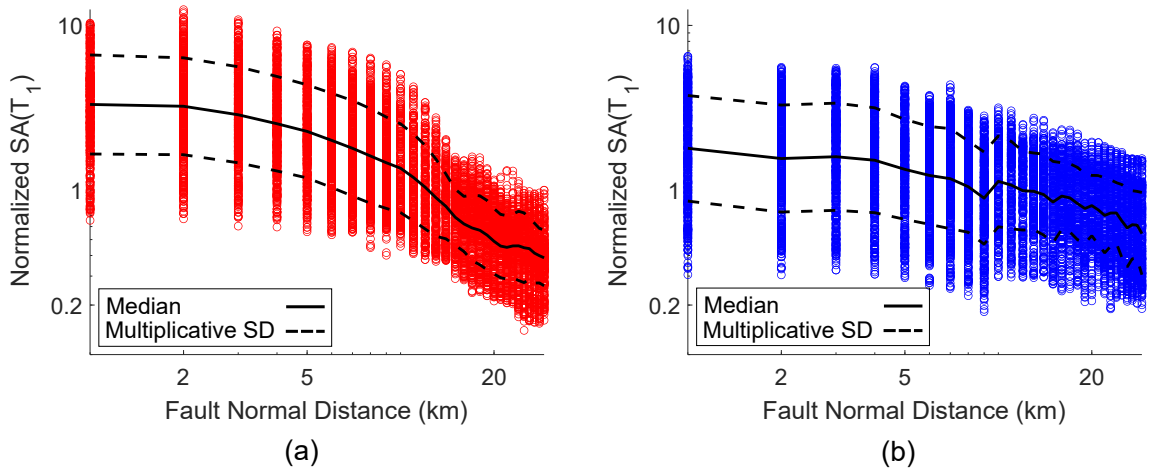

Figure 7.9: Attenuation of $SA(T_1)/\lambda$ with normal distance from the fault: (a) for the 3-story building; (b) for the 12-story building.

field, however, the dispersion in the relationship between the MIDR and both measures ($SA(T_1)$ and PGV) is comparably high, although the scatter associated with the near-field 3-story building response is marginally but consistently lower than that of the 12-story building. This result can be attributed to the slower attenuation of the low frequency waves primarily affecting the 12-story building, and the fact that the flexible buildings may be sensitive to wider range of velocity pulses in the near-fault regions. In general, the PGV is found to better correlate with structural response when the structure experiences significant nonlinear demands, and is less appropriate for structures primarily responding elastically.

7.4 Advanced ground motion intensity measures

The wide scatter in the engineering demand parameter (in this case, MIDR) at large spectral acceleration values confirms findings of previous studies that $SA(T_1)$ is not a sufficient IM for near-fault ground motions. In other words, structural demands at a particular level of $SA(T_1)$ depend on other ground motion or structural characteristics. For the purpose of seismic risk assessment, it is important to identify other ground motion characteristics that affect the structural response. A sufficient IM enables engineers to select ground motions for nonlinear dynamic analyses of structures without considering source and site parameters. Therefore, with the large body of data generated in this study, it is of interest to examine the question of whether the large variability in the structural demands near the fault can be reduced by considering other characteristics of the ground motions. Previous studies found that structural demands are highly sensitive to the ground motion spectral shape, particularly in structures behaving nonlinearly [Baker and Cornell, 2008]. This is because nonlinear structures experience a period lengthening effect after yielding; therefore, their response is no longer adequately characterized by $SA(T_1)$ only. To examine the sensitivity of the buildings

studied herein to the ground motion spectral shape, the structural demands at multiple levels of relatively high $SA(T_1)$ (near-fault locations) were plotted against a normalized measure of the ground motion structural shape proposed by Marafi et al. [2016]. This measure, referred to as SSA, represents a normalized integral of the pseudo acceleration spectrum over a period range that depends on the structure's ductility capacity. This range was defined to be between the first mode period T_1 and an elongated period αT_1, where α was determined as recommended in Marafi et al. [2019] as the square root of the building displacement ductility capacity. In this study, the building displacement ductility capacity was defined as the ratio of the roof displacement level corresponding to 20% loss in the base shear capacity to the yield displacement, during a static pushover analysis of the building. Figure 7.10 shows plots of the MIDR demands vs. the spectral shape parameter SSA at a particular level of $SA(T_1)/\gamma$ for both buildings. Because $SA(T_1)$ is a continuous variable, the demands were sampled at a narrow window of $SA(T_1)$, which corresponds to $SA(T_1)/\gamma$ between 8 and 9. Despite having roughly the same $SA(T_1)/\gamma$, the ground motions differ significantly in spectral shape. Figure 7.10a shows a strong linear correlation between the MIDR and SSA for the 3-story building at this particular level of $SA(T_1)/\gamma$. A similar trend was observed at other $SA(T_1)/\gamma$ levels. This suggests that an IM which incorporates spectral shape would be more appropriate for structural demand analysis of the 3-story building in the near-field. Similar findings were reported by other researchers [Baker and Cornell, 2008]. It is, however, seen that the demands on the 12-story building are not as sensitive to spectral shape, as indicated by the large scatter in figure 7.10b. This trend is believed to be a consequence of the lower level of nonlinear response observed in the 12-story building. A modified spectral shape parameter which integrates the response spectrum over the period range between $T_1/3$ and T_1 was developed to assess the sensitivity of the 12-story building to the shape of the response spectrum in the shorter-period range, and the potential contribution of the second vibration mode. However, the dispersion in the structural demands at a given spectral shape parameter value remained high. These results suggest that an IM incorporating spectral shape may not necessarily reduce the dispersion in characterizing the response of long-period structures, although these results are only applicable at low and moderate structural demand levels. The results also suggest that the correlation between the spectral shape parameter and the collapse capacity is expected to be strong for all structures. The sensitivity of the 12-story building to other long-period characteristics of ground motions in the near-field, namely the shape of the velocity response spectrum and the frequency content of large velocity pulses, is closely examined in chapter 9.

Several researchers suggested the use of advanced IMs which incorporate the ground motion spectral shape [Baker and Cornell, 2008]. Among those is the so-called effective spectral acceleration [Marafi et al., 2016] which incorporates measures of both the ground motion duration and spectral shape:

$$SA_{eff} = SA(T_1)\, \gamma_{shape}^{C_{shape}} \gamma_{dur}^{C_{dur}} \tag{7.1}$$

where γ_{shape} and γ_{dur} are dimensionless parameters that characterize the effect of spectral shape and duration, and C_{shape} and C_{dur} are exponent terms determined based on Marafi et al. [2019]. It was concluded in this study that the MIDR demands do not exhibit substantial sensitivity to the ground motion duration (this topic will be discussed further in the following chapter). Therefore, the duration parameter γ_{dur} was excluded from the correlation by setting the exponential duration

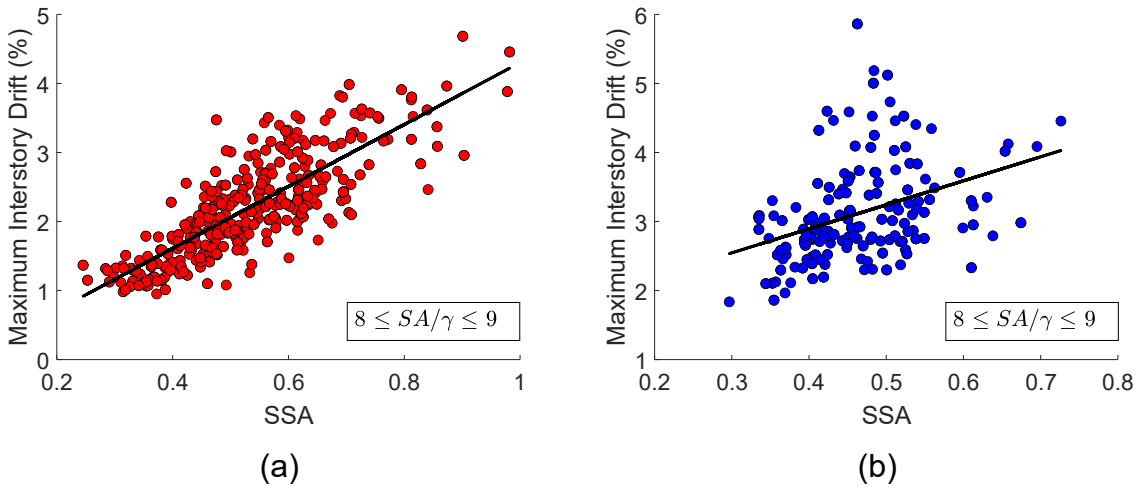

Figure 7.10: Correlation between the maximum interstory drift and the spectral shape parameter SSA at a given $SA(T_1)/\lambda$: (a) for the 3-story building; (b) for the 12-story building.

term to 0.0. The SA_{eff} measure in this study thus accounts for only the spectral acceleration at T_1 and the shape of the response spectrum over a ductility-dependent period range. The SA_{eff} IM is seen to strongly correlate with structural demands of the 3-story building in the near-field, as indicated by figure 7.11b, which shows the MIDR demands vs. SA_{eff} only at locations within a 5-km distance normal to the fault. The error variance, which is a simple measure of the correlation in a linear regression between the logarithms of both parameters, is 0.039, compared to an error variance of 0.087 between the logarithms of the MIDR and $SA(T_1)$ over the same locations (figure 7.11a). As expected, however, structural demands at lower $SA(T_1)$ levels (at longer distances from the fault) are not sensitive to the spectral shape and do not strongly correlate with SA_{eff}. In fact, SA_{eff} does not seem to be an appropriate measure over all SA levels, because it significantly increases the dispersion at lower SA levels. For the 12-story building, whose response does not seem to be as sensitive to the spectral shape, using the SA_{eff} IM does not substantially improve the correlation with the structural demands at either short distances (see figure 7.11c and d) or long distances from the fault. It is recognized that as the levels of SA increase, structures are expected to behave more nonlinearly, experience period elongation and exhibit higher sensitivity to spectral shape. This explains the reduced dispersion in the collapse capacity of structures when their response is correlated with measures such as SA_{eff} [Marafi et al., 2019]. Such measures may, however, not be beneficial for applications requiring correlation between IMs and structural demands at a wide range of ground motion intensities.

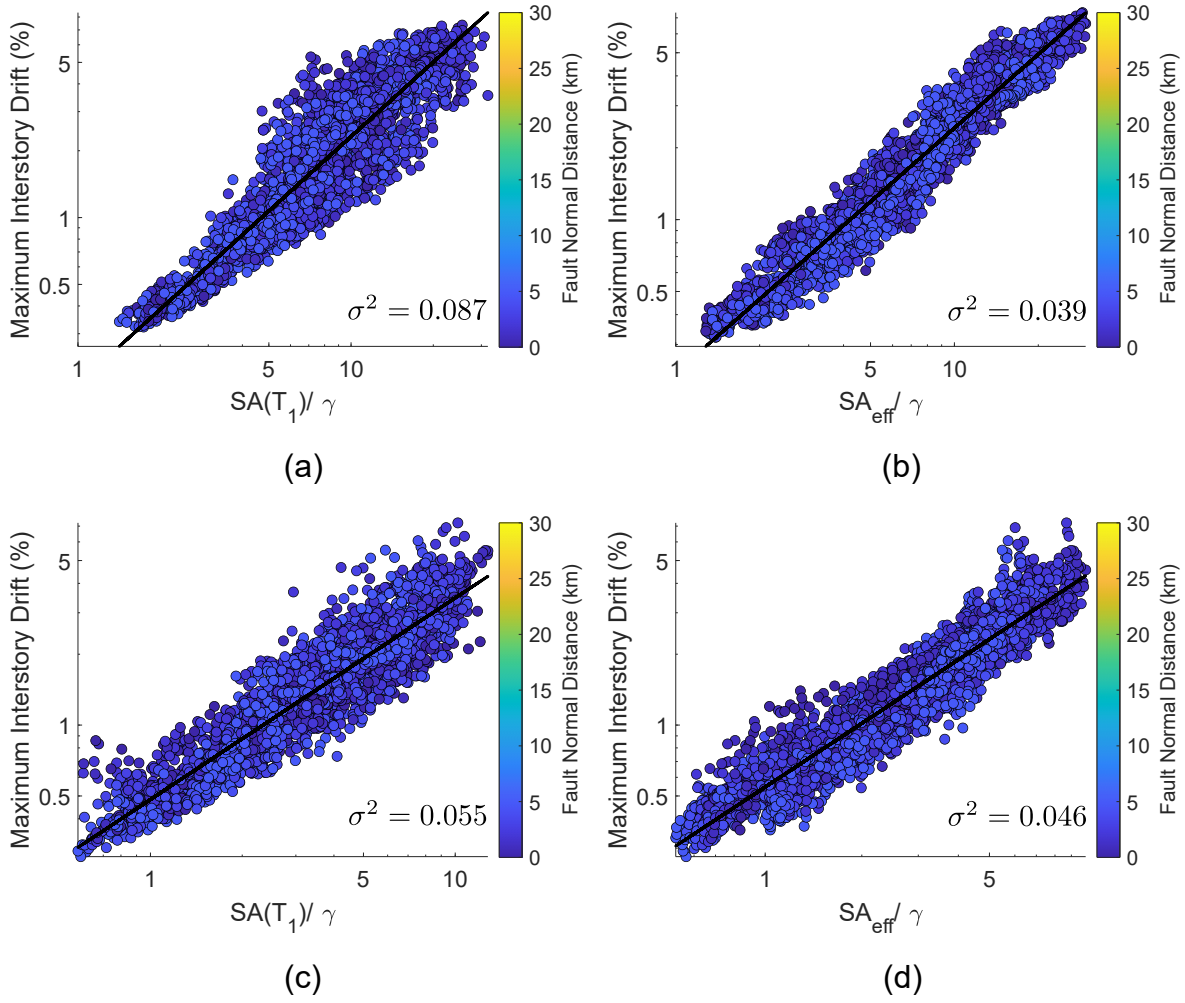

Figure 7.11: Data points and linear regression models characterizing the relationship between the maximum interstory drift for buildings within a 5-km normal distance to the fault and: (a) the normalized $SA(T_1)$ - 3-story building; (b) the normalized SA_{eff} measure - 3-story building; (c) the normalized $SA(T_1)$ - 12-story building; (b) the normalized SA_{eff} measure - 12-story building. The plots represent results of the FN component of ground motions from all three scenarios.

Chapter 8

Regional-Scale Spatial Variability of Risk to Modern RC Buildings

The variability of structural risk within a single earthquake scenario and between different rupture scenarios is the primary focus of this study. In this chapter, important aspects of the response of RC buildings to the simulated ground motions are characterized with respect to (1) the spatial variability of the structural demands near the fault, particularly over regions impacted by forward directivity effects; (2) the effects of the presence of localized high-slip patches on the ground motion intensity and structural demands near the fault; and (3) the differences in the structural demands between sites on basin and rock soils at identical distances from the rupture source. The structural risk to the 12-story and 3-story buildings is studied via map plots representing the response quantities over the computational domain, distributions of the structural response at a given distance from the fault, and detailed analysis performed at selected stations within the domain. The structural risk is quantified in this study using the following quantities:

- Largest interstory drift experienced in the building normalized by the story height. This quantity is referred to as the maximum interstory drift ratio (MIDR), and is ubiquitously used to judge the structural member deformation demands, and define damage limit states for buildings. The MIDR was selected because it provides a reasonable and simple estimate of the ability of the structure to resist side-sway collapse.The map plots in this study use the interstory drift limits defined in ASCE 43-05 [ASCE, 2005] to represent expected damage states in reinforced concrete buildings. The ASCE 43 drift limits (0.5%, 1.0%, 1.5% and 2.5%) are anticipated to correspond to essentially elastic behavior, limited plasticity, moderate plasticity and large plasticity, respectively. Despite the fact that these limits differ depending on the building ductility, the interstory drift provides valuable insight on the relative expected deformation demands over the domain.

- Largest rotation experienced in the plastic hinges at the end of a structural member (beam or column). This measure relates more directly to the plastic rotation capacity of the structural member, and is capable of predicting a localized loss in the load carrying capacity of a member after a plastic hinge reaches its plastic rotation capacity. This measure is presented

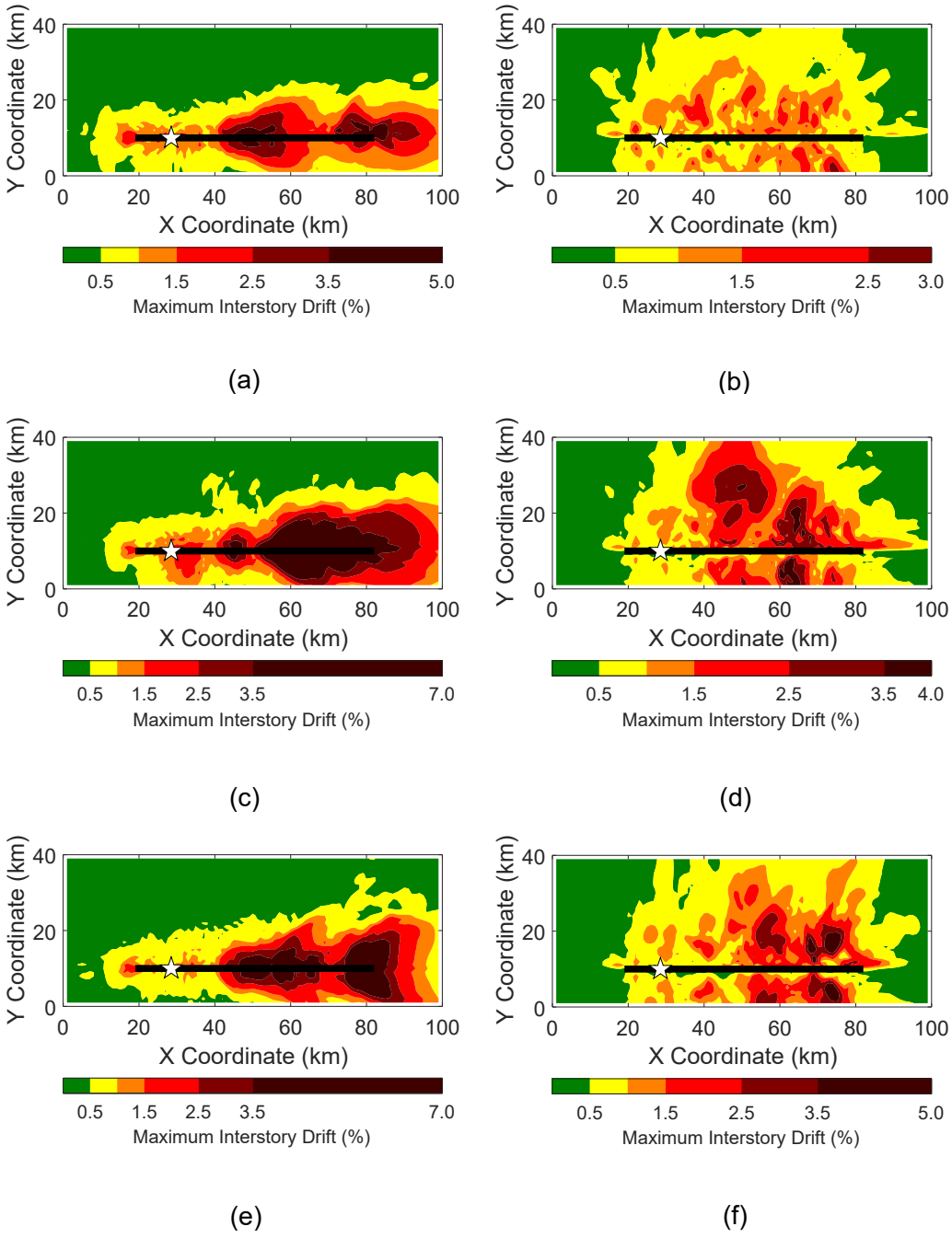

Figure 8.1: Map representation of structural risk - in terms of maximum interstory drift demands - to the 3-story RC building due to: (a) the FN component of scenario A; (b) the FP component of scenario A; (c) the FN component of scenario B; (d) the FP component of scenario B; (e) the FN component of scenario C; (f) the FP component of scenario C.

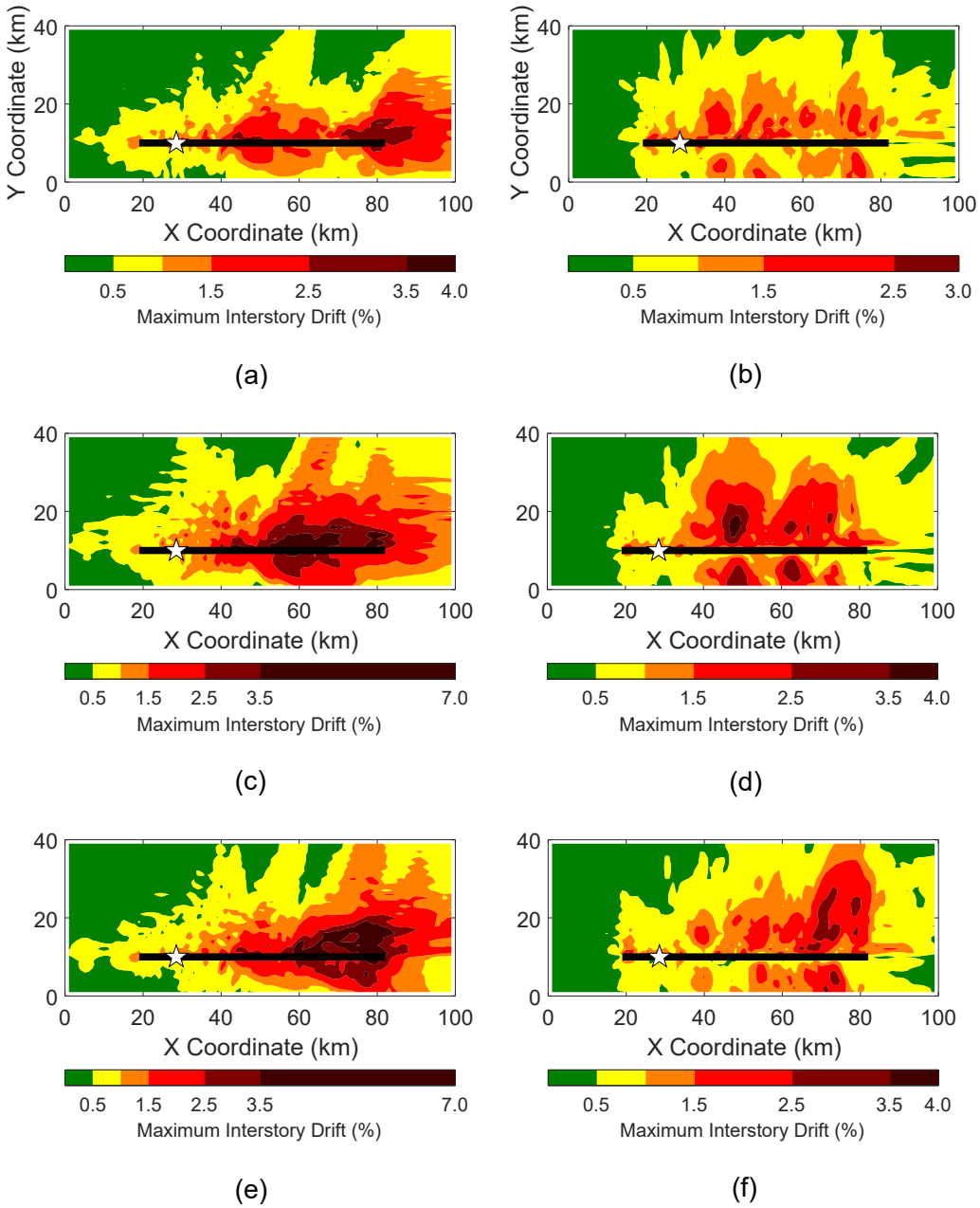

Figure 8.2: Map representation of structural risk in terms of maximum interstory drift demands on the 12-story RC building due to: (a) the FN component of scenario A; (b) the FP component of scenario A; (c) the FN component of scenario B; (d) the FP component of scenario B; (e) the FN component of scenario C; (f) the FP component of scenario C.

in this study as a demand-to-capacity ratio; i.e., a ratio of the maximum rotation demand experienced in a structural member to its plastic rotation capacity. Although this measure depends on the assumptions and calibrations associated with the lumped-plasticity structural modeling approach, it is useful in a relative sense to judge the variability of the response of structural members.

8.1 Spatial variability of structural response in a single earthquake scenario

The map plots of the MIDR demands in figures 8.1 and 8.2 represent the structural risk to the 3-story and 12-story buildings, respectively, due to the all three rupture scenarios (A, B and C); the aforementioned limits of the MIDR demands are assigned different colors to indicate intensity. Both the fault and the location of the hypocenter are also shown in the plots. The structural risk maps highlight the differences between the FN (subplots a, c and e of both figures) and the FP (subplots b, d and f) component of the strike-slip scenarios at short distances. The FN component of each scenario exhibits a strong directivity effect that is concentrated within 10 km of the fault and characterized by relatively high structural demands. The FP component, on the other hand, imposes lower structural demands that are more pervasive over the entire domain. For both buildings, the FN MIDR demands over most of the domain do not exceed 3.5%. However, in a small number of locations at short distances from the fault (up to about 5 km) in the forward directivity zone, MIDR demands up to 7% are observed; these large demands are particularly seen in the hybrid rupture scenarios B and C, which seem to be more damaging than scenario A.

The highest spatial variability in the structural demands for both buildings is seen within 10 km of the fault under the FN component for all scenarios. The MIDR demand trends at several distances from the fault are examined in figures 8.3 and 8.4 for both components of all rupture scenarios. The location of the hypocenter is designated with a dashed line in all subplots. At a one kilometer distance from the fault, the MIDR in the 3-story building due to the FN component varies by a factor up to 7.9 along the length of the fault (this factor is defined by the ratio of the maximum to minimum MIDR at the designated distance). At ten kilometers away, the demands vary by a factor up to 6.8. This factor drops to 3.3 at twenty kilometers away from the fault. A comparable trend is observed in the FN MIDRs of the 12-story building, which vary by a factor of 7.0 at one kilometer, by a factor of 5.7 at ten kilometers, and by a factor of 4.6 at twenty kilometers away. In contrast, the spatial variability in the demands on both buildings due to the FP component is much more limited over the domain. The trends in all scenarios also reveal that, within 10 km of the fault, the demands induced in the 3-story building are relatively higher than those induced in the 12-story building, which may be attributed to the frequency content of the ground motions. In contrast, the demands on the 12-story building exhibit a more significant degree of variability than the 3-story building for locations beyond 10 km; a trend that is likely caused by the slower attenuation of the low frequency waves affecting the 12-story building.

The variation of FN ground motion characteristics and corresponding structural response as the normal distance from the fault increases is further examined at four stations that have the same

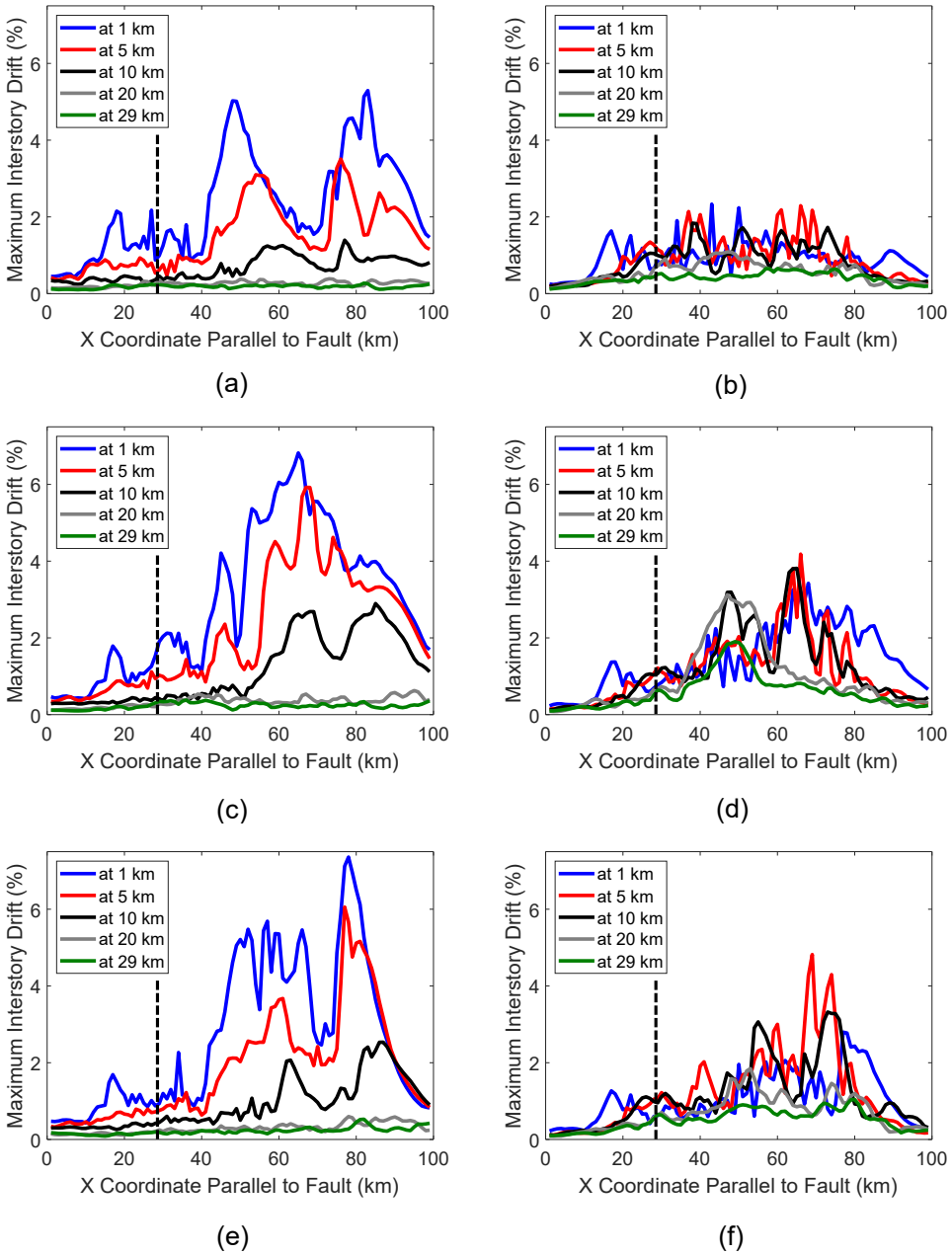

Figure 8.3: Maximum interstory drift trends along the fault for the FN component of ground motions: (a) for the 3-story building in scenario A; (b) for the 3-story building in scenario B; (c) for the 3-story building in scenario C; (d) for the 12-story building in scenario A; (e) for the 12-story building in scenario B; (f) for the 12-story building in scenario C.

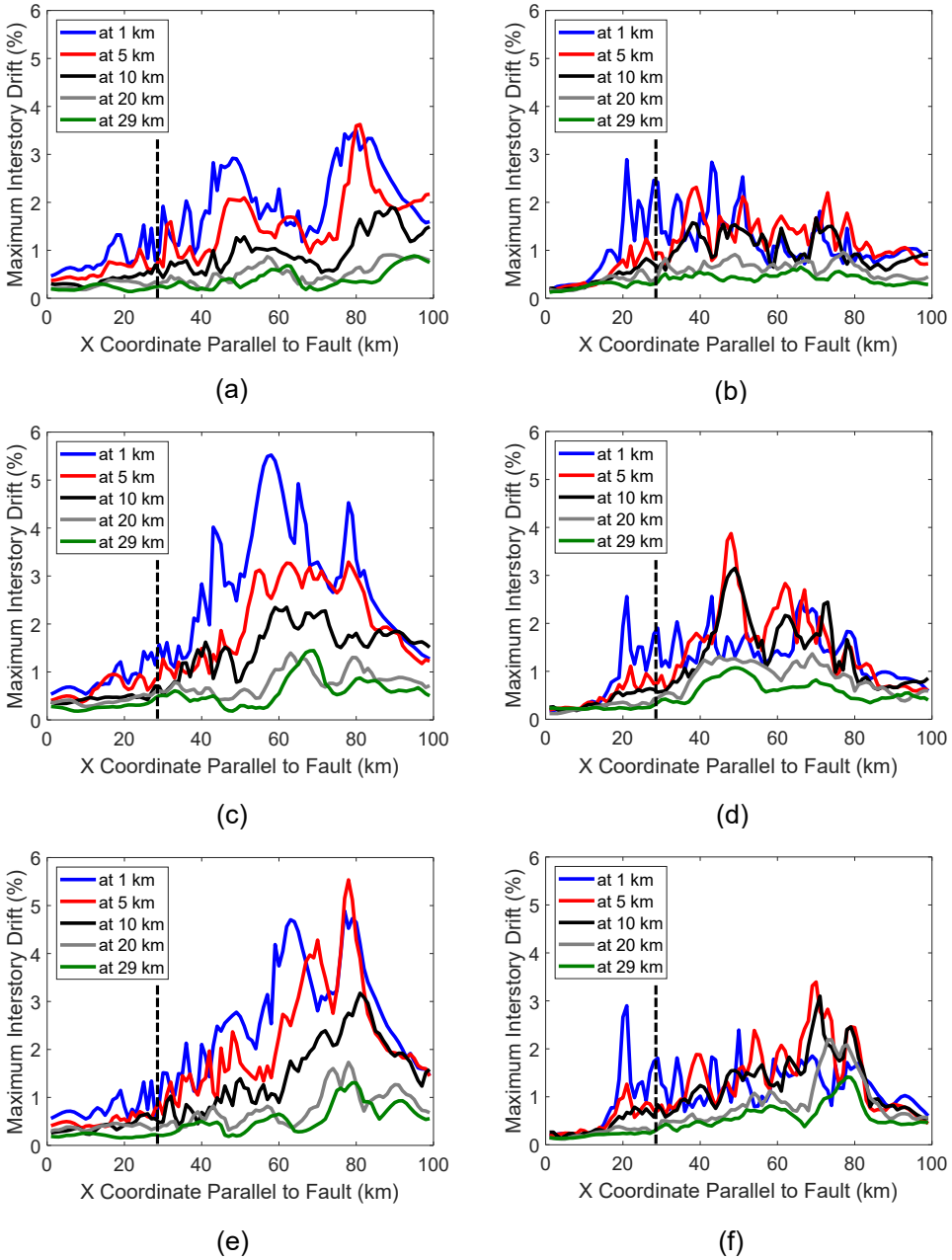

Figure 8.4: Maximum interstory drift trends along the fault for the 12-story RC building due to: (a) the FN component of scenario A; (b) the FP component of scenario A; (c) the FN component of scenario B; (d) the FP component of scenario B; (e) the FN component of scenario C; (f) the FP component of scenario C;

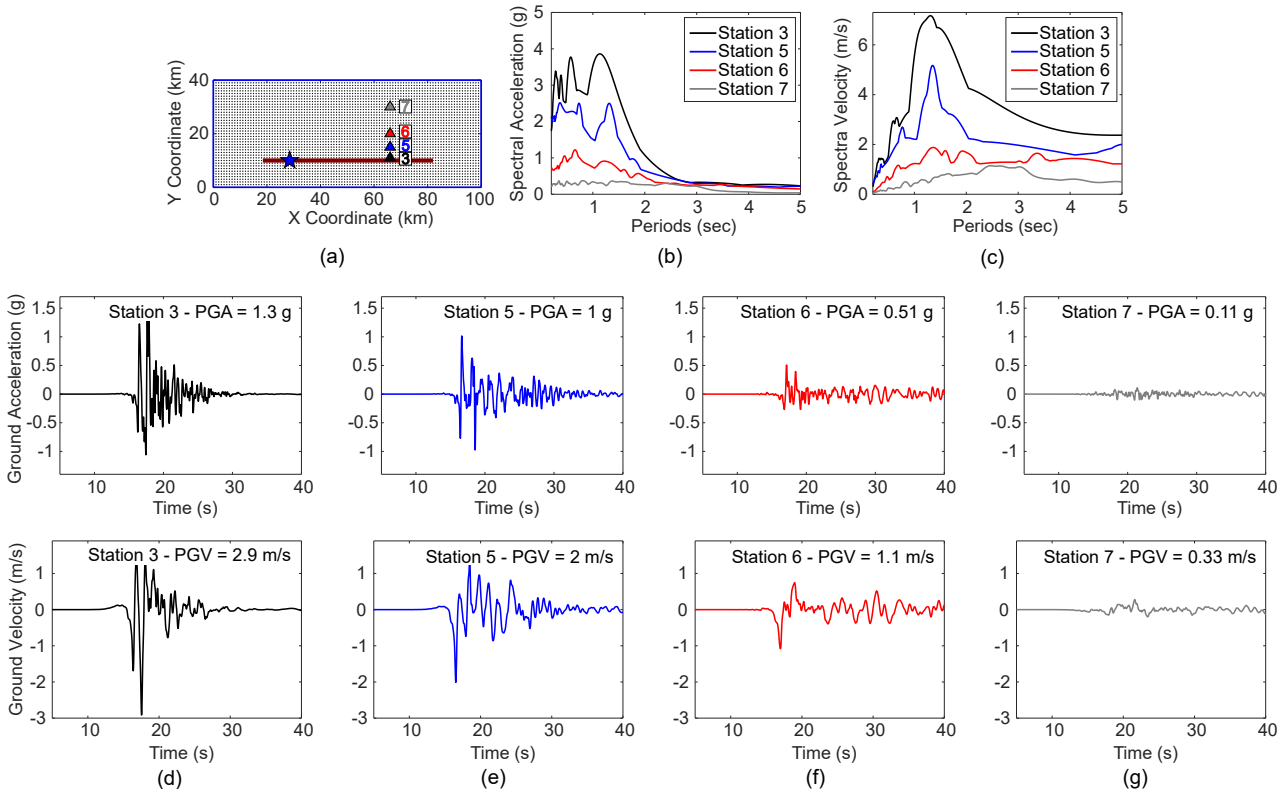

Figure 8.5: The characteristics of the FN component ground motions at stations 3, 5, 6 and 7 in rupture scenario B: (a) locations of the stations in the computational domain; (b) acceleration response spectra at all stations; (c) velocity response spectra at all stations; (d) acceleration and velocity time histories at station 3; (e) acceleration and velocity time histories at station 5; (f) acceleration and velocity time histories at station 6; (g) acceleration and velocity time histories at station 7.

Table 8.1: Ground motion characteristics at stations 1 - 7 in scenario B

Station #	**Distance normal to fault (km)**	**Hypocentral distance parallel to fault (km)**	**PGA (g) - FN**	**PGA (g) - FP**	**PGV (m/s) - FN**	**PGV (m/s) - FP**
1	1.0	13.5	0.75	0.32	1.1	0.84
2	1.0	25.5	0.77	0.38	2.1	0.81
3	1.0	37.5	1.3	0.61	2.9	1.1
4	1.0	49.5	1.1	0.51	1.5	1.0
5	5.0	37.5	1.0	1.1	2.0	1.3
6	10.0	37.5	0.51	0.83	1.1	1.1
7	20.0	37.5	0.11	0.48	0.33	0.62

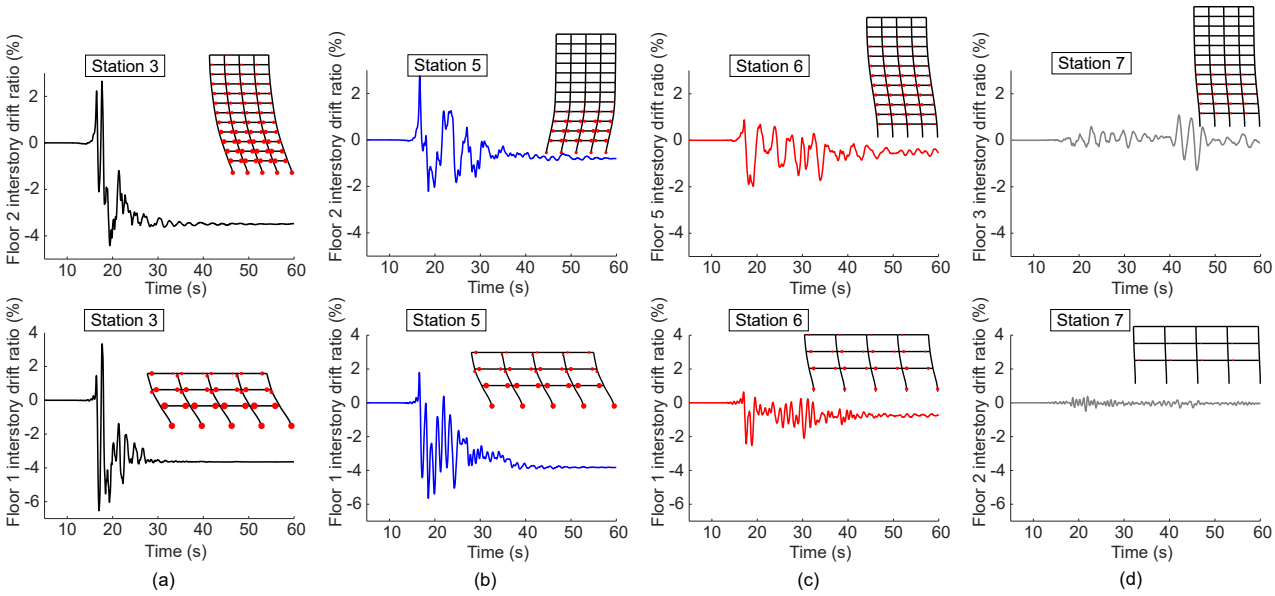

Figure 8.6: Deformed shape, plastic hinges and maximum floor drift histories for the 12-story and 3-story buildings: (a) at station 3; (b) at station 5; (c) at station 6; (d) at station 7.

x-coordinate and different y-coordinates (different normal distances from the fault); in this case, stations 3, 5, 6, 7 defined in table 8.1. All stations are at a horizontal distance of 37.5 km away from the hypocenter, and 1, 5, 10 and 20 kilometers normal to the fault, as shown in figure 8.5a. Figure 8.5d-g show the ground acceleration and velocity of the FN component due to rupture scenario B at each of the four stations. These plots highlight the significant difference in the peak ground accelerations and velocities between stations at very short distances (1 and 5 km away) and stations at relatively longer distances (10 and 20 km away). For instance, the PGV at 1 km (station 3) is 2.6 times the PGV at 10 km (station 6), and almost 9 times the PGV at 20 km (station 7). Similarly, the peak ground acceleration (PGA) at 10 and 20 km drops by factors of 2.5 and 12.0 relative to the PGA value at 1 km, respectively. The significant drop in the ground motion intensity as the normal distance increases is also evident in the spectral characteristics of the ground motions in figure 8.5b and c, particularly in the short to mid period range. For example, $SA(T_1)$ for the 3-story building at 1 km is 2.9 times that at 10 km, and 9 times $SA(T_1)$ at 20 km. In contrast, $SA(T_1)$ for the 12-story building at 1 km is only 2.3 times that at 10 km, and 3 times the spectral acceleration at 20 km. The spatial variability in the structural demands follows a similar trend for both buildings. Tables 8.2 and 8.3 list the MIDR demands on 12-story and 3-story buildings at each station, respectively. The tabulated values indicate a smaller drop in the structural demands on long-period structures between the near-fault and far-field regions, as compared to short-period structures. For instance, the MIDR for the 12-story building varies by a factor of 3.4 between stations 3 and 7 (at 1 and 20 km, respectively), whereas the MIDR for the 3-story building varies by a factor of 13.3 between the same stations. It is noted that ASCE 7-16 defines near-fault sites as those within 15 km of a fault capable of a magnitude 7 earthquake. Based on the results of this study, this definition may provide a conservative estimate because the structural demands due to

the simulated M7.0 scenarios are seen to drop significantly beyond 10 km normal to the fault.

An idealization of the corresponding building deformations are shown in figure 8.6, in addition to the interstory drift time histories of the floor experiencing the maximum interstory drifts in each case. The building deformations are shown at the time instance where the structure experiences the largest MIDR over the entire loading history. In addition to the large variation between the demands at near and far-field stations, the structures at near-fault sites also seem to experience pronounced permanent drifts, as seen in the subplots a and b for stations 3 and 5. At 1 km away from the fault, the 3-story and 12-story buildings experience permanent interstory drifts corresponding as high as 3.6% and 3.5%, respectively. The permanent drifts remain relatively high for the 3-story building at 5 km, but quickly diminish in the 12-story building. The analysis also uncovers localized, large high-frequency content of the ground motions in rupture scenarios B and C at a handful of stations near the fault. This is seen in the large spectral demands at station 3, and reflected in the relatively large drifts of the short-period 3-story building at that location. This observation will be further discussed in subsequent sections, as part of the comparison between the mechanics of the different rupture scenarios.

Table 8.2: Structural response quantities for the 12-story building at stations 1 - 7 in Scenario B

Station #	$SA(T_1)$ **- 12 story (g)**	**MIDR - 12 story (%)**	**maximum beam rotation/capacity**	**maximum column rotation/capacity**
1	0.4	2.0	28%	5%
2	0.9	4.4	61%	76%
3	0.8	4.4	62%	74%
4	0.7	4.5	63%	79%
5	0.5	2.8	38%	38%
6	0.3	2.0	27%	5%
7	0.3	1.3	17%	1%

Table 8.3: Structural response quantities for the 3-story building at stations 1 - 7 in Scenario B

Station #	$SA(T_1)$ **- 3 story (g)**	**MIDR - 3 story (%)**	**maximum beam rotation/capacity**	**maximum column rotation/capacity**
1	1.4	2.4	36%	30%
2	1.7	5.3	77%	75%
3	2.8	6.6	100%	94%
4	2.4	3.7	58%	50%
5	2.5	5.7	86%	81%
6	1.0	2.5	39%	31%
7	0.3	0.5	8%	0.4%

The deformed shape plots in figure 8.6 also include a visual measure of the plasticity experienced by the building structural components, which is represented by plastic rotation of the nonlinear springs at each beam and column end, and schematically shown as red circles whose size scales up with the value of plastic rotation. The maximum hinge rotation experienced by the structural members of both buildings at each station are also listed in tables 8.2 and 8.3 as ratios of the total plastic capacity of the member. This measure quantifies the highest rotation demands in the structure, and flags members where the plastic hinge rotation capacity has been exceeded, which signifies the start of softening (loss of load carrying capacity) due to nonlinear material effects. The member rotation demands follow the trends observed previously for the MIDR. For example, between stations 3 (1 km away) and 7 at (20 km away), the maximum rotation demands drop by a factor of 4.3 for the 12-story, and 12.1 for the 3-story building. The preceding observations emphasize that flexible buildings may experience significant demands even at long distances from the fault.

Figures 8.7 and 8.8 display line plots which tracks the MIDR demands on the 12-story and 3-story buildings due to the FN and FP components of all scenarios along multiple lines normal to the fault at 20, 40, 60, 80 and 99 km. The location of the fault (at 10 km) is also marked with a dashed line. The 20-km line corresponds to a location that is 8.5 km away from the plane of the rupture source in the so called backward directivity path; i.e. the rupture propagates away from that line. The remaining line plots represent all locations that are 11.5, 31.5, 51.5 and 70.5 away from the rupture source and in the forward directivity path. The trends of the FN component demands in figures 8.7 and 8.8 clearly demonstrate the accumulation of seismic waves to produce forward directivity effects as the distance from and parallel to the rupture epicenter increases; this trend is distinguishable in the demands close to the fault indicated by the black and gray lines (which represent the region of highest directivity effects), as compared the red and green lines (which represent regions where the wave accumulation begins and dies off, respectively) and the blue line in the backward directivity region. The plots also suggest that the FP component is largely free of the wave accumulation effects even at very short distances. Both figures indicate that the structural demands near the fault (within 10 km normal to the fault) due to the FN component increase with increasing distance from the epicenter (parallel to the fault). The distance at which the maximum structural demands may be experienced is seen to depend on other details of the rupture scenario. In the case of the scenarios studied herein, the location and magnitude of the maximum structural demands depends on the distribution of slip along the fault plane, as will be discussed later. For all scenarios, the peak structural demands induced by the FN components are located between 29 and 55 kilometers away from the earthquake rupture source. Beyond 55 km, the structural demands begin to drop significantly in all cases. Based on the line plots in figures 8.7 and 8.8, the average MIDR demand on the 3-story building at all locations that are 31.5 km away from the source is 3.4 times the average maximum demand at 11.5 km away from the source. the average maximum demands on the same building at 51.5 km away are 4.2 times those at 11.5 km. Between 51.5 and 70.5 km, the maximum demands drop by 70%. The maximum demands along the right end of the domain (70.5 km away from the source) are, on average, similar to those in the backward directivity region. As expected based on previous results, a similar trend with less pronounced spatial variability is observed in the structural demands imposed on the 12-story building. For

example, between 11.5 and 51.5 km, the maximum demands increase by a factor of 2.3 - about half the increase of the 3-story building demands, and drop by 60% between 51.5 and 70.5 km.

The effects of rupture directivity on the FN component ground motion waveforms and structural demands are further examined at four stations in scenario B (shown in figure 8.9a): stations 1 through 4 whose properties are listed in table 8.1. This group of stations is located 1 km normal to the fault, and 13.5, 25.5, 37.5 and 49.5 km away from the rupture source, respectively (the stations are spaced at 12 km intervals). Figure 8.9b and c show plots of the spectral acceleration and velocity at each of the four stations, whereas subplots d through g present the acceleration and velocity time histories at each station. The figure demonstrates the expected forward directivity effects as the rupture propagates toward each station, particularly in the velocity and displacement (not shown) time histories. While the PGA increases by only 3% between stations 1 and 2, the PGV increases by 91% and the peak ground displacement increases by 153%. Although all four stations lie in the forward directivity region, stations 2 and 3 experience the highest ground acceleration, velocity and displacement pulses. In scenario B, the peak velocities (and peak structural demands) are experienced near station 3, which is about 37.5 km away from the source. At station 4, which is 49.5 km away from the source, both the ground peak velocity and displacement amplitudes decline by 48% and 36%, respectively, whereas the acceleration amplitudes do not substantially change. Similarly, the spectral demands shown in figure 8.9b and c increase significantly between stations 1 and 3, particularly for the short-mid period range (up to 2 seconds) then drop at station 4.

The structural demands on the two buildings at stations 1-4 are listed in tables 8.2 and 8.3, including the MIDR and maximum member rotation demands as a ratio of the member rotation capacity. The corresponding building deformed shape (with plastic hinges) and history of the maximum interstory drift are shown in figure 8.10. The plots and tabulated results illustrate that station 1, although closest to the epicenter, can experience less than half the demands experienced further along the fault. In particular, both the MIDR and maximum member rotation demands for both buildings at station 1 are between 36 - 45% of the demands at station 3. The 3-story building experiences the highest demands at stations 2 and 3, up to 6.6% MIDR and a maximum rotation demand close to 100% of the rotation capacity at station 3 (i.e., at least one plastic hinge reaches its full plastic rotation capacity). Although the plastic rotation limits and post-capping properties in the structural model are based on conservative estimates and contain several idealizations, the high demand-to-capacity ratios encountered in the analysis can be viewed as indicators of undesirable large demands and potentially significant damage in the structural components. The plots also demonstrate differences in the distribution of the demands along the height of the 12-story building. At station 2, the plastic hinges are concentrated in the lowest floors only, which is indicative of a primarily first-mode response, whereas the hinges are seen in almost all floors at stations 3 and 4. The differences in the demand distributions suggest that the the building is sensitive to various frequency components. Consequently, it exhibits a severe response at a larger number of stations in the forward directivity path. For example, the 12-story building experiences similar and relatively large demands at stations 2 through 4 (MIDR of about 4.4 - 4.5%, and maximum member rotation demands between 74 - 79%), despite the drop in the PGV at station 4. This sensitivity is not seen in the demands on the 3-story building, which drop by about 40% at station 4 (49.5 km away from the source), commensurately with the drop in the PGV at this station. The drift history plots in

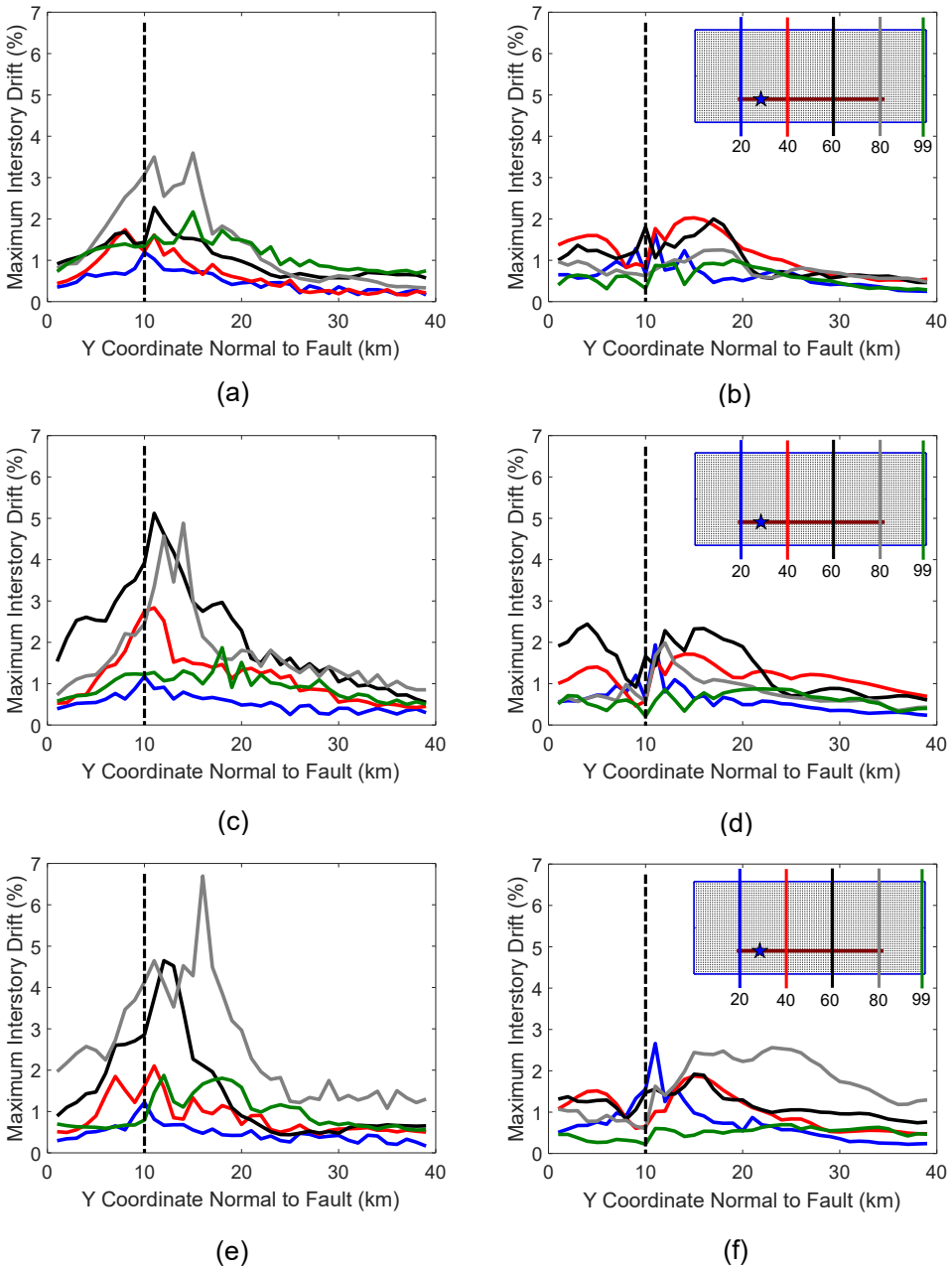

Figure 8.7: Maximum interstory drift trends normal to the fault for the 12-story RC building due to: (a) the FN component of scenario A; (b) the FP component of scenario A; (c) the FN component of scenario B; (d) the FP component of scenario B; (e) the FN component of scenario C; (f) the FP component of scenario C.

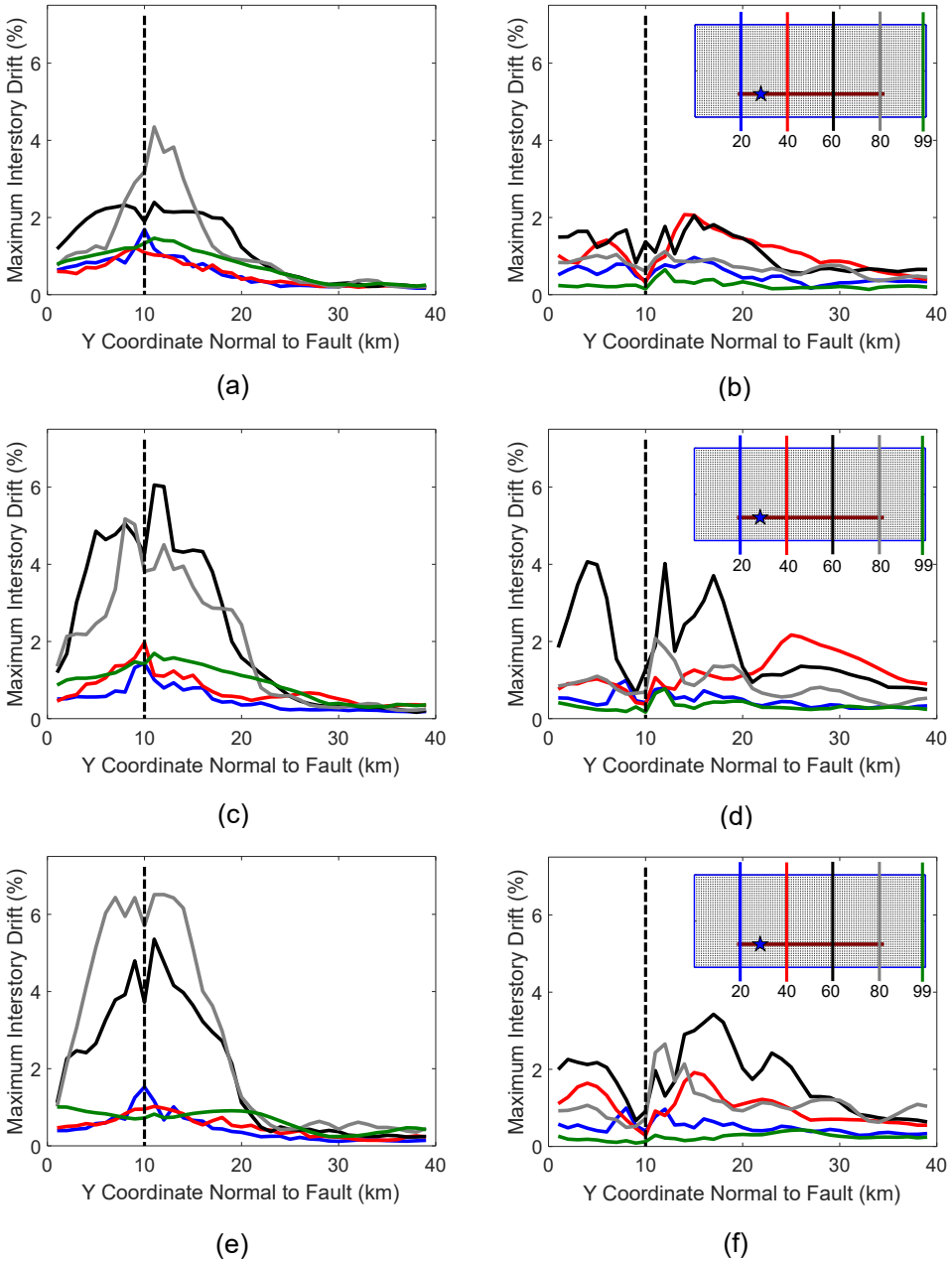

Figure 8.8: Maximum interstory drift trends normal to the fault for the 3-story RC building due to: (a) the FN component of scenario A; (b) the FP component of scenario A; (c) the FN component of scenario B; (d) the FP component of scenario B; (e) the FN component of scenario C; (f) the FP component of scenario C.

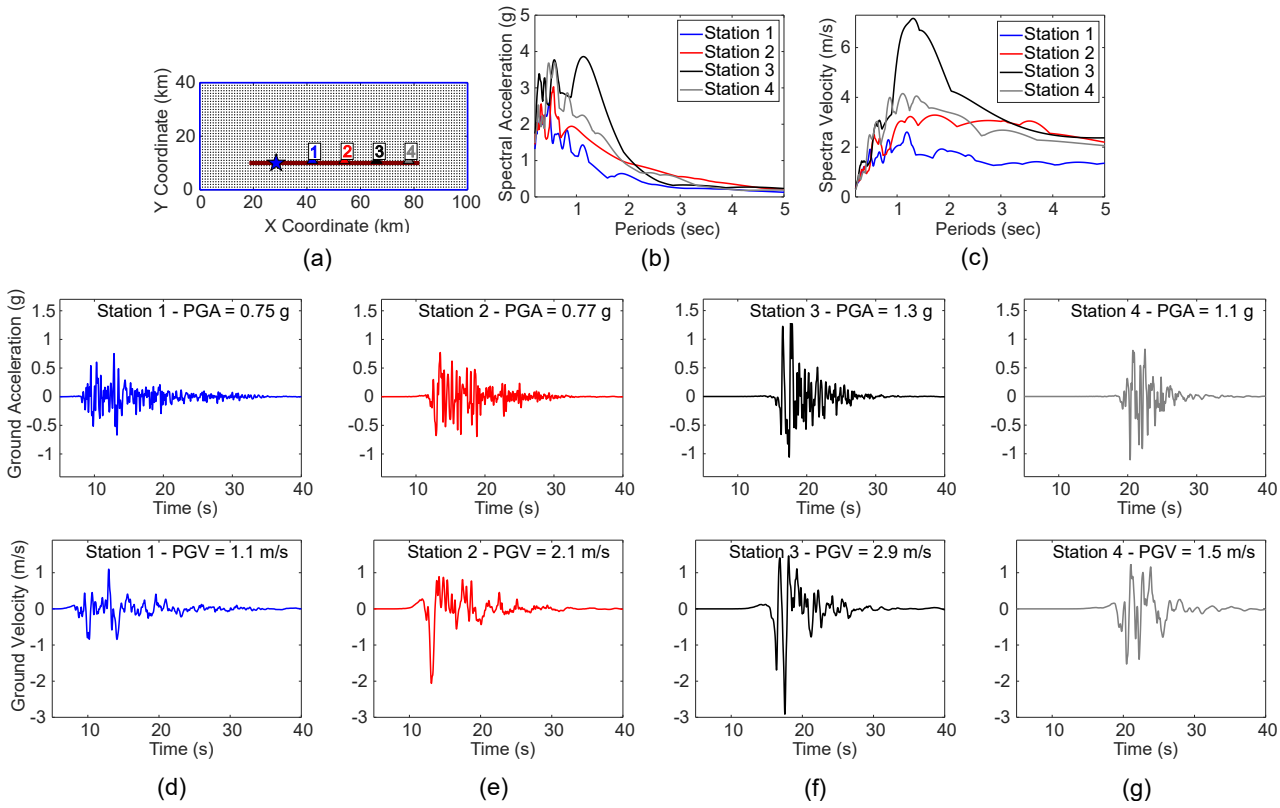

Figure 8.9: The characteristics of the ground motions at stations 1, 2, 3 and 4 in rupture scenario B: (a) locations of the stations in the computational domain; (b) acceleration response spectra at all stations; (c) velocity response spectra at all stations; (d) acceleration and velocity time histories at station 1; (e) acceleration and velocity time histories at station 2; (f) acceleration and velocity time histories at station 3; (g) acceleration and velocity time histories at station 4.

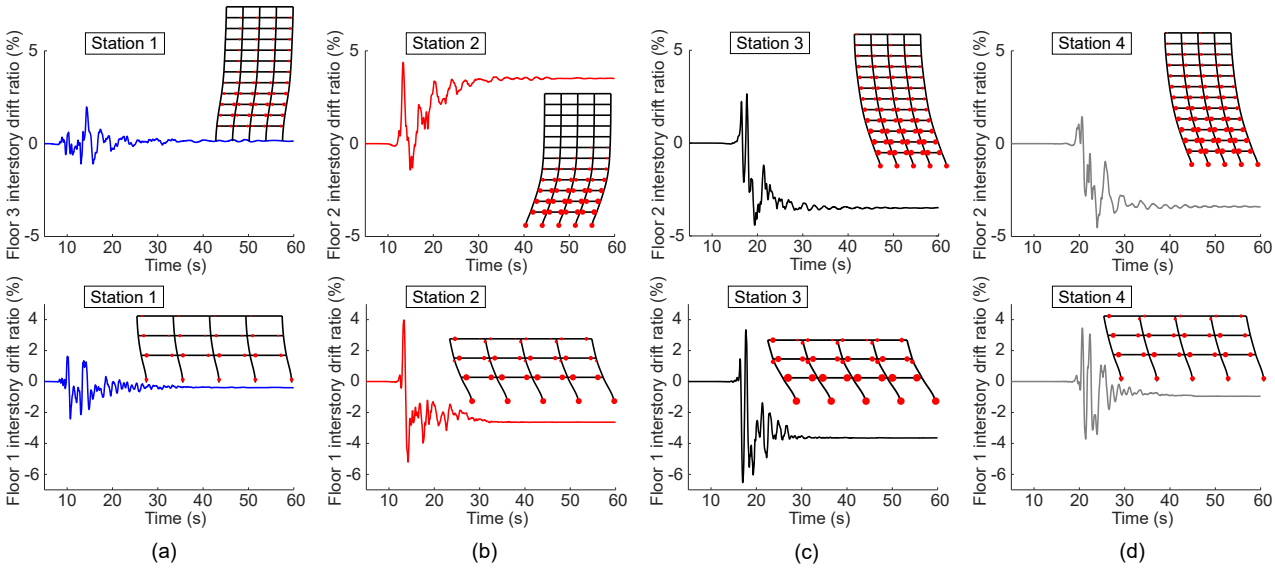

Figure 8.10: Deformed shape, plastic hinges and maximum floor drift histories for the 12-story and 3-story buildings: (a) at station 1; (b) at station 2; (c) at station 3; (d) at station 4.

figure 8.10 also emphasize the relatively large residual drift demands associated with buildings located in the forward directivity region, which may depend on the frequency characteristics of the building. The 3-story building experiences residual interstory drifts up to 3.6% at station 3, whereas the 12-story building experiences permanent drifts at stations 2 through 4 between 3.4 and 3.5%. Residual drifts associated with near-fault sites are important for risk assessments because they typically correlate with the building repairability [ATC, 2018].

It is worth noting that much of the variability observed in the FN component intensity and structural demands is less pronounced in the FP component. For example, examining the FP ground motion characteristics at stations 1 through 4 in figure 8.11 reveals that the structural demands do not vary significantly over the entire domain. Nonetheless, relatively large permanent ground displacement is observed in the FP component of many ground motions near the fault (figure 8.11d); this effect is usually referred to as 'fling step' and may cause relatively high demands on structures located near the fault. Simulated ground motions offer an opportunity to study such permanent displacements and their effects on structural response. This topic will be the focus of future studies.

8.2 Effects of localized slip on structural demands

Studies of large earthquakes have shown that hybrid earthquake rupture models which combine large-slip features with stochastic small-scale variations are better able to reproduce the characteristics of observed earthquakes over a broad range of frequencies [Graves and Pitarka, 2010, Pitarka et al., 2019]. However, the effect of including such localized high-slip regions in the rupture models on structural risk and reliability assessments is not fully understood. The results of this study indicate that local large-scale slip can substantially increase the demands imposed on structures

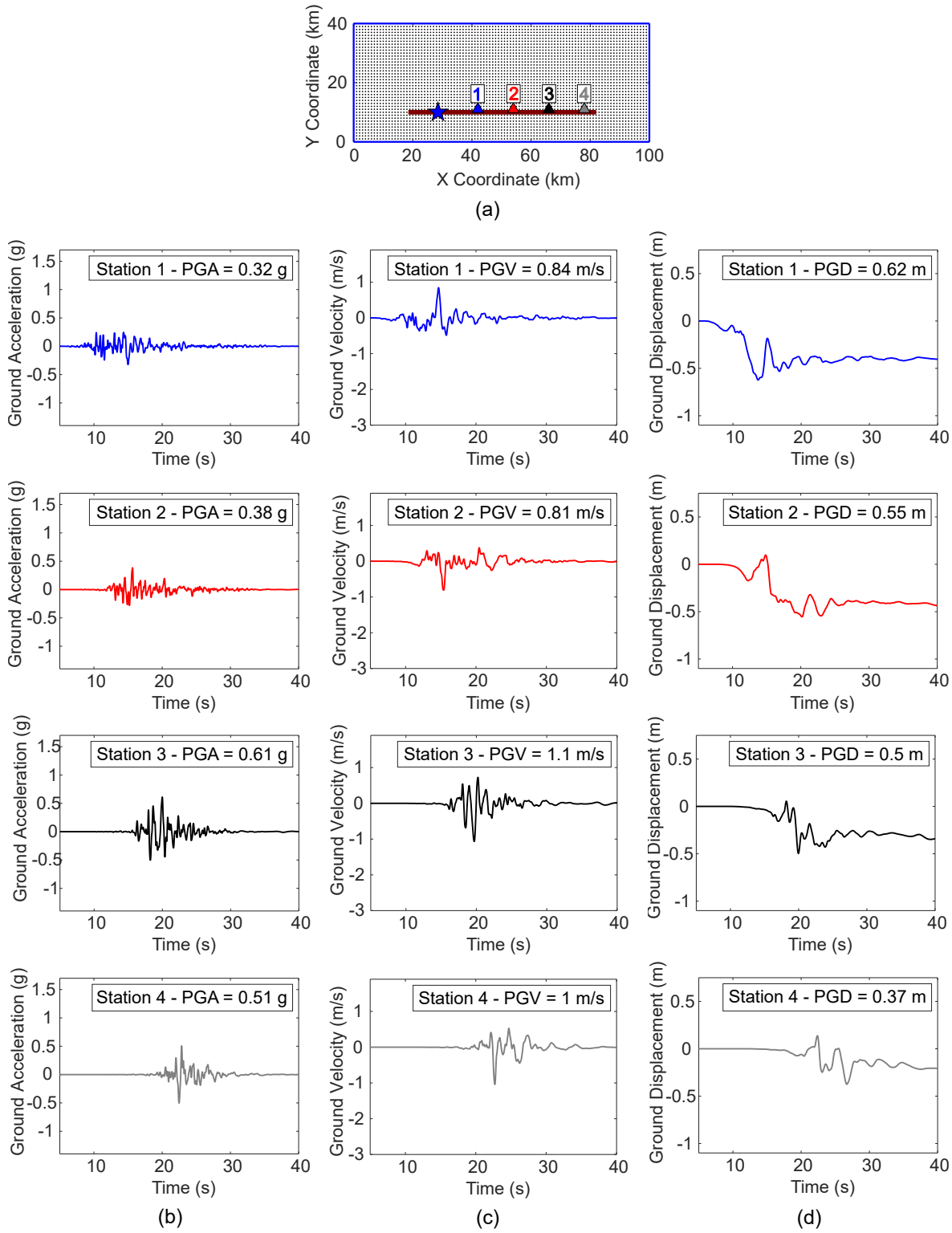

Figure 8.11: The characteristics of the FP component ground motions at stations 1, 2, 3 and 4 in rupture scenario B: (a) locations of the stations in the computational domain; (b) acceleration time histories at all stations; (c) velocity time histories at all stations; (d) displacement time histories at all stations.

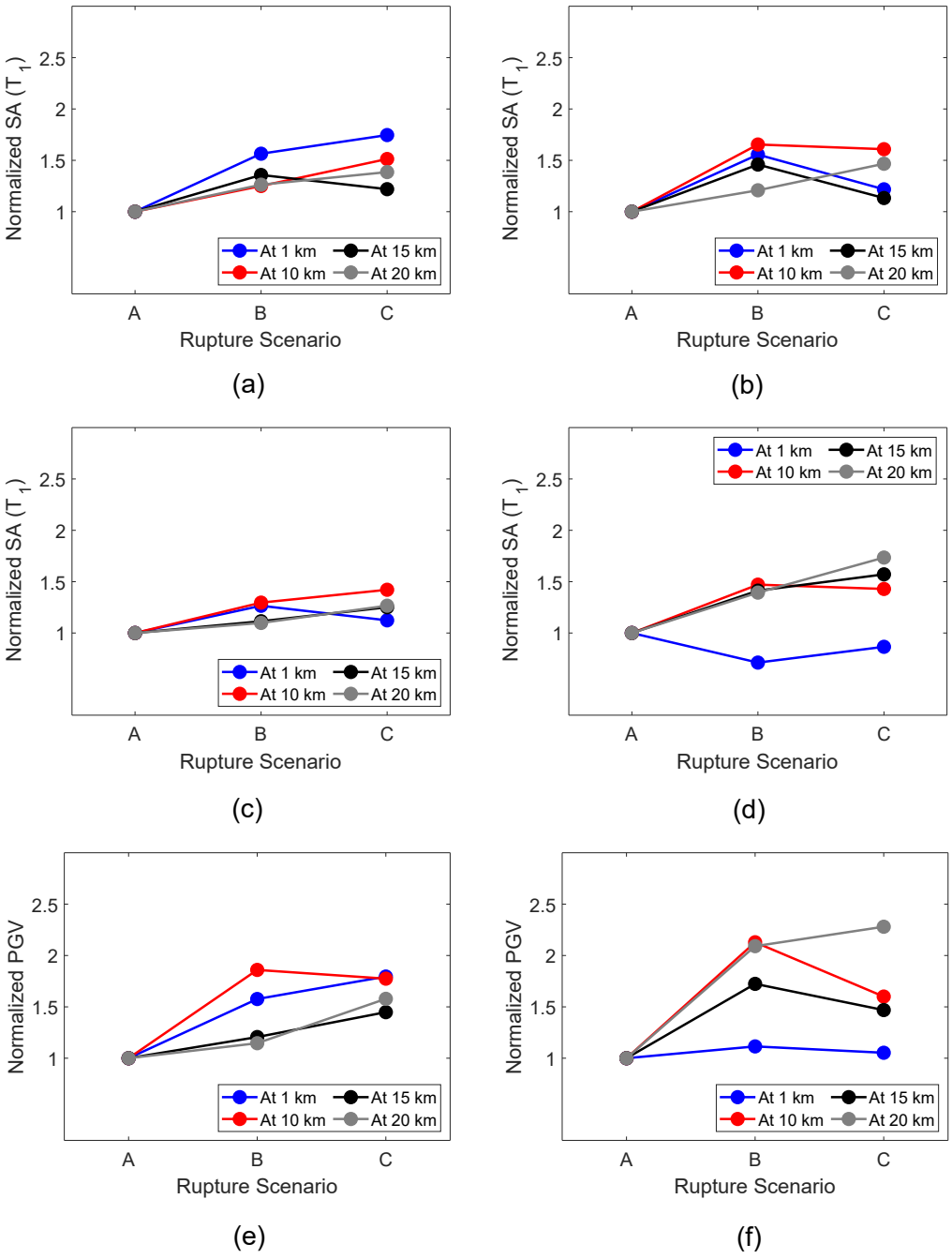

Figure 8.12: Normalized maximum ground motion intensity parameters for all rupture scenarios at several normal distances from the fault: (a) $SA(T_1)$ in the FN component for the 3-story building; (b) $SA(T_1)$ of the FP component for the 3-story building; (c) $SA(T_1)$ of the FN component for the 12-story building; (d) $SA(T_1)$ of the FP component for the 12-story building; (e) PGV of the FN component; (f) PGV of the FP component.

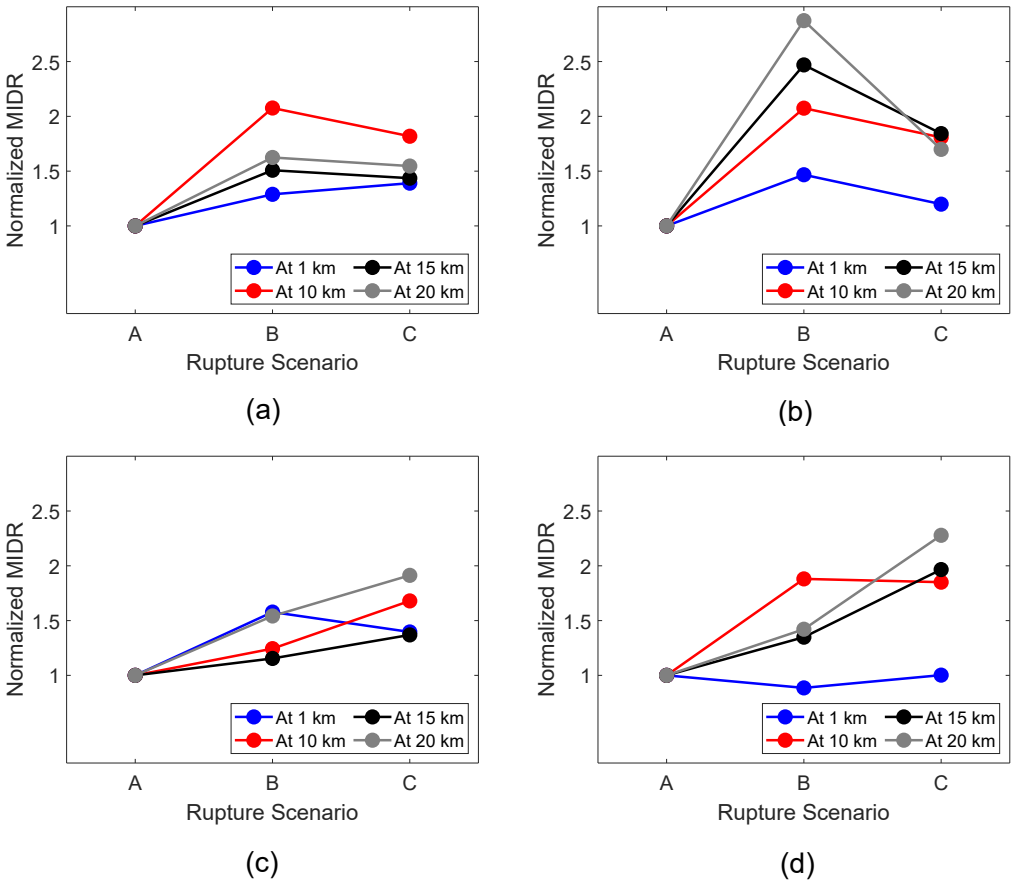

Figure 8.13: Normalized maximum MIDR demands for all rupture scenarios at several normal distances from the fault due to: (a) the FN component for the 3-story building; (b) the FP component for the 3-story building; (c) the FN component for the 12-story building; (d) the FP component for the 12-story building.

located near the fault. These effects are apparent in the risk map plots of figures 8.1 and 8.2, and the MIDR line plots of figures 8.3 and 8.4. The maximum values of the spectral demands, peak ground velocities, and MIDR for both buildings due to all three scenarios are compared at different fault distances, and representative results are plotted in figures 8.12 and 8.13. The figures display the maximum values of the selected parameters at 1, 10, 15 and 20 km normal distance from the fault for both the FN and FP components of all three scenarios, normalized by their values in scenario A, in order to highlight the amplifications seen in scenarios B and C. The plots reveal that at any distance from the fault, most of the FN and FP spectral demands, peak ground velocities and MIDRs are higher in scenarios B and C than scenario A. The changes in the ground motion intensity and structural demands of the FN component due to the presence of the localized slip patches are mostly concentrated within a 10 km distance from the fault (specifically, in the forward directivity region). In contrast, these effects seem to be become more substantial in the FP component as the distance from the fault increases. This trend is indicated in figures 8.12 and 8.13 by the steeper slopes of the 15 km and 20 km FP component parameter lines, whereas the 1 km and 10 km lines have steeper slopes for the FN component. Despite being lower than the FN component demands, the FP component demands can experience a more significant increase at distances between 10 and 20 km from the fault due to the presence of the slip patches. For instance, at a 20 km distance, the maximum MIDR demand on the 3-story building induced by the FP component is amplified by a factor up to 2.9 due to the presence of the slip patches, as compared to a factor of 1.6 for the FN component. Similarly, the maximum FP MIDR demand on the 12-story building at a 20 km distance is amplified by a factor up to 2.3, as compared to a factor of 1.9 for the FN component demand. The same trends are observed for the ground motion intensity parameters, especially the long-period components, with amplifications up to 44% higher for the FP component than the FN component at a 20 km distance. These observations suggests that relying on the stochastic scenario alone (without consideration of the effects of localized high slip) may underestimate the structural risk at both short and long distances from the fault.

The presence of the slip patches is shown to impact both the magnitude and the relative locations of the highest ground motion intensity and structural response quantities, such that stations proximate to the patches experience the highest demands. Trends of FN component intensity and demands ($SA(T_1)$, PGV and MIDR) at different fault distances are plotted in figures 8.14, 8.15, and 8.16, respectively, for all rupture scenarios. The plots demonstrate that the demands "peak" near the locations of the asperities in scenarios B and C, particularly at very short distances from the fault. For example, the highest structural demands in scenario B are near $x = 65$ km, whereas the highest demands in scenario C are near $x = 80$ km; both points are close to the end of the second slip patch in each scenario (see figure 6.1). Despite having no deterministic asperities, the demands in scenario A also show multiple peaks because the stochastic nature of the slip yields some slip concentrations. However, these concentrations typically have lower slip rates than the large-scale asperities in the hybrid scenarios. Therefore, the intensity and demands associated with scenarios B and C are significantly higher than those of scenario A over regions of the domain that are forward of the localized asperities (in the direction of rupture).

The geographically varying effects of the rupture asperities are further highlighted by examining the response spectra and waveforms of ground motions at locations proximate to and in

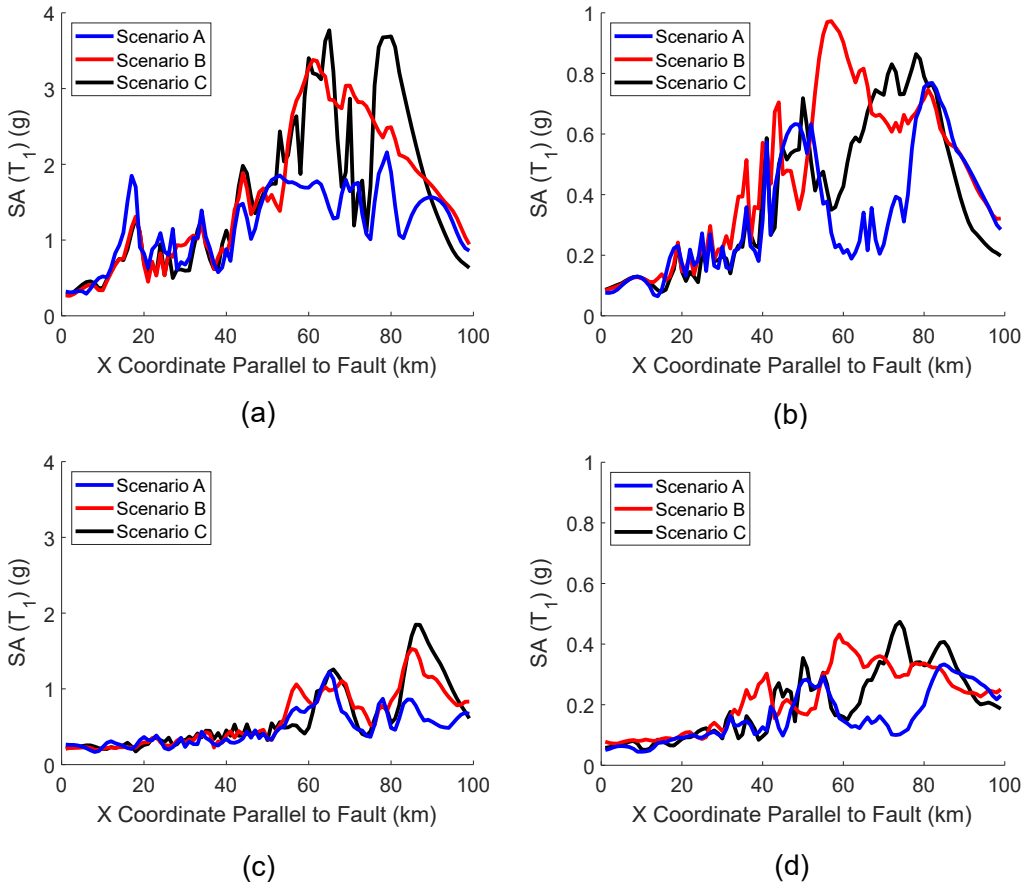

Figure 8.14: Trends of $SA(T_1)$ parallel to the fault due to the FN component of all rupture scenarios at different normal distances: (a) at 1 km for the 3-story building; (b) at 1 km for the 12-story building; (c) at 10 km for the 3-story building; (d) at 10 km for the 12-story building.

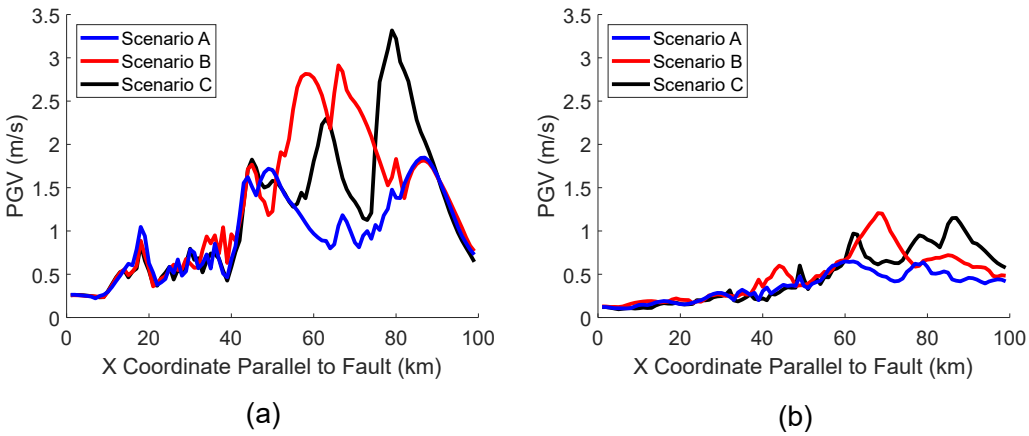

Figure 8.15: Trends of the PGV parallel to the fault due to the FN component of all rupture scenarios at different normal distances: (a) at 1 km; (b) at 10 km.

the forward direction of the asperities. The acceleration and velocity response spectra of the FN component of the ground motions at stations 2, 3 and 4 - which were examined previously for a single scenario - are compared between the three different scenarios. The locations of these stations relative to the localized slip patches are shown in figure 8.17a and b, for scenarios B and C, respectively, and the remaining subplots represent the response spectra at the three stations. In addition, the ground acceleration and velocity time histories for stations 3 and 4 are plotted in figure 8.18. The analysis reveals that the effects of the concentrated slip in the forward directivity zone are largest at stations immediately following the slip patches, and decrease as the distance from the asperities increases. The localized slip in scenario B seems to primarily impact the mid-long period component, whereas the slip patches in scenario C have higher impact on the short-period component. For example, station 2 - which is in front of a single patch in scenario B - coincides with a higher amplitude of the spectral velocity in scenario B (figure 8.17c) over a wide range of long periods (upwards of 1.5 seconds), and the spectral accelerations are marginally higher. The PGV of scenario B at station 2 is amplified by 62% compared to scenario A, yet the peak ground accelerations are lower than scenario A by 18%. Similarly, at station 3, which follows the second patch in scenario B and a single patch in C, the long-period component is significantly impacted in scenario B. This observation is apparent in both the acceleration and velocity spectra in figure 8.17d, which are amplified substantially over periods larger than 0.5 sec, compared to scenario A. Some amplification is observed in scenario C over the same range of periods as well. However, the amplification in scenario C is higher for short periods (less than 1.0 second), and is detected in the magnitudes of both the ground accelerations and velocities (figure 8.18c.) For instance, at station 3, the ratios of the PGA and PGV of scenario C/scenario A are 1.5 and 1.6, respectively, indicating both low and high frequency component amplification. In contrast, the ratios of the PGA and PGV of scenario B/scenario A are 1.2 and 2.6, indicating a primarily low-frequency effect. At station 4 - which is close to the end of the scenario C asperities - a similar broadband impact on the ground motion intensity is observed in Scenario C. In addition, both the peak ground accelerations and

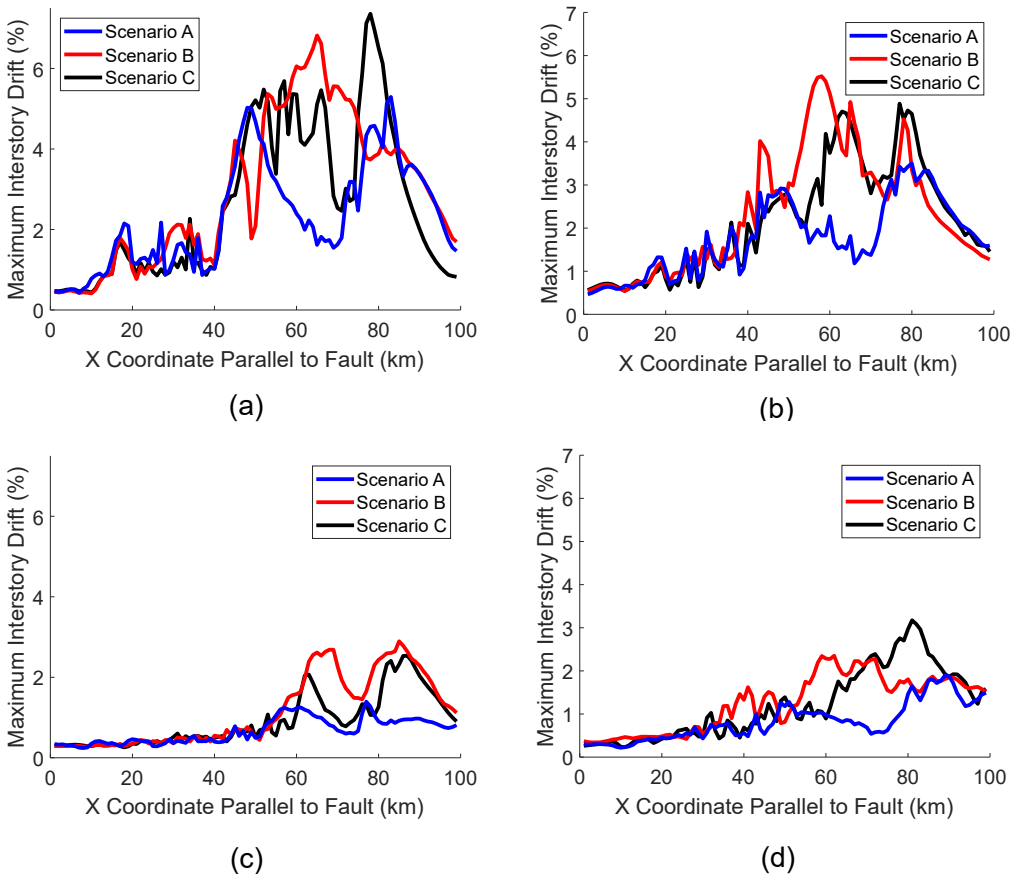

Figure 8.16: Trends of maximum interstory drift parallel to the fault due to the FN component of all rupture scenarios at different normal distances: (a) at 1 km for the 3-story building; (b) at 1 km for the 12-story building; (c) at 10 km for the 3-story building; (d) at 10 km for the 12-story building.

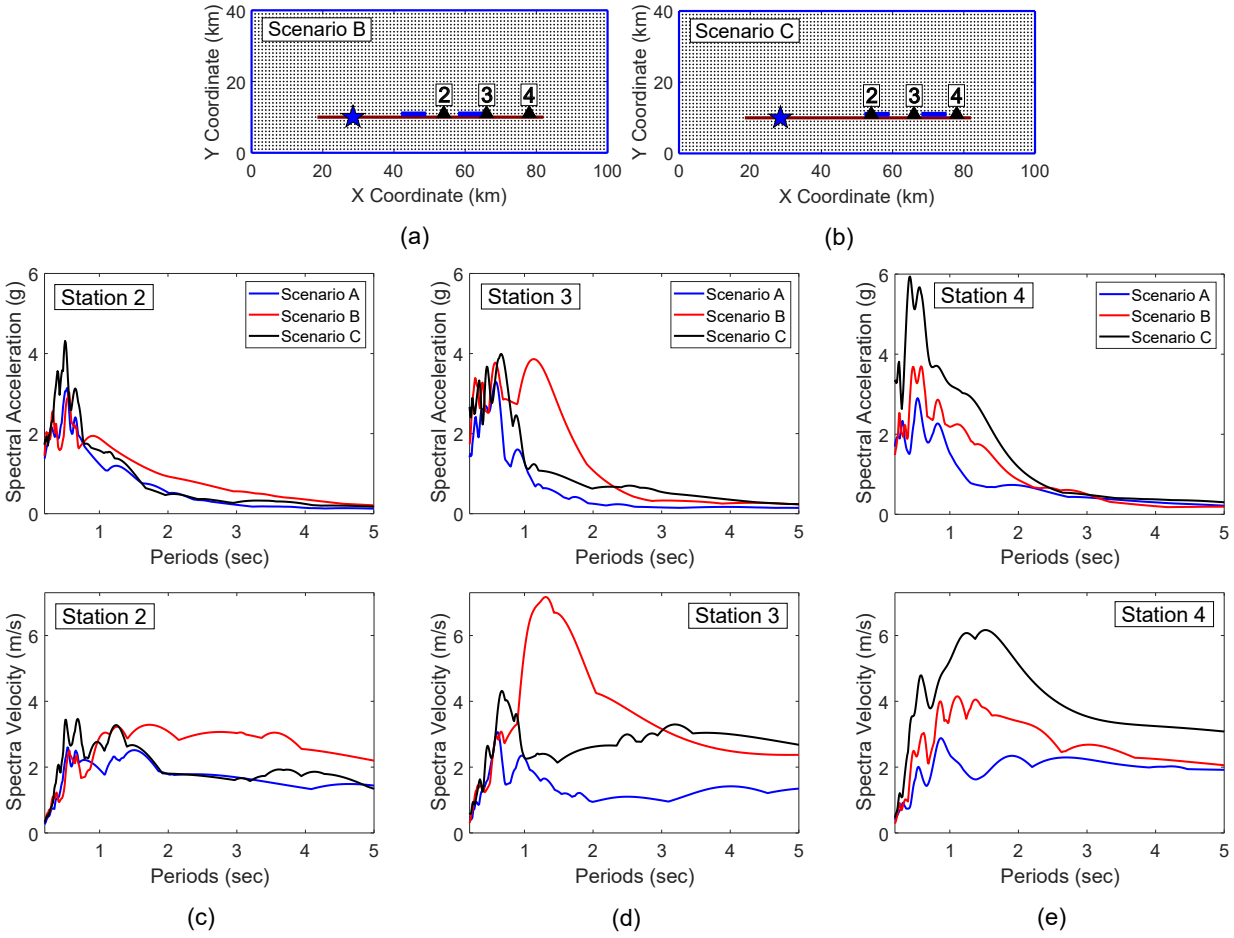

Figure 8.17: Response spectra at stations 2, 3 and 4 for all three rupture scenarios: (a) locations of the stations relative to the slip patches of scenario B; (b) locations of the stations relative to the slip patches of scenario C; (c) acceleration and velocity spectra at station 2; (d) acceleration and velocity spectra at station 3; (e) acceleration and velocity spectra at station 4.

velocities are amplified by factors of 2.8 and 2.4, compared to scenario A. A modest impact is seen at this station in scenario B because this station is relatively far from the slip patches.

An important implication of the previous observations is that, depending on the locations of the asperities, buildings with different frequency characteristics may see varying impacts. At station 4, for example, where the high-frequency amplification is significant in scenario C, the 3-story building experiences extreme drift and component rotation demands. In contrast, the 12-story building at the same station experiences similar demands due to both scenarios B and C. These observations are demonstrated in figure 8.19 which displays the drift envelopes, plastic hinges and maximum rotation demands at station 4 in all three scenarios. It is also surprising that, contrary to the previous observations, the demands imposed on the 3-story building by scenario A at station 4 are marginally higher than the demands due to scenario B. This observation may be explained

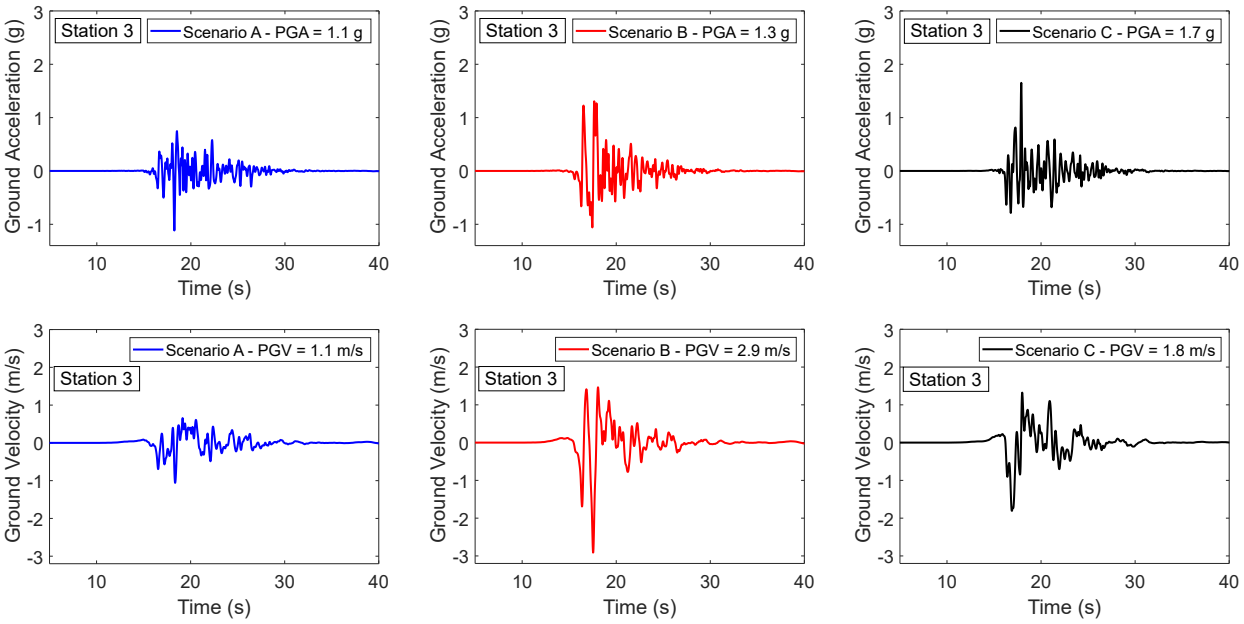

(a)

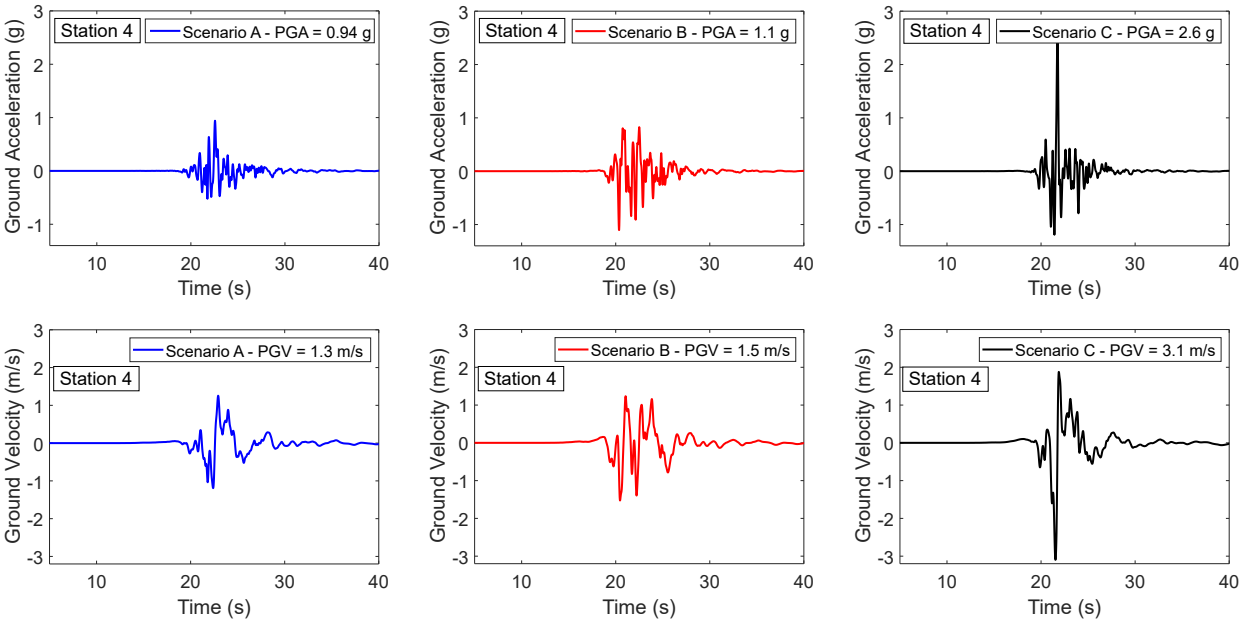

(b)

Figure 8.18: Ground acceleration and velocity time histories for all rupture scenarios at: (a) station 3; (b) station 4.

by the fact that the presence of the concentrated slip may lead to reducing the background slip over some locations in the domain (because all scenarios have the same overall magnitude). Such locations are typically far from the asperities, as is the case for station 4 which is only 1 km away from the fault, yet about 12 km away from the scenario B slip patch.

Although the preceding results show significant spatial variability in the structural and spectral demands depending on the relative locations of the building and the slip patches, the absolute effects of the asperities are primarily similar. For seismic risk assessments which utilize simulated earthquake ground motions, an important question is the number of different scenarios that shall be used to encompass the full range of expected variability of ground motion intensity. Answering this question requires studying a large number of rupture scenarios, and the effects of the slip patch geometry on the different frequency ranges. With that in mind, assessment of the rupture scenarios in this study shows primarily spatial, but not quantitative, differences between the hybrid rupture scenarios. This finding suggests that a small number of rupture scenarios would likely be sufficient to represent the expected variability in risk.

8.3 Scenario-based distributions of ground motion intensity and structural demands

A primary objective of this study is to inform the seismic performance assessment of structures with regard to the expected spatial variability at a particular fault distance in a single earthquake scenario, and the variability at a singular location due to multiple scenarios. The deterministic observations made in the previous sections are summarized using cumulative distribution curves which quantify the probabilities of not exceeding certain levels of ground motion intensity or structural demands for a given scenario; thus highlighting the expected values and dispersion associated with these parameters due to the variability of the ground shaking. A group of such plots is shown in figures 8.20 and 8.21 displaying the probabilities of non-exceedance for the spectral accelerations, peak ground velocities and interstory drift demands for all stations located at 1, 10 and 15 km closest distance to the fault, particularly on the basin side of the domain and along the length of the fault. The data points are plotted for all three scenarios, and a lognormal distribution is fitted to the data. The median values (based on the actual data) and the logarithmic standard deviation are shown in the legend of each subplot. The figures provide the following observations:

- As anticipated, for each given scenario, the spatial variability of $SA(T_1)$, PGV and MIDR for both buildings is highest at a 1 km closest distance. In particular, the logarithmic standard deviation ranges between 0.36 and 0.63 for $SA(T_1)$, between 0.41 and 0.61 for the PGV, and between 0.43 and 0.72 for the MIDR demands. At a 10 km closest distance from the fault, the median demands and ground motion intensity decrease significantly for all scenarios, but the dispersion remains relatively high. For instance, the median MIDR for the 3-story building decreases, on average, by a factor of 4.4 between the data points at a 1 km and 10 km closest distance, and the median MIDR for the 12-story building decreases by a factor of 2.3, whereas the logarithmic standard deviation for both buildings remains almost the same.

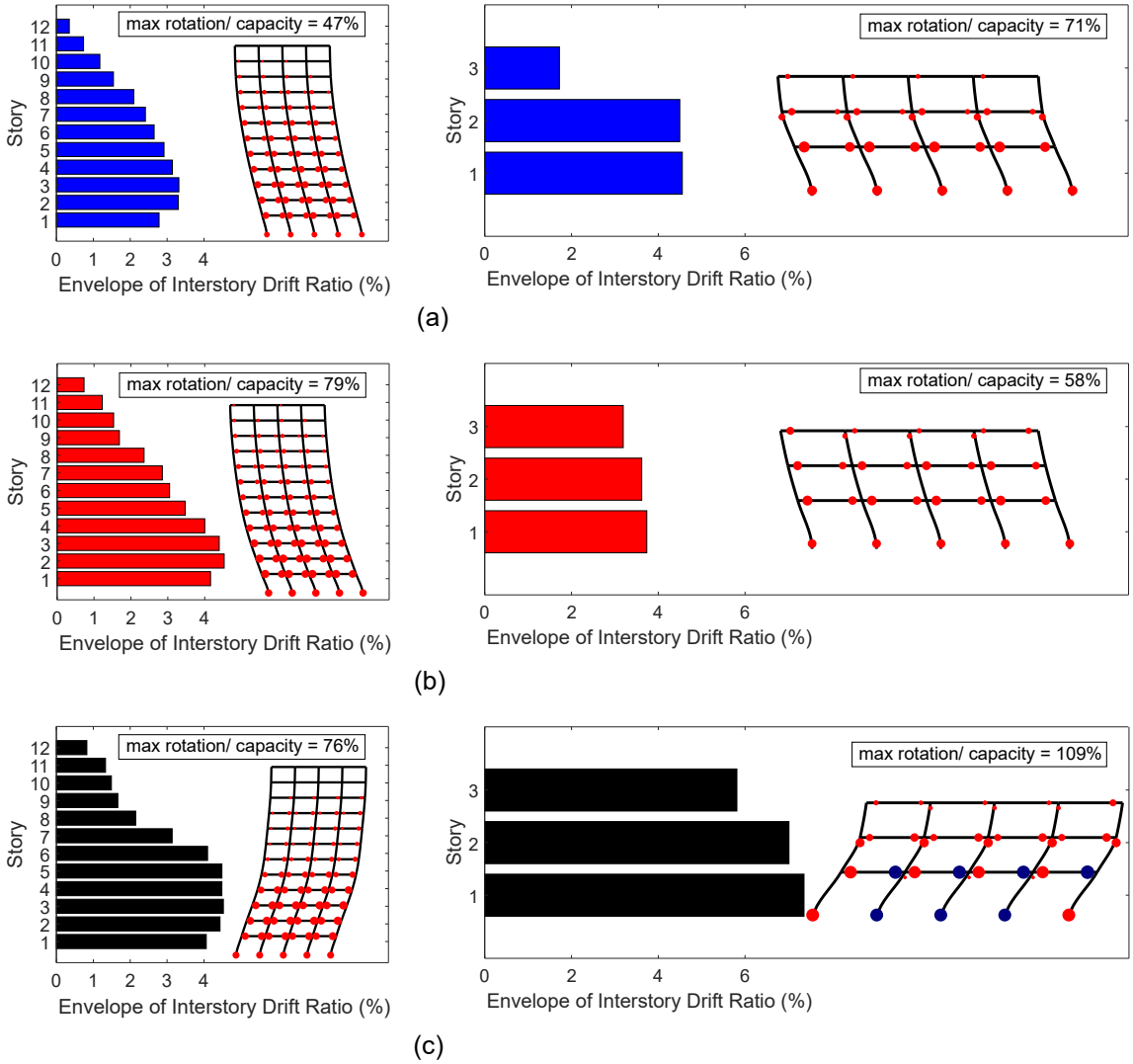

Figure 8.19: Deformed shaped and MIDR envelopes at station 4 for the 12-story and the 3-story buildings in: (a) scenario A; (b) scenario B; (c) Scenario C. Plastic hinges exceeding their rotation capacities are flagged in blue.

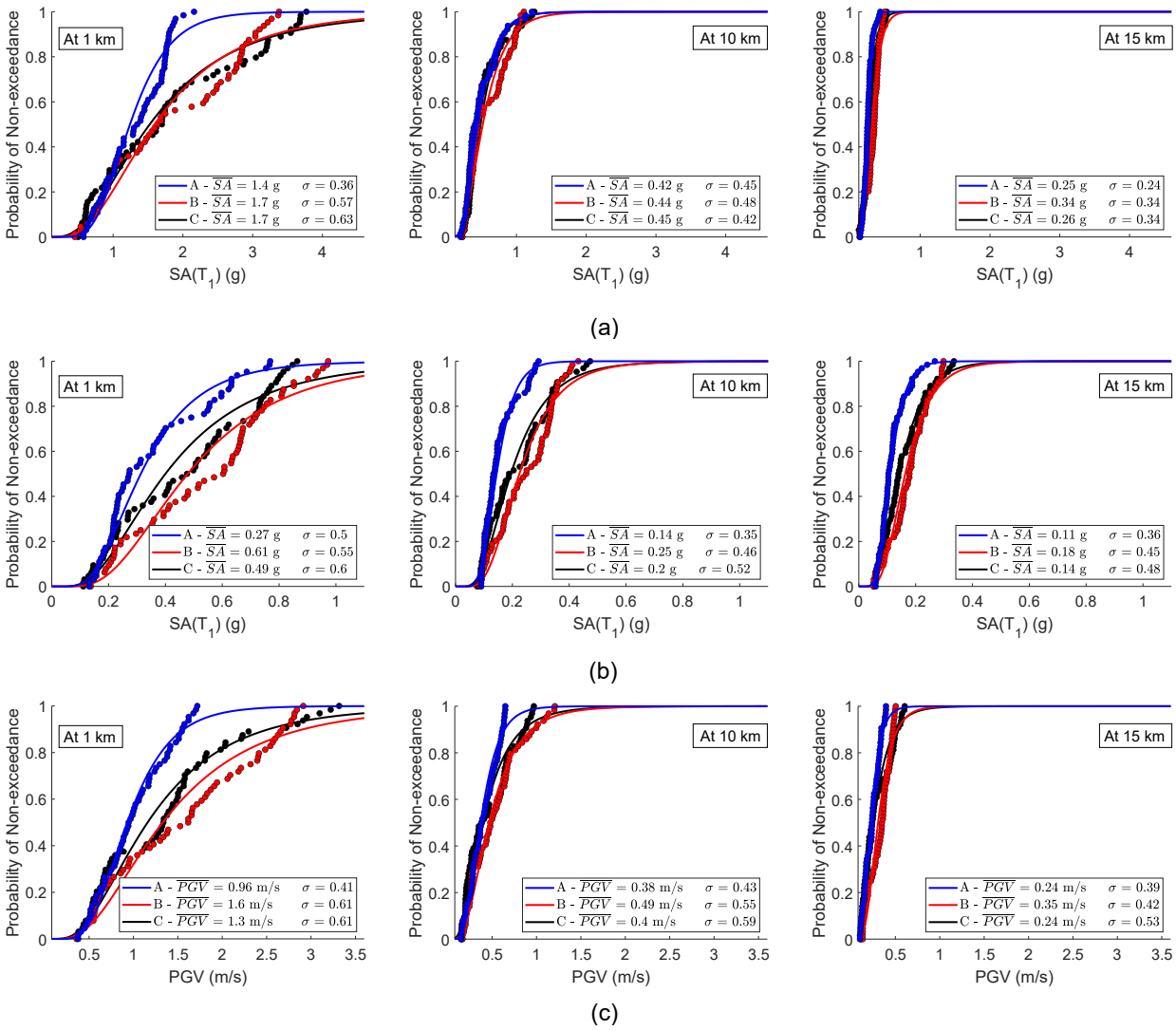

Figure 8.20: Cumulative distribution functions of ground motion intensity parameters for all rupture scenarios at 1, 10 and 15 kilometers from the fault: (a) spectral acceleration at the first-mode period of the 3-story building; (b) spectral acceleration at the first-mode period of the 12-story building; (c) peak ground velocity.

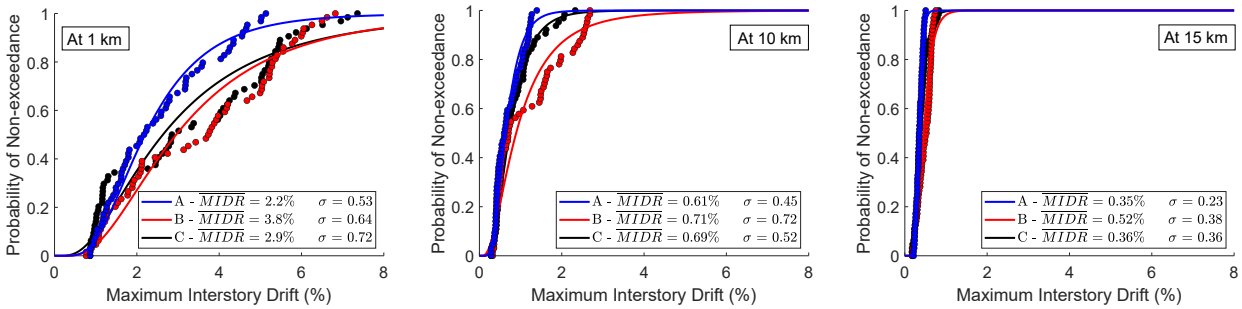

(a)

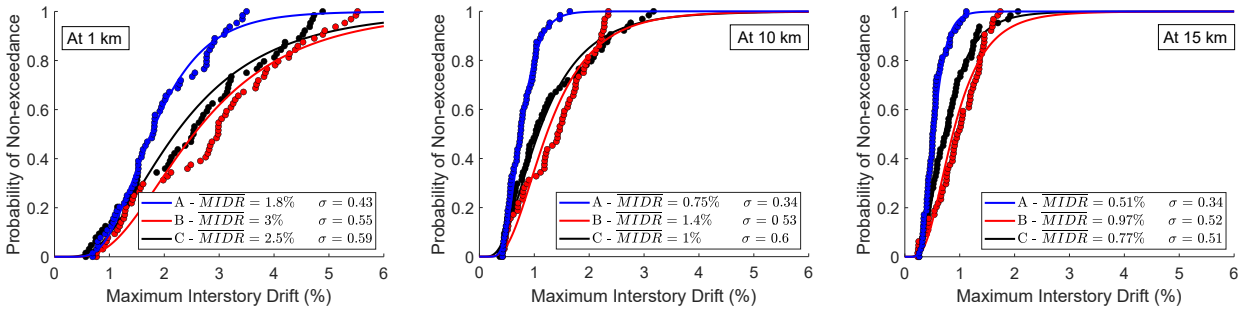

(b)

Figure 8.21: Cumulative distribution functions of the maximum interstory drift for all rupture scenarios at 1, 10 and 15 kilometers from the fault: (a) for the 3-story building; (b) for the 12-story building.

- At a 15 km closest distance, the median values of all parameters decrease by a factor between 1.4 and 1.6 compared to their values at 10 km. The dispersion in the spectral and structural demands for the 3-story building decreases significantly, whereas the the dispersion in the demands of the 12-story building and the peak ground velocities remains high. For instance, the logarithmic standard deviation of the 3-story MIDR decreases by a factor of 1.7 between the data at 10 and 15 km closest distance, whereas the same parameter decreases by a factor of only 1.1 for the 12-story building. This is consistent with the observations made in previous sections regarding the variability of the response of both buildings.

- The median values associated with the hybrid rupture scenarios (B and C) are consistently higher than those associated with the stochastic scenario (A) at all distances, and - as demonstrated previously - these differences do not decrease at longer distances from the fault. For example, the average median MIDR of the hybrid rupture scenarios for the 12-story building is 1.5 and 1.7 times that of the stochastic rupture scenario at a distance of 1 km and 15 km, respectively. The median short-period spectral acceleration ($SA(T_1)$ for the 3-story) is the parameter that is least affected by the introduction of the asperities in the hybrid scenarios and changes only by up to 20% between the stochastic and hybrid rupture scenarios. On the other hand, the median long-period spectral accelerations ($SA(T_1)$ for the 12-story) change by a factor of up to 2.0.

- The dispersion of all the variables associated with the hybrid rupture scenarios is also consistently higher for all parameters than the dispersion associated with the stochastic rupture scenario, especially at longer distances. This observation is attributed to the higher demands introduced in the hybrid ruptures only near the asperities, whereas the demands at locations far from the asperities (or behind the asperities in the direction of rupture) remain relatively low. The average logarithmic standard deviation for the MIDR of the 3-story building due to the hybrid rupture scenarios is 1.3 and 1.6 times that due to scenario A at 1 km and 15 km, respectively. Similarly, for the 12-story building, the average dispersion in the MIDR due to the hybrid ruptures is 1.3 and 1.5 times the dispersion associated with the stochastic rupture scenario at 1 and 15 km, respectively. The higher dispersion associated with the hybrid rupture scenarios at longer distances asserts the presence of large uncertainty due to record-to-record variability at long distances from the fault, as well as short distances. Although these findings are yet to be validated with a large recorded dataset of observations, this study indicates that the hybrid rupture scenarios would give more conservative results in seismic risk assessments.

- The results also suggest that the differences between the stochastic and hybrid ruptures become more significant at relatively high demand or intensity levels. This is implied by the similar probabilities of non-exceedance for all scenarios at the distribution tails, whereas these probabilities differ significantly at higher demand levels. For instance, the 12-story MIDR has a similar probability of not exceeding 1.5% for all scenarios (close to 25%); however, the probability of not exceeding 3.0% interstory drift is 90% for scenario A, and only 61% and 68% for scenarios B and C. This observation also suggests that the differences be-

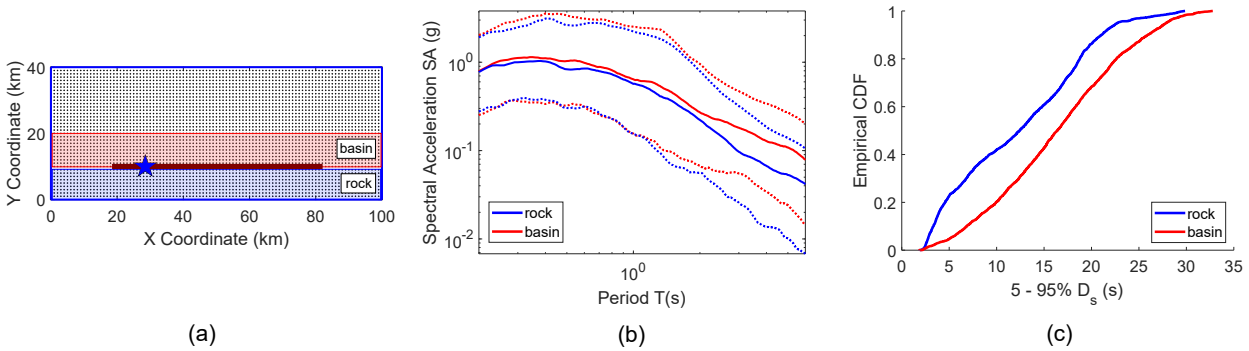

(a) (b) (c)

Figure 8.22: Characteristics of the ground motions at basin and rock sites within a 10 kilometer distance from the fault: (a) locations of the considered ground motions; (b) acceleration response spectra of basin and rock ground motion datasets; (c) a cumulative density function of the significant shaking durations of basin and rock ground motion datasets.

tween the rupture scenarios would play an important role in determining the median collapse capacity of structures.

- There is no significant difference between the dispersion associated with the two hybrid rupture scenarios for all parameters. However, comparing the median values suggests that scenario B, on average, is somewhat more damaging than scenario C. This is visually apparent in the plots which show scenario C data points falling between those of scenario A and B for all parameters and almost the entire range of probabilities. This trend does not change as the distance from the fault increases. The median MIDR demand on the 12-story building is on average 30% higher for scenario B than Scenario C, and the demand on the 3-story building is 20% higher between the same two scenarios. Similarly, the median $SA(T_1)$ for the 12-story building is on average 30% higher for scenario B than Scenario C. The short-period spectral acceleration $SA(T_1)$ for the 3-story building is also the least affected parameter by the changes in the asperities, with the average ratio between scenarios B and C equal to 1.1. In general, the results suggest that localized slip that is closer to the rupture source in a unilateral rupture would result in higher spectral accelerations and more damaging effects to structures. This indicates that, despite the large uncertainty associated with the rupture slip patterns of earthquake faults, it is possible to determine locations of rupture slip that provide more conservative risk estimates. Confirming such conclusions requires further analysis of the effects of the locations and sizes of the slip patches. Nonetheless, the plots in figures 8.20 and 8.21 indicate that a performance assessment using scenarios A and B only would not yield a substantial difference from an assessment using scenarios A, B and C.

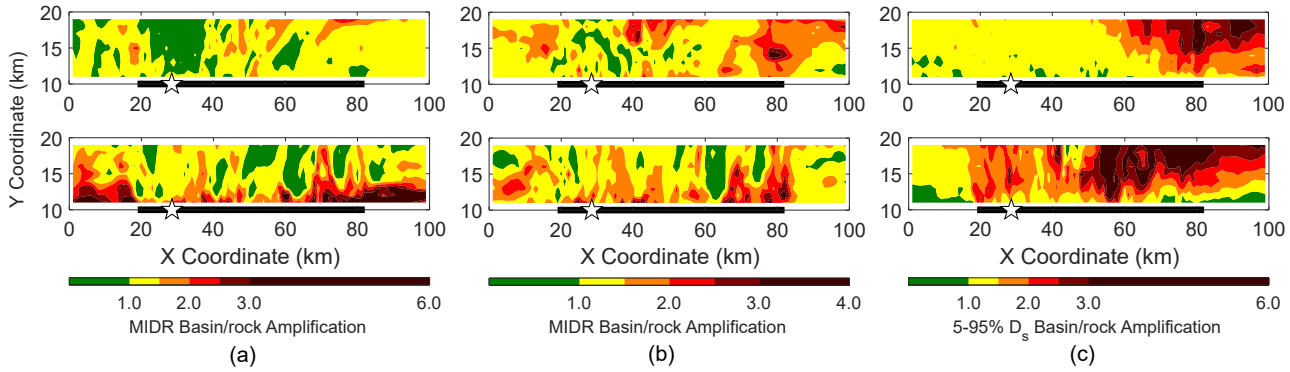

Figure 8.23: Basin amplification ratio due to the FN (upper) and FP (lower) ground motions of Scenario B for: (a) the MIDR in the 3-story building; (b) the MIDR in the 12-story building; (c) the significant shaking duration.

8.4 Effects of the basin edge on ground motion intensity and structural demands

The amplification of ground response due to focusing of the seismic energy by shallow sedimentary basins has been analyzed in a number of studies for earthquakes such as the 1994 Northridge, California and the 1995 Kobe, Japan earthquakes. Previous studies suggested that constructive interference of direct waves with the surface waves generated at the basin edge can significantly contribute to structural damage [Graves et al., 1998, Pitarka et al., 1996]. Despite the inclusion of site effects in GMPEs [Campbell and Bozorgnia, 2014], systematic differences due to site conditions and basin-edge effects remain difficult to characterize at short distances, because the available databases combine motions from regions all around the world. The size and geologic structure of the computational domain in this study allow for studying the amplification effects of shallow basins (0.6 km deep), and the systematic differences between ground motion waveforms and structural demands at the basin sites, compared to sites of identical source distances on rock. The ground motion characteristics are analyzed at the basin and rock stations within 10 km of the fault; this includes 3,267 stations on the sedimentary basin side, and 2,673 stations on the rock side. These stations are highlighted in figure 8.22a. For all three scenarios, the spectral response is consistently higher on the basin side. This is shown in figure 8.22b which displays the median acceleration response spectrum and associated dispersion (2.5 and 97.5 percentile spectra) for both sets of ground motions. The difference between the basin and rock motions is small at short periods, and increases for longer periods - becoming significant for periods longer than 2 seconds. As a result, the structural demands near the fault are higher on the basin side for most locations than the corresponding locations on the rock side, although there is significant variability in the size of the difference. To understand the variation of the ground motion amplification near the fault, maps of the basin amplification ratio of the ground motion intensity and structural demands were created for the near-fault basin area specified in figure 8.22a. The amplification ratio for a given parameter is defined as the ratio of the parameter's value at a basin site to its value at the rock site

of identical source distance. Examples of such maps are shown in figure 8.23a and b for the MIDR of the 3-story and 12-story buildings due to the FN and FP components of scenario B. These maps show that the structural demand amplification near the basin-edge is generally lower for the FN component than the FP component, particularly for the high-frequency building. This observation suggests that the strong directivity effects in the FN component may dominate the response at very short-distances, such that basin and rock sites experience similar demands. In contrast, the demands due to the FP component, which is primarily free of directivity effects, experience the highest amplification very close to the basin-edge. For instance, the 3-story FP MIDRs are shown to be amplified by a factor of close to 6.0 at a 1 km distance from the fault. These results point to systematic differences between the FN and FP components of motions near the fault on basin soils, which can be important for ground motion selection in engineering risk analyses.

The amplification effects associated with the FN component of motions at basin sites tend to increase with increasing distance away from the fault, particularly for low frequency components, which is an expected trend caused by the slower attenuation of the low-frequency seismic waves. These observations are demonstrated by examining the spectral accelerations, peak ground velocities and MIDRs at all stations that are 1 km away and 8 km away from the fault on both the basin and rock sites; examples of such plots are shown in figure 8.24 and 8.25 for scenario A. The plots support the observation that the basin amplification impacts are distance-dependent, because the amplification at 8 km is consistently higher than the amplification at a 1-km distance, when looking at the average values of the PGV, $SA(T_1)$ and MIDR. For example, at 1 km, the PGV on the basin side is on average 20% higher than the PGV at the rock sites for all three scenarios, whereas the ratio is 30% at an 8-km distance. The amplification trends at 8 km also reveal that the long-period demands experience higher amplification than the short-period demands. For instance, $SA(T_1)$ for the 12-story at the basin sites is on average 51% higher than rock sites, whereas the $SA(T_1)$ for the 3-story building increases by only 11% for all scenarios. The corresponding structural demands follow a similar trend: the 12-story MIDR at basin sites (at an 8-km distance) increases by 57% on average - compared to the corresponding rock sites - and the 3-story MIDR increases only by 15%.

The more severe demands imposed on the buildings located at basin sites are believed to be due to the combined effect of the amplified ground motion intensity and increased shaking durations. The 5-95% significant duration metric ($5-95\%D_s$) is used in this study to assess the shaking duration. This measure represents the duration between 5% and 95% of Arias Intensity, which is computed as the integral of the square of the ground acceleration history over time ($\frac{\pi}{2g}\int_0^T a^2(t)dt$) where T is the total time of the accelerogram, and g is the gravitational acceleration. The $5-95\%D_s$ is intended to represent the duration where most of the seismic energy is released, and is seen to correlate well with structural risk [Raghunandan and Liel, 2013, Marafi et al., 2016]. The empirical cumulative distribution function of the $5-95\%D_s$ for both sets of ground motions (at basin and rock sites) in figure 8.22c reveals that the basin motions tend to have longer shaking durations than rock sites, which is consistent with the observations of previous studies [Graves et al., 1998]. The amplification maps in figure 8.23c indicate that the shaking duration at near-fault basin sites is amplified significantly for both the FN and FP components (by a factor of up to 6.0). The increase in the shaking duration is found to be lowest at shorter distances, and increases

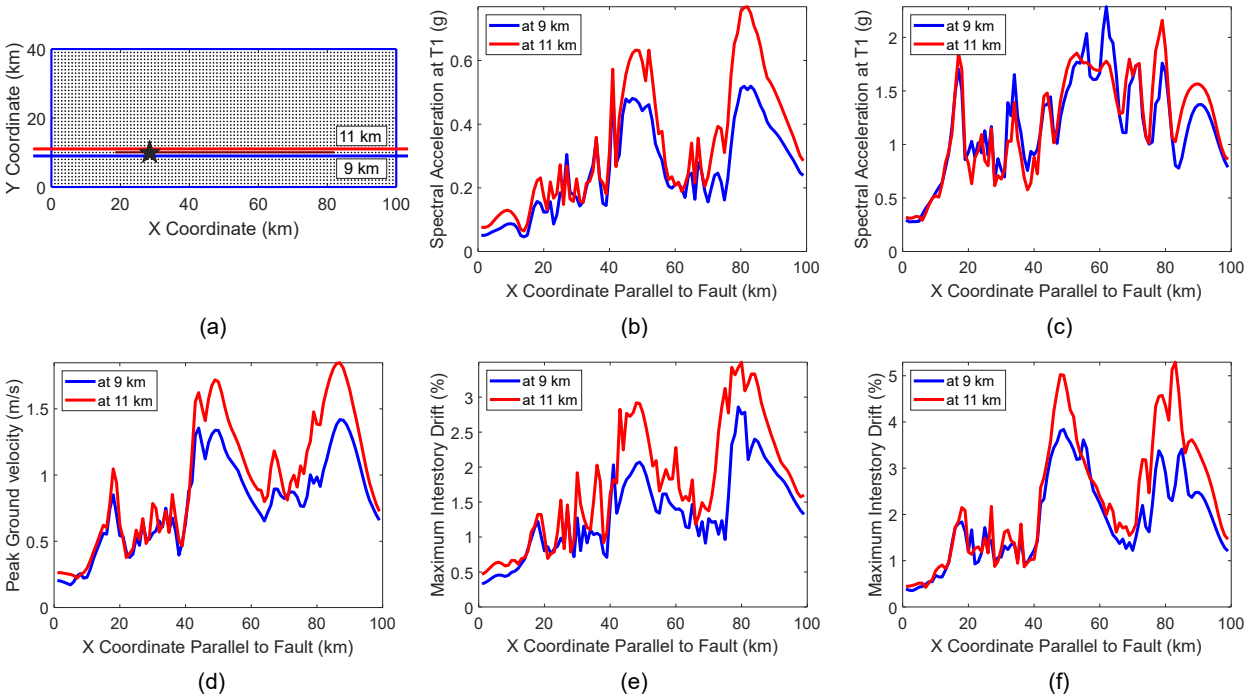

Figure 8.24: Trends of the ground motion intensity and structural demands along the 9-km (rock) and 11-km (basin) coordinate lines: (a) locations of the considered stations; (b) $SA(T_1)$ for the 12-story building; (c) $SA(T_1)$ for the 3-story building; (d) peak ground velocities; (e) maximum interstory drift demands on the 12-story building; (f) maximum interstory drift demands on the 3-story building.

substantially as the distance increases (up to the 9 km distance limit of the map). It is also worth noting that the increase in the shaking duration tends to follow different patterns for the FN and FP components, implying that the strong directivity effects (which are typically associated with shorter durations) may limit the amplification of the FN motion durations in the forward directivity zone.

The ground motion waveforms were also examined at several stations on the basin and rock sides of the domain with identical source distances: stations 9 and 10 (figure 8.26a), and stations 8 and 11 (figure 8.27a). All four stations have the same x-coordinate; stations 8 and 11 are 8 km away from the fault on the rock and basin sides, respectively, and stations 9 and 10 are 1 km away on each side. Comparing the waveforms at each station pair indicates that sites at very short distances from the fault experience relatively small amplification in the ground motion intensity, although the amplification seems to be larger for smaller amplitudes. As shown in figure 8.26, the amplitudes of the acceleration, velocity and displacement time histories at basin sites at very short distances are somewhat higher than at the corresponding rock sites; however, the shaking duration is not significantly impacted. As the distance from the fault increases, the increase in ground motion amplitude and shaking duration becomes more significant compared to the corresponding rock sites. This observation is evident in figure 8.27, which shows the time histories of the ground

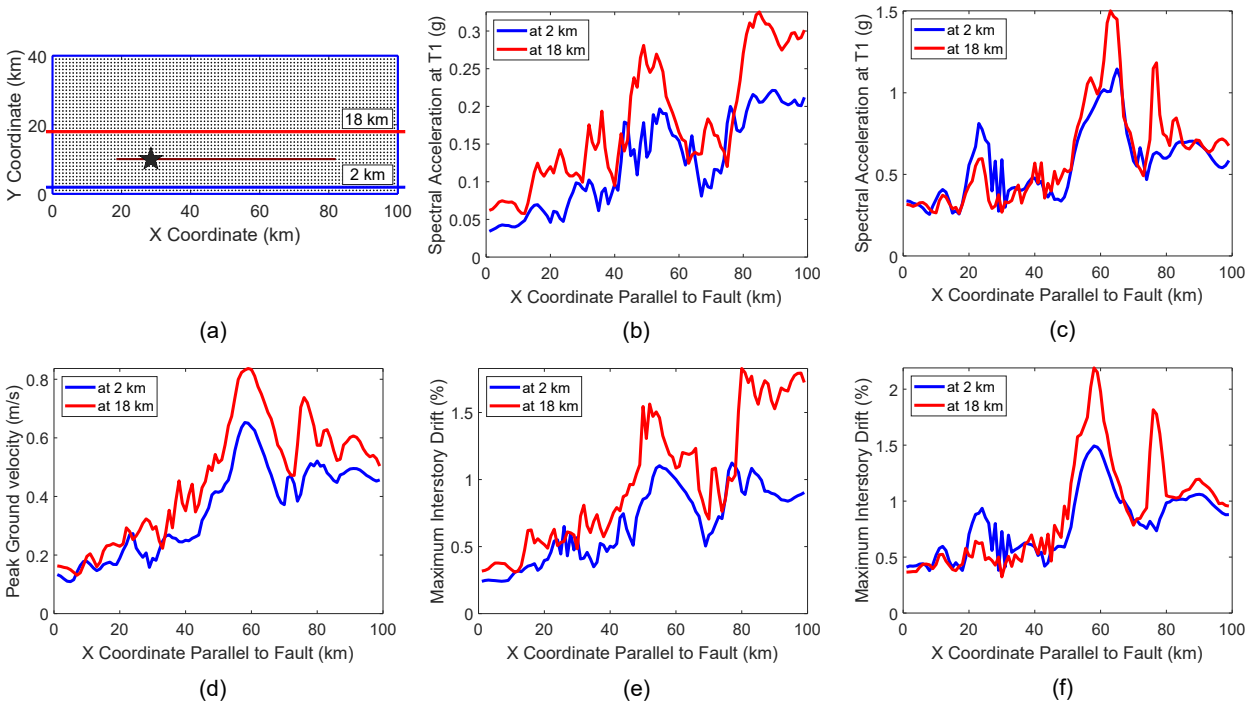

Figure 8.25: Trends of the ground motion intensity and structural demands along the 2-km (rock) and 18-km (basin) coordinate lines: (a) locations of the considered stations; (b) $SA(T_1)$ for the 12-story building; (c) $SA(T_1)$ for the 3-story building; (d) peak ground velocities; (e) maximum interstory drift demands on the 12-story building; (f) maximum interstory drift demands on the 3-story building.

motions at stations 8 and 11. The 5-95% significant duration increases from 5 seconds at station 8 (rock) to 14.7 seconds at station 11 (basin). A significant increase is also observed in the amplitudes of the acceleration, velocity and displacement time histories. Consequently, the time histories at the basin site contain several large velocity and displacement cycles that are not observed at the rock site. The more severe velocity time history explains the larger spectral demands in the long-period range at station 11 (figure 8.27b and c), and the larger increase in the 12-story MIDR demands as compared to the 3-story building at the same location.

The analysis also suggests that a measure of the story drifts alone may underestimate the demands imposed on the structural components at these near-fault basin sites. In particular, the effect of the longer shaking durations may not necessarily manifest as increased story drifts, because the additional cycles typically have smaller amplitudes. Instead, the larger number of cycles experienced at basin sites significantly affects structures that are most susceptible to cyclic deterioration effects, such as the reinforced concrete buildings considered in this study. The findings of this study reveal that buildings at near-fault basin sites experience higher maximum rotation demands compared to rock sites of identical source distances. The representative envelopes of the MIDR on the 12-story building in figure 8.28 at stations 8 through 11 - along with the building plastic hinges and maximum component rotation demands - demonstrate this observation. Although the maximum interstory drifts are similar for the buildings at stations 8 and 11, the building located at the basin site experiences more significant plastic hinge formation at most floors, and the maximum member rotation demand is doubled (from 12% to 25%), compared to the building at the rock site. Similarly, the maximum rotation demand at basin station 10 is 2.7 times the maximum demand at rock station 9, although the ratio between the MIDR demands at the two locations is only 1.3. The significant increase of the plasticity demands may be related to the additional energy dissipation and deterioration caused by the larger number of severe loading cycles. These results suggest that the distance-dependent shallow basin amplification impact may be important for selecting ground motions for a near-fault engineering analysis, as these longer-duration motions can substantially amplify the demands on reinforced concrete structures, particularly those sensitive to the low-frequency waves. These findings are consistent with those of Raghunandan and Liel [2013], who studied the effects of earthquake duration on the collapse risk of reinforced concrete structures, and Marafi et al. [2016] who showed that longer durations affect structures with cyclic deterioration, but not elastic-perfectly plastic structures (i.e., structures modeled to primarily behave as such).

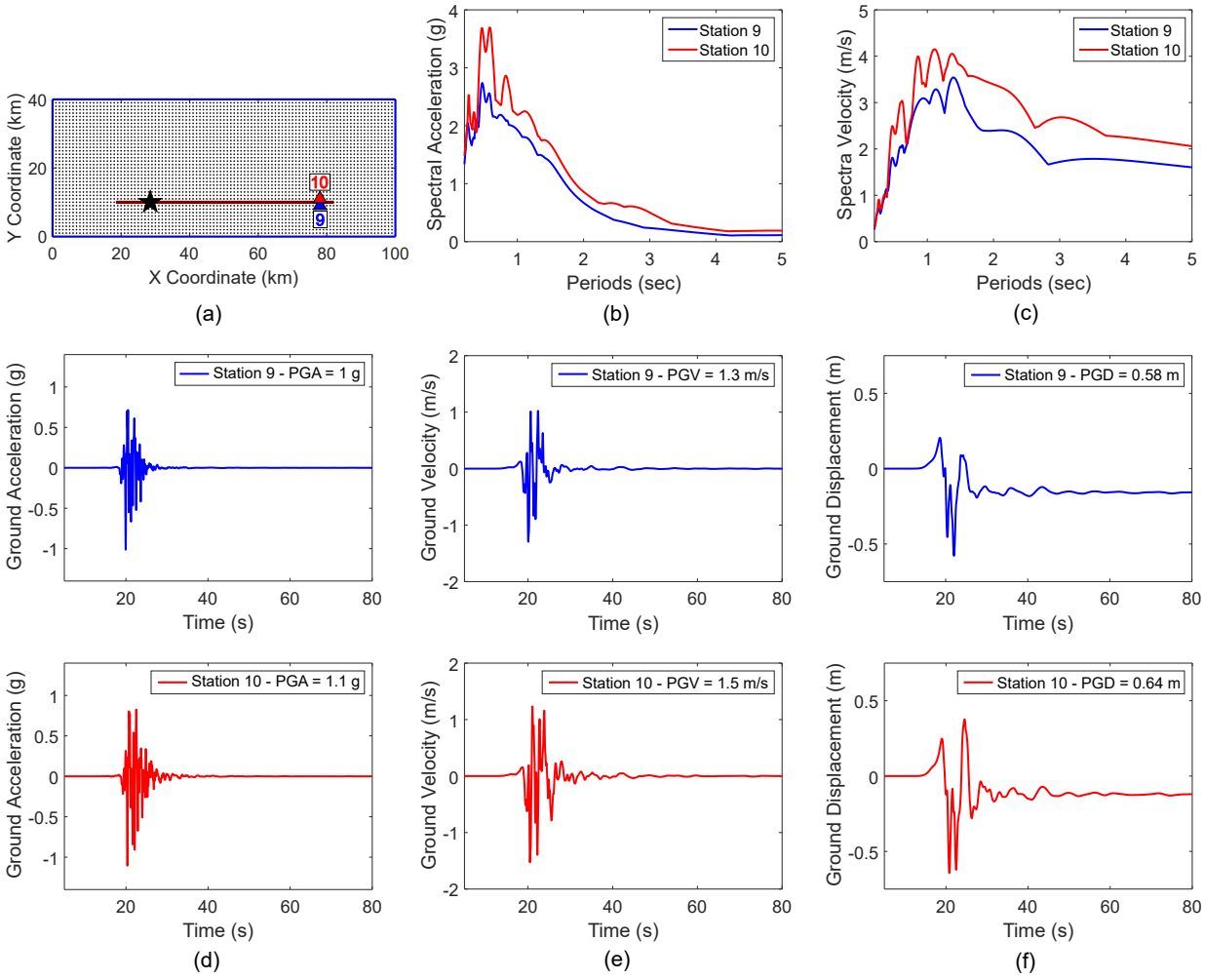

Figure 8.26: Locations and characteristics of the ground motions at a pair of basin and rock stations of identical fault and source distances: (a) locations of stations 9 and 10; (b) acceleration response spectra at stations 9 and 10; (c) velocity response spectra at stations 9 and 10; (d) acceleration time histories at stations 9 and 10; (e) velocity time histories at stations 9 and 10; (f) displacement time histories at stations 9 and 10.

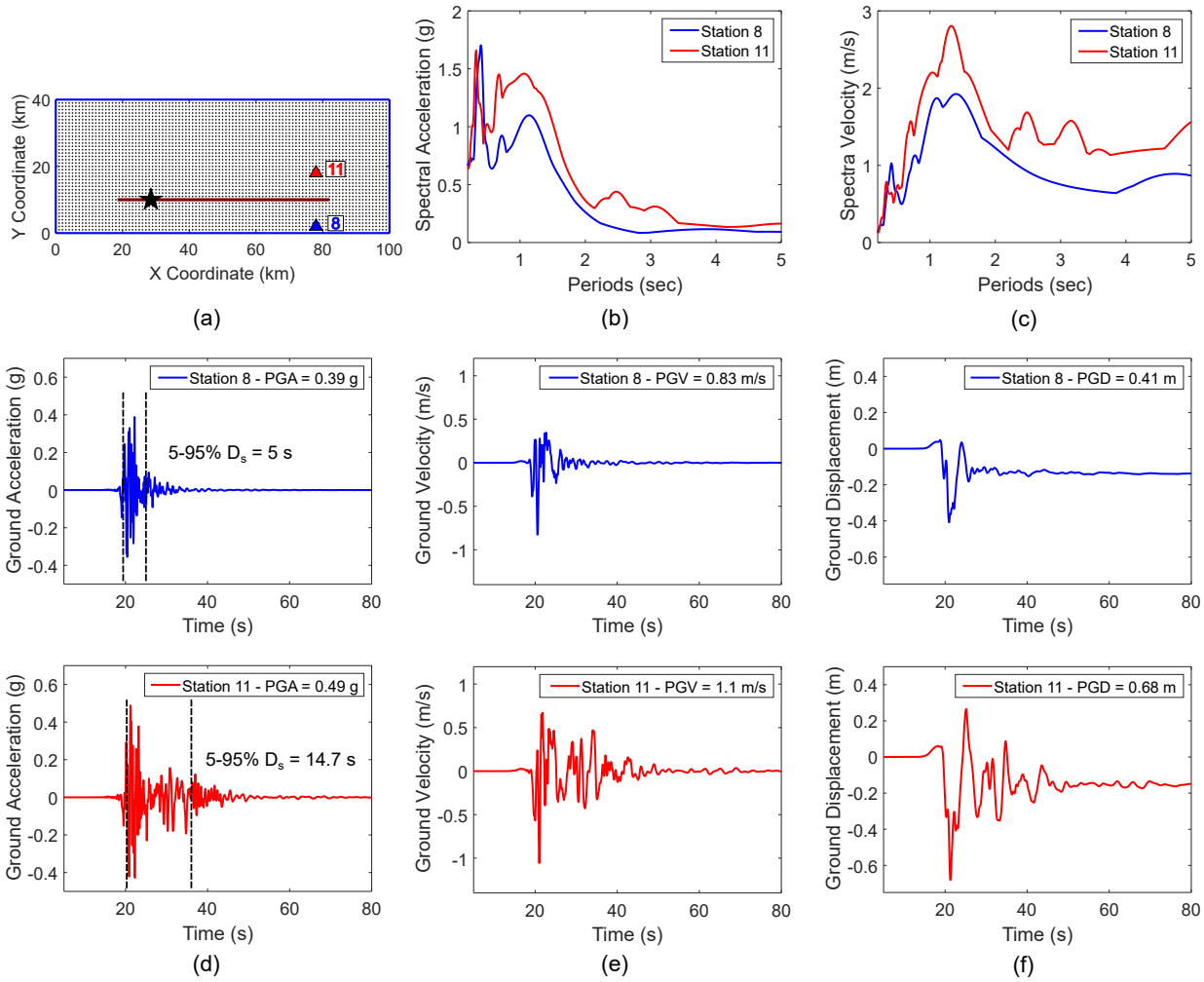

Figure 8.27: Locations and characteristics of the ground motions at a pair of basin and rock stations of identical fault and source distances: (a) locations of stations 8 and 11; (b) acceleration response spectra at stations 8 and 11; (c) velocity response spectra at stations 8 and 11; (d) acceleration time histories at stations 8 and 11; (e) velocity time histories at stations 8 and 11; (f) displacement time histories at stations 8 and 11.

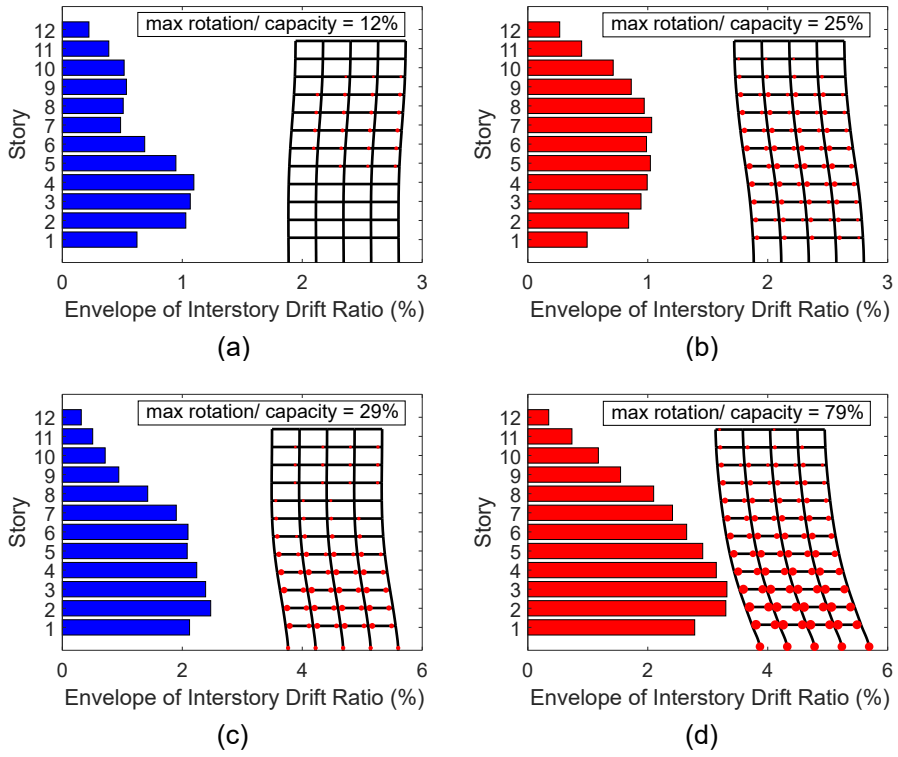

Figure 8.28: Interstory drift envelopes, deformed shapes and maximum rotation demands for the 12-story building at two pairs of basin and rock stations with identical source and fault distance: (a) station 8 (rock) at 8 km; (b) station 11 (basin) at 8 km; (c) station 9 (rock) at 1 km; (d) station 10 (basin) at 1 km.

Chapter 9

Influence of Pulse-Like Ground Motion Characteristics on Structural Risk

9.1 Characteristics of pulse-like ground motions

Evidence suggests that ground motions which have strong velocity pulses tend to have a more damaging effect on structures, compared to ordinary ground motions [Baker and Cornell, 2008, Champion and Liel, 2012]. For nonlinear near-fault analysis, ASCE 7-16 requires selecting ground motion records with pulse-like characteristics, as a fraction of the selected ground motions [ASCE, 2017]. It has also been shown that near-fault ground motions do not necessarily have pulse-like characteristics. A few studies have proposed methodologies to characterize the probability of encountering pulse motions in the near-field; these probabilities are then used to inform the selection of ground motions for nonlinear time history analysis. However, due to the limited dataset of available near-fault pulse-like records, classification of pulse-like motions and their likelihood at near-fault locations remains an active research area that continues to improve as the available dataset grows. Among other factors, the large scatter in the correlation between the spectral accelerations and the structural demands, particularly for long-period structures, is thought to be related to the presence of large pulses in the velocity records whose impact is not accounted for by $SA(T_1)$ [Baker and Cornell, 2008]. The simulated ground motions in this study provide a large, high-resolution and spatially uniform dataset for evaluating the effectiveness of available pulse-characterization algorithms, and for studying the effect of these ground motions on structures. Identifying the important effects of near-fault pulse-like motions on structures using a large and well-distributed dataset of simulated ground motions, which would not be possible using real records, can aid the development of more efficient ground motion intensity measures and structural reliability assessment approaches.

Among the available pulse-characterization approaches, the two algorithms selected for this study [Baker, 2008, Shahi and Baker, 2014] generate reproducible results, and have been used in a number of studies [Champion and Liel, 2012]. Both methods are based upon using wavelet analysis to extract the largest velocity pulse in a ground motion velocity time series [Baker, 2008]. Both algorithms also use two additional conditions to classify a ground motion as pulse-like: the

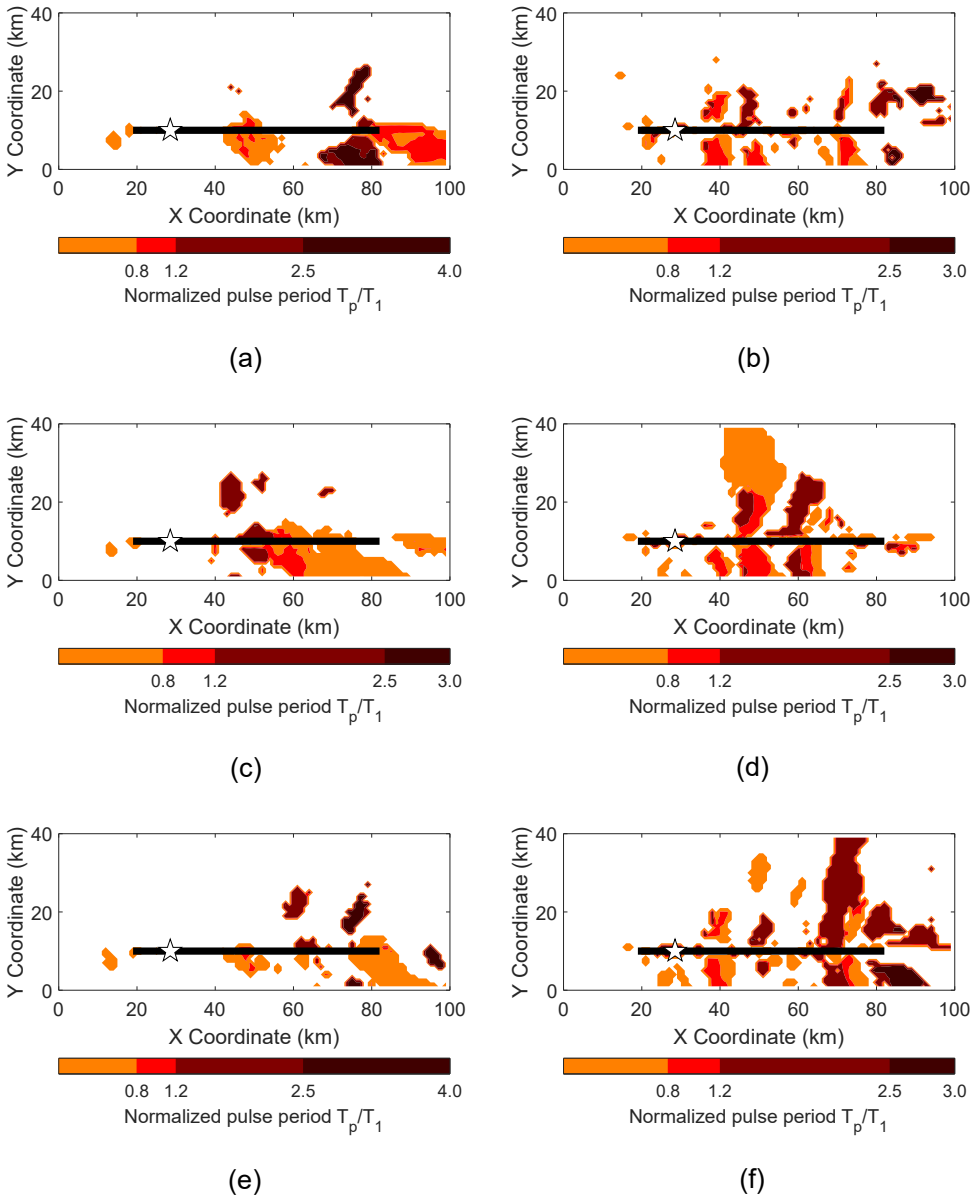

Figure 9.1: Map plots of the pulse-like ground motions and the associated pulse periods normalized by the first mode period of the 12-story building for: (a) the FN component of scenario A; (b) the FP component of scenario A; (c) the FN component of scenario B; (d) the FP component of scenario B; (e) the FN component of scenario C; (f) the FP component of scenario C.

pulse must arrive early in the velocity time history and have a larger amplitude than 30 cm/s. The first approach [Baker, 2008], termed here as the single-component classification, processes a single ground motion component; whereas the second approach [Shahi and Baker, 2014], termed as the multi-component classification, processes two horizontal and perpendicular components of ground motions to determine the presence of a pulse in any orientation. Both approaches were used in this study to examine the pulse-like motions over the entire computational domain. However, since the response history analyses are performed using a single ground motion component, the single-component algorithm was used to correlate structural response with the pulse characteristics. Figure 9.1 shows the result of applying the single-component classification algorithm to the full computational domain of all rupture scenarios. The plotted pulse maps show the pulse classification of the FN components (subplots a, c and e) and the FP components (b, d and f) for scenarios A, B and C, respectively. The pulse maps are color-coded by the value of the dominant period of the largest pulse normalized by the first-mode period of the 12-story building.

Overall, both classification approaches detect most of the pulse-like ground motions within 15 km away from the rupturing fault. The pulse-like motions are primarily detected in the forward directivity region, whereas very few pulses are detected in the backward directivity region, which agrees with observations of previous earthquakes. The algorithm also detects many pulse-like motions in the FP component. Interestingly, some of the detected pulse motions in the FP component extend to longer distances over the domain for scenarios B and C (up to the end of the domain - 29 km away from the fault). These pervasive FP pulses are arguably associated with the presence of the concentrated slip patches of scenarios B and C, and seem to geographically coincide with the locations of these asperities. Compared to the MIDR risk maps in figure 8.2, the locations of pulse motions of the FP component also align with the geographical regions of the highest MIDR demands. This correlation between the presence of pulse motions and the MIDR demands is less clear for the FN component, and in general, less pulse motions are detected in the FN component, despite the presence of large velocity pulses in many of the FN near-field sites. Close analysis of the ground motions 1 km away from the fault suggests that the classification algorithms may classify motions as non-pulse despite having pulse-like characteristics, and that the classification may depend on the particular waveform of the classification criterion. Three pairs of velocity time histories are shown in figure 9.2 which are extracted from the FN components of several stations that are 1 km normal to the fault and in the forward directivity region. The ground motion stations in each pair are separated by only 1 km, as shown in figure 9.2a. Despite having very similar waveforms and almost identical peak velocity amplitudes, only one record in each pair is classified as a pulse-like ground motion, whereas the other is classified as non-pulse (as tagged in the figure). Comparing these records suggests that a larger number of ground motions with pulse characteristics are present in the domain but may not be detected by the classification algorithms. In general, however, ground motion records with visibly large velocity pulses - relative to the remaining part of the velocity record - are classified by the algorithm as pulse-like motions, and are seen to correlate with large structural demands, compared to ground motions with no large pulses at similar distances. This trend is evident in the FN component records of stations 1 through 4 in figures 8.9 and 8.10 in the preceding chapter, in which the ground motions at stations 2 and 3 have strong velocity pulses and induce higher structural demands, as compared to stations 1 and 4. It is, there-

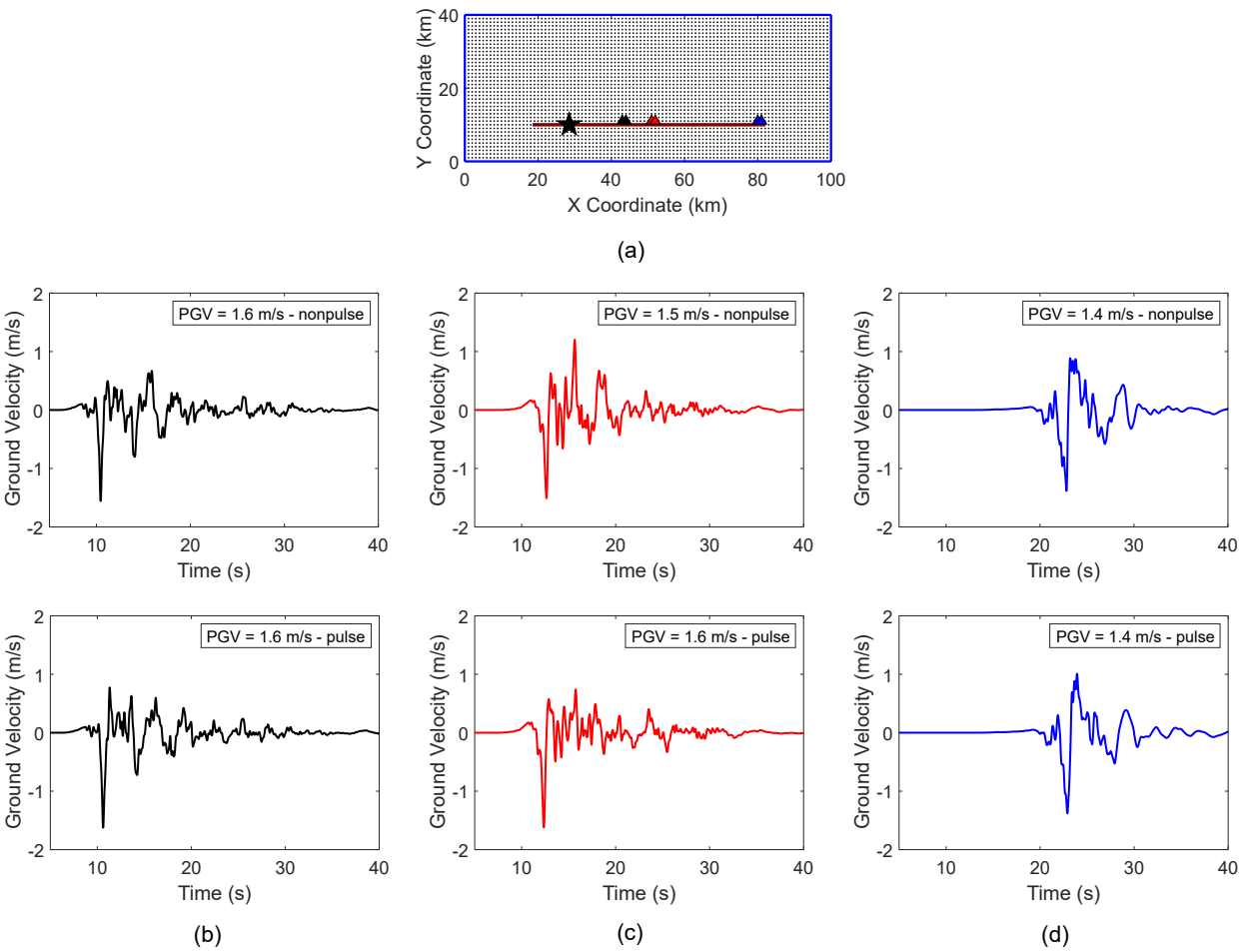

Figure 9.2: (a) locations of three station pairs 1 km away from the fault and separated by 1 km; (b), (c) and (d) ground velocity time histories and pulse classifications (by the Baker [Baker, 2008] algorithm) for the FN component at each station pair.

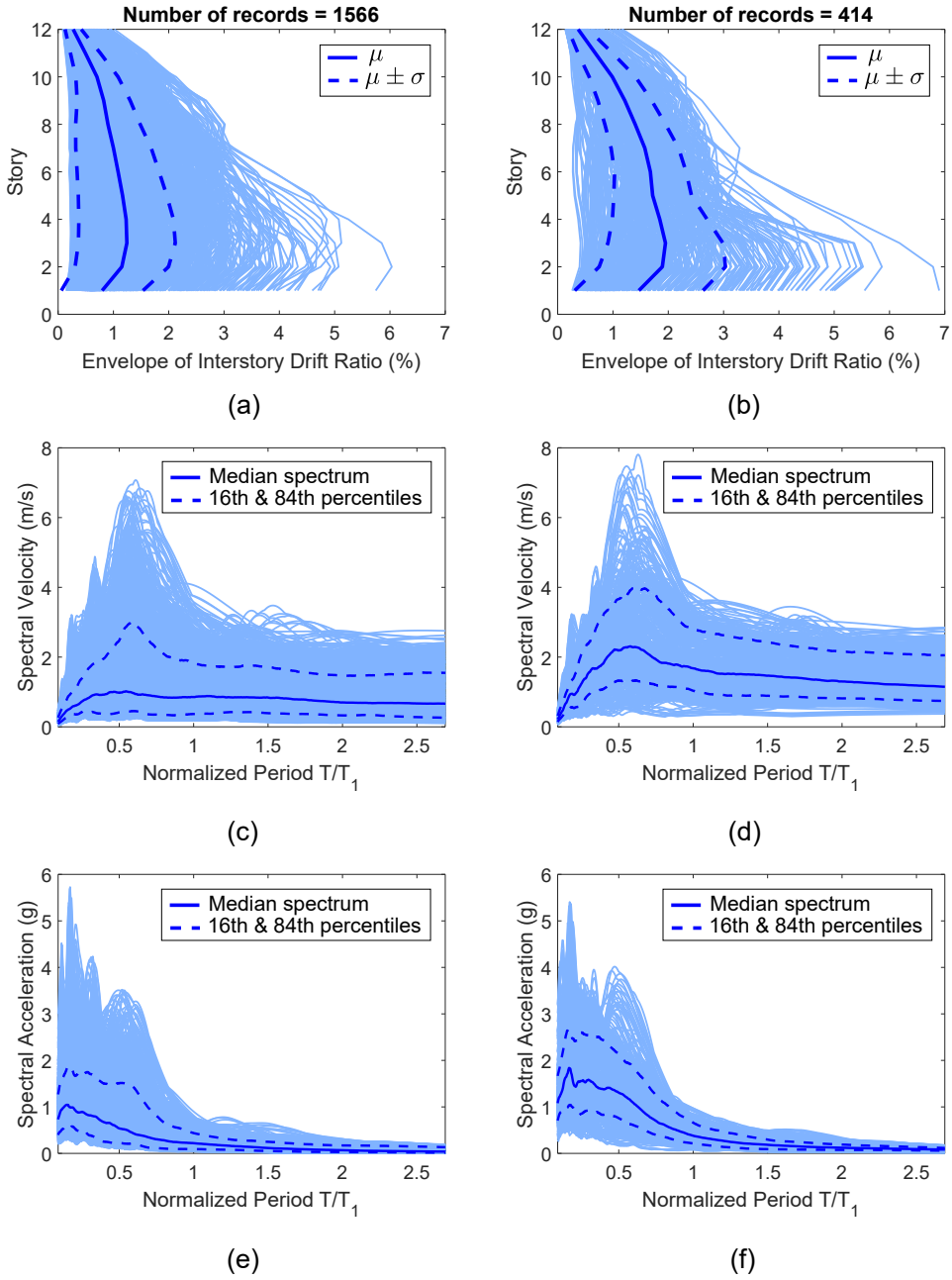

Figure 9.3: Structural response and ground motion spectral characteristics of pulse and nonpulse type motions in the FN component of scenario B: (a) MIDR envelopes for nonpulse motions; (b) MIDR envelopes for pulse motions; (c) velocity spectra for nonpulse motions; (d) velocity spectra for pulse motions; (e) acceleration spectra for nonpulse motions; (f) acceleration spectra for pulse motions.

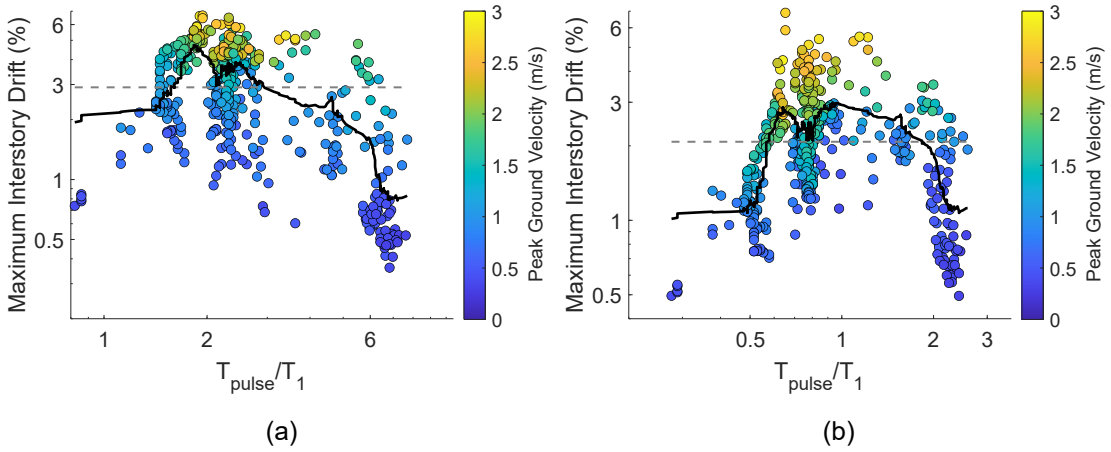

Figure 9.4: Relationship between the maximum interstory drift ratios and the pulse period normalized by the building first mode period in Scenario B: (a) for the 3-story building; (b) for the 12-story building.

fore, of interest to compare the ground motion and structural response properties associated with pulse and non-pulse ground motions at short distances from the fault.

Despite the drawbacks of the classification algorithm, examining the motions classified as pulse and non-pulse offers useful insight on the relationship between the pulse characteristics and structural response. The differences in the pulse characteristics of the simulated ground motions are studied for sites within 10 km normal to the fault. In scenario B, for example, only 21% of the ground motions in that region are characterized as pulse-like. The acceleration and velocity response spectra for these motions are shown in figure 9.3c through f for both pulse and non-pulse subsets, along with the median, 16th and 84th percentiles. The figure also shows envelopes of the maximum interstory drift of the 12-story building for each ground motion subset (subplots a and b), in addition to the mean and standard deviation of all envelopes. Examining the median acceleration spectrum demonstrates that pulse motions tend to have larger spectral acceleration than non-pulse motions over the entire range of periods, although the differences are more significant up to a period of about 2.5 seconds. Similarly, the median velocity spectrum of pulse motions has larger values over the entire range of periods, and has a distinct peak near half the first-mode period of the 12-story building, which is not seen in the non-pulse median spectrum. Despite the trends indicated by the median spectra, individual non-pulse ground motions in the near-field can have comparable spectral accelerations and velocities to those of pulse-like motions, which is speculated to be due to misclassification of records by the criterion used in this study, although a more sophisticated classification algorithm is needed to confirm this observation.

The envelopes of the MIDR for the 12-story building are observed to follow a similar trend: the mean MIDR for the pulse type group is higher than that of the non-pulse group over the entire height of the building, with a maximum difference of 84% at the first story, yet relatively large MIDR demands are caused by ground motions in both groups. The same observations can be made for pulse-like motions in scenarios A and C. Table 9.1 lists the PGV and spectral and structural

Table 9.1: Characteristics of pulse vs. non-pulse ground motions in the forward directivity region

Dataset	**Number of records**	**Mean PGV (m/s)**	**Mean $SA(T_1)/\gamma$ - 3 story**	**Mean $SA(T_1)/\gamma$ - 12 story**	**Mean MIDR - 3-story (%)**	**Mean MIDR - 12-story (%)**
Pulse	1054	1.19	10.16	5.01	2.78	1.98
Non-pulse	3206	0.82	7.96	3.92	1.89	1.62

response characteristics associated with pulse and non-pulse motions of the FN component in the forward directivity region, which is defined as the region within 10 km normal to the fault and in the direction of the rupture propagation (between the rupture source and the right end of the domain; i.e., excluding stations in the backward directivity zone). For all three scenarios, only 25% of the records are classified as pulse motions in that region. The near-fault pulse subset has a mean PGV that is 45% higher than the PGV of the non-pulse subset. Similarly, the mean $SA(T_1)$ values for the 3-story and 12-story buildings in the pulse-like dataset are both 28% higher than those of the non-pulse motions. The mean MIDR for both buildings associated with the pulse-like dataset is also higher by 47% and 22% for the 3-story and 12-story building, respectively, compared to the non-pulse dataset. The findings of this study support the empirical observation that ground motions at short distances from the fault do not necessarily contain large velocity pulses with significant damaging effects to structures. The fraction of pulse motions in the near-field is, however, likely higher than the 25% determined in the rupture scenarios analyzed herein and classified by the Baker algorithm. Nonetheless, the general trends demonstrate the complexity of near-fault motions, and suggest that the results of nonlinear time history analyses of structures at near-fault locations are sensitive to the analyst's selection of ground motion records. Simulated ground motions from different rupture scenarios, such as those created in this study, provide large and spatially-dense datasets that can help improve the sophistication of pulse-classification algorithms, and the procedures which predict the likelihood of encountering a large pulse at a given near-fault location.

9.2 Relationship between structural properties and frequency of ground motion pulses

An important characteristic of ground motions containing strong velocity pulses is the frequency content of the largest pulses. Several researchers characterized this property by determining the dominant period of the largest pulse in the velocity time series T_p, and many concluded that the response of structures is sensitive to the ratio of the pulse period to the first-mode period of a given structure T_p/T_1 [Baker and Cornell, 2008, Champion and Liel, 2012]. Comparing the pulse maps of the FN component in figure 9.1 and the corresponding risk maps of the 12-story building in figure 8.2 suggests that the relationship between T_p/T_1 and the MIDR is rather complicated. In

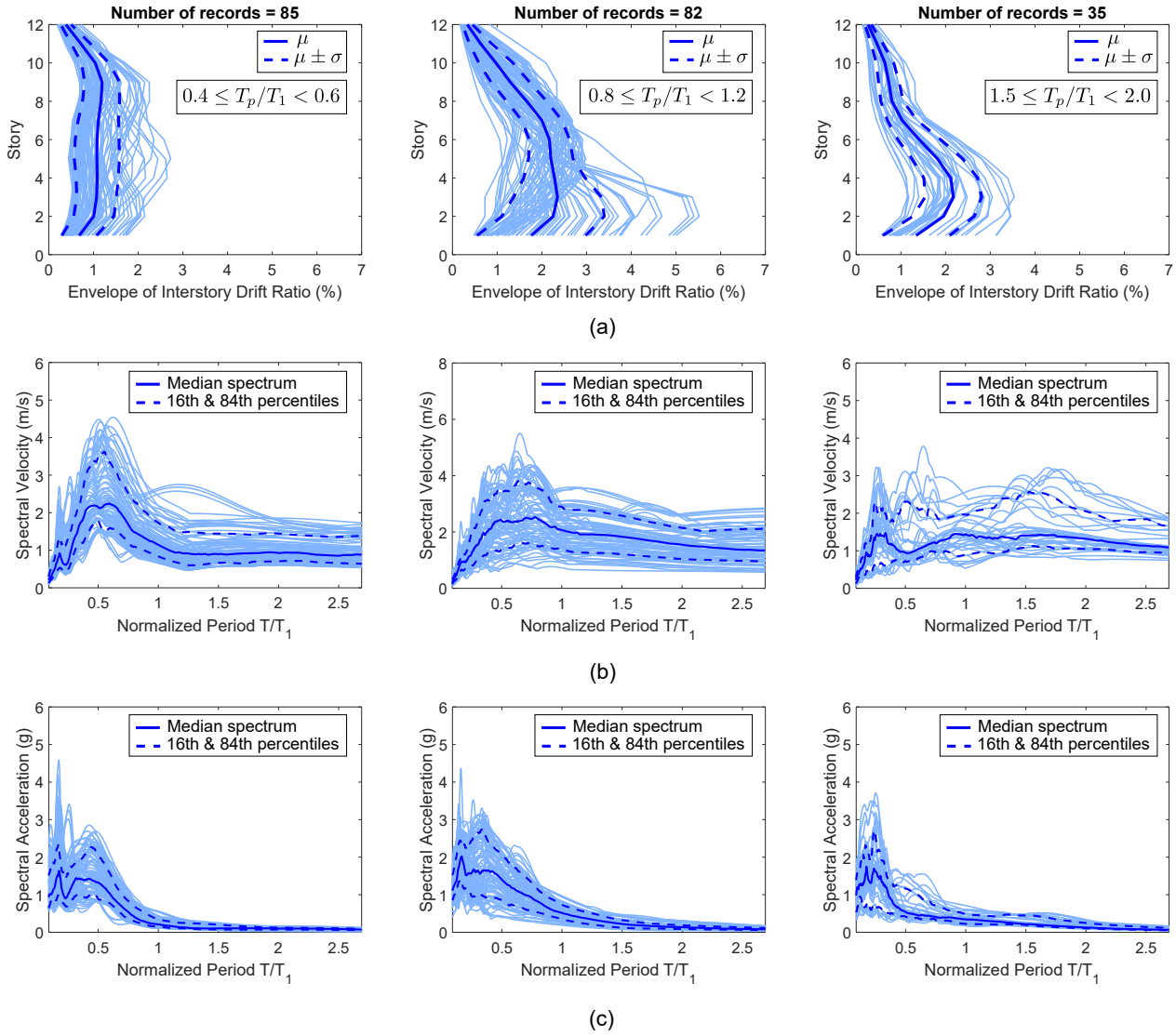

Figure 9.5: Structural response and spectral characteristics for three groups of ground motions in Scenario B with different T_p/T_1 ratios: (a) MIDR envelopes for the 12-story building; (b) velocity response spectra; (c) acceleration response spectra.

other words, the highest structural demands may coincide with locations of pulse motions with short or long-period pulses, or non-pulse motions (as classified by the algorithm). Nonetheless, examining the variation of the MIDR as a function of T_p/T_1 for each scenario reveals local trends in the data that are different for the 12-story and the 3-story buildings. Figure 9.4a shows an example of such a plot depicting the 3-story building response to the FN pulse motions of scenario B, and figure 9.4b shows a similar plot for the 12-story building response to the same motions. In both plots, the color-coding incorporates a third parameter, the peak ground velocity, to illustrate the dependence of the results on that parameter. The mean MIDR for the entire dataset is also highlighted with the dotted gray line. To examine the local variations in the data, a nearest-neighbor kernel smoothing estimator of the data (a moving average) is plotted as well, with a moving window size of about 10% of the number of the data points in each plot. Analysis of the relationship between the MIDR and the pulse period reveals the following trends:

- For both buildings, there is a considerable dispersion in the MIDR demands with respect to the T_p/T_1 ratio. This dispersion is found to be primarily due to variations in the record's PGV, as highlighted by the color-coding in the figure. In other words, the structural demands at stations with the same pulse period strongly correlate with amplitude of the pulse. A similar correlation exists with the spectral accelerations $SA(T_1)$. The results suggest that ground motion IMs which incorporate $SA(T_1)$ or the PGV along with a measure of the pulse period would perform comparably for structures subjected to pulse-like motions.

- For the 3-story building, the largest structural demands are generally observed at T_p/T_1 ratios between 2.0 and 3.0, although the results show that significant demands may be imposed at stations with relatively long pulse periods (close to 6 times the structure's first-mode period) in some cases. The large demands near T_p/T_1 ratios of 2.0 are consistent with the results of previous studies [Baker and Cornell, 2008, Champion and Liel, 2012], and are presumed to be a result of the elongation of the building's first-mode period as the ground motion intensity increases and the building behaves inelastically. Therefore, the building effective period is usually near $2T_1$. It is noted, however, that very few pulses with a period near the 3-story building first mode period are present in the data. Therefore, it is difficult to accurately determine the mean demands near T_1. Another implication of the lack of short-period pulses is that they may not generally be expected in a rupture scenario of magnitude 7. Therefore, for stiffer buildings, pulse-like motions would only be relevant for risk assessments at near-fault sites only, where the ground motion intensity is high enough to induce yielding and period elongation, making the structure sensitive to the relatively long-period velocity pulses in the ground motions.

- For the 12-story building, the highest MIDR demands are observed at T_p/T_1 ratios between 2/3 and 1.5, for all scenarios. Relatively large demands are observed at a T_p/T_1 ratio close to 2.0 in some locations, but the demands drop significantly for periods larger than twice the first-mode period. This observation is consistent with the findings presented in the preceding chapter which suggest that the 12-story building does not experience as much yielding as the 3-story building at most locations. Therefore, the building's first-mode period does not

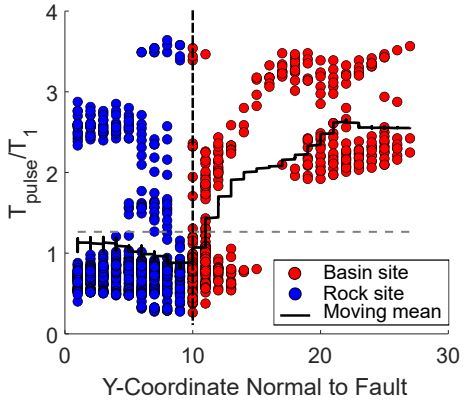

Figure 9.6: Pulse periods (normalized by the 12-story building period) along the y-coordinate normal to the fault for basin and rock sites.

elongate significantly and the building remains primarily sensitive to pulses with periods near its first-mode period. Considering the range of pulse periods generated in all scenarios, and because the 12-story building response may be influenced by higher mode contributions, the 12-story building appears to be sensitive to a wider range of the generated pulses in this study, as compared to the 3-story building.

The frequency content of the velocity pulses seems to also play a significant role in determining the distribution of the structural demands over the height of the 12-story building. The relative distribution of structural demands over the building height may depend on the frequency content of the largest pulse, regardless of the spectral acceleration content. For example, ground motions with pulses much shorter than the building's first-mode period may result in higher demands on the upper stories, compared to motions with pulse periods near the building's first-mode period. Figure 9.5a displays the envelope of the MIDR over the height of the 12-story buildings due to ground motions in Scenario B with pulses that have normalized periods T_p/T_1 in the following ranges: group 1 between 0.4 and 0.6, group 2 between 0.8 and 1.2 and group 3 between 1.5 and 2.0. The mean demands and dispersion (standard deviation) are also plotted in each subplot. The underlying ground motions were selected based solely on their classified pulse period, with no regard for other intensity measures. Along with the MIDR envelope plots, the causative ground motion acceleration and velocity response spectra are also depicted in the figure (subplots b and c), in addition to the median, 16th and 84th percentile spectra. The distribution of structural demands along the building height is relatively uniform for pulses with periods near half the building's first mode period, which generally impose lower demands compared to other periods. However, the ground motions in this group may cause relatively large demands on the upper stories as a result of exciting the building's higher modes. For instance, the mean MIDR demands at stories 10 through 12 are marginally higher for this group of ground motions than the mean MIDR in the other groups with longer pulses, although the demands at the lower stories (1-7) are much smaller. The largest MIDR demands are concentrated in the lowest stories for the motions in the second group (with pulses near T_1), because these motions would primarily excite a first-mode response. Finally, at

pulse periods larger than 1.5 T_1, the mean demands decrease but the highest demands become even more concentrated in the lowest stories, although only a small number of records was available in this group. This observation indicates that the contribution of higher vibration modes is less important when the building is subjected to relatively long-period pulses. For example, while the mean demands are similar in the first three stories in groups 2 and 3, the MIDR demand at the 8th story in group 3 is half of the mean demand in group 2 at the same floor. For ground motions with pulse periods larger than $2T_1$ (not plotted), the maximum mean structural demands decrease significantly (in this case, by 46% compared to group 3), although they remain concentrated in the lowest stories.

The findings above suggest that the frequency content of the ground motion velocity pulses may substantially impact the perceived structural risk, and the demands expected at different stories, particularly for long-period buildings. They also indicate that second or higher mode contributions may become important for risk assessments for relatively flexible structures. Examination of the ground motion spectra reflects the changes in the median $SA(T_1)$ as the pulse frequency content increases. $SA(T_1)$ differs significantly between groups 1 and 2 (increases by 146%), whereas the spectral acceleration at the second-mode period (around 1/3 of T_1) increases by only 15%. Although $SA(T_1)$ decreases by 33% between groups 2 and 3, both groups induce similar mean maximum demands on the building but relatively differing demand distributions over the building height. In contrast, the shape of the median velocity spectrum differs significantly between groups of ground motions with different pulse periods. The median and percentile spectra of group 1 have a distinctive peak near half of T_1, whereas the median spectra of groups 2 and 3 show shifting of the energy toward longer periods, with flatter peaks near the selected range of the pulse periods. These observations indicate that ground motion velocity spectra can provide a reasonable indication of the frequency content of the velocity pulses; however, not all individual ground motions show distinctive peaks in their velocity spectrum near the pulse period, particularly for long-period pulses. A similar study for the 3-story building demonstrates that the largest structural demands coincide with pulses that are twice the building's first-mode period, and that the demands remain significant up to T_p/T_1 ratios of 4.0, which is indicative of significant yielding in the building components.

9.3 Relationship between velocity pulses and site conditions

Examining the spatial variability of the frequency content of the velocity pulses suggests a site-dependent effect on the detected pulse periods. In general, more pulse motions are detected on the rock side of the near-fault region compared to the basin side. However, the mean pulse periods on rock sites are considerably lower than those on sedimentary basin soils within the same distance range. This is apparent in figure 9.6 which shows the pulse periods (normalized by T_1 of the 12-story building for all the pulse motions detected in all scenarios (1196 records) vs. the y-coordinate of the domain (normal to the fault); the location of the fault is also marked with a dashed line. The moving mean of the data is plotted, in addition to the mean of the entire dataset (represented by the dashed gray line). A significantly smaller number of pulse ground motions is detected at basin sites relative to rock sites within 10 km of the fault, although this could partially be an artifact of

the pulse waveform criterion implemented by the classification algorithm, as previously discussed. At the same time, basin sites within 10 km have higher mean pulse periods than rock sites within the same distance range. Between 10 and 20 km away from the fault, some pulse motions are detected, but these represent only about 4% of the ground motions in that distance range. The detected pulse motions at longer distances have distinctively longer period content, and would probably be of concern to flexible structures at long distances from the fault. The effect of the site properties on the structural response, however, remains dependent on the effective period of the building. For the 12-story building, basin sites with long-period pulses are associated with the highest structural demands, whereas the 3-story building at the same sites is not significantly affected by the long-period pulses.

Chapter 10

Part II Summary, Conclusions and Recommendations

The study presented in part II of this report utilized a suite of broadband physics-based simulated earthquake ground motions to characterize the regional-scale variability of risk to reinforced concrete (RC) structures, particularly at short distances from the rupturing fault. The ground motions were generated using kinematic fault rupture models with three-dimensional wave propagation physics over domains containing billions of grid points, and resolved up to a frequency of 5 Hz. Over forty thousand nonlinear response history simulations were conducted on two short and mid-rise RC special moment frame buildings, which were designed to satisfy modern code requirements. The simulation models for the buildings are based on the lumped-plasticity modeling approach, which incorporates the expected nonlinear behavior of structural components due the combined effects of concrete spalling and crushing, steel rebar slip, buckling and fracture using plastic-hinge models. The nonlinearities manifest in the model as deterioration in the strength and stiffness of the structural components subjected to repeated loading cycles, and their inclusion is critical for understanding the demands imposed by earthquake events on RC structures. The goal of this study was to explore several questions of engineering importance regarding the variability of structural risk within a single earthquake scenario and between different rupture scenarios, and the impact of the characteristics of near-fault ground motions on the expected structural demands for buildings with different stiffness and ductility properties. Ground motion waveforms, common measures of ground motion intensity and structural response quantities were studied at several distances from the earthquake fault and epicenter, and the associated dispersion was quantified. The findings of this study are summarized as follows:

- Studying the ground motion and structural response characteristics at identical fault distances over the domain demonstrates the large variability at short distances associated with the intensity measures (peak ground velocities and spectral accelerations) and structural demands (maximum interstory drift ratios (MIDR) and member rotation demands). The MIDR demands on short-period structures may vary by a factor of close to 8.0 at a distance of 1 km from the rupturing fault. The large dispersion in the structural response drastically decreases as the distance from the fault increases. In this study, both the magnitudes and dispersion of

the spectral and structural demands decrease significantly beyond a distance of 15 km away from the fault.

- Accumulation of the seismic waves as the rupture front propagates generates strong velocity pulses in the FN component of ground motions in the forward directivity path, as established in many studies. This study shows that such effect is primarily concentrated with a 10 km normal distance to the fault for unilateral M7.0 vertical strike-slip scenarios, and may lead to extreme MIDR and member rotation demands. Analysis of the ground motion intensity and structural demands at several stations in the forward directivity path suggests that the demands may increase significantly as the distance from the rupture source increases up to a certain distance dependent on the rupture characteristics (in this study, it is about 60 km away from the rupture source in all scenarios). Beyond this distance, the structural demands decrease substantially, and the ground motions exhibit lower intensity and characteristics similar to far-field motions, and motions in the backward directivity region. A strong directivity effect is absent from the FP component of all motions, yet relatively significant structural demands are observed over larger parts of the domain, as compared to the FN component.

- Ground motions at sites on shallow sedimentary basin soils have higher acceleration, velocity and displacement amplitudes and shaking durations compared to sites with identical source distances on rock. The interstory drift demands at basin sites are on average higher than the corresponding rock sites, particularly for flexible buildings. In addition, the longer shaking durations at basin sites significantly impact the maximum rotation demands of the structural members, and are anticipated to lead to more deterioration and structural damage.

- Many aspects of the structural response at short distances from the fault are shown to depend on the dynamic properties of the buildings, and their relationship with the frequency content of the ground motions. The response of the long-period building in this study, which is expected to be sensitive to a broader range of frequencies, retains significant variability over longer distances from the fault, as compared to the short-period building. The long-period building is also found to be more sensitive to ground motions with strong velocity pulses, because many pulse-like motions contain low-frequency pulses that are near the effective period of the building. Most of the detected long-period pulses do not substantially impact the demands on the short-period building.

- The acceleration response spectra of the simulated ground motions compare reasonably well with the spectra of available recorded near-fault motions, particularly in the long-period range. The medians of the simulated ground motions generally overestimate the spectral response in the short-period range, compared to the available dataset of observations. The response of the buildings to the simulated motions is generally consistent with their response to recorded motions, particularly the long-period 12-story building. The hybrid rupture scenarios with localized slip patches generate ground motions that produce high spectral demands, peak ground velocities and structural demands that closely agree with the demands of avail-

able real records. This finding supports the use of the hybrid rupture models in conducting seismic risk assessments.

- The presence of localized high-slip patches along the fault consistently leads to higher ground motion intensity and structural demands over regions of the domain that are near the patches, and presumably leads to higher demand variability at a given distance from the fault. The comparison between the demands induced by the stochastic rupture scenario, hybrid rupture scenarios and real records suggests that utilizing the stochastic scenario alone in a seismic risk assessment may lead to underestimating the structural demands and record-to-record variability at both near-fault and far-field sites.

- The amplification effects of the slip patches in the hybrid rupture scenarios are seen in both the FN and FP components of the ground motions. In the FN component, these impacts ate concentrated in the forward directivity zone, whereas the amplification of the structural demands due to the FP component is more significant at longer distances from the fault.

- Changes in the locations of the high-slip patches are seen to shift the locations of the maximum structural demands, and have a minor effect on the frequency content of the ground motions and expected magnitudes of the spectral and structural demands. Examining a large number of rupture scenarios with different slip-patch locations and geometries is necessary to determine the sufficient number of scenarios for an engineering risk assessment. However, the preliminary findings of this study suggest that slip patches that are located closer to the rupture source in a unilateral rupture may produce more damaging effects. The minor differences between both hybrid rupture scenarios also suggest that a small number of scenarios would likely suffice for an engineering risk analysis.

- Examining the pulse characteristics of the simulated ground motions indicates that only about 25% of the records within a 10 km distance from the fault are detected as 'pulse-like' by the classification algorithm developed by Shahi and Baker [2014]. Closer examination of the velocity waveforms of ground motions within 1 km of the fault suggests potential issues with the classification algorithm, which may mis-classify records to be non-pulse despite having relatively strong velocity pulses. In general, pulse-like motions were detected within a 15 km distance from the fault in the FN component, and most of them in the forward directivity region. Looking at the FP component, several pulse-like motions were detected over longer distances away from the fault, particularly in the hybrid rupture scenarios. The locations of these ground motions coincided with the locations of the localized slip patches and highest structural demands in the domain.

- The pulse-like simulated ground motions are found to have higher median spectral accelerations, mean peak ground velocities and mean structural demands than non-pulse motions. The maximum values of the MIDR and the distribution of demands over the building height are seen to depend on the relationship between the frequency content of the building and that of the most significant velocity pulse in the ground motion record. The more flexible and less ductile 12-story building in this study was most sensitive to pulse motions with a

pulse period between 2/3 and 1.5 of the building's first-mode period, and the longer-period pulses imposed the highest demands on the lowest stories. The stiffer and more ductile 3-story building experienced the largest deformations when subjected to ground motions with pulse periods between 2 and 3 times the building's first-mode period, which is indicative of significant yielding.

The findings of this study provide important insight regarding the variability of ground shaking and structural demands for seismic risk assessments of structures subjected to shallow crustal earthquakes, and recommendations regarding the use of simulated earthquake ground motions to conduct such assessments. Parametric sensitivity studies are necessary to examine characteristics of the rupture that were not considered in this study and would be expected to affect the resulting structural demands; these include different source locations, different geometries of the rupture slip patches, and varying depths to the top of the rupture. Future studies with a larger number of scenarios will also characterize the dispersion in the structural collapse risk at a particular distance from the fault due to many possible ruptures from a single fault, in addition to examining the impact of the large permanent ground displacements (fling step) associated with the FP component of the ground motions on the structural risk near the fault.

Part III

Appendices

Appendix A

Stiffness of the Structural Members in the Lumped Plasticity Models

This appendix describes the process for obtaining the structural stiffness of the beam elements with different boundary conditions, which is used to determine the lumped plasticity analysis model input parameters. The 4x4 stiffness matrix for a beam element (ignoring the axial deformations), can be derived using a cubic polynomial function for the transverse displacement field along the element:

$$\mathbf{K} = \begin{bmatrix} \frac{12EI}{L^3} & \frac{6EI}{L^2} & \frac{-12EI}{L^3} & \frac{6EI}{L^2} \\ \frac{6EI}{L^2} & \frac{4EI}{L} & \frac{-6EI}{L^2} & \frac{2EI}{L} \\ \frac{-12EI}{L^3} & \frac{-6EI}{L^2} & \frac{12EI}{L^3} & \frac{-6EI}{L^2} \\ \frac{6EI}{L^2} & \frac{2EI}{L} & \frac{-6EI}{L^2} & \frac{4EI}{L} \end{bmatrix} \tag{A.1}$$

which includes two degrees of freedom (DOFs) at each node: transverse displacement and rotation.

A.1 Members in double-curvature bending

Beam and column members in moment frames subjected to lateral loading are in double-curvature bending (see figure A.1). To arrive at the stiffness expression for these members, we apply the boundary conditions (BCs) shown in figure 1.1a, thereby restraining the transverse displacements at both nodes, and allowing rotations; i.e., $\theta_1 \neq 0; \theta_2 \neq 0; v_1 = v_2 = 0$. The force-deformation

relationship of the element becomes:

$$\begin{bmatrix} V_1 \\ M_1 \\ V_2 \\ M_2 \end{bmatrix} = \begin{bmatrix} \frac{6EI}{L^2} & \frac{6EI}{L^2} \\ \frac{4EI}{L} & \frac{2EI}{L} \\ \frac{-6EI}{L^2} & \frac{-6EI}{L^2} \\ \frac{2EI}{L} & \frac{4EI}{L} \end{bmatrix} \begin{bmatrix} \theta_1 \\ \theta_2 \end{bmatrix} \tag{A.2}$$

For members in double-curvature, let $\theta_1 = \theta_2 = \theta$, which leads to the following relationship between the end moment and rotation:

$$M_1 = M_2 = \frac{6EI}{L}\theta \tag{A.3}$$

Therefore, the rotational stiffness of the beam element is:

$$K_{double} = \frac{6EI}{L} \tag{A.4}$$

and the resulting shear forces at the nodes are:

$$V_1 = -V_2 = \frac{M1 + M2}{L} = \frac{12EI}{L}\theta \tag{A.5}$$

A.2 Members in single-curvature bending

A cantilever beam, or a beam in single curvature bending, may be considered equivalent to a beam in double-curvature of twice the length (refer to figure A.1). Therefore, the rotational stiffness of the cantilever beam may be determined based on equation (A.4) as:

$$K_{single} = \frac{6EI}{2L} = \frac{3EI}{L} \tag{A.6}$$

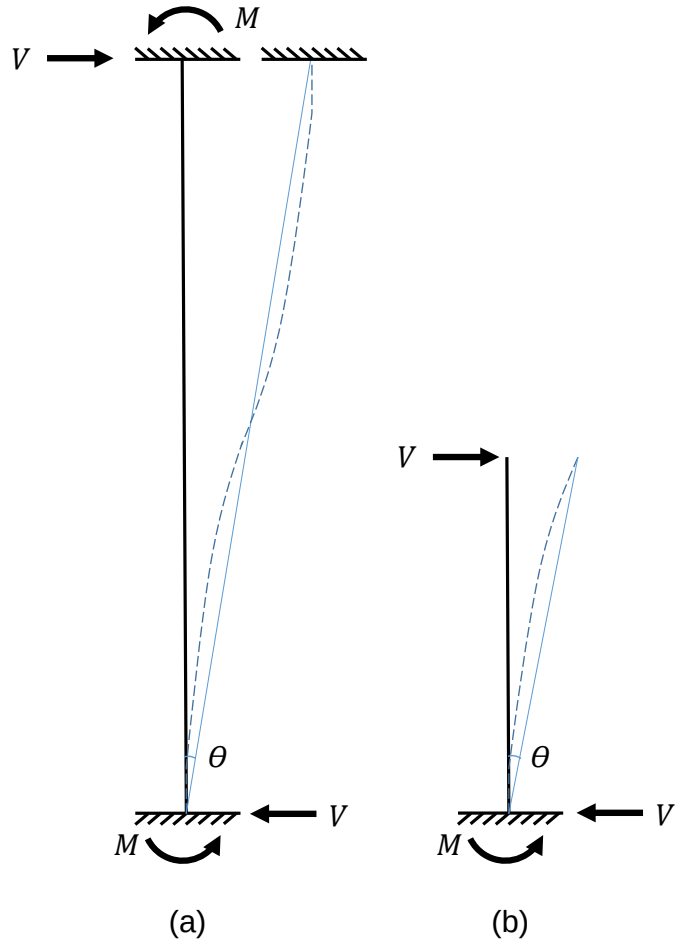

Figure A.1: equivalence between beam members in double- and single-curvature bending

Appendix B

RC Building Structural Design Workflow

This appendix presents the workflow used for designing the RC buildings created in this study. The design process was conducted using a Jupyter Notebook [Kluyver et al., 2016], which is a combination of text, python-based scripts and figures. A design example of a 12-story special moment frame building is presented in this appendix.

Seismic Design of a 12-story RC SMF Building-3D

1 Structural design of a 12-story reinforced concrete special moment frame building in Berkeley, CA - 3D Analysis

Notes:

- Following the ASCE 7-16 provisions for determining loads, and ACI 318-14 for concrete design.
- Most of the design follows the design example of the 2015 NEHRP Seismic Provisions
- Near fault sites: (with 15 km of an active fault capable of M7, or 10 km of an active fault capable of M6 - with exceptions in ASCE 7-16)
- Reinforced concrete frame members not designed as part of the seismic force-resisting system shall comply with Section 18.14 of ACI 318.

Design parameters:

- Location: Berkeley, CA
- Site class: C (very dense soil and soft rock)
- Risk Category: II
- Importance factor = 1.0
- Seismic response spectral parameters were obtained from the ATC hazard by location map (according to ASCE 7-16)

Structural modeling: The following reduction factors were applied to the moment of interia of the model sections to account for cracking, presence of axial loads and loading duration effects (creep): 0.5 for columns, and 0.3 for beams.

[1]:
```
# units
inch = 1.0;
kip = 1.0;
sec = 1.0;
ft = 12*inch;
lb = kip/1000;
ksi = 1.0;
psi = ksi/1000;
psf = ksi/1000/(12*12);
pcf = kip/1000/(12*12*12);

# normal weight concrete
rcdensity = 150*pcf;
lam = 1.0;
```

```
g = 386.1*inch/(sec**2)
```

[2]:
```
# Building Geometric Parameters
import numpy as np

Nstory = 12;
Nbayx = 4;
Nbayy = 4;
Wbayx = 20*ft;
Wbayy = Wbayx;
Hcol1 = 18*ft;
Hcol = 13*ft;
Lbeam = Wbayx;

# Assume these dimensions for now
hbeam = 30*inch;
bbeam = 20*inch;
dcol = 30*inch;
bcol = dcol;

I_reduction_col = 0.5 # a little different than ACI 318 factors
I_reduction_beam = 0.3

Ncol = 25;
Nframe = 5; # Number of frames carrying the seismic weight per direction
Hbuilding = Hcol1 + Hcol*(Nstory - 1);

Lstory = np.empty(Nstory)
Lstory[0] = Hcol1
Lstory[1:] = Hcol

# material properties
## normal weight concrete
fc = 5*ksi
fy = 60*ksi
Est = 29000*ksi


# Slab thickness is determined using table 8.3.1.1 (ACI-318-14) - also check␣
 ↪table 8.3.1.2
# for Steel grade 60
tmin = Lbeam/33; print('minimum slab thickness = ',round(tmin,1),' inches')
tslab = 8*inch;
```

```
minimum slab thickness =  7.3  inches
```

[3]:
```
# Dimensional limits for beams of special moment frames
clear_span = Lbeam - dcol
if clear_span < 4*hbeam:
    print('INCREASE SPAN OR DECREASE BEAM DEPTH')

bbeam_min = min(0.3*hbeam,10)
if bbeam < bbeam_min:
    print('INCREASE BEAM WIDTH')

# If the width of the beam exceeds the width of the supporting column, check the␣
 ↪requirements of ACI 318-14 section 18.6.2.1

# Dimensional limits for columns
if dcol < 12.0:
    print('INCREASE COLUMN DIMENSION')
if bcol < 12.0:
    print('INCREASE COLUMN DIMENSION')
```

1.1 1. Seismic Design Requirements

[4]:
```
Ss = 2.154 # Short period MCE response spectral acceleration (USGS hazard tools
S1 = 0.83 # 1-sec period MCE response spectral acceleration
Fa = 1.2 # Short period site coefficient - ASCE7-16 Table 11.4-1
Fv = 1.4 # 1-sec period site coefficient - ASCE7-16 Table 11.4-1

print ('Response spectral acceleration parameters adjusted for site effects')
S_ms = Fa*Ss; print ('S_ms = ',S_ms)
S_m1 = Fv*S1; print ('S_m1 = ',S_m1)

print ('Design spectral acceleration parameters')
S_DS = round(2/3*S_ms,3); print ('S_DS = ',S_DS)
S_D1 = round(2/3*S_m1,3); print ('S_D1 = ',S_D1)
```

```
Response spectral acceleration parameters adjusted for site effects
S_ms =  2.5848
S_m1 =  1.162
Design spectral acceleration parameters
S_DS =  1.723
S_D1 =  0.775
```

[45]:
```
# create the response spectrum plot

import matplotlib.pyplot as plt

## determine period limits first
T0 = round(0.2*S_D1/S_DS,5); print('T0 = ',T0)
TS = round(S_D1/S_DS,5); print('TS = ',TS)
```

```
TL = 8 # Long period transition period (USGS hazard tools - ATC hazard map or␣
 ↪ASCE7-16)

# design response spectrum
T = np.arange(0.,10.,0.01)
Sa = np.empty(len(T))

for i in range (0,len(T)):
    if T[i] < T0:
        Sa[i] = S_DS*(0.4 + 0.6*(T[i]/T0))
    elif T[i] >= T0 and T[i] < TS:
        Sa[i] = S_DS
    elif T[i] > TS and T[i] <= TL:
        Sa[i] = S_D1/T[i]
    else:
        Sa[i] = S_D1*TL/(T[i]**2)

plt.plot(T,Sa)
plt.xlim([0,10])
plt.xlabel('Period (sec)')
plt.ylabel('Spectral Acceleration Sa (g)')
plt.title('Design Response Spectrum');
```

```
T0 =  0.08996
TS =  0.4498
```

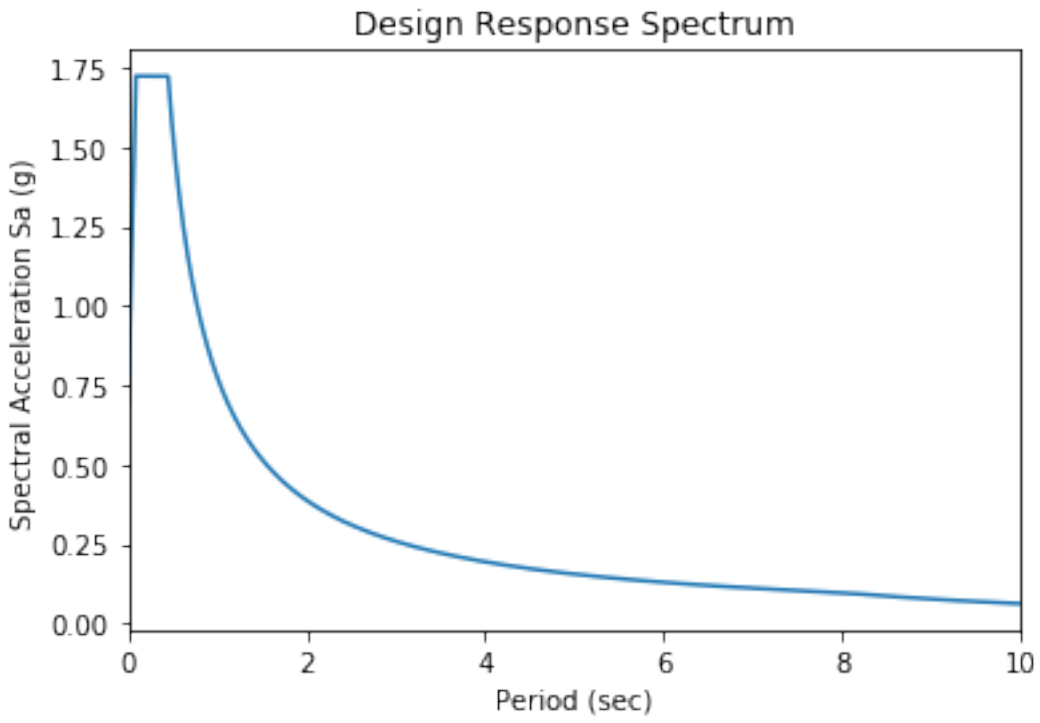

[6]:
```
# Determine seismic design category (section 11.6 - ASCE 7-16)
I = 1.0 # importance factor
# Risk Category II buildings with S1 >= 0.75 -> Seismic Design Category E

# Structural system design parameters (table 12.2-1 - ASCE 7-16)
# system: Special RC moment frame
# requirement sections: 12.2.5.5 and 14.2
R = 8 # response modification factor
omega = 3 # overstrength factor
Cd = 5.5 # deflection amplification factor

# Allowable interstory drift limit
delta_a = 0.02

# no torsional irregularity
# It is assumed (and will be verified later) that no soft/weak story␣
 ↪irregularity exists.
# Assumed redundancy factor
rho = 1.0

# write the scaled design response spectrum for MRSA
file1 = open(r'RS.txt','w+')
for i in range(0,len(T)):
    file1.write(str(round(T[i],2))+'     '+str(round(Sa[i]/(R/I),3))+'\n')
file1.close()
```

1.2 2. Determination of Seismic Forces

Assumptions: - Because the building is symmetric in configuration, no horizontal irregularities of the types listed in table 12.3-1 exist; therefore, the building is modeled using a 2D representation - For the purpose of determining the diaphragm flexibility, the span of the diahphragm should be considered as the distance between the lateral-load resisting elements. In this case, the span-to-depth ratio of the diagphram is 1.0; therefore, a rigid diaphragm assumption is permitted.

[7]:
```
# Preliminary member sizing
# To determine preliminary sizes, analyze the building using approximate␣
 ↪analysis methods under the appropriate
# combinations of dead, live and seismic loads
# This is actually not necessary, but I just like doing it the way Amit Kanvinde␣
 ↪taught me for steel design

# Compute dead and live loads
perimeter = (Wbayx*Nbayx + Wbayy*Nbayy)*2;
Area = Nbayx*Wbayx * Nbayy*Wbayy;
```

```
## dead loads
DL_slab = tslab*rcdensity;

#compute cladding weight (which is actually on the perimeter only but will be␣
 ↪distributed to floor)
clad_surf = 10*psf; # weight of vertical cladding
# assume the cladding is supported at all floors - assign tributary area loads
clad_load = clad_surf*Hcol*perimeter;
clad_load1 = clad_surf*(Hcol1 + Hcol)/2*perimeter; #first floor
clad_loadr = clad_surf*(Hcol/2)*perimeter; #roof

# Now distribute to floor area
clad = clad_load/Area
clad1 = clad_load1/Area
cladr = clad_loadr/Area

# Other superimposed dead loads
partition = 10*psf
roof = 10*psf
ceil = 10*psf

# Total distributed superimposed loads
DL_imp = clad + partition + ceil; # typical floor
DL_imp1 = clad1 + partition + ceil; # first floor
DL_impr = cladr + roof + ceil; #roof
print('Slab imposed dead loads in kip/inch^2 - typical floor = ',DL_imp)
print('Slab imposed dead loads in kip/inch^2 - first floor = ',DL_imp1)
print('Slab imposed dead loads in kip/inch^2 - roof floor = ',DL_impr)

# Total distributed dead loads
DL = DL_slab + DL_imp; # typical floor
DL_1 = DL_slab + DL_imp1; # first floor
DL_r = DL_slab + DL_impr; #roof

# Beam self weight
DL_beamwt = hbeam*bbeam*rcdensity;

#Live loads
LL = 50*psf; # Office building occupancy level
LL_r = 20*psf; # roof
print('Slab live loads in kip/inch^2 - typical floor = ',LL)
print('Slab live loads in kip/inch^2 - roof floor = ',LL_r)

# Reduction is permitted for  live loads but will be ignored for now
```

```
Slab imposed dead loads in kip/inch^2 - typical floor =  0.0001840277777777778
Slab imposed dead loads in kip/inch^2 - first floor =  0.00019270833333333336
```

```
Slab imposed dead loads in kip/inch^2 - roof floor =  0.00016145833333333333
Slab live loads in kip/inch^2 - typical floor =  0.00034722222222222224
Slab live loads in kip/inch^2 - roof floor =  0.0001388888888888889
```

[8]:
```
# Compute loads on typical frame beams
## A two-way slab is used, so triangular slab tributary areas on beams are␣
 ↪appropropriate, but for simplicity,
## rectangular loads are used in liu of triangular slab loads

#############################################################################
# INTERIOR OR EXTERIOR FRAME?
Ext_fac = 1.0; # for interior frame, Ext_fac = 1.0; for exterior frame, Ext_fac␣
 ↪= 0.5;
#############################################################################

# Beam dead loads
## "redistribute slab loads"
#beam_TA = Ext_fac*2*(Wbayx*Wbayy)/4; # tributary area for beam (note: only use␣
 ↪this if creating 3D model)
beam_TA = Ext_fac*Wbayx*Wbayy; # tributary area for beam (note: only works if␣
 ↪the slab is square)
DL_beam1 = DL_1*beam_TA/Lbeam; #beam distributed dead load at first floor␣
 ↪(heavier than other floors)
DL_beam = DL*beam_TA/Lbeam; #beam distributed dead load at typical floor
DL_beamr = DL_r*beam_TA/Lbeam; #beam distributed dead load at roof level

print('For the analysis model:')
print('Total slab and superimposed DL on the first floor beam = ',DL_beam1,' kip/
 ↪in')
print('Total slab and superimposed DL on a typical floor beam = ',DL_beam,' kip/
 ↪in')
print('Total slab and superimposed DL on the roof beam = ',DL_beamr,' kip/in')

# total dead load on first floor beam (due to slab and self loads)
DL_beam1_tot = DL_beam1 + DL_beamwt;

# Beam live loads
LL_beam = LL*beam_TA/Lbeam; #beam distributed live load at first floor
LL_beamr = LL_r*beam_TA/Lbeam; #beam distributed live load at roof level
print('Total slab LL on a typical beam = ',LL_beam,' kip/in')
print('Total slab LL on the roof beam = ',LL_beamr,' kip/in')

print('For the manual analysis:')
print('Analyze a typical frame with the following distributed loads on the beams:
 ↪ ')
print('DL = ',DL_beam1_tot*12,' kips/ft')
print('LL = ',LL_beam*12,' kips/ft')
```

```
# Compute loads on columns
## use column tributary areas
col_TA = Ext_fac*Wbayx*Wbayy; # Tributary area for an interior column

DL_col = DL*col_TA; # DL for a typical column from a single floor
DL_col1 = DL_1*col_TA; # DL for the first floor column from a single floor
DL_colr = DL_r*col_TA; # DL for the roof column from the roof only

# self weight of beam on one column at one floor
DL_col_beamwt = DL_beamwt*Lbeam/2*2;

# Column self weight - distributed
DL_colwt = bcol*dcol*rcdensity;
#total self weight at first floor level
DL_colwt_tot = DL_colwt*Hbuilding;

# total DL on the first floor column
DL_col_tot = DL_col*(Nstory - 2) + DL_col1 + DL_colr + DL_colwt_tot +␣
 ↪DL_col_beamwt*Nstory;

# live loads on column
LL_col = LL*col_TA; # DL for a typical column from a single floor
LL_colr = LL_r*col_TA; # DL for the roof column from the roof

# total LL on the first floor column
LL_col_tot = LL_col*(Nstory - 1) + LL_colr;

print('Axial loads on an interior first floor column: ')
print('DL = ',DL_col_tot,' kips')
print('LL = ',LL_col_tot,' kips')
```

```
For the analysis model:
Total slab and superimposed DL on the first floor beam =  0.21291666666666667
kip/in
Total slab and superimposed DL on a typical floor beam =  0.21083333333333337
kip/in
Total slab and superimposed DL on the roof beam =  0.2054166666666667  kip/in
Total slab LL on a typical beam =  0.08333333333333333  kip/in
Total slab LL on the roof beam =  0.03333333333333333  kip/in
For the manual analysis:
Analyze a typical frame with the following distributed loads on the beams:
DL =  3.18  kips/ft
LL =  1.0  kips/ft
Axial loads on an interior first floor column:
DL =  907.3375000000001  kips
LL =  228.0  kips
```

[9]:
```
# Beam moments
# Note: getting the moments is easily programmable, but the whole point of␣
 ↪preliminary sizing is to make sure you are able to
# do quick manual checks when needed, so chop chop
# In this case, we are assuming the beam inflection points are at 0.1 L from␣
 ↪each joint (half way between fixed and simply
# supported)
print('Manual Analysis results:')
M_DL_pos_manual = 0.08*DL_beam1_tot*Lbeam**2; print('Beam maximum positive␣
 ↪moment due to DL = ',M_DL_pos_manual/12, 'kip.ft')
M_DL_neg_manual = -0.045*DL_beam1_tot*Lbeam**2; print('Beam maximum negative␣
 ↪moment due to DL = ',M_DL_neg_manual/12, 'kip.ft')

M_LL_pos_manual = 0.08*LL_beam*Lbeam**2; print('Beam maximum positive moment due␣
 ↪to LL = ',M_LL_pos_manual/12, 'kip.ft')
M_LL_neg_manual = -0.045*LL_beam*Lbeam**2; print('Beam maximum negative moment␣
 ↪due to LL = ',M_LL_neg_manual/12, 'kip.ft')
```

```
Manual Analysis results:
Beam maximum positive moment due to DL =  101.76 kip.ft
Beam maximum negative moment due to DL =  -57.24 kip.ft
Beam maximum positive moment due to LL =  32.0 kip.ft
Beam maximum negative moment due to LL =  -18.0 kip.ft
```

[10]:
```
# SAP2000 model results - 2D analysis
# Note: the model has rigid offsets
# first floor beam

print('2D SAP model analysis results:')
M_DL_pos = 645.99; print('Beam maximum positive moment due to DL = ',M_DL_pos/
 ↪12, 'kip.ft')
M_DL_neg = -829.16; print('Beam maximum negative moment due to DL = ',M_DL_neg/
 ↪12, 'kip.ft')

M_LL_pos = 202.94; print('Beam maximum positive moment due to LL = ',M_LL_pos/
 ↪12, 'kip.ft')
M_LL_neg = -260.61; print('Beam maximum negative moment due to LL = ',M_LL_neg/
 ↪12, 'kip.ft')

# SAP2000 model results - 3D analysis
# Note: the model has rigid offsets
# first floor beam

print('3D SAP model analysis results:')
M_DL_pos = 416.2; print('Beam maximum positive moment due to DL = ',M_DL_pos/12,␣
 ↪'kip.ft')
```

```
M_DL_neg = -482.0; print('Beam maximum negative moment due to DL = ',M_DL_neg/
 ↪12, 'kip.ft')

M_LL_pos = 127.9; print('Beam maximum positive moment due to LL = ',M_LL_pos/12,␣
 ↪'kip.ft')
M_LL_neg = -138.5; print('Beam maximum negative moment due to LL = ',M_LL_neg/
 ↪12, 'kip.ft')

# Note that the analysis results from a 3d analysis are almost half those of the␣
 ↪2d analysis, which is to be expected because
# the beam tributary loads in the 2D analysis were doubled.
```

```
2D SAP model analysis results:
Beam maximum positive moment due to DL =  53.8325 kip.ft
Beam maximum negative moment due to DL =  -69.09666666666666 kip.ft
Beam maximum positive moment due to LL =  16.911666666666665 kip.ft
Beam maximum negative moment due to LL =  -21.7175 kip.ft
3D SAP model analysis results:
Beam maximum positive moment due to DL =  34.68333333333333 kip.ft
Beam maximum negative moment due to DL =  -40.166666666666664 kip.ft
Beam maximum positive moment due to LL =  10.658333333333333 kip.ft
Beam maximum negative moment due to LL =  -11.541666666666666 kip.ft
```

[11]:
```
# compute building weight

# find the total length of all beams per floor
Lbeamx = (Nbayy + 1) * Wbayx * Nbayx;
Lbeamy = (Nbayx + 1) * Wbayy * Nbayy;

##########################################

# Compute total loads
Wslab = tslab*Area*rcdensity;

Wimp = DL_imp*Area;
Wimp1 = DL_imp1*Area;
Wimp_roof = DL_impr*Area;

Wbeams = (Lbeamx + Lbeamy)* bbeam * hbeam * rcdensity;

Wcols = Hcol*bcol*dcol*rcdensity*Ncol;
Wcols1 = (Hcol1 + Hcol)/2*bcol*dcol*rcdensity*Ncol;
Wcolsr = (Hcol/2)*bcol*dcol*rcdensity*Ncol;

# Floor weights
floorWt = Wslab + Wimp + Wbeams + Wcols; print('Typical floor weight = ',floorWt)
```

```
floorWt1 = Wslab + Wimp1 + Wbeams + Wcols1; print('First floor weight =␣
 ↪',floorWt1)
floorWtr = Wslab + Wimp_roof + Wbeams + Wcolsr; print('Roof weight = ',floorWtr)

W_seismic = floorWt*(Nstory - 2) + floorWt1 + floorWtr; print('Total seismic␣
 ↪weight = ',W_seismic,'\n')

# Divide the seismic weight over the number of frames resisting the seismic load␣
 ↪in each direction
print('Number of frames resisting the seismic force = ',Nframe)
W_frame_story = floorWt/Nframe; print('Typical floor weight on each frame =␣
 ↪',W_frame_story)
W_frame_story1 = floorWt1/Nframe; print('First floor weight on each frame =␣
 ↪',W_frame_story1)
W_frame_roof = floorWtr/Nframe; print('roof floor weight on each frame =␣
 ↪',W_frame_roof)
W_frame = W_seismic/Nframe;  print('Total seismic weight on each frame =␣
 ↪',W_frame,'\n')

# Compute floor and nodal masses for the analysis model
m_frame_story = W_frame_story/g; print('Typical floor mass per seismic frame =␣
 ↪',m_frame_story)
m_frame_story1 = W_frame_story1/g; print('First floor mass per seismic frame =␣
 ↪',m_frame_story1)
m_frame_roof = W_frame_roof/g; print('roof mass per seismic frame =␣
 ↪',m_frame_story,'\n')

Nnodes = Nbayx + 1;
m_node = m_frame_story/Nnodes; print('Typical floor nodal mass = ',m_node)
m_node1 = m_frame_story1/Nnodes; print('First floor nodal mass = ',m_node1)
m_noder = m_frame_roof/Nnodes; print('roof floor nodal mass = ',m_noder)
```

```
Typical floor weight =  1614.2875
First floor weight =  1680.88125
Roof weight =  1441.14375
Total seismic weight =  19264.899999999998

Number of frames resisting the seismic force =  5
Typical floor weight on each frame =  322.85749999999996
First floor weight on each frame =  336.17625
roof floor weight on each frame =  288.22875
Total seismic weight on each frame =  3852.9799999999996

Typical floor mass per seismic frame =  0.836201761201761
First floor mass per seismic frame =  0.870697358197358
roof mass per seismic frame =  0.836201761201761
```

```
Typical floor nodal mass =  0.16724035224035222
First floor nodal mass =  0.1741394716394716
roof floor nodal mass =  0.1493026418026418
```

Estimate the building period
$T_{approx} = C_t h^x$
where h is the structural height and C_t and x can be determined from table 12.8-2

[12]:
```
# Estimate the building period

Ct = 0.016; # Table 12.8-2
x = 0.9; # Table 12.8-2

# Compute the coefficient for upper limit on calculated period
Cu_val = [1.7,1.6,1.5,1.4]
SD1_lim = [0.1,0.15,0.2,0.3]
slopes = np.empty(len(Cu_val)-1)

for i in range(0,len(Cu_val)-1):
    slopes[i] = (Cu_val[i+1] - Cu_val[i]) / (SD1_lim[i+1] - SD1_lim[i]);

if S_D1 <= SD1_lim[0]:
    Cu = Cu_val[0]
elif S_D1 <= SD1_lim[1]:
    Cu = Cu_val[0] + slopes[0]*(S_D1 - SD1_lim[0])
elif S_D1 <= SD1_lim[2]:
    Cu = Cu_val[1] + slopes[1]*(S_D1 - SD1_lim[1])
elif S_D1 <= SD1_lim[3]:
    Cu = Cu_val[2] + slopes[2]*(S_D1 - SD1_lim[2])
elif S_D1 > SD1_lim[3]:
    Cu = Cu_val[3]

print('The coefficient for upper limit on calculated period Cu = ',Cu)

height = ((Nstory - 1)*Hcol + Hcol1)/ft; #in feet

T_app = Ct*height**x; print('The approximate building period = ',T_app)
T_max = Cu*T_app; print('The maximum allowed building period for design = ',␣
 ↪T_max)
```

```
The coefficient for upper limit on calculated period Cu =  1.4
The approximate building period =  1.549755802497669
The maximum allowed building period for design =  2.1696581234967365
```

[13]:
```
# After running modal analysis using the SAP2000 model, the following period was␣
 ↪obtained for the frame
T_model = 1.97;
```

```
# for the purpose of computing the seismic forces, T should not exceed T_max
if T_model > T_max:
    T1 = T_max
else:
    T1 = T_model
print('The building period for the purpose of computing the seimic forces = ',T1)

# Permitted analysis procedure
T_cond = 3.5*TS;

if T_model >= T_cond:
    print('Building period T > 3.5 Ts')
# because the building height > 160 ft and T > 3.5 Ts, ELF cannot be used as the␣
 ↪analysis procedure for design, and Modal
# Response Spectrum Analysis is required.
```

```
The building period for the purpose of computing the seimic forces =  1.97
Building period T > 3.5 Ts
```

Note: two different approaches for application of masses were used 1. The nodal masses computed here were distributed to floor nodes, all elements were assigned a zero-mass modifier,and the mass source was defined from the element masses and additional masses. 2. The mass source was defined from the dead load case with a factor = 1. This case includes all dead loads, inlcuding self weight of members

Both approaches result in very similar frame periods - it should be noted that the second approach cannot be used if not all frames are seismic load resisting frames; i.e. if the seismic mass inlcudes additional gravity frames

[14]:
```
# calculation of the seismic response coefficient
Cs = S_DS/(R/I); # The ASCE guide states that this is applicable when T <= Ts

if T1<=TL:
    Cs_max = S_D1/(T1*R/I)
elif T1>TL:
    Cs_max = S_D1*TL/(T1**2*R/I)

Cs_min1 = max(0.044*S_DS*I,0.01)

if S1 >= 0.6:
    Cs_min2 = 0.5*S1/(R/I) # accounts for near-field effects

Cs_min3 = 0.01;

if Cs> Cs_max:
    Cs = Cs_max

if Cs < Cs_min1:
    Cs = Cs_min1
```

```
if Cs < Cs_min2:
    Cs = Cs_min2

if Cs < Cs_min3:
    Cs = Cs_min3

print('The seismic response coefficient Cs = ',round(Cs,5))
print('The seismic response coefficient for scaling drifts = ',round(Cs_min2,3))
```

```
The seismic response coefficient Cs =  0.07581
The seismic response coefficient for scaling drifts =  0.052
```

1.3 3. Equivalent Lateral Force Analysis

[15]:
```
# ELF calculations
V = Cs*W_seismic; #get the base shear for the whole building (3D analysis)
print('Design base shear V = ',V)

# Vertical distribution of seismic forces

# compute the distribution factor k
perlim = [0.5,2.5];
klim = [1.0,2.0];

if T1 <= perlim[0]:
    k = klim[0];
elif T1 > perlim[0] and T1 < perlim[1]:
    slope = (klim[1]-klim[0])/(perlim[1] - perlim[0]);
    k = klim[0] + slope*(T1 - perlim[0]);
elif T1 >= 2.5:
    k = 2.0;

print('coefficient k = ',round(k,2))

# Compute the lateral forces
# Compute story heights
h_story = np.empty(Nstory)
h_story[0] = Hcol1

for n in range(1,Nstory):
    h_story[n] = h_story[n-1] + Hcol;
#print(h_story)

# Prepare all floor weights (for a single frame)
w_story = np.empty(Nstory)
for n in range(0,Nstory):
```

```
    if n == 0:
        w_story[n] = W_frame_story1
    elif n == Nstory-1:
        w_story[n] = W_frame_roof
    else:
        w_story[n] = W_frame_story

# Compute the sum wihi
sum_wihi = 0.0;
for n in range(0,Nstory):
    sum_wihi = sum_wihi + w_story[n]*h_story[n]

# compute load factors and loads
Cvx = np.empty(Nstory)
Fx = np.empty(Nstory)
Vx = np.empty(Nstory)
Mx = np.empty(Nstory)

print('ELF forces:')
for n in range(0,Nstory):
    Cvx[n] = w_story[n]*h_story[n]/sum_wihi
    Fx[n] = Cvx[n]*V # lateral force at each building level
    print('The lateral force at level ',n+1,' = ',round(Fx[n],2))


# compute the story shears and overturning moments
for n in range(0,Nstory):
    Vx[n] = sum(Fx[n:])
    Mx[n] = 0.0
    for i in range(n,Nstory):
        Mx[n] = Mx[n] + Fx[i]*(h_story[i] - h_story[n])
    #print(Mx[n])
print('Story shears in kips are: ',[round(i,2) for i in Vx])

Mx_base = 0.0;
for i in range(0,Nstory):
    Mx_base += Fx[i]*h_story[i]
print('Overturning moment = ',round(Mx_base/12,2),'kip.ft')
```

```
Design base shear V =  1460.5105988
coefficient k =  1.73
ELF forces:
The lateral force at level  1  =  25.89
The lateral force at level  2  =  42.82
The lateral force at level  3  =  60.77
The lateral force at level  4  =  78.72
The lateral force at level  5  =  96.68
```

```
The lateral force at level  6  =  114.63
The lateral force at level  7  =  132.59
The lateral force at level  8  =  150.54
The lateral force at level  9  =  168.5
The lateral force at level  10  =  186.45
The lateral force at level  11  =  204.41
The lateral force at level  12  =  198.51
Story shears in kips are:  [1460.51, 1434.62, 1391.81, 1331.04, 1252.32,
1155.64, 1041.0, 908.41, 757.87, 589.37, 402.92, 198.51]
Overturning moment =  162314.9 kip.ft
```

[16]:
```
# Plot the story shears

plt.step(Vx,h_story/ft);
plt.xlabel('Story shear (kips)');
plt.ylabel('height (ft)');
plt.title('Building Story Shears');
```

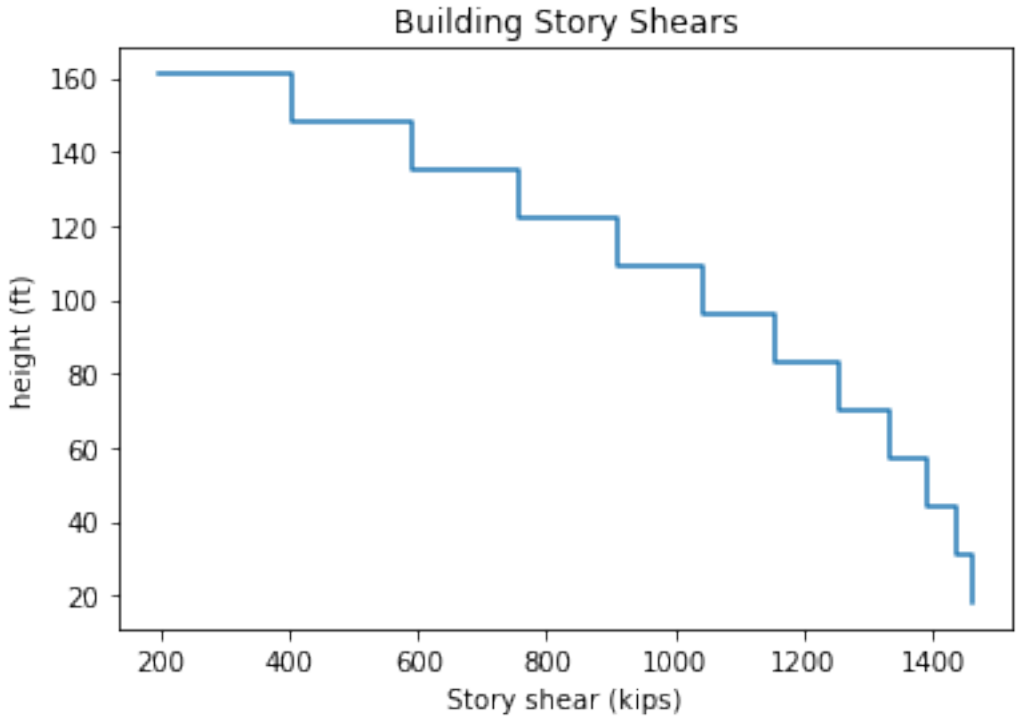

[17]:
```
# Compute moments due to lateral loads
## Using approximate portal frame analysis. Get out your pen and paper, mate

# Maximum beam moments at first floor due to seismic lateral loads
M_beam_E_manual = 561.9*kip*ft; # positive or negative, obviously
```

```
# Maximum interior column moments at first floor due to seismic lateral loads
M_col_E_manual = 657.0*kip*ft; # positive or negative, obviously
```

[18]:
```
# Results of the SAP2000 analysis model - 2D analysis
# Note: the model has rigid member offsets

# Maximum beam moments at first floor due to seismic lateral loads
M_beam_E = 364.9*kip*ft; # positive or negative, obviously

# Maximum interior column moments at first floor due to seismic lateral loads
M_col_E = 715.3*kip*ft; # positive or negative, obviously
```

Basic strength design load combination

(1) $1.2D + 1.6L$

(2) $1.2D + 0.5L \pm 1.0E$

(3) $0.9D \pm 1.0E$

Earthquake load effect
$E = \rho Q_E \pm 0.2 S_{DS} D$
The second and third load combinations become:

(2) $(1.2 + 0.2S_{DS})D + 0.5L \pm Q_E$

(3) $(0.9 - 0.2S_{DS})D \pm Q_E$

No need for seismic load combinations with overstrength

[19]:
```
# Preliminary Beam Design
def Ultimate_beam(beam,DL_pos,DL_neg,LL_pos,LL_neg,E):
    # This function determines the ultimate design load effects for beams
    # note that the positive DL and LL value is only used in load combo 1,␣
 ↪because it occurs mid-span, and the negative DL
    # and LL values are used for the other load combos because they occur at the␣
 ↪end (along with the seismic load maxima)
    Mu1 = 1.2*DL_pos + 1.6*LL_pos; # mid-span
    Mu2 = (1.2 + 0.2*S_DS)*DL_neg + 0.5*LL_neg + 1.0*E;
    Mu3 = (1.2 + 0.2*S_DS)*DL_neg + 0.5*LL_neg - 1.0*E;
    Mu4 = (0.9 - 0.2*S_DS)*DL_neg + 1.0*E;
    Mu5 = (0.9 - 0.2*S_DS)*DL_neg - 1.0*E;

    Mu_mid = Mu1; print('Utimate moment in mid span of beam',beam,' = ',Mu_mid/
 ↪12,' kip.ft')
    Mu_end_max = max(Mu2,Mu3,Mu4,Mu5); print('Maximum ultimate moment at end of␣
 ↪beam',beam,' = ',Mu_end_max/12,' kip.ft')
    Mu_end_min = min(Mu2,Mu3,Mu4,Mu5); print('Minimum ultimate moment at end of␣
 ↪beam',beam,' = ',Mu_end_min/12,' kip.ft')
    return [Mu_mid,Mu_end_max,Mu_end_min];
```

```
Ultimate_beam(1,M_DL_pos,M_DL_neg,M_LL_pos,M_LL_neg,M_beam_E)

# just fyi
print('DL factor in combinations 2 and 3 = ',1.2 + 0.2*S_DS)
print('DL factor in combinations 4 and 5 = ',0.9 - 0.2*S_DS)
```

```
Utimate moment in mid span of beam 1  =  58.673333333333325  kip.ft
Maximum ultimate moment at end of beam 1  =  342.59143333333327  kip.ft
Minimum ultimate moment at end of beam 1  =  -432.7122666666666  kip.ft
DL factor in combinations 2 and 3 =  1.5446
DL factor in combinations 4 and 5 =  0.5554
```

1.4 4. Accidental Torsion Check

[20]:
```
# Accidental torsion
# The building is symmetric so no torsional irregularity but accidental torsion␣
 ↪needs to be considered
# Acciodental torsional moment at each floor is equal to the story force␣
 ↪multiplied by 5% the story width perpendicular to
# the loading direction
tor = np.empty(Nstory);
arm = 0.05*Wbayx*Nbayx;
for i in range(0,Nstory):
    tor[i] = Fx[i]*arm

print('Accidental torsional moments in kip.ft [floors 1 through 12]:')
print(tor/12)
print('total torsional reaction should be ',sum(tor[:]))
```

```
Accidental torsional moments in kip.ft [floors 1 through 12]:
[103.54367955 171.2602738  243.0790983  314.89792279 386.71674729
 458.53557179 530.35439628 602.17322078 673.99204528 745.81086977
 817.62969427 794.04887529]
total torsional reaction should be  70104.50874240001
```

Accidental Torsion - It is unlikely that the building has a torsional irregularity, but the standard requires that an accidental torsion check be performed using a 3D model with acceidental torsion (typically in a static analysis). - Instead of applying the calculated torsional moments, the ELF forces are applied in the model with a 0.05 eccentricity. - Since the building is symmetric, the check is performed in the x-direction only. - The torsional amplification factor A_x is 1.0 for checking accidental torsion. - If no torsional irregularity exists, which is the case here, then the accidental torsion moments need not be included in the design.

Loading direction: - for design category E: columns that are part of two intersecting seismic-force resisting systems, and are subjected to seismic axial force >= 20% of the axial design strength need to be designed for 100% of the seismic force in one direction + 30% of the force in the other direction. This will be checked later.

[21]:
```
# Because the building is symmetric and the diaphragm is rigid, no twisting was␣
 ↪observed in the model when the ELF forces
# were applied with no eccentricity

# Joint displacements at edges of the building (lateral ELF forces + accidental␣
 ↪torsion)
disp1 = [0,0.494321,0.966106,1.432285,1.883094,2.310996,2.709401,3.071836,3.
 ↪39195,3.663511,3.880666,4.038851,4.140045]
disp2 = [0,0.602176,1.177589,1.745587,2.29419,2.814257,3.297819,3.737046,4.
 ↪124253,4.451884,4.712842,4.901603,5.02068]

#interstory drifts
drift1 = np.empty(Nstory)
drift2 = np.empty(Nstory)


for i in range(1,Nstory+1):
    drift1[i-1] = disp1[i] - disp1[i-1]
    drift2[i-1] = disp2[i] - disp2[i-1]

print('drifts at 1st edge = \n',drift1)
print('drifts at 2nd edge = \n',drift2)


# check for torsional irregularity
# ratio of maximum to average drifts
tor_ratio = np.empty(Nstory)
max_drift = np.empty(Nstory)
avg_drift = np.empty(Nstory)
for i in range(0,Nstory):
    avg_drift[i] = (drift1[i] + drift2[i])/2
    max_drift[i] = max(drift1[i],drift2[i])
    tor_ratio[i] = max_drift[i]/avg_drift[i]
    if tor_ratio[i] > 1.2 and tor_ratio[i] <= 1.4:
        print('TORSIONAL IRREGULARITY EXISTS')
    elif tor_ratio[i] > 1.4:
        print('EXTREME TORSIONAL IRREGULARITY EXISTS')

print('average drifts are = \n',avg_drift)
print('Ratios of maximum to average drifts are = \n',tor_ratio)
```

```
drifts at 1st edge =
 [0.494321 0.471785 0.466179 0.450809 0.427902 0.398405 0.362435 0.320114
 0.271561 0.217155 0.158185 0.101194]
drifts at 2nd edge =
 [0.602176 0.575413 0.567998 0.548603 0.520067 0.483562 0.439227 0.387207
 0.327631 0.260958 0.188761 0.119077]
```

```
average drifts are =
 [0.5482485 0.523599  0.5170885 0.499706  0.4739845 0.4409835 0.400831
 0.3536605 0.299596  0.2390565 0.173473  0.1101355]
Ratios of maximum to average drifts are =
 [1.09836324 1.09895741 1.09845413 1.09785154 1.09722364 1.0965535
 1.09579099 1.09485509 1.09357602 1.09161642 1.08812899 1.08118636]
```

1.5 5. Modal Response Spectrum Analysis

- MRSA was performed using the 3D model on SAP2000
- The number of modes required in ASCE 7-16 should be such that the combined modal mass is 100% of the structure's mass, or 90% in each orthognal direction
- In this case, all 12 modes were included in obtaining the response, which represents a little over 98% of the mass in each orthogonal direction
- The MRS analysis was applied in the x-direction only. However, for the purpose of finding the member design forces later, we will use 100% seismic loading in x direction plus 30% in y direction

[22]:
```
# Scaling of the base shear and member forces
# section 12.9.1.4 of ASCE 7-16 requires scaling of MRSA forces if they are less␣
 ↪than 100% of the calculated base shear
# using ELF procedure
V_mrsa = 855.155*kip; #base shear obtained from MRS
scalefac = V/V_mrsa;
print('The design member forces need to be scaled by ',round(scalefac,3))

# MRSA story shears (from SAP model)

Vx_mrsa = [855.168,818.826,771.853,726.917,682.459,635.756,587.354,534.118,472.
 ↪433,398.894,300.021,162.329]

Vx_design = [round(scalefac*i,1) for i in Vx_mrsa]
print('The design story shears in kips are ',Vx_design)

# ratio of design shears (scaled MRSA) to ELF shears
shear_ratios = np.empty(len(Vx))
for i in range(0,len(Vx)):
    shear_ratios[i] = round(Vx_design[i]/Vx[i],2)
print('Just fyi, the ratios of the design story shear (scaled MRSA) to the story␣
 ↪shears predicted by ELF are: \n',shear_ratios)
```

```
The design member forces need to be scaled by  1.708
The design story shears in kips are  [1460.5, 1398.5, 1318.2, 1241.5, 1165.6,
1085.8, 1003.1, 912.2, 806.9, 681.3, 512.4, 277.2]
Just fyi, the ratios of the design story shear (scaled MRSA) to the story shears
predicted by ELF are:
 [1.   0.97 0.95 0.93 0.93 0.94 0.96 1.   1.06 1.16 1.27 1.4 ]
```

1.6 6. Story Drift Checks

- One of the changes in ASCE 7-16 is scaling of the drifts taken from MRSA analysis if the base shear from MRSA is less than $C_s W$, where C_s is:

$C_s = 0.5 \frac{S_1}{R/I_e}$ (which only applies for structures located where $S_1 > 0.6g$)

- Based on that, the drifts here are scaled by $\frac{C_s W}{V_{MRSA}}$

[23]:
```
# Drift checks
#import xlrd

drift_scalefac = Cs_min2*W_seismic/V_mrsa
print('The scale factor for drift checks is ',drift_scalefac)
drift_limit = 2.0 #percent of the story height (table 12.12-1)

story_disp = [0,0.316626,0.611769,0.893471,1.156806,1.400071,1.622266,1.822174,1.
↪998215,2.148197,2.269342,2.358644,2.41615]
# these are from the SAP MRSA analysis - in the future, can read them from Excel␣
↪file directly

drift_e = np.empty(Nstory)

for i in range(1,len(story_disp)):
    drift_e[i-1] = story_disp[i] - story_disp[i-1]
print('elastic drifts = \n',[round(i,3) for i in drift_e])

# Design drifts
drift = [Cd/I*i for i in drift_e]
print('inelastic drifts = \n',[round(i,3) for i in drift])

scaled_drift = [i*drift_scalefac for i in drift]
print('design(scaled) drifts = \n',[round(i,3) for i in scaled_drift])

# now compute the drift ratios
drift_ratio = np.empty(len(drift))
for i in range(0,len(drift)):
    drift_ratio[i] = round(drift[i]/Lstory[i]*100,3)

print('Amplified drift ratios (by C_d) are \n',[round(i,3) for i in drift_ratio])

scaled_drift_ratio = [drift_scalefac*i for i in drift_ratio]
print('The interstory drift ratios (after scaling, if needed) are:␣
↪\n',[round(i,3) for i in scaled_drift_ratio])

for i in range(0,len(drift)):
    if scaled_drift_ratio[i] <= drift_limit:
        print('story',i+1,'pass')
```

```
    else:
        print('story',i+1,'fail')

plt.plot(story_disp[1:],h_story/12);
plt.plot([Cd/I*i for i in story_disp[1:]],h_story/12);
plt.legend(['Elastic','Amplified Cd = 5.5']);
plt.xlabel('Total deflection (inches)');
plt.ylabel('Height (ft)');

print('-----------------------------------------------------------------------')
# compute drifts for the ELF case (needed for P-Delta stability check)

story_disp_ELF = [0,0.5482,1.0718,1.5889,2.0886,2.5626,3.004,3.4044,3.7581,4.
 ↪0577,4.2968,4.4702,4.5804]
# these are from the SAP ELF analysis - 3D model EQ case only

drift_e_ELF = np.empty(Nstory)

for i in range(1,len(story_disp_ELF)):
    drift_e_ELF[i-1] = story_disp_ELF[i] - story_disp_ELF[i-1]
#print('elastic drifts (ELF)= \n',drift_e_ELF)

# Design drifts
drift_ELF = [Cd/I*i for i in drift_e_ELF]
print('inelastic drifts (ELF) = \n',[round(i,3) for i in drift_ELF])
```

```
The scale factor for drift checks is  1.1686380685372826
elastic drifts =
 [0.317, 0.295, 0.282, 0.263, 0.243, 0.222, 0.2, 0.176, 0.15, 0.121, 0.089,
0.058]
inelastic drifts =
 [1.741, 1.623, 1.549, 1.448, 1.338, 1.222, 1.099, 0.968, 0.825, 0.666, 0.491,
0.316]
design(scaled) drifts =
 [2.035, 1.897, 1.811, 1.693, 1.564, 1.428, 1.285, 1.132, 0.964, 0.779, 0.574,
0.37]
Amplified drift ratios (by C_d) are
 [0.806, 1.041, 0.993, 0.928, 0.858, 0.783, 0.705, 0.621, 0.529, 0.427, 0.315,
0.203]
The interstory drift ratios (after scaling, if needed) are:
 [0.942, 1.217, 1.16, 1.084, 1.003, 0.915, 0.824, 0.726, 0.618, 0.499, 0.368,
0.237]
story 1 pass
story 2 pass
story 3 pass
story 4 pass
story 5 pass
```

```
story 6 pass
story 7 pass
story 8 pass
story 9 pass
story 10 pass
story 11 pass
story 12 pass
-----------------------------------------------------------------
inelastic drifts (ELF) =
 [3.015, 2.88, 2.844, 2.748, 2.607, 2.428, 2.202, 1.945, 1.648, 1.315, 0.954,
0.606]
```

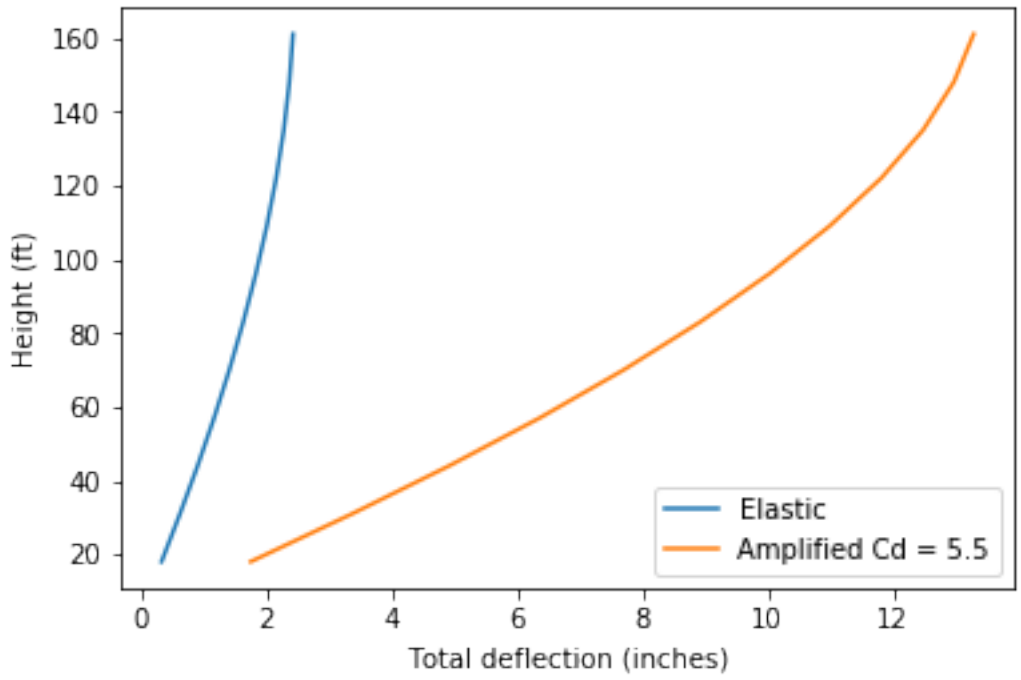

1.7 7. Soft Story Irregularity Check

- Having a soft-story irregularity will not impact the design because we are using MRSA for design anyway. Having an extreme soft-story irregularity is prohibited in Seismic Design Category E.
- Vertical structural irregularities types 1a, 1b or 2 (table 12.3-) do not apply when no story drift ratio under design lateral load is greater than 130% of the drift ratio of the next story above. The drift ratio between the top two stories is not required to be evaluated.

[24]:
```
ratio_story_above = np.empty(Nstory - 2)
for i in range(0,Nstory-2):
    ratio_story_above[i] = drift_ratio[i]/drift_ratio[i+1]
```

```
    if ratio_story_above[i] > 1.3:
        print('A story stiffness check needs to be performed to check for␣
 ↪vertical soft-story irregularity')
print('ratios between the interstory drift of each story to the story above␣
 ↪(except last two): \n',\
      [round(i,3) for i in ratio_story_above])
```

```
A story stiffness check needs to be performed to check for vertical soft-story
irregularity
ratios between the interstory drift of each story to the story above (except
last two):
 [0.774, 1.048, 1.07, 1.082, 1.096, 1.111, 1.135, 1.174, 1.239, 1.356]
```

- Note: even though the ratio at the 11th floor exceeds 1.3, a stiffness-check is not really needed because the presence of a 1a soft story irregularity will not impact the design (because we are already using MRSA). Based on the current value of of the ratio at 11th floor, it is highly unlikely that a 1b extreme soft-story irregularity exists.
- However, the stiffness check is performed anyway. This check was performed on SAP2000 by applying equal and opposite lateral forces to the top and bottom of each story, and determining the stiffness by dividing the force over the interstory drift.
- The soft-story irregularity check was performed for a 2D model and will not be repeated with a 3D model

[25]:
```
# Story stiffness check
# story drifts from each individual analysis on SAP (NOT THE SAME ANALYSIS)
soft_check_dr = [0.2202 - 0.0925, 0.1985 - 0.085, 0.1947 - 0.0824, 0.1924 - 0.
 ↪0804, 0.1905 - 0.0787, 0.1887 - 0.0771,\
                0.1871 - 0.0758, 0.1857 - 0.0745, 0.1839 - 0.073, 0.1805 - 0.
 ↪0697, 0.1705 - 0.0591, 0.1462 - 0.0 ]
lateral_force = 100.0;
story_stiffness = [lateral_force/i for i in soft_check_dr]

story_stiffness_ratio = np.empty(len(story_stiffness)-1)
story_stiffness_ratio_avg = np.empty(len(story_stiffness)-3)
for i in range(0,len(story_stiffness)-1):
    story_stiffness_ratio[i] = story_stiffness[i]/story_stiffness[i+1]
    if story_stiffness_ratio[i] < 0.7 and story_stiffness_ratio[i] > 0.6:
        print('A soft story irregularity exists...')
    elif story_stiffness_ratio[i] < 0.6:
        print('OH NO an extreme soft story irregularity exists...')

for i in range(0,len(story_stiffness)-3):
    story_stiffness_ratio_avg[i] = story_stiffness[i]/((story_stiffness[i+1] +␣
 ↪story_stiffness[i+2] + story_stiffness[i+3])/3)
    if story_stiffness_ratio_avg[i] < 0.8 and story_stiffness_ratio[i] > 0.7:
        print('A soft story irregularity exists...')
    elif story_stiffness_ratio[i] < 0.7:
```

```
        print('OH NO an extreme soft story irregularity exists...')

print('The ratios of each story stiffness to the story above: \n',[round(i,3)␣
 ↪for i in story_stiffness_ratio])
print('The ratios of each story stiffness to the average of the three stories␣
 ↪above: \n',\
      [round(i,3) for i in story_stiffness_ratio_avg])
```

```
The ratios of each story stiffness to the story above:
 [0.889, 0.989, 0.997, 0.998, 0.998, 0.997, 0.999, 0.997, 0.999, 1.005, 1.312]
The ratios of each story stiffness to the average of the three stories above:
 [0.882, 0.987, 0.996, 0.996, 0.996, 0.996, 0.997, 0.998, 1.089]
```

1.8 8. P-Delta Stability Check

- P-Delta effects need not be considered in the analysis if the stability coefficient for each floor is less than the maximum allowed stability coefficient.
- ASCE 7-16 requires that P-Delta stability check be performed using ELF forces

[26]:
```
# maximum stability coefficient
theta_max1 = 0.1
theta_max2 = min(0.5/(1.*Cd),0.25)
theta_max = min(theta_max1,theta_max2)
print('The limit on the stability coefficient is :',round(theta_max,4))


DL_story = np.empty(Nstory)
#DL weight on each story
for i in range(0,Nstory):
    DL_story[i] = floorWt;
    if i == 0:
        DL_story[i] = floorWt1;
    elif i == Nstory-1:
        DL_story[i] = floorWtr;

print('The dead load on each story is: ',DL_story)

LL_story = np.empty(Nstory)
#LL weight on each story
for i in range(0,Nstory):
    LL_story[i] = LL*Area;
    if i == Nstory-1:
        LL_story[i] = LL_r*Area;
print('The live load on each story is: ',LL_story)

# compute the total axial load above each story
P_story = np.empty(Nstory)
```

```
theta_story = np.empty(Nstory)
for i in range(0,Nstory):
    P_story[i] = np.sum(DL_story[i:]) + np.sum(LL_story[i:])
print('The total unfactored axial load on each story in kips is \n',P_story)

########################################################################

for i in range(0,Nstory):
    theta_story[i] = P_story[i]*drift_ELF[i]*I/(Vx[i]*Lstory[i]*Cd)
    if theta_story[i] > theta_max:
        print('P-DELTA EFFECTS NEED TO BE CONSIDERED...')

print('The stability coefficient for each story is: \n',[round(i,3) for i in␣
 ↪theta_story])

mag = [round(max(1/(1-i),1),3) for i in theta_story]

print('moment magnification for each story (IF NEEDED) is: \n',mag)
```

```
The limit on the stability coefficient is : 0.0909
The dead load on each story is:  [1680.88125 1614.2875  1614.2875  1614.2875
1614.2875  1614.2875
 1614.2875  1614.2875  1614.2875  1614.2875  1614.2875  1441.14375]
The live load on each story is:  [320. 320. 320. 320. 320. 320. 320. 320. 320.
320. 320. 128.]
The total unfactored axial load on each story in kips is
 [22912.9     20912.01875 18977.73125 17043.44375 15109.15625 13174.86875
 11240.58125  9306.29375  7372.00625  5437.71875  3503.43125  1569.14375]
The stability coefficient for each story is:
 [0.04, 0.049, 0.045, 0.041, 0.037, 0.032, 0.028, 0.023, 0.019, 0.014, 0.01,
0.006]
moment magnification for each story (IF NEEDED) is:
 [1.041, 1.051, 1.047, 1.043, 1.038, 1.033, 1.029, 1.024, 1.019, 1.014, 1.01,
1.006]
```

1.9 9. Structural Design of Frame Members

- Note: the MRSA output seismic forces are NOT the design forces. They need to be scaled by the scale factor scalefac first.
- In this case, this was worked into the model by creating load combinations with a scaled MRSA case by the scale factor (after the analysis)
- The model used for the design has 100% seismic force in x + 30% seismic force in y. The same model should probably be used for all other checks as well, but it does not matter that much.
- Beams are designed first, because the beam capacity affects the design of the column and beam-column joint

- Beam reinforcement is critical to ensure ductility (plastic hinging at the end of the beam)
- ACI 318 requires the beam width to be at least 75% of the column width to consider the beam-column joints confined.
- The design shears are based on the probable moment strength of the beam joint, as detailed in ACI 318 section 18.6.5
- The design shear strength of concrete must be taken as zero where axial force is small (less than 5% of the axial capacity) and where V_E/V_u is larger than 0.5 (V_E is the shear force due to the probable moment strength, and V_u is the ultimate design shear at the joint including the shear due to the probable moment and factored gravity loads) - concrete design shear strength is assumed to be zero for all beams.

Other beam design requirements that need to be satisfied - minimum two bars continous top and bottom - positive moment strength greater than 50% negative moment strength at a joint - minimum strength along member greater than 25% maximum strength

beam-column joint checks - the joint shear demand is computed based on the probable moment strength of the beam. - Here, the shear in the joint is computed as a function of the shear in the columm and tension/compression couple contributed by the beam moments - refer to ACI 318 section 18.7.5.4 for the required amount of transverse reinforcement in the joint

[27]:
```
# scaling factors
design_phi_conc = 0.9;
nominal_phi_conc = 1.0;
prob_phi_conc = 1.0;

design_phi_st = 1.0;
nominal_phi_st = 1.0;
prob_phi_st = 1.25;
```

1.9.1 9.1 Column Slenderness Analysis

- slenderness effects can be neglected if:

$\frac{kL}{r} <= 22$ for columns not braced against sidesway
$\frac{kL}{r} = 34 + 12(M\_1/M\_2)$ and $\frac{kl}{r} <= 40$ for columns braced against sidesway
where:

- k is the effective length factor, estimated from the Jackson and Moreland Alignment Charts (shown below)
- L is the column length
- r is the radius of gyration $r = \sqrt{\frac{I_g}{A_g}}$ or approximated as 0.3 times the dimension in the direction stability is being considered for rectangular columns.
- M_1/M_2 is the ratio between the moments at the column ends; negative if the column is in single curvature and postitive for double curvature.
- columns are considered braced against sidesway when bracing elements have a total lateral stiffness of at least 12 times the gross stiffness of the columns within the story.

If slenderness cannot be neglected: design must include second order effects in one of the following ways:

- multiply first-order moments by a moment magnifier (ACI 318-14 provides different methods for non- and sway frames in section 6.6.4)
- elastic second-order analysis, or
- inelastic second order analysis.

Note: magnified second-order moments cannot exceed 1.4 first order moments.

Here I am using a P-Delta analysis in SAP2000 3D model, because it is the simplest method. Make sure to divide the column members along their length in the model to account for member curvature second order effects.

This frame is designated as a sway frame because no walls or other lateral bracing elements are present (although ACI 318 permits columns to be designed as part of a non-sway frame if the increase in column end moments due to second-order effects does not exceed 5% of first-order end moments)

In the alignment charts, ψ_A and ψ_B represent the ratio $\sum EI/L_c$ the columns to $\sum EI/L_b$ of the beams at each end of the column. L_b and L_c are the beam and column spans measured center-line to center-line.

[28]:
```
##########################################################################################
############################## RELATIVE STIFFNESS RATIO CALCULATOR␣
 ↪#########################################
##########################################################################################
# this function is related to finding the relative stiffness ratios used for␣
 ↪evaluating column slenderness. The function
# is NOT used in the design process (the slenderness check is done manually␣
 ↪because it has a lot of nuances). However,
# you can use this function as a calculator of the stiffness factors for each␣
 ↪column individually to aid the calculations.

# IT IS ASSUMED THAT THE MODULUS OF ELASTICITY E IS THE SAME FOR BEAMS AND␣
 ↪COLUMNS
def stiffness_ratios(col_group,intorext,btm_bound,top_bound,bcol,dcol

,Lcol,bcol_top,dcol_top,Lcol_top,
                     ␣
 ↪bcol_btm,dcol_btm,Lcol_btm,bbeam,hbeam,Lbeam,I_reduction_col,I_reduction_beam):
    # col_group: group number of the column considered
    # intorext: whether the column considered is interior or exterior. options␣
 ↪are 'int' and 'ext'
    # btm_bound: the bottm bounday condition - options are 'fixed' or 'beam' (i.
 ↪e. connected to a beam)
    # top_bound: the bottm bounday condition - options are 'fixed' or 'beam' (i.
 ↪e. connected to a beam)
    # bcol,dcol,Lcol: dimensions of the column under consideration
    # bcol_top,dcol_top,Lcol_top: dimensions of the column connecting at the top␣
 ↪end
    # bcol_btm,dcol_btm,Lcol_btm: dimensions of the column connecting at the␣
 ↪bottom end (if fixed, the value does not matter)
    # bbeam,dbeam,Lbeam: dimensions of the connecting beam(s)
```

```
    # I_reduction_col,I_reduction_beam: reduction factors for the moment of␣
 ↪interia of beams and columns (already established)

    Icol = I_reduction_col*bcol*dcol**3/12
    Icol_top = I_reduction_col*bcol_top*dcol_top**3/12
    Icol_btm = I_reduction_col*bcol_btm*dcol_btm**3/12
    Ibeam = I_reduction_beam*bbeam*hbeam**3/12

    if intorext == 'int':
        nbeams = 2
    elif intorext == 'ext':
        nbeams = 1

    if btm_bound == 'fixed':
        psi_btm = 1.0
    else:
         psi_btm = (Icol_btm/Lcol_btm + Icol/Lcol)/(nbeams*Ibeam/Lbeam);

    if top_bound == 'fixed':
        psi_top = 1.0
    else:
         psi_top = (Icol_top/Lcol_top + Icol/Lcol)/(nbeams*Ibeam/Lbeam);

    print('The columns/beam stiffness ratios (psi) for column ',col_group,' top␣
 ↪and bottom are ',round(psi_top,2)\
          ,' and ',round(psi_btm,2))
    print('Look up the effective length factor k in the alignment charts...')

# for example: first floor exterior column
bcol_top = bcol
dcol_top = dcol
Hcol_top = Hcol
bcol_btm = 0; # fixed
dcol_btm = 0
Hcol_btm = 0
stiffness_ratios(1,'ext','fixed','beam',bcol,dcol,Hcol1,bcol_top,dcol_top,Hcol_top,
                 ␣
 ↪bcol_btm,dcol_btm,Hcol_btm,bbeam,hbeam,Lbeam,I_reduction_col,I_reduction_beam)
```

```
The columns/beam stiffness ratios (psi) for column  1  top and bottom are  6.62
and  1.0
Look up the effective length factor k in the alignment charts...
```

1.9.2 9.2 Member forces

9.2.1 Column design actions

[29]:
```
# The structural members are grouped into three different designs for beams, and␣
 ↪three different designs for columns

floor_assign = [1,5,9] # starting floors of each column and beam group

#Column groups
col_groups = [1,2,3]
Pu_D_L = [1613.3,1061.1,519.0]
Pu_D_L_E = [1726.4,1115.2,553.3]
Pu_D_E = [581.0,389.1,196.4] #no uplift!

# first order moments
Mu_D_L_E_lin = [7880.1,4272.7,3288.0]# not used because the column design is␣
 ↪based on the beam nominal moment capacity
Mu_D_E_lin = [7872.2,4086.7,3016.8]

# second order moments (based on P-delta analysis on SAP2000)
Mu_D_L_E = [8140.5,4410.3,3291.7]# not going to be used because the column␣
 ↪design is based on the beam nominal moment capacity
Mu_D_E = [8132.9,4234.1,3044.1]

ratio1 = np.empty(len(col_groups))
ratio2 = np.empty(len(col_groups))
# check that second order moments are not more than 1.4 first order moments
for i in range(0,len(col_groups)):
    ratio1[i] = Mu_D_L_E[i]/Mu_D_L_E_lin[i]
    if ratio1[i] > 1.4:
        print("Unacceptably high P-Delta effect - REDESIGN COLUMNS OF GROUP ",i)

    ratio2[i] = Mu_D_E[i]/Mu_D_E_lin[i]
    if ratio2[i] > 1.4:
        print("Unacceptably high P-Delta effect - REDESIGN COLUMNS OF GROUP ",i)

# Column design actions
print('COLUMN DESIGN ACTIONS:\n')
Pu_max = np.empty(len(col_groups))
Pu_min = np.empty(len(col_groups))

for i in range(0,len(col_groups)):
    Pu_max[i] = max(Pu_D_L[i],Pu_D_L_E[i],Pu_D_E[i])
    Pu_min[i] = min(Pu_D_L[i],Pu_D_L_E[i],Pu_D_E[i])

print('the maximum factored axial load on each column group is',Pu_max)
print('the minimum factored axial load on each column group is',Pu_min)

# get the column design moments
```

```
print("""Note: COLUMN MOMENTS ARE BASED ON SECOND ORDER ANALYSIS ARE USED␣
 ↪BECAUSE THE ANALYSIS SHOWED THAT
SLENDERNESS EFFECTS MUST BE CONSIDERED - MEANING THAT SECOND ORDER MOMENTS NEED␣
 ↪TO BE INCLUDED""")
Mu_col = np.empty(len(col_groups))
mag_Mu_col = np.empty(len(col_groups))

for i in range(0,len(col_groups)):
    Mu_col[i] = max(Mu_D_L_E[i],Mu_D_E[i])
 #   mag_Mu_col[i] = Mu_col[i]*mag[floor_assign[i]-1]
    mag_Mu_col[i] = Mu_col[i] # this is the value used for the rest of the␣
 ↪design process - since P-Delta effects are
    # accounted for using second order analysis, no magnification is needed -␣
 ↪magnify if using first order analysis

print('Second order (or magnified) column moments are:',mag_Mu_col)
print("""the required moment capacity of the column is taken to be the maximum␣
 ↪of the strong column-weak beam
asumption moments, and second-order moments from factored loads \n""")

print("ratio of second to first order column moments are (D + L + E):
 ↪",[round(i,3) for i in ratio1])
print("ratio of second to first order column moments are (D + E):",[round(i,3)␣
 ↪for i in ratio2])
```

```
COLUMN DESIGN ACTIONS:

the maximum factored axial load on each column group is [1726.4 1115.2  553.3]
the minimum factored axial load on each column group is [581.  389.1 196.4]
Note: COLUMN MOMENTS ARE BASED ON SECOND ORDER ANALYSIS ARE USED BECAUSE THE
ANALYSIS SHOWED THAT
SLENDERNESS EFFECTS MUST BE CONSIDERED - MEANING THAT SECOND ORDER MOMENTS NEED
TO BE INCLUDED
Second order (or magnified) column moments are: [8140.5 4410.3 3291.7]
the required moment capacity of the column is taken to be the maximum of the
strong column-weak beam
asumption moments, and second-order moments from factored loads

ratio of second to first order column moments are (D + L + E): [1.033, 1.032,
1.001]
ratio of second to first order column moments are (D + E): [1.033, 1.036, 1.009]
```

9.2.2 Beam design actions

[30]:
```
#Beam groups
beam_groups = [1,2,3]
```

```
# first order moments:
# Mid-span maxima
Mu_D_L_mid = [704.0,676.8,670.9]
Mu_D_L_E_mid_lin = [855.5,770.4,730.1]

# end-span maxima
Mu_D_L_E_end_pos_lin = [2874.3,2293.6,1441.3]
Mu_D_L_E_end_neg_lin = [-4147.4,-3693.7,-2886.3]
Mu_D_E_end_pos_lin = [3254.4,2496.0,1573.0]
Mu_D_E_end_neg_lin = [-3637.0,-2918.2,-2008.1]

#shears
V_G_design_lin = [27.1,28.7,29.7] # shear due to factored gravity load (with the␣
 ↪seismic combo factors - (load combo 2))

##############################################################################
# second order moments:
# Mid-span maxima
Mu_D_L_E_mid = [865.3,785.2,746.7]

# end-span maxima
Mu_D_L_E_end_pos = [3050.2,2374.5,1443.9]
Mu_D_L_E_end_neg = [-4317.5,-3800.0,-2928.0]
Mu_D_E_end_pos = [3430.0,2620.6,1575.6]
Mu_D_E_end_neg = [-3812.2,-3000.9,-2039.1]

#shears
V_G_design = [27.5,29.5,30.6] # shear due to factored gravity load (with the␣
 ↪seismic combo factors - (load combo 2))

print('BEAM DESIGN ACTIONS:\n')
#Beam design moments and shears
Mu_mid = np.empty(len(beam_groups))
Mu_end_pos = np.empty(len(beam_groups))
Mu_end_neg = np.empty(len(beam_groups))
Vu = np.empty(len(beam_groups))

for i in range(0,len(beam_groups)):
    Mu_mid[i] = max(Mu_D_L_mid[i],Mu_D_L_E_mid[i])
    Mu_end_neg[i] = min(Mu_D_L_E_end_neg[i],Mu_D_E_end_neg[i])
    Mu_end_pos[i] = max(Mu_D_L_E_end_pos[i],Mu_D_E_end_pos[i])
    #Vu[i] = max(Vu_D_L_E[i],Vu_D_E[i])

#print('The design mid-span moments are: ',Mu_mid)
print('The design end-span negative moments are: ',Mu_end_neg)
print('The design end-span positive moments are: ',Mu_end_pos)
#print('The design shears are: ',Vu)
```

```
BEAM DESIGN ACTIONS:

The design end-span negative moments are:  [-4317.5 -3800.  -2928. ]
The design end-span positive moments are:  [3430.  2620.6 1575.6]
```

1.9.3 9.3 Beam Design Functions

9.3.1 Compute beam effective depth

[31]:
```
def effective_depth(h,ccover,phi_t,phi_l):
    # Because the beams are spanning two orthogonal directions, the effective␣
 ↪depth is different for each direction
    d_EW = h - ccover - phi_t - phi_l/2;
    d_NS = h - ccover - phi_t - phi_l - phi_l/2;
    d = d_NS # conservatively
    return d
    # if you change this assumption here, it will change everywhere!
```

9.3.2 Compute T-beam effective width

[32]:
```
def T_beam_flange(int_or_ext,bbeam,Lbeam,tslab):
    if int_or_ext == 'int':
        # Effective T-beam width for positive moment (ACI 318 6.3.2)
        # interior
        b_tbeam_int1 = 8*tslab;
        clear_span = Lbeam - bbeam
        b_tbeam_int2 = clear_span/2; # modify this for non-symmetric geometry
        b_tbeam_int3 = clear_span/8;
        b_tbeam_int = min(b_tbeam_int1,b_tbeam_int2,b_tbeam_int3)

        bf = bbeam + 2*b_tbeam_int; # Effective T-beam width for positive moment␣
 ↪for an interior beam
    elif int_or_ext == 'ext':
        # exterior (one side of web)
        b_tbeam_ext1 = 6*tslab;
        b_tbeam_ext2 = clear_span/2; # modify this for non-symmetric geometry
        b_tbeam_ext3 = clear_span/12;
        b_tbeam_ext = min(b_tbeam_ext1,b_tbeam_ext2,b_tbeam_ext3)

        bf = bbeam + b_tbeam_ext; # Effective T-beam width for positive moment␣
 ↪for an extrerior beam
    return bf
```

9.3.3 Compute the nominal capacity of a beam section

[33]:
```
# FLEXURAL REINFORCEMENT FUNCTION
import math
def beam_Mn(beam,Mu,nbar,phi_l,phi_t,b,h,ccover):
```

```
    # compute the nominal strength of a beam
    d = effective_depth(h,ccover,phi_t,phi_l)
    Abar_l = math.pi*phi_l**2/4
    As = nbar*Abar_l;
    # depth of compression block
    a = As*fy/(0.85*fc*b)
    #nominal strength
    Mn = As*fy*(d - a/2)

    return Mn
```

9.3.4 Design beam flexural reinforcement

[34]:
```
# FLEXURAL REINFORCEMENT FUNCTION
import math
def beam_reinf(beam,Mu,nbar,phi_l,phi_t,b,h,ccover,bbeam):
    # compute the nominal, design and probable strength of a beam
    # for positive moments, the beam will be designed as  a T-beam -> width of␣
 ↪beam will include the allowed slab flage width
    # the probable strength will include the slab reinforcement outside the beam␣
 ↪width
    # the slab is assumed to be reinforced with minimum reinforcement = 0.002

    d = effective_depth(h,ccover,phi_t,phi_l)
    Abar_l = math.pi*phi_l**2/4;
    As = nbar*Abar_l;

    # Minimum rft in any beam section (ACI 318 18.6.3.1)
    As_min1 = 3*math.sqrt(fc*1000)*bbeam*d/(fy*1000); # the stresses have to be␣
 ↪in psi
    As_min2 = 200*bbeam*d/(fy*1000)
    As_min = max(As_min1,As_min2)

    if As < As_min:
        print('INCREASE REINFORCEMENT TO SATISFY MINIMUM REQUIRED')
    if As/(b*d) > 0.025:
        print('THE REINFORCEMENT RATIO EXCEEDS THE MAXIMUM - REDESIGN MEMBER')
    # depth of compression block
    a = As*fy/(0.85*fc*b)
    #nominal strength
    Mn = As*fy*(d - a/2)
    # design strength
    M_design = design_phi_conc*Mn

    #probable strength
    # slab reinforcement
    As_slab = 0.002*tslab*(b-bbeam)
```

```
    As_prob = As + As_slab;
    # depth of compression block
    a_prob = As_prob*1.25*fy/(0.85*fc*b)
    #probable strength
    M_prob = As_prob*1.25*fy*(d - a_prob/2)

    print('Ratio of design moment over ultimate moment for␣
↪beam',beam,'=',round(M_design/abs(Mu),3))
    print('design strength = ',round(M_design,1))
    print('probable strength = ',round(M_prob,1))
    if M_design > abs(Mu):
        print('OKAY \n')
    else:
        print('REDESIGN \n')

    # check development length requirements (may control the dimensions of␣
↪exterior columns)
    ldh = (fy*1000*phi_l)/(65*lam*math.sqrt(fc*1000)) # development length for␣
↪hooked bars
    ldh_min1 = 6
    ldh_min2 = 8*phi_l

    ldh_min = max(ldh_min1,ldh_min2)
    if ldh < ldh_min:
        ldh = ldh_min

    # development lengths for different bars
    ld_typ = 2.5*ldh; #straight typical bars
    ld_top = 3.25*ldh; # straight top bars

    #print('required development length for hooked bars = ',ldh)
    #print('required development length for straight typical bars = ',ld_typ)
    #print('required development length for straight top bars = ',ld_top)

    # column sizing note
    # a minimum ratio of 20 is required between the column width and diameter of␣
↪largest lonitudinal beam bar passing
    # through the joint
    bcol_min = 20*phi_l
    print('Note: The column dimension cannot be less than ',bcol_min,'\n')

    return M_prob
```

9.3.5 Shear design of a beam section

[35]:
```
# SHEAR DESIGN
def shear_design(V_design,nlegs,dbar_t,d,dbar_pos,dbar_neg,trans_spacing):
```

```
    Av = nlegs*math.pi*dbar_t**2/4;
    s_beam = 0.75*Av*fy*d/V_design;
    s_max1 = d/4
    s_max2 = 6*dbar_pos
    s_max3 = 6*dbar_neg

    s_max_end = min(s_max1,s_max2,s_max3) # maximum spacing at the beam end␣
↪region
    s_max_all = d/2 # maximum spacing outside the beam end region

    if s_beam >s_max_all:
        s_beam = s_max_all

    print('maximum allowed spacing og transverse reinforcement along the beam␣
↪is',round(s_beam,1))

    if trans_spacing <= s_beam:
        print('SUPPLIED TRANSVERSE REINFORCEMENT IS ADEQUATE')

    print('Maximum transverse reinforcement spacing at the beam ends =␣
↪',s_max_end,'\n')
    return s_max_end
```

9.3.6 Check the beam-column joint capacity

[36]:
```
# BEAM-COLUMN JOINT CHECK
def joint_check(M_prob_neg,M_prob_pos,V_E_design,bcol,dcol,Hcol,dbar_neg,nbar_neg

,dbar_pos,nbar_pos):
    # internal joint
    # shear in the column
    V_col = (M_prob_neg + M_prob_pos + 2*V_E_design*dcol/2)/Hcol #note that␣
↪shear due to gravity loads is not included because
    # it is insignificant (except at the end columns where the seismic shear is␣
↪much less)
    # probable forces in the negative moment rft
    Abar_neg = math.pi*dbar_neg**2/4
    f_bar_neg = nbar_neg*Abar_neg*1.25*fy
    # probable forces in the positive moment rft
    Abar_pos = math.pi*dbar_pos**2/4
    f_bar_pos = nbar_pos*Abar_pos*1.25*fy
    # joint shear demand
    V_joint = f_bar_neg + f_bar_pos - V_col

    # compute nominal shear strength
    ## effective joint area
    h_joint = dcol;
```

```
    if bbeam >= bcol:
        w_joint = bcol
    else:
        w_joint_max1 = bbeam + h_joint
        w_joint_max2 = bcol # assuming that the longitudinal axes of the beam␣
↪and column are on the same plane (i.e., the beam
        # is centered on the column)
        w_joint = min(w_joint_max1,w_joint_max2)
    A_joint = h_joint*w_joint;
    # joint shear strength
    if bbeam  < 0.75*bcol:
        print('joint is not confined')
        Vn_joint = 12*lam*math.sqrt(fc*1000)*A_joint/1000
    else:
        print('it is assumed that joint is confined on three faces or two␣
↪opposite faces')
        Vn_joint = 15*lam*math.sqrt(fc*1000)*A_joint/1000

    V_design_joint = 0.85*Vn_joint
    print('ratio of joint probable capacity to demand =',round(V_design_joint/
↪V_joint,2))
    if V_design_joint > V_joint:
        print('JOINT OKAY')
    else:
        print('REDESIGN JOINT')
```

9.3.7 Overall beam design function (flexural, shear, joint check)

[37]:
```
# BEAM DESIGN FUNCTION
def beam_design(beam,int_or_ext,Mu_pos,Mu_neg,V_G,nbar_pos,nbar_neg,dbar_pos

,dbar_neg,bbeam,h,nlegs,dbar_t,ccover,trans_spacing):

    print('DESIGN FOR BEAM',beam)
    print('1. FLEXURAL DESIGN')

    # design the beam top and bottom reinforcement, and shear reinforcement
    print('reinforcement design for end-negative moments')
    # beam widths and depths
    M_prob_neg =␣
↪beam_reinf(beam,Mu_neg,nbar_neg,dbar_neg,dbar_t,bbeam,h,ccover,bbeam)
    print('reinforcement design for end-positive moments')
    bf = T_beam_flange(int_or_ext,bbeam,Lbeam,tslab)
    M_prob_pos =␣
↪beam_reinf(beam,Mu_pos,nbar_pos,dbar_pos,dbar_t,bf,h,ccover,bbeam)

    print('2. SHEAR DESIGN')
```

```
    d = effective_depth(h,ccover,dbar_t,dbar_neg) # use d based on the size of␣
↪the negative rft bars
    clear_span = Lbeam - dcol;
    V_E_design = (M_prob_neg + M_prob_pos)/clear_span

    V_design_end1 = V_E_design + V_G
    V_design_end2  = V_E_design - V_G
    V_design = max(abs(V_design_end1),abs(V_design_end2))
    print('The design shear for beam ',beam,'= ',round(V_design,1))
    # Note: here we will not care about shear design mid-span because we will␣
↪use the same spacing throughout the beam
    s_max_end =␣
↪shear_design(V_design,nlegs,dbar_t,d,dbar_pos,dbar_neg,trans_spacing)

    print('3. BEAM-COLUMN JOINT CHECK')
    joint_check(M_prob_neg,M_prob_pos,V_E_design,bcol,dcol,Hcol,dbar_neg,nbar_neg

    ,dbar_pos,nbar_pos)
  ␣
↪print('-------------------------------------------------------------------------')
    return M_prob_neg,M_prob_pos,s_max_end
```

1.9.4 9.4. Column design functions

9.4.1. Column interaction diagram

[38]:
```
def interact_diagram(col,d_vec,As_vec,bcol,dcol,col_Mn_req,Pu_max,Pu_min):
    # assumed parameters
    epsu = 0.003;
    ety = 0.002;
    beta1 = 0.85;
    fy_pr = 1.25*fy;

    ## 1. Find the depth of the neutral axis c by solving the force equilibrium␣
↪equation graphically

    # loop through different values of NA depths
    x = np.arange(dcol/30,1.4*dcol,dcol/200)

    Pn = np.empty(len(x))
    Mn = np.empty(len(x))
    P_design = np.empty(len(x))
    M_design_col = np.empty(len(x))
    P_pr = np.empty(len(x))
    M_pr = np.empty(len(x))
    design_phi = np.empty(len(x))
    epss = np.empty(len(d_vec))
```

```
    fs = np.empty(len(d_vec))
    fs_pr = np.empty(len(d_vec))

    # loop over all values of c
    for i in range(0,len(x)):
        # loop over all rows of steel and compute strains and stresses for given␣
↪c
        for k in range (0,len(d_vec)):
            epss[k] = (x[i] - d_vec[k])/x[i]*epsu
            fs[k] = epss[k]*Est
            fs_pr[k] = epss[k]*Est
            if abs(fs[k]) > fy:
                fs[k] = fy*np.sign(fs[k]);
            if abs(fs_pr[k]) > fy_pr:
                fs_pr[k] = fy_pr*np.sign(fs_pr[k]);
        #print(epss)
        # compute equilibrium function
        Pn[i] = 0.85*fc*beta1*x[i]*bcol + As_vec[0]*fs[0] + As_vec[1]*fs[1] +\
            As_vec[2]*fs[2] + As_vec[3]*fs[3]

        # calculate the nominal moment capacity (take moments about the centroid)
        Mn[i] = 0.85*fc*beta1*x[i]*bcol*(dcol/2 - (beta1*x[i])/2) +␣
↪As_vec[0]*fs[0]*(dcol/2 - d_vec[0])\
            + As_vec[1]*fs[1]*(dcol/2 - d_vec[1]) + As_vec[2]*fs[2]*(dcol/2 -␣
↪d_vec[2])\
            + As_vec[3]*fs[3]*(dcol/2 - d_vec[3])

        # calculate the probable axial and moment strength
        P_pr[i] = 0.85*fc*beta1*x[i]*bcol + As_vec[0]*fs_pr[0] +␣
↪As_vec[1]*fs_pr[1] +\
            As_vec[2]*fs_pr[2] + As_vec[3]*fs_pr[3]

        M_pr[i] = 0.85*fc*beta1*x[i]*bcol*(dcol/2 - (beta1*x[i])/2) +␣
↪As_vec[0]*fs_pr[0]*(dcol/2 - d_vec[0])\
            + As_vec[1]*fs_pr[1]*(dcol/2 - d_vec[1]) + As_vec[2]*fs_pr[2]*(dcol/
↪2 - d_vec[2])\
            + As_vec[3]*fs_pr[3]*(dcol/2 - d_vec[3])

        # check the tensile strain in the tension rft to determine if the␣
↪section is: 1. compression-controlled, 2. transition,
        # or 3. tension controlled
        if abs(epss[-1]) <= ety:
            design_phi[i] = 0.65
        elif abs(epss[-1]) > ety and abs(epss[-1]) < 0.005:
            design_phi[i] = 0.65 + 0.25*(abs(epss[-1]) - ety)/(0.005 - ety)
        elif abs(epss[-1]) >= 0.005:
```

```
            design_phi[i] = 0.9

        P_design[i] = Pn[i]*design_phi[i]
        M_design_col[i] = Mn[i]*design_phi[i]


␣
↪#############################################################################
    # compute the case of pure compression (to determine maximum allowed axial␣
↪load)
    # subject to compression only -> compression controlled -> phi = 0.65
    P_max = 0.65*0.85*fc*(dcol*bcol - np.sum(As_vec)) + fy*np.sum(As_vec)
    P_max_allowable = 0.8*P_max # from Table 22.4.2.1 in ACI 318-14

    # plot the column interaction diagram
    xlimit = 1.1*max(Mn)
    plt.figure();
    plt.plot(Mn,Pn);
    plt.xlim([0,xlimit]);
    plt.xlabel('Mn (kip.in)');
    plt.ylabel('Pn (kips)');
    plt.title('Column '+str(col)+' Interaction Diagram');

    plt.plot(M_design_col,P_design);
    plt.plot(M_pr,P_pr);

    # check adequacy of column
    M_design_value1 = np.interp(Pu_max,P_design,M_design_col)
    M_design_value2 = np.interp(Pu_min,P_design,M_design_col)
    if col_Mn_req < M_design_value1:
        if col_Mn_req < M_design_value2:
            if Pu_max <= P_max_allowable:
                print('COLUMN ',col,' IS ADEQUATE AGAINST AXIAL FORCE AND␣
↪BENDING MOMENT')
            else:
                print('REDESIGN COLUMN',col)
        else:
            print('REDESIGN COLUMN',col)
    else:
        print('REDESIGN COLUMN',col)

    plt.scatter(col_Mn_req,Pu_max)
    plt.scatter(col_Mn_req,Pu_min)

    M_pr1 = np.interp(Pu_max,P_pr,M_pr)
    M_pr2 = np.interp(Pu_min,P_pr,M_pr)
    M_pr_col = max(M_pr1,M_pr2)
    print('The maximum probable moment of the column is',round(M_pr_col,0),'\n')
```

```
    if M_pr1 > M_pr2:
        plt.scatter(M_pr_col,Pu_max)
    else:
        plt.scatter(M_pr_col,Pu_min)

    plt.legend(['Nominal Strength','Design Strength','Probable Strength','Mu,␣
↪Pu_max','Mu, Pu_min']);

    # plot the maximum allowable axial load
    plt.plot(M_design_col,[P_max_allowable] *␣
↪len(M_design_col),linestyle='dashed');

    print("""- check that the axial force due to earthquake load in a single␣
↪direction is less than 20% of
    the axial column capacity. Otherwise, the column must be designed for␣
↪biaxial bending with 100% and 30%
    earthquake force \n""")
    return M_pr_col
```

9.4.2. Column section reinforcement configuration

[39]:
```
def col_config(ccover,dcol,phi_l_col,phi_t_col):
    # based on reinforcement of 12 bars distributed uniformly
    Abar_l_col = math.pi*phi_l_col**2/4

    d1 = ccover + phi_t_col + phi_l_col/2
    bar_spacing = (dcol - 2*ccover - 2*phi_t_col - phi_l_col)/3
    d2 = d1 + bar_spacing
    d3 = d2 + bar_spacing
    d4 = d3 + bar_spacing
    d_vec = [d1,d2,d3,d4]

    As1 = 4*Abar_l_col
    As2 = 2*Abar_l_col
    As3 = 2*Abar_l_col
    As4 = 4*Abar_l_col
    As_vec = [As1,As2,As3,As4]
    return d_vec,As_vec,bar_spacing
```

9.4.3. Column transverse reinforcement

[40]:
```
def transverse_reinf(hoop_s_final,bcol,dcol,Hcol,hbeam,phi_l_col,phi_t_col

,bar_spacing,nbar_col,Ag,A_sh,bc,A_ch,clear_h,M_pr_col,M_prob_neg,M_prob_pos

,Pu_max,Pu_min):
```

```
   # confinement requirements
   # tighter spacing is required at the ends of the column over distance␣
↪l_hoops (ACI 318 section 18.7.5.1)
   dist_hoops1 = dcol
   dist_hoops2 = (Hcol - hbeam)/6
   dist_hoops3 = 18.0
   dist_hoops = max(dist_hoops1,dist_hoops2,dist_hoops3)
   #print('The distance at the column ends for tighter hoop spacing should␣
↪be',dist_hoops)

   # hoop spacing requirements (ACI 318 section 18.7.5.3)
   hoop_s1 = bcol/4
   hoop_s2 = 6*phi_l_col
   hoop_s3 = 4 + (14 - bar_spacing)/3
   if hoop_s3 < 4.0:
       hoop_s3 = 4.0
   if hoop_s3 > 6.0:
       hoop_s3 = 6.0

   # transverse reinforcement quantity minimum (ACI 318 section 18.7.5.4)
   # concrete strength factors
   kn = nbar_col/(nbar_col - 2)
   kf = max(fc*1000/25000 + 0.6,1.0)

   hoop_s4 = A_sh/(0.3*bc*(Ag/A_ch - 1)*fc/fy)
   hoop_s5 = A_sh/(0.09*bc*fc/fy)
   hoop_s6 = A_sh/(0.2*kf*kn*bc*Pu_max/(fy*A_ch))

   if Pu_max <= 0.3*Ag*fc and fc <= 10.0:
       hoop_s_end = math.floor(min(hoop_s1,hoop_s2,hoop_s3,hoop_s4,hoop_s5))
   elif Pu_max > 0.3*Ag*fc or fc > 10.0:
       hoop_s_end = math.
↪floor(min(hoop_s1,hoop_s2,hoop_s3,hoop_s4,hoop_s5,hoop_s6))

   # minimum hoop spacing
   print('The maximum allowed hoop spacing over a length of␣
↪',round(dist_hoops,1),' at the column ends is',\
         round(hoop_s_end,1),'inches')

   # transverse reinforcement beyond the column ends
   hoop_s_gen1 = 6
   hoop_s_gen2 = 6*phi_l_col
   hoop_s_gen = min(hoop_s_gen1,hoop_s_gen2)
   print('Beyond',round(dist_hoops,1),'inches, the hoop spacing in the column␣
↪need not be less than',hoop_s_gen,'inches')

   if hoop_s_final <= hoop_s_gen:
```

```
        print('COLUMN TRANSVERSE REINFORCEMENT AND SPACING IS SUFFICIENT FOR␣
↪CONFINEMENT \n')
    else:
        print('INCREASE COLUMN TRANSVERSE REINFORCEMENT \n')

    # shear design
    # compute the shear due to the probable column moment
    V_col1 = 2*M_pr_col/clear_h # using this shear value for design is␣
↪conservative

    # compute the column shear due to the probable beam moments
    V_col2 = (M_prob_neg + M_prob_pos)/clear_h # the column shear need not␣
↪exceed this value.
    print('-the column shear based on the column probable moments␣
↪is',round(V_col1,0))
    print('-The column shear need not be more than the shear based on the beam␣
↪probable moments',round(V_col2,0))
    print('-Check that the shear design values are not less than the factored␣
↪shear determined from the analysis model')

    # check adequacy of transeverse rft for shear
    # concrete contribution to shear resistance
    d_eff_col = dcol - ccover - phi_t_col - phi_l_col/2
    if Pu_min <= Ag*fc/20:
        Vc = 0.0
    else:
        Vc = 2*math.sqrt(fc*1000)*bcol*d_eff_col/1000

    # contribution of steel
    Vs = A_sh*fy*d_eff_col/hoop_s_gen

    Vn_col = Vc + Vs
    V_design_col = 0.75*Vn_col

    if V_design_col >= V_col1:
        print('COLUMN SHEAR REINFORCEMENT IS ADEQUATE \n')
    elif V_design_col < V_col1 and V_design_col >= V_col2:
        print('COLUMN SHEAR REINFORCEMENT IS ADEQUATE BUT NOT VERY CONSERVATIVE␣
↪\n')
    elif V_design_col < V_col2:
        print('REDESIGN SHEAR REINFORCEMENT \n')

    return hoop_s_end
```

9.4.2. Overall column design function

[41]:
```
def col_design(col,beam,Hcol,hbeam,bcol,dcol,ccover,phi_l_col,phi_t_col,nlegs_col

,Pu_max,Pu_min,M_prob_neg,M_prob_pos,hoop_s_final,k,mag_Mu_col):

    # Column design function
    # the column will be designed for axial load and uniaxial bending (ignoring␣
 ↪the orthogonal effects - the validity of this
    # approach should be verified later by checking that the axial force due to␣
 ↪a )
    print('COLUMN',col,'DESIGN: \n')

    print('1. CHECK NEED FOR SECOND-ORDER ANALYSIS')
    # determine whether or not slenderness effects need to be considered
    Ag = bcol*dcol
    r = math.sqrt(bcol*dcol**3/12/Ag)
    clear_h = Hcol - hbeam

    # columns are not braced against sidesway
    if k*clear_h/r <= 22.0:
        print('slenderness effects can be neglected for column',col,'\n')
    else:
        print('SLENDERNESS EFFECTS MUST BE CONSIDERED FOR COLUMN',col,'\n')
        #print(k*clear_h/r)


    print('2. DESIGN FOR AXIAL AND FLEXURAL DESIGN')
    bc = bcol - 2*ccover # as defined in ACI 318
    dc = dcol - 2*ccover
    A_ch = bc*dc

    Abar_l_col = math.pi*phi_l_col**2/4
    Abar_t_col = math.pi*phi_t_col**2/4
    A_sh = nlegs_col*Abar_t_col

    As_col = nbar_col*Abar_l_col
    if As_col < 0.01*Ag:
        print('INCREASE COLUMN',col,'REINFORCEMENT TO COMPLY WITH MINIMUM␣
 ↪REQUIREMENTS')
    elif As_col > 0.06*Ag:
        print('REDCUDE COLUMN',col,'REINFORCEMENT - EXCEEDS THE MAXIMUM ALLOWED')

    # obtain the nominal flexural strength of the beams framing into the joint
    Mn_neg =␣
 ↪beam_Mn(beam,Mu_end_neg[beam-1],nbars_neg[beam-1],dbars_neg[beam-1],dbar_t

    ,bbeams[beam-1],hbeams[beam-1],ccover)
    bf = T_beam_flange(int_or_ext,bbeams[beam-1],Lbeam,tslab)
```

```
    Mn_pos =␣
↪beam_Mn(beam,Mu_end_pos[beam-1],nbars_pos[beam-1],dbars_pos[beam-1],dbar_t,bf

    ,hbeams[beam-1],ccover)

    sum_beam_Mn = Mn_neg + Mn_pos
    sum_col_Mn = 6/5*sum_beam_Mn # strong column - weak beam
    col_Mn_req = sum_col_Mn/2
    col_Moment = max(mag_Mu_col,col_Mn_req) # the required moment capacity of␣
↪the column is taken to be the maximum of
    # the strong column asumption moments, and magnified moments from factored␣
↪loads

    d_vec,As_vec,bar_spacing = col_config(ccover,dcol,phi_l_col,phi_t_col)
    M_pr_col =␣
↪interact_diagram(col,d_vec,As_vec,bcol,dcol,col_Moment,Pu_max,Pu_min)

    print('3. CONFINEMENT REQUIREMENTS AND DESIGN FOR SHEAR')
    hoop_s_end =␣
↪transverse_reinf(hoop_s_final,bcol,dcol,Hcol,hbeam,phi_l_col,phi_t_col

    ,bar_spacing,nbar_col,Ag,A_sh,bc,A_ch,clear_h,M_pr_col,M_prob_neg,M_prob_pos

    ,Pu_max,Pu_min)
  ␣
↪print('-----------------------------------------------------------------------')

    return hoop_s_end
```

1.9.5 9.5 Design of Beams

[42]:
```
######################################## INPUT THE BEAM GEOMETRY␣
↪##########################################
bbeams = [20,20,20]
hbeams = [30,30,30]
int_or_ext = 'int' # will apply to beams and columns
# longitudinal rft using #9 bar
# transverse rft using #4 bar
ccover = 1.5

# reinforcement details for each beam group
nbars_neg = [4,4,4] # number of bars at the top
dbars_neg = [1.128,1.128,1.0] # diameter of bars at the top

nbars_pos = [4,4,3] # number of bars at the bottom
dbars_pos = [1.0,1.0,1.0] # diameter of bars at the bottom
```

```
dbar_t = 0.5 # transverse bar diameter
s_beam_final = [6.0,6.0,6.0] # transverse bar spacing along entire beam
nlegs = 4 # number of legs of the transverse rft
#########################################################################
M_prob_neg = np.empty(len(beam_groups))
M_prob_pos = np.empty(len(beam_groups))
s_max_end = np.empty(len(beam_groups))
# call the beam design function
for i in range (0,len(beam_groups)):
    M_prob_neg[i],M_prob_pos[i],s_max_end[i] =␣
 ↪beam_design(beam_groups[i],int_or_ext,Mu_end_pos[i],Mu_end_neg[i],\
                                                                    ␣
 ↪V_G_design[i],nbars_pos[i],nbars_neg[i],dbars_pos[i],\
                                                                    ␣
 ↪dbars_neg[i],bbeams[i],hbeams[i],nlegs,dbar_t,ccover,\
                                                      s_beam_final[i])
```

```
DESIGN FOR BEAM 1
1. FLEXURAL DESIGN
reinforcement design for end-negative moments
Ratio of design moment over ultimate moment for beam 1 = 1.245
design strength =  5374.2
probable strength =  7358.4
OKAY

Note: The column dimension cannot be less than  22.56

reinforcement design for end-positive moments
Ratio of design moment over ultimate moment for beam 1 = 1.296
design strength =  4445.5
probable strength =  7850.2
OKAY

Note: The column dimension cannot be less than  20.0

2. SHEAR DESIGN
The design shear for beam  1 =  99.9
maximum allowed spacing og transverse reinforcement along the beam is 9.3
SUPPLIED TRANSVERSE REINFORCEMENT IS ADEQUATE
Maximum transverse reinforcement spacing at the beam ends =  6.0

3. BEAM-COLUMN JOINT CHECK
joint is not confined
ratio of joint probable capacity to demand = 1.53
JOINT OKAY
--------------------------------------------------------------------------------
```

```
----------------------
DESIGN FOR BEAM 2
1. FLEXURAL DESIGN
reinforcement design for end-negative moments
Ratio of design moment over ultimate moment for beam 2 = 1.414
design strength =  5374.2
probable strength =  7358.4
OKAY

Note: The column dimension cannot be less than  22.56

reinforcement design for end-positive moments
Ratio of design moment over ultimate moment for beam 2 = 1.696
design strength =  4445.5
probable strength =  7850.2
OKAY

Note: The column dimension cannot be less than  20.0

2. SHEAR DESIGN
The design shear for beam  2 =  101.9
maximum allowed spacing og transverse reinforcement along the beam is 9.1
SUPPLIED TRANSVERSE REINFORCEMENT IS ADEQUATE
Maximum transverse reinforcement spacing at the beam ends =  6.0

3. BEAM-COLUMN JOINT CHECK
joint is not confined
ratio of joint probable capacity to demand = 1.53
JOINT OKAY
--------------------------------------------------------------------------------
----------------------
DESIGN FOR BEAM 3
1. FLEXURAL DESIGN
reinforcement design for end-negative moments
Ratio of design moment over ultimate moment for beam 3 = 1.471
design strength =  4307.5
probable strength =  5917.3
OKAY

Note: The column dimension cannot be less than  20.0

reinforcement design for end-positive moments
Ratio of design moment over ultimate moment for beam 3 = 2.122
design strength =  3343.5
probable strength =  6339.5
OKAY

Note: The column dimension cannot be less than  20.0
```

```
2. SHEAR DESIGN
The design shear for beam  3 =  89.0
maximum allowed spacing og transverse reinforcement along the beam is 10.5
SUPPLIED TRANSVERSE REINFORCEMENT IS ADEQUATE
Maximum transverse reinforcement spacing at the beam ends =  6.0

3. BEAM-COLUMN JOINT CHECK
joint is not confined
ratio of joint probable capacity to demand = 2.01
JOINT OKAY
--------------------------------------------------------------------------------
----------------------
```

1.9.6 9.6 Design of Columns

[43]:
```
# columns design
#ccover = 1.5 # clear cover

bcols = [bcol,bcol,bcol] # widths of columns
dcols = [dcol,dcol,dcol] # depth of columns
dbar_l_col = [1.0,1.0,1.0] # diameter of longitudinal bars
nbar_col = 12 # number of longitudinal bars distributed uniformly
dbar_t_col = 0.5 # diameter of transverse bars
hoop_s_final = [4,4,4] # spacing of hoops along the entire column (will be␣
 ↪checked against minima)
nlegs_col = 4 # number of transverse bars legs

Hcols = [Hcol1,Hcol,Hcol]
hoop_s_end = np.empty(len(col_groups)) # transverse reinforcement spacing at␣
 ↪column ends

print("Get the effective length factor k using section 9.1 of this document to␣
 ↪evaluate column slenderness. \n")
print("------------------------------------------------------------------------")
k_vec = [1.77,2.55,2.55]
# effective length factor, calculated based on the chart in ACI 318-14 R6.2.5
# note: these k factors should be the factors for the "edge" columns, which are␣
 ↪more critical than the interior columns
# because they are only bounded by one beam

for i in range(0,len(col_groups)):
    hoop_s_end[i] =␣
 ↪col_design(col_groups[i],beam_groups[i],Hcols[i],hbeams[i],bcols[i],dcols[i],

    ccover,dbar_l_col[i],dbar_t_col,nlegs_col,Pu_max[i],Pu_min[i],M_prob_neg[i],
```

```
    M_prob_pos[i],hoop_s_final[i],k_vec[i],mag_Mu_col[i])
```

```
Get the effective length factor k using section 9.1 of this document to evaluate
column slenderness.

--------------------------------------------------------------------------------
----------------------
COLUMN 1 DESIGN:

1. CHECK NEED FOR SECOND-ORDER ANALYSIS
SLENDERNESS EFFECTS MUST BE CONSIDERED FOR COLUMN 1

2. DESIGN FOR AXIAL AND FLEXURAL DESIGN
COLUMN  1  IS ADEQUATE AGAINST AXIAL FORCE AND BENDING MOMENT
The maximum probable moment of the column is 19925.0

- check that the axial force due to earthquake load in a single direction is
less than 20% of
    the axial column capacity. Otherwise, the column must be designed for
biaxial bending with 100% and 30%
    earthquake force

3. CONFINEMENT REQUIREMENTS AND DESIGN FOR SHEAR
The maximum allowed hoop spacing over a length of  31.0  at the column ends is 3
inches
Beyond 31.0 inches, the hoop spacing in the column need not be less than 6
inches
COLUMN TRANSVERSE REINFORCEMENT AND SPACING IS SUFFICIENT FOR CONFINEMENT

-the column shear based on the column probable moments is 214.0
-The column shear need not be more than the shear based on the beam probable
moments 82.0
-Check that the shear design values are not less than the factored shear
determined from the analysis model
COLUMN SHEAR REINFORCEMENT IS ADEQUATE

--------------------------------------------------------------------------------
----------------------
COLUMN 2 DESIGN:

1. CHECK NEED FOR SECOND-ORDER ANALYSIS
SLENDERNESS EFFECTS MUST BE CONSIDERED FOR COLUMN 2

2. DESIGN FOR AXIAL AND FLEXURAL DESIGN
COLUMN  2  IS ADEQUATE AGAINST AXIAL FORCE AND BENDING MOMENT
The maximum probable moment of the column is 18526.0
```

```
- check that the axial force due to earthquake load in a single direction is
less than 20% of
    the axial column capacity. Otherwise, the column must be designed for
biaxial bending with 100% and 30%
    earthquake force

3. CONFINEMENT REQUIREMENTS AND DESIGN FOR SHEAR
The maximum allowed hoop spacing over a length of  30.0  at the column ends is 3
inches
Beyond 30.0 inches, the hoop spacing in the column need not be less than 6
inches
COLUMN TRANSVERSE REINFORCEMENT AND SPACING IS SUFFICIENT FOR CONFINEMENT

-the column shear based on the column probable moments is 294.0
-The column shear need not be more than the shear based on the beam probable
moments 121.0
-Check that the shear design values are not less than the factored shear
determined from the analysis model
COLUMN SHEAR REINFORCEMENT IS ADEQUATE BUT NOT VERY CONSERVATIVE

------------------------------------------------------------------------------
-----------------------
COLUMN 3 DESIGN:

1. CHECK NEED FOR SECOND-ORDER ANALYSIS
SLENDERNESS EFFECTS MUST BE CONSIDERED FOR COLUMN 3

2. DESIGN FOR AXIAL AND FLEXURAL DESIGN
COLUMN  3  IS ADEQUATE AGAINST AXIAL FORCE AND BENDING MOMENT
The maximum probable moment of the column is 14836.0

- check that the axial force due to earthquake load in a single direction is
less than 20% of
    the axial column capacity. Otherwise, the column must be designed for
biaxial bending with 100% and 30%
    earthquake force

3. CONFINEMENT REQUIREMENTS AND DESIGN FOR SHEAR
The maximum allowed hoop spacing over a length of  30.0  at the column ends is 3
inches
Beyond 30.0 inches, the hoop spacing in the column need not be less than 6
inches
COLUMN TRANSVERSE REINFORCEMENT AND SPACING IS SUFFICIENT FOR CONFINEMENT

-the column shear based on the column probable moments is 235.0
-The column shear need not be more than the shear based on the beam probable
moments 97.0
-Check that the shear design values are not less than the factored shear
```

```
determined from the analysis model
COLUMN SHEAR REINFORCEMENT IS ADEQUATE BUT NOT VERY CONSERVATIVE

------------------------------------------------------------------------------
-----------------------
```

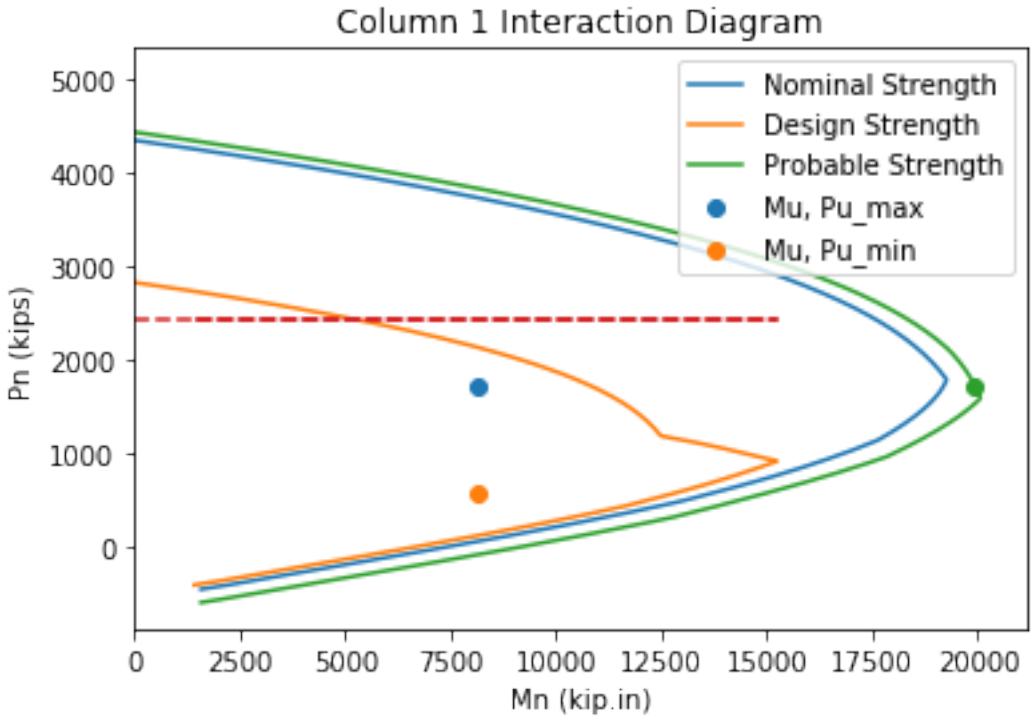

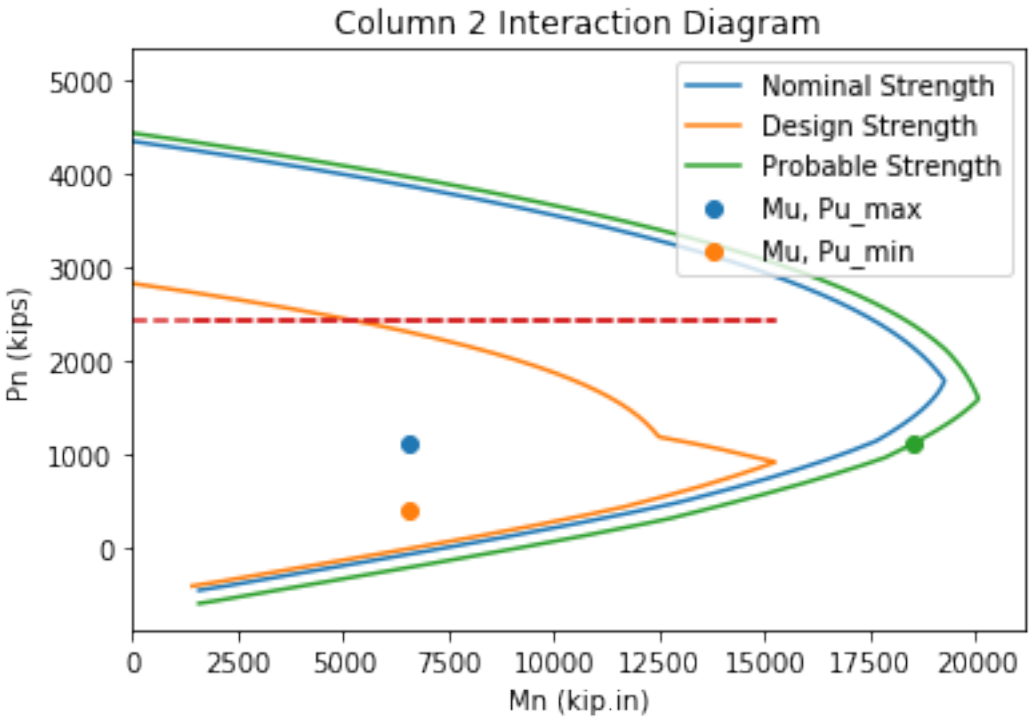
Column 2 Interaction Diagram
Nominal Strength
Design Strength
Probable Strength
Mu, Pu_max
Mu, Pu_min
Pn (kips)
Mn (kip.in)
5000
4000
3000
2000
1000
0
0
2500
5000
7500
10000
12500
15000
17500
20000

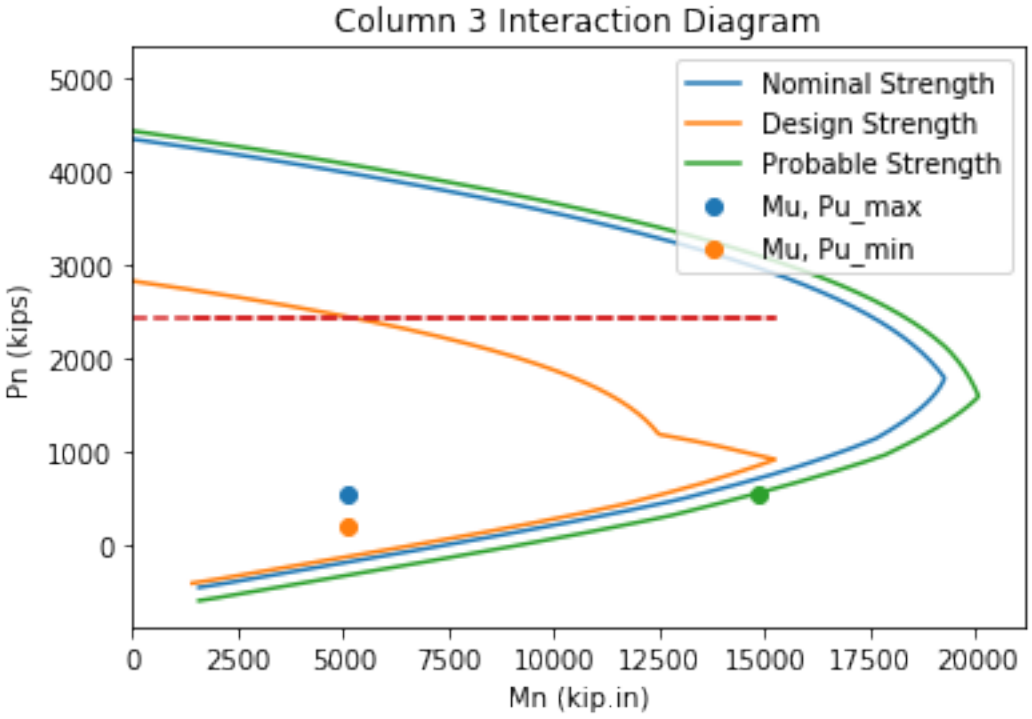
Column 3 Interaction Diagram
Nominal Strength
Design Strength
Probable Strength
Mu, Pu_max
Mu, Pu_min
Pn (kips)
Mn (kip.in)
5000
4000
3000
2000
1000
0
0
2500
5000
7500
10000
12500
15000
17500
20000

1.9.7 9.7. Summary of Member Designs

[44]:
```
# Summarize all member designs
print('DESIGN OF BEAMS:')
for i in range(0,len(beam_groups)):
    print('- BEAM',i+1,'GROUP:')
    print('Dimensions:',bbeams[i],'inches by',hbeams[i],'inches')
    print('Longitudinal rft:',nbars_neg[i],'bars of',dbars_neg[i],'inch diameter␣
 ↪bars at the top')
    print('Longitudinal rft:',nbars_pos[i],'bars of',dbars_pos[i],'inch diameter␣
 ↪bars at the bottom')
    print('Transverse rft:',nlegs,'legs of',dbar_t,'inch diameter bars␣
 ↪at',s_beam_final[i],'inch spacing, with reduced',\
          s_max_end[i],'inch spacing at beam ends \n')
print('-----------------------------------------------------------------')
print('DESIGN OF COLUMNS:')
for i in range(0,len(col_groups)):
    print('- COLUMN',i+1,'GROUP:')
    print('Dimensions:',bcols[i],'inches by',dcols[i],'inches')
    print('Longitudinal rft:',nbar_col,'bars of',dbar_l_col[i],'inch diameter␣
 ↪bars distributed uniformly')
    print('Transverse rft:',nlegs_col,'legs of',dbar_t_col,'inch diameter bars␣
 ↪at',hoop_s_final[i],\
          'inch spacing, with reduced',hoop_s_end[i],'inch spacing at column␣
 ↪ends \n')
```

```
DESIGN OF BEAMS:
- BEAM 1 GROUP:
Dimensions: 20 inches by 30 inches
Longitudinal rft: 4 bars of 1.128 inch diameter bars at the top
Longitudinal rft: 4 bars of 1.0 inch diameter bars at the bottom
Transverse rft: 4 legs of 0.5 inch diameter bars at 6.0 inch spacing, with
reduced 6.0 inch spacing at beam ends

- BEAM 2 GROUP:
Dimensions: 20 inches by 30 inches
Longitudinal rft: 4 bars of 1.128 inch diameter bars at the top
Longitudinal rft: 4 bars of 1.0 inch diameter bars at the bottom
Transverse rft: 4 legs of 0.5 inch diameter bars at 6.0 inch spacing, with
reduced 6.0 inch spacing at beam ends

- BEAM 3 GROUP:
Dimensions: 20 inches by 30 inches
Longitudinal rft: 4 bars of 1.0 inch diameter bars at the top
Longitudinal rft: 3 bars of 1.0 inch diameter bars at the bottom
Transverse rft: 4 legs of 0.5 inch diameter bars at 6.0 inch spacing, with
reduced 6.0 inch spacing at beam ends
```

```
--------------------------------------------------------------------------------
--------------------------------
DESIGN OF COLUMNS:
- COLUMN 1 GROUP:
Dimensions: 30.0 inches by 30.0 inches
Longitudinal rft: 12 bars of 1.0 inch diameter bars distributed uniformly
Transverse rft: 4 legs of 0.5 inch diameter bars at 4 inch spacing, with reduced
3.0 inch spacing at column ends

- COLUMN 2 GROUP:
Dimensions: 30.0 inches by 30.0 inches
Longitudinal rft: 12 bars of 1.0 inch diameter bars distributed uniformly
Transverse rft: 4 legs of 0.5 inch diameter bars at 4 inch spacing, with reduced
3.0 inch spacing at column ends

- COLUMN 3 GROUP:
Dimensions: 30.0 inches by 30.0 inches
Longitudinal rft: 12 bars of 1.0 inch diameter bars distributed uniformly
Transverse rft: 4 legs of 0.5 inch diameter bars at 4 inch spacing, with reduced
3.0 inch spacing at column ends
```

Bibliography

1997 Uniform Building Code. International Conference of Building Officials, 1997. ISBN 1-884590-93-4.

Building Code Requirements for Structural Concrete (ACI 318-14). American Concrete Institute, 2014. ISBN 978-0-87031-930-3.

Norman A Abrahamson. Effects of rupture directivity on probabilistic seismic hazard analysis. Proceedings of the 6th international conference on seismic zonation, Palm Springs, CA, pages 151–156, 2000.

Babak Alavi and Helmut Krawinkler. Consideration of near-fault ground motion effects in seismic design. Proceedings of the 12th World Conference on Earthquake Engineering. International Association for Earthquake Engineering, 2000.

Babak Alavi and Helmut Krawinkler. Behavior of moment-resisting frame structures subjected to near-fault ground motions. *Earthquake engineering & structural dynamics*, 33(6):687–706, 2004.

Beng Ghee Ang, M. J. N. Priestley, and R. Park. *Ductility of reinforced concrete bridge piers under seismic loading*. PhD thesis, University of Canterbury, Christchurch, New Zealand, 1981.

ASCE. *Seismic Design Criteria for Structures, Systems, and Components in Nuclear Facilities (ASCE/SEI 43-05)*. American Society of Civil Engineers, 2005.

ASCE. *Minimum Design Loads and Associated Criteria for Buildings and Other Structures (ASCE/SEI 7-16)*. American Society of Civil Engineers, 2017. ISBN 9780784479964.

Mehmet Bilgin Atalay and Joseph Penzien. The seismic behavior of critical regions of reinforced concrete components as influenced by moment, shear and axial force. Technical report, Earthquake Engineering Research Center, University of California, 1975.

ATC. *Seismic performance assessment of buildings (FEMA P-58)*, volume 1. 2018.

Jack W Baker. Identification of near-fault velocity pulses and prediction of resulting response spectra. In *Geotechnical Earthquake Engineering and Soil Dynamics IV*, pages 1–10. 2008.

Jack W Baker and C Allin Cornell. Vector-valued intensity measures for pulse-like near-fault ground motions. *Engineering structures*, 30(4):1048–1057, 2008.

Jack W Baker, Ting Lin, Shrey K Shahi, and Nirmal Jayaram. New ground motion selection procedures and selected motions for the peer transportation research program. *PEER report*, 3, 2011.

Jack W Baker, Nicolas Luco, Norman A Abrahamson, Robert W Graves, Philip J Maechling, and Kim B Olsen. Engineering uses of physics-based ground motion simulations. Proceedings of the Tenth US Conference on Earthquake Engineering, 2014.

Jeff Bayless and Norman A Abrahamson. Evaluation of the interperiod correlation of ground-motion simulations. *Bulletin of the Seismological Society of America*, 108(6):3413–3430, 2018.

Vitelmo V Bertero, Stephen A Mahin, and Ricardo A Herrera. Aseismic design implications of near-fault san fernando earthquake records. *Earthquake engineering & structural dynamics*, 6 (1):31–42, 1978.

Jacobo Bielak, Kostas Loukakis, Yoshiaki Hisada, and Chiaki Yoshimura. Domain reduction method for three-dimensional earthquake modeling in localized regions, part i: Theory. *Bulletin of the seismological Society of America*, 93(2):817–824, 2003.

Nenad Bijelić, Ting Lin, and Gregory G Deierlein. Evaluation of building collapse risk and drift demands by nonlinear structural analyses using conventional hazard analysis versus direct simulation with cybershake seismograms. *Bulletin of the Seismological Society of America*, 109(5): 1812–1828, 2019a.

Nenad Bijelić, Ting Lin, and Gregory G Deierlein. Quantification of the influence of deep basin effects on structural collapse using scec cybershake earthquake ground motion simulations. *Earthquake Spectra*, 35(4):1845–1864, 2019b.

David M Boore. Orientation-independent, nongeometric-mean measures of seismic intensity from two horizontal components of motion. *Bulletin of the Seismological Society of America*, 100(4): 1830–1835, 2010.

Jonathan D Bray and Adrian Rodriguez-Marek. Characterization of forward-directivity ground motions in the near-fault region. *Soil dynamics and earthquake engineering*, 24(11):815–828, 2004.

Lynne S Burks, Reid B Zimmerman, and Jack W Baker. Evaluation of hybrid broadband ground motion simulations for response history analysis and design. *Earthquake Spectra*, 31(3):1691–1710, 2015.

Lynne Schleiffarth Burks. *Ground motion simulations: Validation and application for civil engineering problems*. PhD thesis, Stanford University, 450 Serra Mall, Stanford, CA, 2014.

Kenneth W Campbell and Yousef Bozorgnia. Nga-west2 ground motion model for the average horizontal components of pga, pgv, and 5% damped linear acceleration response spectra. *Earthquake Spectra*, 30(3):1087–1115, 2014.

Casey Champion and Abbie Liel. The effect of near-fault directivity on building seismic collapse risk. *Earthquake Engineering & Structural Dynamics*, 41(10):1391–1409, 2012.

PF Chen. Generalized plastic hinge concepts for 3d beam-column elements. 1982.

Anil K Chopra and Chatpan Chintanapakdee. Comparing response of sdf systems to near-fault and far-fault earthquake motions in the context of spectral regions. *Earthquake engineering & structural dynamics*, 30(12):1769–1789, 2001.

Anil K Chopra and Frank McKenna. Modeling viscous damping in nonlinear response history analysis of buildings for earthquake excitation. *Earthquake Engineering & Structural Dynamics*, 45(2):193–211, 2016.

CSI. Analysis reference manual. *Computers and Structures, Inc., Walnut Creek, California, USA*, 2003.

Maurice A Dides and Juan C De la Llera. A comparative study of concentrated plasticity models in dynamic analysis of building structures. *Earthquake engineering & structural dynamics*, 34 (8):1005–1026, 2005.

John Douglas and Hideo Aochi. A survey of techniques for predicting earthquake ground motions for engineering purposes. *Surveys in geophysics*, 29(3):187, 2008.

MN Fardis and DE Biskinis. Deformation capacity of rc members, as controlled by flexure or shear. In *Otani Symposium*, volume 511530, 2003.

FEMA. 2015 nehrp recommended seismic provisions: Design examples (fema p-1051), 2016.

Carmine Galasso, Peng Zhong, Farzin Zareian, Iunio Iervolino, and Robert W Graves. Validation of ground-motion simulations for historical events using mdof systems. *Earthquake Engineering & Structural Dynamics*, 42(9):1395–1412, 2013.

Melbourne Fernald Giberson. *The response of nonlinear multi-story structures subjected to earthquake excitation*. PhD thesis, California Institute of Technology, Pasadena, CA, 1967.

Wayne Douglas Gill, R. Park, and M. J. N. Priestley. Ductility of rectangular reinforced concrete columns with axial load. Master's thesis, University of Canterbury, Christchurch, New Zealand, 1979.

R Graves and A Pitarka. Validating ground-motion simulations on rough faults in complex 3-d media. Proceedings of the 11th National Conference in Earthquake Engineering, EERI, Los Angeles, California, 2018.

Robert Graves and Arben Pitarka. Kinematic ground-motion simulations on rough faults including effects of 3d stochastic velocity perturbations. *Bulletin of the Seismological Society of America*, 106(5):2136–2153, 2016.

Robert W Graves and Arben Pitarka. Broadband ground-motion simulation using a hybrid approach. *Bulletin of the Seismological Society of America*, 100(5A):2095–2123, 2010.

Robert W Graves, Arben Pitarka, and Paul G Somerville. Ground-motion amplification in the santa monica area: Effects of shallow basin-edge structure. *Bulletin of the Seismological Society of America*, 88(5):1224–1242, 1998.

John F Hall, Thomas H Heaton, Marvin W Halling, and David J Wald. Near-source ground motion and its effects on flexible buildings. *Earthquake spectra*, 11(4):569–605, 1995.

Curt B Haselton. *Beam-column element model calibrated for predicting flexural response leading to global collapse of RC frame buildings*. Pacific Earthquake Engineering Research Center, 2008.

Curt B Haselton, Abbie B Liel, Sarah C Taylor-Lange, and Gregory G Deierlein. Calibration of model to simulate response of reinforced concrete beam-columns to collapse. *ACI Structural Journal*, 113(6), 2016.

GW Housner and MD Trifunac. Analysis of accelerograms—parkfield earthquake. *Bulletin of the seismological society of America*, 57(6):1193–1220, 1967.

Luis F Ibarra and Helmut Krawinkler. *Global collapse of frame structures under seismic excitations*. Pacific Earthquake Engineering Research Center Berkeley, CA, 2005.

Luis F Ibarra, Ricardo A Medina, and Helmut Krawinkler. Hysteretic models that incorporate strength and stiffness deterioration. *Earthquake engineering & structural dynamics*, 34(12): 1489–1511, 2005.

WD Iwan, Ching-Tung Huang, and Andrew C Guyader. Important features of the response of inelastic structures to near-field ground motion. Proc. of the 12th World Conf. on Earthquake Engineering. International Association for Earthquake Engineering, 2000.

Nirmal Jayaram and Nilesh Shome. A statistical analysis of the response of tall buildings to recorded and simulated ground motions. 15th World Conference on Earthquake Engineering, pages 1–10, 2012.

Hans Johansen, Arthur Rodgers, N Anders Petersson, David McCallen, Bjorn Sjogreen, and Mamun Miah. Toward exascale earthquake ground motion simulations for near-fault engineering analysis. *Computing in Science & Engineering*, 19(5):27–37, 2017.

Makoto Kanda, Nobuaki Shirai, Hiromi Adachi, and Toshio Sato. Analytical study on elastoplastic hysteretic behaviors of reinforced concrete members. *Transactions of the Japan Concrete Institute*, 10(1):257–264, 1988.

Maha Kenawy, Sashi Kunnath, Subodh Kolwankar, and Amit Kanvinde. Concrete uniaxial nonlocal damage-plasticity model for simulating post-peak response of reinforced concrete beam-columns under cyclic loading. *Journal of Structural Engineering*, 146(5):04020052, 2020.

Thomas Kluyver, Benjamin Ragan-Kelley, Fernando Pérez, Brian E Granger, Matthias Bussonnier, Jonathan Frederic, Kyle Kelley, Jessica B Hamrick, Jason Grout, Sylvain Corlay, et al. Jupyter notebooks-a publishing format for reproducible computational workflows. In *ELPUB*, pages 87–90, 2016.

Susumu Kono and Fumio Watanabe. Damage evaluation of reinforced concrete columns under multiaxial cyclic loadings. In *The Second US-Japan Workshop on Performance-Based Earthquake Engineering Methodology for Reinforced Concrete Building Structures*, pages 221–231, 2000.

SK Kunnath, AM Reinhorn, and JF Abel. A computational tool for evaluation of seismic performance of reinforced concrete buildings. *Computers & structures*, 41(1):157–173, 1991.

Wen-I Liao, Chin-Hsiung Loh, and Shiuan Wan. Earthquake responses of rc moment frames subjected to near-fault ground motions. *The Structural Design of Tall Buildings*, 10(3):219–229, 2001.

Dimitrios Lignos. *Sidesway collapse of deteriorating structural systems under seismic excitations*. Stanford university, 2008.

Dimitrios G Lignos and Helmut Krawinkler. Deterioration modeling of steel components in support of collapse prediction of steel moment frames under earthquake loading. *Journal of Structural Engineering*, 137(11):1291–1302, 2010.

Nicolas Luco and C Allin Cornell. Structure-specific scalar intensity measures for near-source and ordinary earthquake ground motions. *Earthquake Spectra*, 23(2):357–392, 2007.

Gregory A MacRae, Daniel V Morrow, and Charles W Roeder. Near-fault ground motion effects on simple structures. *Journal of Structural Engineering*, 127(9):996–1004, 2001.

Praveen K Malhotra. Response of buildings to near-field pulse-like ground motions. *Earthquake engineering & structural dynamics*, 28(11):1309–1326, 1999.

Nasser A Marafi, Jeffrey W Berman, and Marc O Eberhard. Ductility-dependent intensity measure that accounts for ground-motion spectral shape and duration. *Earthquake Engineering & Structural Dynamics*, 45(4):653–672, 2016.

Nasser A Marafi, Marc O Eberhard, Jeffrey W Berman, Erin A Wirth, and Arthur D Frankel. Impacts of simulated m9 cascadia subduction zone motions on idealized systems. *Earthquake Spectra*, 35(3):1261–1287, 2019.

MATLAB. *R2020a*. The MathWorks Inc., Natick, Massachusetts, 2020.

GP Mavroeidis, G Dong, and AS Papageorgiou. Near-fault ground motions, and the response of elastic and inelastic single-degree-of-freedom (sdof) systems. *Earthquake Engineering & Structural Dynamics*, 33(9):1023–1049, 2004.

David Mccallen, N. Petersson, Arthur Rodgers, Mamun Miah, Arben Pitarka, Floriana Petrone, and Houjun Tang. The earthquake simulation (eqsim) framework for physics-based fault-to-structure simulations. Proceedings of the 17th World Conference on Earthquake Engineering, Sendai, Japan, 06 2020.

Frank McKenna, Gregory L Fenves, Michael H Scott, et al. Open system for earthquake engineering simulation. *University of California, Berkeley, CA*, 2000.

NIST. *Selecting and Scaling Earthquake Ground Motions for Performing Response-History Analyses (NIST GCR 11-917-15)*. National Institute of Standards and Technology, 2011.

Telemachos B Panagiotakos and Michael N Fardis. Deformations of reinforced concrete members at yielding and ultimate. *Structural Journal*, 98(2):135–148, 2001.

PEER/ATC. Modeling and acceptance criteria for seismic design and analysis of tall buildings, 2010.

N Anders Petersson and Björn Sjögreen. Wave propagation in anisotropic elastic materials and curvilinear coordinates using a summation-by-parts finite difference method. *Journal of Computational Physics*, 299:820–841, 2015.

A Pitarka, R Graves, K Irikura, K Miyakoshi, and A Rodgers. Kinematic rupture modeling of ground motion from the m7 kumamoto, japan earthquake. *Pure and Applied Geophysics*, pages 1–23, 2019.

Arben Pitarka, Kojiro Irikura, Tomotaka Iwata, and Takao Kagawa. Basin structure effects in the kobe area inferred from the modeling of ground motions from two aftershocks of the january 17, 1995, hyogo-ken nanbu earthquake. *Journal of Physics of the Earth*, 44(5):563–576, 1996.

Graham H Powell and Paul Fu-Song Chen. 3d beam-column element with generalized plastic hinges. *Journal of engineering mechanics*, 112(7):627–641, 1986.

Meera Raghunandan and Abbie B Liel. Effect of ground motion duration on earthquake-induced structural collapse. *Structural Safety*, 41:119–133, 2013.

Arthur J Rodgers, N Anders Petersson, Arben Pitarka, David B McCallen, Bjorn Sjogreen, and Norman Abrahamson. Broadband (0–5 hz) fully deterministic 3d ground-motion simulations of a magnitude 7.0 hayward fault earthquake: Comparison with empirical ground-motion models and 3d path and site effects from source normalized intensities. *Seismological Research Letters*, 90(3):1268–1284, 2019a.

Arthur J Rodgers, Arben Pitarka, and David B McCallen. The effect of fault geometry and minimum shear wavespeed on 3d ground-motion simulations for an m w 6.5 hayward fault scenario earthquake, san francisco bay area, northern california. *Bulletin of the Seismological Society of America*, 109(4):1265–1281, 2019b.

Murat Saatcioglu and Mongi Grira. Confinement of reinforced concrete columns with welded reinforced grids. *ACI Structural Journal*, 96(1):29–39, 1999. ISSN 0889-3241.

Reza Sehhati, Adrian Rodriguez-Marek, Mohamed ElGawady, and William F Cofer. Effects of near-fault ground motions and equivalent pulses on multi-story structures. *Engineering Structures*, 33(3):767–779, 2011.

Shrey K Shahi and Jack W Baker. An empirically calibrated framework for including the effects of near-fault directivity in probabilistic seismic hazard analysis. *Bulletin of the Seismological Society of America*, 101(2):742–755, 2011.

Shrey K Shahi and Jack W Baker. An efficient algorithm to identify strong-velocity pulses in multicomponent ground motions. *Bulletin of the Seismological Society of America*, 104(5): 2456–2466, 2014.

Mettupalayam V Sivaselvan and Andrei M Reinhorn. Hysteretic models for deteriorating inelastic structures. *Journal of Engineering Mechanics*, 126(6):633–640, 2000.

Björn Sjögreen and N Anders Petersson. A fourth order accurate finite difference scheme for the elastic wave equation in second order formulation. *Journal of Scientific Computing*, 52(1): 17–48, 2012.

M. T. Soesianawati, R. Park, and M. J. N. Priestley. Limited ductility design of reinforced concrete columns. M.Eng. thesis, University of Canterbury, Christchurch, New Zealand, 1986.

Paul G Somerville. Magnitude scaling of the near fault rupture directivity pulse. *Physics of the earth and planetary interiors*, 137(1-4):201–212, 2003.

Paul G Somerville. Engineering characterization of near fault ground motions. Proc., NZSEE 2005 Conf, Taupo, New Zealand, 2005.

Paul G Somerville, Nancy F Smith, Robert W Graves, and Norman A Abrahamson. Modification of empirical strong ground motion attenuation relations to include the amplitude and duration effects of rupture directivity. *Seismological research letters*, 68(1):199–222, 1997.

Jong-Keol Song and JoseA Pincheira. Spectral displacement demands of stiffness-and strength-degrading systems. *Earthquake Spectra*, 16(4):817–851, 2000.

Ricardo Taborda and Jacobo Bielak. Large-scale earthquake simulation: computational seismology and complex engineering systems. *Computing in Science & Engineering*, 13(4):14–27, 2011.

Hitoshi Tanaka and R. Park. *Effect of lateral confining reinforcement on the ductile behaviour of reinforced concrete columns*. PhD thesis, University of Canterbury, Christchurch, New Zealand, 1990.

Polsak Tothong and C Allin Cornell. Structural performance assessment under near-source pulse-like ground motions using advanced ground motion intensity measures. *Earthquake Engineering & Structural Dynamics*, 37(7):1013–1037, 2008.

Polsak Tothong, C Allin Cornell, and JW Baker. Explicit directivity-pulse inclusion in probabilistic seismic hazard analysis. *Earthquake Spectra*, 23(4):867–891, 2007.

Guido Van Rossum and Fred L Drake Jr. *Python reference manual*. Centrum voor Wiskunde en Informatica Amsterdam, 1995.

Soesianawati Watson and R. Park. *Design of reinforced concrete frames of limited ductility*. PhD thesis, University of Canterbury, Christchurch, New Zealand, 1989.

Franz August Zahn, R. Park, and M. J. N. Priestley. *Design of reinforced concrete bridge columns for strength and ductility*. PhD thesis, University of Canterbury, Christchurch, New Zealand, 1985.

LIST OF CCEER PUBLICATIONS

Report No.	Publication
CCEER-84-1	Saiidi, M., and R. Lawver, "User's Manual for LZAK-C64, A Computer Program to Implement the Q-Model on Commodore 64," Civil Engineering Department, Report No. CCEER-84-1, University of Nevada, Reno, January 1984.
CCEER-84-1	Douglas, B., Norris, G., Saiidi, M., Dodd, L., Richardson, J. and Reid, W., "Simple Bridge Models for Earthquakes and Test Data," Civil Engineering Department, Report No. CCEER-84-1 Reprint, University of Nevada, Reno, January 1984.
CCEER-84-2	Douglas, B. and T. Iwasaki, "Proceedings of the First USA-Japan Bridge Engineering Workshop," held at the Public Works Research Institute, Tsukuba, Japan, Civil Engineering Department, Report No. CCEER-84-2, University of Nevada, Reno, April 1984.
CCEER-84-3	Saiidi, M., J. Hart, and B. Douglas, "Inelastic Static and Dynamic Analysis of Short R/C Bridges Subjected to Lateral Loads," Civil Engineering Department, Report No. CCEER-84-3, University of Nevada, Reno, July 1984.
CCEER-84-4	Douglas, B., "A Proposed Plan for a National Bridge Engineering Laboratory," Civil Engineering Department, Report No. CCEER-84-4, University of Nevada, Reno, December 1984.
CCEER-85-1	Norris, G. and P. Abdollaholiaee, "Laterally Loaded Pile Response: Studies with the Strain Wedge Model," Civil Engineering Department, Report No. CCEER-85-1, University of Nevada, Reno, April 1985.
CCEER-86-1	Ghusn, G. and M. Saiidi, "A Simple Hysteretic Element for Biaxial Bending of R/C in NEABS-86," Civil Engineering Department, Report No. CCEER-86-1, University of Nevada, Reno, July 1986.
CCEER-86-2	Saiidi, M., R. Lawver, and J. Hart, "User's Manual of ISADAB and SIBA, Computer Programs for Nonlinear Transverse Analysis of Highway Bridges Subjected to Static and Dynamic Lateral Loads," Civil Engineering Department, Report No. CCEER-86-2, University of Nevada, Reno, September 1986.
CCEER-87-1	Siddharthan, R., "Dynamic Effective Stress Response of Surface and Embedded Footings in Sand," Civil Engineering Department, Report No. CCEER-86-2, University of Nevada, Reno, June 1987.
CCEER-87-2	Norris, G. and R. Sack, "Lateral and Rotational Stiffness of Pile Groups for Seismic Analysis of Highway Bridges," Civil Engineering Department, Report No. CCEER-87-2, University of Nevada, Reno, June 1987.
CCEER-88-1	Orie, J. and M. Saiidi, "A Preliminary Study of One-Way Reinforced Concrete Pier Hinges Subjected to Shear and Flexure," Civil Engineering Department, Report No. CCEER-88-1, University of Nevada, Reno, January 1988.
CCEER-88-2	Orie, D., M. Saiidi, and B. Douglas, "A Micro-CAD System for Seismic Design of Regular Highway Bridges," Civil Engineering Department, Report No. CCEER-88-2, University of Nevada, Reno, June 1988.
CCEER-88-3	Orie, D. and M. Saiidi, "User's Manual for Micro-SARB, a Microcomputer Program for Seismic Analysis of Regular Highway Bridges," Civil Engineering Department, Report No. CCEER-88-3, University of Nevada, Reno, October 1988.

CCEER-89-1 Douglas, B., M. Saiidi, R. Hayes, and G. Holcomb, "A Comprehensive Study of the Loads and Pressures Exerted on Wall Forms by the Placement of Concrete," Civil Engineering Department, Report No. CCEER-89-1, University of Nevada, Reno, February 1989.

CCEER-89-2 Richardson, J. and B. Douglas, "Dynamic Response Analysis of the Dominion Road Bridge Test Data," Civil Engineering Department, Report No. CCEER-89-2, University of Nevada, Reno, March 1989.

CCEER-89-2 Vrontinos, S., M. Saiidi, and B. Douglas, "A Simple Model to Predict the Ultimate Response of R/C Beams with Concrete Overlays," Civil Engineering Department, Report NO. CCEER-89-2, University of Nevada, Reno, June 1989.

CCEER-89-3 Ebrahimpour, A. and P. Jagadish, "Statistical Modeling of Bridge Traffic Loads - A Case Study," Civil Engineering Department, Report No. CCEER-89-3, University of Nevada, Reno, December 1989.

CCEER-89-4 Shields, J. and M. Saiidi, "Direct Field Measurement of Prestress Losses in Box Girder Bridges," Civil Engineering Department, Report No. CCEER-89-4, University of Nevada, Reno, December 1989.

CCEER-90-1 Saiidi, M., E. Maragakis, G. Ghusn, Y. Jiang, and D. Schwartz, "Survey and Evaluation of Nevada's Transportation Infrastructure, Task 7.2 - Highway Bridges, Final Report," Civil Engineering Department, Report No. CCEER 90-1, University of Nevada, Reno, October 1990.

CCEER-90-2 Abdel-Ghaffar, S., E. Maragakis, and M. Saiidi, "Analysis of the Response of Reinforced Concrete Structures During the Whittier Earthquake 1987," Civil Engineering Department, Report No. CCEER 90-2, University of Nevada, Reno, October 1990.

CCEER-91-1 Saiidi, M., E. Hwang, E. Maragakis, and B. Douglas, "Dynamic Testing and the Analysis of the Flamingo Road Interchange," Civil Engineering Department, Report No. CCEER-91-1, University of Nevada, Reno, February 1991.

CCEER-91-2 Norris, G., R. Siddharthan, Z. Zafir, S. Abdel-Ghaffar, and P. Gowda, "Soil-Foundation-Structure Behavior at the Oakland Outer Harbor Wharf," Civil Engineering Department, Report No. CCEER-91-2, University of Nevada, Reno, July 1991.

CCEER-91-3 Norris, G., "Seismic Lateral and Rotational Pile Foundation Stiffnesses at Cypress," Civil Engineering Department, Report No. CCEER-91-3, University of Nevada, Reno, August 1991.

CCEER-91-4 O'Connor, D. and M. Saiidi, "A Study of Protective Overlays for Highway Bridge Decks in Nevada, with Emphasis on Polyester-Styrene Polymer Concrete," Civil Engineering Department, Report No. CCEER-91-4, University of Nevada, Reno, October 1991.

CCEER-91-5 O'Connor, D.N. and M. Saiidi, "Laboratory Studies of Polyester-Styrene Polymer Concrete Engineering Properties," Civil Engineering Department, Report No. CCEER-91-5, University of Nevada, Reno, November 1991.

CCEER-92-1 Straw, D.L. and M. Saiidi, "Scale Model Testing of One-Way Reinforced Concrete Pier Hinges Subject to Combined Axial Force, Shear and Flexure," edited by D.N. O'Connor, Civil Engineering Department, Report No. CCEER-92-1, University of Nevada, Reno, March 1992.

CCEER-92-2 Wehbe, N., M. Saiidi, and F. Gordaninejad, "Basic Behavior of Composite Sections Made of Concrete Slabs and Graphite Epoxy Beams," Civil Engineering Department, Report No. CCEER-92-2, University of Nevada, Reno, August 1992.

CCEER-92-3 Saiidi, M. and E. Hutchens, "A Study of Prestress Changes in A Post-Tensioned Bridge During the First 30 Months," Civil Engineering Department, Report No. CCEER-92-3, University of Nevada,

Reno, April 1992.

CCEER-92-4 Saiidi, M., B. Douglas, S. Feng, E. Hwang, and E. Maragakis, "Effects of Axial Force on Frequency of Prestressed Concrete Bridges," Civil Engineering Department, Report No. CCEER-92-4, University of Nevada, Reno, August 1992.

CCEER-92-5 Siddharthan, R., and Z. Zafir, "Response of Layered Deposits to Traveling Surface Pressure Waves," Civil Engineering Department, Report No. CCEER-92-5, University of Nevada, Reno, September 1992.

CCEER-92-6 Norris, G., and Z. Zafir, "Liquefaction and Residual Strength of Loose Sands from Drained Triaxial Tests," Civil Engineering Department, Report No. CCEER-92-6, University of Nevada, Reno, September 1992.

CCEER-92-6-A Norris, G., Siddharthan, R., Zafir, Z. and Madhu, R. "Liquefaction and Residual Strength of Sands from Drained Triaxial Tests," Civil Engineering Department, Report No. CCEER-92-6-A, University of Nevada, Reno, September 1992.

CCEER-92-7 Douglas, B., "Some Thoughts Regarding the Improvement of the University of Nevada, Reno's National Academic Standing," Civil Engineering Department, Report No. CCEER-92-7, University of Nevada, Reno, September 1992.

CCEER-92-8 Saiidi, M., E. Maragakis, and S. Feng, "An Evaluation of the Current Caltrans Seismic Restrainer Design Method," Civil Engineering Department, Report No. CCEER-92-8, University of Nevada, Reno, October 1992.

CCEER-92-9 O'Connor, D., M. Saiidi, and E. Maragakis, "Effect of Hinge Restrainers on the Response of the Madrone Drive Undercrossing During the Loma Prieta Earthquake," Civil Engineering Department, Report No. CCEER-92-9, University of Nevada, Reno, February 1993.

CCEER-92-10 O'Connor, D., and M. Saiidi, "Laboratory Studies of Polyester Concrete: Compressive Strength at Elevated Temperatures and Following Temperature Cycling, Bond Strength to Portland Cement Concrete, and Modulus of Elasticity," Civil Engineering Department, Report No. CCEER-92-10, University of Nevada, Reno, February 1993.

CCEER-92-11 Wehbe, N., M. Saiidi, and D. O'Connor, "Economic Impact of Passage of Spent Fuel Traffic on Two Bridges in Northeast Nevada," Civil Engineering Department, Report No. CCEER-92-11, University of Nevada, Reno, December 1992.

CCEER-93-1 Jiang, Y., and M. Saiidi, "Behavior, Design, and Retrofit of Reinforced Concrete One-way Bridge Column Hinges," edited by D. O'Connor, Civil Engineering Department, Report No. CCEER-93-1, University of Nevada, Reno, March 1993.

CCEER-93-2 Abdel-Ghaffar, S., E. Maragakis, and M. Saiidi, "Evaluation of the Response of the Aptos Creek Bridge During the 1989 Loma Prieta Earthquake," Civil Engineering Department, Report No. CCEER-93-2, University of Nevada, Reno, June 1993.

CCEER-93-3 Sanders, D.H., B.M. Douglas, and T.L. Martin, "Seismic Retrofit Prioritization of Nevada Bridges," Civil Engineering Department, Report No. CCEER-93-3, University of Nevada, Reno, July 1993.

CCEER-93-4 Abdel-Ghaffar, S., E. Maragakis, and M. Saiidi, "Performance of Hinge Restrainers in the Huntington Avenue Overhead During the 1989 Loma Prieta Earthquake," Civil Engineering Department, Report No. CCEER-93-4, University of Nevada, Reno, June 1993.

CCEER-93-5 Maragakis, E., M. Saiidi, S. Feng, and L. Flournoy, "Effects of Hinge Restrainers on the Response of the San Gregorio Bridge during the Loma Prieta Earthquake," (in final preparation) Civil Engineering Department, Report No. CCEER-93-5, University of Nevada, Reno.

CCEER-93-6 Saiidi, M., E. Maragakis, S. Abdel-Ghaffar, S. Feng, and D. O'Connor, "Response of Bridge Hinge Restrainers during Earthquakes -Field Performance, Analysis, and Design," Civil Engineering Department, Report No. CCEER-93-6, University of Nevada, Reno, May 1993.

CCEER-93-7 Wehbe, N., Saiidi, M., Maragakis, E., and Sanders, D., "Adequacy of Three Highway Structures in Southern Nevada for Spent Fuel Transportation," Civil Engineering Department, Report No. CCEER-93-7, University of Nevada, Reno, August 1993.

CCEER-93-8 Roybal, J., Sanders, D.H., and Maragakis, E., "Vulnerability Assessment of Masonry in the Reno-Carson City Urban Corridor," Civil Engineering Department, Report No. CCEER-93-8, University of Nevada, Reno, May 1993.

CCEER-93-9 Zafir, Z. and Siddharthan, R., "MOVLOAD: A Program to Determine the Behavior of Nonlinear Horizontally Layered Medium Under Moving Load," Civil Engineering Department, Report No. CCEER-93-9, University of Nevada, Reno, August 1993.

CCEER-93-10 O'Connor, D.N., Saiidi, M., and Maragakis, E.A., "A Study of Bridge Column Seismic Damage Susceptibility at the Interstate 80/U.S. 395 Interchange in Reno, Nevada," Civil Engineering Department, Report No. CCEER-93-10, University of Nevada, Reno, October 1993.

CCEER-94-1 Maragakis, E., B. Douglas, and E. Abdelwahed, "Preliminary Dynamic Analysis of a Railroad Bridge," Report CCEER-94-1, January 1994.

CCEER-94-2 Douglas, B.M., Maragakis, E.A., and Feng, S., "Stiffness Evaluation of Pile Foundation of Cazenovia Creek Overpass," Civil Engineering Department, Report No. CCEER-94-2, University of Nevada, Reno, March 1994.

CCEER-94-3 Douglas, B.M., Maragakis, E.A., and Feng, S., "Summary of Pretest Analysis of Cazenovia Creek Bridge," Civil Engineering Department, Report No. CCEER-94-3, University of Nevada, Reno, April 1994.

CCEER-94-4 Norris, G.M., Madhu, R., Valceschini, R., and Ashour, M., "Liquefaction and Residual Strength of Loose Sands from Drained Triaxial Tests," Report 2, Vol. 1&2, Civil Engineering Department, Report No. CCEER-94-4, University of Nevada, Reno, August 1994.

CCEER-94-5 Saiidi, M., Hutchens, E., and Gardella, D., "Prestress Losses in a Post-Tensioned R/C Box Girder Bridge in Southern Nevada," Civil Engineering Department, CCEER-94-5, University of Nevada, Reno, August 1994.

CCEER-95-1 Siddharthan, R., El-Gamal, M., and Maragakis, E.A., "Nonlinear Bridge Abutment , Verification, and Design Curves," Civil Engineering Department, CCEER-95-1, University of Nevada, Reno, January 1995.

CCEER-95-2 Ashour, M. and Norris, G., "Liquefaction and Undrained Response Evaluation of Sands from Drained Formulation," Civil Engineering Department, Report No. CCEER-95-2, University of Nevada, Reno, February 1995.

CCEER-95-3 Wehbe, N., Saiidi, M., Sanders, D. and Douglas, B., "Ductility of Rectangular Reinforced Concrete Bridge Columns with Moderate Confinement," Civil Engineering Department, Report No. CCEER-95-3, University of Nevada, Reno, July 1995.

CCEER-95-4 Martin, T.., Saiidi, M. and Sanders, D., "Seismic Retrofit of Column-Pier Cap Connections in Bridges in Northern Nevada," Civil Engineering Department, Report No. CCEER-95-4, University of Nevada, Reno, August 1995.

CCEER-95-5 Darwish, I., Saiidi, M. and Sanders, D., "Experimental Study of Seismic Susceptibility Column-

Footing Connections in Bridges in Northern Nevada," Civil Engineering Department, Report No. CCEER-95-5, University of Nevada, Reno, September 1995.

CCEER-95-6 Griffin, G., Saiidi, M. and Maragakis, E., "Nonlinear Seismic Response of Isolated Bridges and Effects of Pier Ductility Demand," Civil Engineering Department, Report No. CCEER-95-6, University of Nevada, Reno, November 1995.

CCEER-95-7 Acharya, S.., Saiidi, M. and Sanders, D., "Seismic Retrofit of Bridge Footings and Column-Footing Connections," Civil Engineering Department, Report No. CCEER-95-7, University of Nevada, Reno, November 1995.

CCEER-95-8 Maragakis, E., Douglas, B., and Sandirasegaram, U., "Full-Scale Field Resonance Tests of a Railway Bridge," A Report to the Association of American Railroads, Civil Engineering Department, Report No. CCEER-95-8, University of Nevada, Reno, December 1995.

CCEER-95-9 Douglas, B., Maragakis, E. and Feng, S., "System Identification Studies on Cazenovia Creek Overpass," Report for the National Center for Earthquake Engineering Research, Civil Engineering Department, Report No. CCEER-95-9, University of Nevada, Reno, October 1995.

CCEER-96-1 El-Gamal, M.E. and Siddharthan, R.V., "Programs to Computer Translational Stiffness of Seat-Type Bridge Abutment," Civil Engineering Department, Report No. CCEER-96-1, University of Nevada, Reno, March 1996.

CCEER-96-2 Labia, Y., Saiidi, M. and Douglas, B., "Evaluation and Repair of Full-Scale Prestressed Concrete Box Girders," A Report to the National Science Foundation, Research Grant CMS-9201908, Civil Engineering Department, Report No. CCEER-96-2, University of Nevada, Reno, May 1996.

CCEER-96-3 Darwish, I., Saiidi, M. and Sanders, D., "Seismic Retrofit of R/C Oblong Tapered Bridge Columns with Inadequate Bar Anchorage in Columns and Footings," A Report to the Nevada Department of Transportation, Civil Engineering Department, Report No. CCEER-96-3, University of Nevada, Reno, May 1996.

CCEER-96-4 Ashour, M., Pilling, R., Norris, G. and Perez, H., "The Prediction of Lateral Load Behavior of Single Piles and Pile Groups Using the Strain Wedge Model," A Report to the California Department of Transportation, Civil Engineering Department, Report No. CCEER-96-4, University of Nevada, Reno, June 1996.

CCEER-97-1-A Rimal, P. and Itani, A. "Sensitivity Analysis of Fatigue Evaluations of Steel Bridges," Center for Earthquake Research, Department of Civil Engineering, University of Nevada, Reno, Nevada Report No. CCEER-97-1-A, September, 1997.

CCEER-97-1-B Maragakis, E., Douglas, B., and Sandirasegaram, U. "Full-Scale Field Resonance Tests of a Railway Bridge," A Report to the Association of American Railroads, Civil Engineering Department, University of Nevada, Reno, May, 1996.

CCEER-97-2 Wehbe, N., Saiidi, M., and D. Sanders, "Effect of Confinement and Flares on the Seismic Performance of Reinforced Concrete Bridge Columns," Civil Engineering Department, Report No. CCEER-97-2, University of Nevada, Reno, September 1997.

CCEER-97-3 Darwish, I., M. Saiidi, G. Norris, and E. Maragakis, "Determination of In-Situ Footing Stiffness Using Full-Scale Dynamic Field Testing," A Report to the Nevada Department of Transportation, Structural Design Division, Carson City, Nevada, Report No. CCEER-97-3, University of Nevada, Reno, October 1997.

CCEER-97-4-A Itani, A. "Cyclic Behavior of Richmond-San Rafael Tower Links," Center for Civil Engineering

Earthquake Research, Department of Civil Engineering, University of Nevada, Reno, Nevada, Report No. CCEER-97-4, August 1997.

CCEER-97-4-B Wehbe, N., and M. Saiidi, "User's Manual for RCMC v. 1.2 : A Computer Program for Moment-Curvature Analysis of Confined and Unconfined Reinforced Concrete Sections," Center for Civil Engineering Earthquake Research, Department of Civil Engineering, University of Nevada, Reno, Nevada, Report No. CCEER-97-4, November, 1997.

CCEER-97-5 Isakovic, T., M. Saiidi, and A. Itani, "Influence of new Bridge Configurations on Seismic Performance," Department of Civil Engineering, University of Nevada, Reno, Report No. CCEER-97-5, September, 1997.

CCEER-98-1 Itani, A., Vesco, T. and Dietrich, A., "Cyclic Behavior of "as Built" Laced Members With End Gusset Plates on the San Francisco Bay Bridge," Center for Civil Engineering Earthquake Research, Department of Civil Engineering, University of Nevada, Reno, Nevada Report No. CCEER-98-1, March, 1998.

CCEER-98-2 G. Norris and M. Ashour, "Liquefaction and Undrained Response Evaluation of Sands from Drained Formulation," Center for Civil Engineering Earthquake Research, Department of Civil Engineering, University of Nevada, Reno, Nevada, Report No. CCEER-98-2, May, 1998.

CCEER-98-3 Qingbin, Chen, B. M. Douglas, E. Maragakis, and I. G. Buckle, "Extraction of Nonlinear Hysteretic Properties of Seismically Isolated Bridges from Quick-Release Field Tests," Center for Civil Engineering Earthquake Research, Department of Civil Engineering, University of Nevada, Reno, Nevada, Report No. CCEER-98-3, June, 1998.

CCEER-98-4 Maragakis, E., B. M. Douglas, and C. Qingbin, "Full-Scale Field Capacity Tests of a Railway Bridge," Center for Civil Engineering Earthquake Research, Department of Civil Engineering, University of Nevada, Reno, Nevada, Report No. CCEER-98-4, June, 1998.

CCEER-98-5 Itani, A., Douglas, B., and Woodgate, J., "Cyclic Behavior of Richmond-San Rafael Retrofitted Tower Leg," Center for Civil Engineering Earthquake Research, Department of Civil Engineering, University of Nevada, Reno. Report No. CCEER-98-5, June 1998

CCEER-98-6 Moore, R., Saiidi, M., and Itani, A., "Seismic Behavior of New Bridges with Skew and Curvature," Center for Civil Engineering Earthquake Research, Department of Civil Engineering, University of Nevada, Reno. Report No. CCEER-98-6, October, 1998.

CCEER-98-7 Itani, A and Dietrich, A, "Cyclic Behavior of Double Gusset Plate Connections," Center for Civil Engineering Earthquake Research, Department of Civil Engineering, University of Nevada, Reno, Nevada, Report No. CCEER-98-5, December, 1998.

CCEER-99-1 Caywood, C., M. Saiidi, and D. Sanders, "Seismic Retrofit of Flared Bridge Columns with Steel Jackets," Civil Engineering Department, University of Nevada, Reno, Report No. CCEER-99-1, February 1999.

CCEER-99-2 Mangoba, N., M. Mayberry, and M. Saiidi, "Prestress Loss in Four Box Girder Bridges in Northern Nevada," Civil Engineering Department, University of Nevada, Reno, Report No. CCEER-99-2, March 1999.

CCEER-99-3 Abo-Shadi, N., M. Saiidi, and D. Sanders, "Seismic Response of Bridge Pier Walls in the Weak Direction," Civil Engineering Department, University of Nevada, Reno, Report No. CCEER-99-3, April 1999.

CCEER-99-4 Buzick, A., and M. Saiidi, "Shear Strength and Shear Fatigue Behavior of Full-Scale Prestressed Concrete Box Girders," Civil Engineering Department, University of Nevada, Reno, Report No. CCEER-99-4, April 1999.

CCEER-99-5 Randall, M., M. Saiidi, E. Maragakis and T. Isakovic, "Restrainer Design Procedures For Multi-Span Simply-Supported Bridges," Civil Engineering Department, University of Nevada, Reno, Report No. CCEER-99-5, April 1999.

CCEER-99-6 Wehbe, N. and M. Saiidi, "User's Manual for RCMC v. 1.2, A Computer Program for Moment-Curvature Analysis of Confined and Unconfined Reinforced Concrete Sections," Civil Engineering Department, University of Nevada, Reno, Report No. CCEER-99-6, May 1999.

CCEER-99-7 Burda, J. and A. Itani, "Studies of Seismic Behavior of Steel Base Plates," Civil Engineering Department, University of Nevada, Reno, Report No. CCEER-99-7, May 1999.

CCEER-99-8 Ashour, M. and G. Norris, "Refinement of the Strain Wedge Model Program," Civil Engineering Department, University of Nevada, Reno, Report No. CCEER-99-8, March 1999.

CCEER-99-9 Dietrich, A., and A. Itani, "Cyclic Behavior of Laced and Perforated Steel Members on the San Francisco-Oakland Bay Bridge," Civil Engineering Department, University, Reno, Report No. CCEER-99-9, December 1999.

CCEER 99-10 Itani, A., A. Dietrich, "Cyclic Behavior of Built Up Steel Members and their Connections," Civil Engineering Department, University of Nevada, Reno, Report No. CCEER-99-10, December 1999.

CCEER 99-10-A Itani, A., E. Maragakis and P. He, "Fatigue Behavior of Riveted Open Deck Railroad Bridge Girders," Civil Engineering Department, University of Nevada, Reno, Report No. CCEER-99-10-A, August 1999.

CCEER 99-11 Itani, A., J. Woodgate, "Axial and Rotational Ductility of Built Up Structural Steel Members," Civil Engineering Department, University of Nevada, Reno, Report No. CCEER-99-11, December 1999.

CCEER-99-12 Sgambelluri, M., Sanders, D.H., and Saiidi, M.S., "Behavior of One-Way Reinforced Concrete Bridge Column Hinges in the Weak Direction," Department of Civil Engineering, University of Nevada, Reno, Report No. CCEER-99-12, December 1999.

CCEER-99-13 Laplace, P., Sanders, D.H., Douglas, B, and Saiidi, M, "Shake Table Testing of Flexure Dominated Reinforced Concrete Bridge Columns", Department of Civil Engineering, University of Nevada, Reno, Report No. CCEER-99-13, December 1999.

CCEER-99-14 Ahmad M. Itani, Jose A. Zepeda, and Elizabeth A. Ware "Cyclic Behavior of Steel Moment Frame Connections for the Moscone Center Expansion," Department of Civil Engineering, University of Nevada, Reno, Report No. CCEER-99-14, December 1999.

CCEER 00-1 Ashour, M., and Norris, G. "Undrained Lateral Pile and Pile Group Response in Saturated Sand," Civil Engineering Department, University of Nevada, Reno, Report No. CCEER-00-1, May 1999. January 2000.

CCEER 00-2 Saiidi, M. and Wehbe, N., "A Comparison of Confinement Requirements in Different Codes for Rectangular, Circular, and Double-Spiral RC Bridge Columns," Civil Engineering Department, University of Nevada, Reno, Report No. CCEER-00-2, January 2000.

CCEER 00-3 McElhaney, B., M. Saiidi, and D. Sanders, "Shake Table Testing of Flared Bridge Columns With Steel Jacket Retrofit," Civil Engineering Department, University of Nevada, Reno, Report No. CCEER-00-3, January 2000.

CCEER 00-4 Martinovic, F., M. Saiidi, D. Sanders, and F. Gordaninejad, "Dynamic Testing of Non-Prismatic Reinforced Concrete Bridge Columns Retrofitted with FRP Jackets," Civil Engineering Department, University of Nevada, Reno, Report No. CCEER-00-4, January 2000.

CCEER 00-5 Itani, A., and M. Saiidi, "Seismic Evaluation of Steel Joints for UCLA Center for Health Science Westwood Replacement Hospital," Civil Engineering Department, University of Nevada, Reno, Report No. CCEER-00-5, February 2000.

CCEER 00-6 Will, J. and D. Sanders, "High Performance Concrete Using Nevada Aggregates," Civil Engineering Department, University of Nevada, Reno, Report No. CCEER-00-6, May 2000.

CCEER 00-7 French, C., and M. Saiidi, "A Comparison of Static and Dynamic Performance of Models of Flared Bridge Columns," Civil Engineering Department, University of Nevada, Reno, Report No. CCEER-00-7, October 2000.

CCEER 00-8 Itani, A., H. Sedarat, "Seismic Analysis of the AISI LRFD Design Example of Steel Highway Bridges," Civil Engineering Department, University of Nevada, Reno, Report No. CCEER 00-08, November 2000.

CCEER 00-9 Moore, J., D. Sanders, and M. Saiidi, "Shake Table Testing of 1960's Two Column Bent with Hinges Bases," Civil Engineering Department, University of Nevada, Reno, Report No. CCEER 00-09, December 2000.

CCEER 00-10 Asthana, M., D. Sanders, and M. Saiidi, "One-Way Reinforced Concrete Bridge Column Hinges in the Weak Direction," Civil Engineering Department, University of Nevada, Reno, Report No. CCEER 00-10, April 2001.

CCEER 01-1 Ah Sha, H., D. Sanders, M. Saiidi, "Early Age Shrinkage and Cracking of Nevada Concrete Bridge Decks," Civil Engineering Department, University of Nevada, Reno, Report No. CCEER 01-01, May 2001.

CCEER 01-2 Ashour, M. and G. Norris, "Pile Group program for Full Material Modeling a Progressive Failure," Civil Engineering Department, University of Nevada, Reno, Report No. CCEER 01-02, July 2001.

CCEER 01-3 Itani, A., C. Lanaud, and P. Dusicka, "Non-Linear Finite Element Analysis of Built-Up Shear Links," Civil Engineering Department, University of Nevada, Reno, Report No. CCEER 01-03, July 2001.

CCEER 01-4 Saiidi, M., J. Mortensen, and F. Martinovic, "Analysis and Retrofit of Fixed Flared Columns with Glass Fiber-Reinforced Plastic Jacketing," Civil Engineering Department, University of Nevada, Reno, Report No. CCEER 01-4, August 2001

CCEER 01-5 Not Published

CCEER 01-6 Laplace, P., D. Sanders, and M. Saiidi, "Experimental Study and Analysis of Retrofitted Flexure and Shear Dominated Circular Reinforced Concrete Bridge Columns Subjected to Shake Table Excitation," Civil Engineering Department, University of Nevada, Reno, Report No. CCEER 01-6, June 2001.

CCEER 01-7 Reppi, F., and D. Sanders, "Removal and Replacement of Cast-in-Place, Post-tensioned, Box Girder Bridge," Civil Engineering Department, University of Nevada, Reno, Report No. CCEER 01-7, December 2001.

CCEER 02-1 Pulido, C., M. Saiidi, D. Sanders, and A. Itani, "Seismic Performance and Retrofitting of Reinforced Concrete Bridge Bents," Civil Engineering Department, University of Nevada, Reno, Report No. CCEER 02-1, January 2002.

CCEER 02-2 Yang, Q., M. Saiidi, H. Wang, and A. Itani, "Influence of Ground Motion Incoherency on Earthquake Response of Multi-Support Structures," Civil Engineering Department, University of Nevada, Reno, Report No. CCEER 02-2, May 2002.

CCEER 02-3 M. Saiidi, B. Gopalakrishnan, E. Reinhardt, and R. Siddharthan, "A Preliminary Study of Shake Table Response of A Two-Column Bridge Bent on Flexible Footings," Civil Engineering Department, University of Nevada, Reno, Report No. CCEER 02-03, June 2002.

CCEER 02-4 Not Published

CCEER 02-5 Banghart, A., Sanders, D., Saiidi, M., "Evaluation of Concrete Mixes for Filling the Steel Arches in the Galena Creek Bridge," Civil Engineering Department, University of Nevada, Reno, Report No. CCEER 02-05, June 2002.

CCEER 02-6 Dusicka, P., Itani, A., Buckle, I. G., "Cyclic Behavior of Shear Links and Tower Shaft Assembly of San Francisco – Oakland Bay Bridge Tower," Civil Engineering Department, University of Nevada, Reno, Report No. CCEER 02-06, July 2002.

CCEER 02-7 Mortensen, J., and M. Saiidi, "A Performance-Based Design Method for Confinement in Circular Columns," Civil Engineering Department, University of Nevada, Reno, Report No. CCEER 02-07, November 2002.

CCEER 03-1 Wehbe, N., and M. Saiidi, "User's manual for SPMC v. 1.0 : A Computer Program for Moment-Curvature Analysis of Reinforced Concrete Sections with Interlocking Spirals," Center for Civil Engineering Earthquake Research, Department of Civil Engineering, University of Nevada, Reno, Nevada, Report No. CCEER-03-1, May, 2003.

CCEER 03-2 Wehbe, N., and M. Saiidi, "User's manual for RCMC v. 2.0 : A Computer Program for Moment-Curvature Analysis of Confined and Unconfined Reinforced Concrete Sections," Center for Civil Engineering Earthquake Research, Department of Civil Engineering, University of Nevada, Reno, Nevada, Report No. CCEER-03-2, June, 2003.

CCEER 03-3 Nada, H., D. Sanders, and M. Saiidi, "Seismic Performance of RC Bridge Frames with Architectural-Flared Columns," Civil Engineering Department, University of Nevada, Reno, Report No. CCEER 03-3, January 2003.

CCEER 03-4 Reinhardt, E., M. Saiidi, and R. Siddharthan, "Seismic Performance of a CFRP/ Concrete Bridge Bent on Flexible Footings," Civil Engineering Department, University of Nevada, Reno, Report No. CCEER 03-4, August 2003.

CCEER 03-5 Johnson, N., M. Saiidi, A. Itani, and S. Ladkany, "Seismic Retrofit of Octagonal Columns with Pedestal and One-Way Hinge at the Base," Center for Civil Engineering Earthquake Research, Department of Civil Engineering, University of Nevada, Reno, Nevada, and Report No. CCEER-03-5, August 2003.

CCEER 03-6 Mortensen, C., M. Saiidi, and S. Ladkany, "Creep and Shrinkage Losses in Highly Variable Climates," Center for Civil Engineering Earthquake Research, Department of Civil Engineering, University of Nevada, Reno, Report No. CCEER-03-6, September 2003.

CCEER 03- 7 Ayoub, C., M. Saiidi, and A. Itani, "A Study of Shape-Memory-Alloy-Reinforced Beams and Cubes," Center for Civil Engineering Earthquake Research, Department of Civil Engineering, University of Nevada, Reno, Nevada, Report No. CCEER-03-7, October 2003.

CCEER 03-8 Chandane, S., D. Sanders, and M. Saiidi, "Static and Dynamic Performance of RC Bridge Bents with Architectural-Flared Columns," Center for Civil Engineering Earthquake Research, Department of Civil Engineering, University of Nevada, Reno, Nevada, Report No. CCEER-03-8, November 2003.

CCEER 04-1 Olaegbe, C., and Saiidi, M., "Effect of Loading History on Shake Table Performance of A Two-Column Bent with Infill Wall," Center for Civil Engineering Earthquake Research, Department of Civil Engineering, University of Nevada, Reno, Nevada, Report No. CCEER-04-1, January 2004.

CCEER 04-2 Johnson, R., Maragakis, E., Saiidi, M., and DesRoches, R., "Experimental Evaluation of Seismic Performance of SMA Bridge Restrainers," Center for Civil Engineering Earthquake Research, Department of Civil Engineering, University of Nevada, Reno, Nevada, Report No. CCEER-04-2, February 2004.

CCEER 04-3 Moustafa, K., Sanders, D., and Saiidi, M., "Impact of Aspect Ratio on Two-Column Bent Seismic Performance," Center for Civil Engineering Earthquake Research, Department of Civil Engineering, University of Nevada, Reno, Nevada, Report No. CCEER-04-3, February 2004.

CCEER 04-4 Maragakis, E., Saiidi, M., Sanchez-Camargo, F., and Elfass, S., "Seismic Performance of Bridge Restrainers At In-Span Hinges," Center for Civil Engineering Earthquake Research, Department of Civil Engineering, University of Nevada, Reno, Nevada, Report No. CCEER-04-4, March 2004.

CCEER 04-5 Ashour, M., Norris, G. and Elfass, S., "Analysis of Laterally Loaded Long or Intermediate Drilled Shafts of Small or Large Diameter in Layered Soil," Center for Civil Engineering Earthquake Research, Department of Civil Engineering, University of Nevada, Reno, Nevada, Report No. CCEER-04-5, June 2004.

CCEER 04-6 Correal, J., Saiidi, M. and Sanders, D., "Seismic Performance of RC Bridge Columns Reinforced with Two Interlocking Spirals," Center for Civil Engineering Earthquake Research, Department of Civil Engineering, University of Nevada, Reno, Nevada, Report No. CCEER-04-6, August 2004.

CCEER 04-7 Dusicka, P., Itani, A. and Buckle, I., "Cyclic Response and Low Cycle Fatigue Characteristics of Plate Steels," Center for Civil Engineering Earthquake Research, Department of Civil Engineering, University of Nevada, Reno, Nevada, Report No. CCEER-04-7, November 2004.

CCEER 04-8 Dusicka, P., Itani, A. and Buckle, I., "Built-up Shear Links as Energy Dissipaters for Seismic Protection of Bridges," Center for Civil Engineering Earthquake Research, Department of Civil Engineering, University of Nevada, Reno, Nevada, Report No. CCEER-04-8, November 2004.

CCEER 04-9 Sureshkumar, K., Saiidi, S., Itani, A. and Ladkany, S., "Seismic Retrofit of Two-Column Bents with Diamond Shape Columns," Center for Civil Engineering Earthquake Research, Department of Civil Engineering, University of Nevada, Reno, Nevada, Report No. CCEER-04-9, November 2004.

CCEER 05-1 Wang, H. and Saiidi, S., "A Study of RC Columns with Shape Memory Alloy and Engineered Cementitious Composites," Center for Civil Engineering Earthquake Research, Department of Civil Engineering, University of Nevada, Reno, Nevada, Report No. CCEER-05-1, January 2005.

CCEER 05-2 Johnson, R., Saiidi, S. and Maragakis, E., "A Study of Fiber Reinforced Plastics for Seismic Bridge Restrainers," Center for Civil Engineering Earthquake Research, Department of Civil Engineering, University of Nevada, Reno, Nevada, Report No. CCEER-05-2, January 2005.

CCEER 05-3 Carden, L.P., Itani, A.M., Buckle, I.G, "Seismic Load Path in Steel Girder Bridge Superstructures," Center for Civil Engineering Earthquake Research, Department of Civil Engineering, University of Nevada, Reno, Nevada, Report No. CCEER-05-3, January 2005.

CCEER 05-4 Carden, L.P., Itani, A.M., Buckle, I.G, "Seismic Performance of Steel Girder Bridge Superstructures with Ductile End Cross Frames and Seismic Isolation," Center for Civil Engineering Earthquake Research, Department of Civil Engineering, University of Nevada, Reno, Nevada, Report No. CCEER-05-4, January 2005.

CCEER 05-5 Goodwin, E., Maragakis, M., Itani, A. and Luo, S., "Experimental Evaluation of the Seismic Performance of Hospital Piping Subassemblies," Center for Civil Engineering Earthquake Research, Department of Civil Engineering, University of Nevada, Reno, Nevada, Report No. CCEER-05-5, February 2005.

CCEER 05-6 Zadeh M. S., Saiidi, S, Itani, A. and Ladkany, S., "Seismic Vulnerability Evaluation and Retrofit Design of Las Vegas Downtown Viaduct," Center for Civil Engineering Earthquake Research, Department of Civil Engineering, University of Nevada, Reno, Nevada, Report No. CCEER-05-6, February 2005.

CCEER 05-7 Phan, V., Saiidi, S. and Anderson, J., "Near Fault (Near Field) Ground Motion Effects on Reinforced Concrete Bridge Columns," Center for Civil Engineering Earthquake Research, Department of Civil Engineering, University of Nevada, Reno, Nevada, Report No. CCEER-05-7, August 2005.

CCEER 05-8 Carden, L., Itani, A. and Laplace, P., "Performance of Steel Props at the UNR Fire Science Academy subjected to Repeated Fire," Center for Civil Engineering Earthquake Research, Department of Civil Engineering, University of Nevada, Reno, Nevada, Report No. CCEER-05-8, August 2005.

CCEER 05-9 Yamashita, R. and Sanders, D., "Shake Table Testing and an Analytical Study of Unbonded Prestressed Hollow Concrete Column Constructed with Precast Segments," Center for Civil Engineering Earthquake Research, Department of Civil Engineering, University of Nevada, Reno, Nevada, Report No. CCEER-05-9, August 2005.

CCEER 05-10 Not Published

CCEER 05-11 Carden, L., Itani., A., and Peckan, G., "Recommendations for the Design of Beams and Posts in Bridge Falsework," Center for Civil Engineering Earthquake Research, Department of Civil Engineering, University of Nevada, Reno, Nevada, Report No. CCEER-05-11, October 2005.

CCEER 06-01 Cheng, Z., Saiidi, M., and Sanders, D., "Development of a Seismic Design Method for Reinforced Concrete Two-Way Bridge Column Hinges," Center for Civil Engineering Earthquake Research, Department of Civil Engineering, University of Nevada, Reno, Nevada, Report No. CCEER-06-01, February 2006.

CCEER 06-02 Johnson, N., Saiidi, M., and Sanders, D., "Large-Scale Experimental and Analytical Studies of a Two-Span Reinforced Concrete Bridge System," Center for Civil Engineering Earthquake Research, Department of Civil Engineering, University of Nevada, Reno, Nevada, Report No. CCEER-06-02, March 2006.

CCEER 06-03 Saiidi, M., Ghasemi, H. and Tiras, A., "Seismic Design and Retrofit of Highway Bridges," Proceedings, Second US-Turkey Workshop, Center for Civil Engineering Earthquake Research, Department of Civil Engineering, University of Nevada, Reno, Nevada, Report No. CCEER-06-03, May 2006.

CCEER 07-01 O'Brien, M., Saiidi, M. and Sadrossadat-Zadeh, M., "A Study of Concrete Bridge Columns Using Innovative Materials Subjected to Cyclic Loading," Center for Civil Engineering Earthquake Research, Department of Civil Engineering, University of Nevada, Reno, Nevada, Report No. CCEER-07-01, January 2007.

CCEER 07-02 Sadrossadat-Zadeh, M. and Saiidi, M., "Effect of Strain rate on Stress-Strain Properties and Yield Propagation in Steel Reinforcing Bars," Center for Civil Engineering Earthquake Research, Department of Civil Engineering, University of Nevada, Reno, Nevada, Report No. CCEER-07-02, January 2007.

CCEER 07-03 Sadrossadat-Zadeh, M. and Saiidi, M., "Analytical Study of NEESR-SG 4-Span Bridge Model Using OpenSees," Center for Civil Engineering Earthquake Research, Department of Civil Engineering, University of Nevada, Reno, Nevada, Report No. CCEER-07-03, January 2007.

CCEER 07-04 Nelson, R., Saiidi, M. and Zadeh, S., "Experimental Evaluation of Performance of Conventional Bridge Systems," Center for Civil Engineering Earthquake Research, Department of Civil Engineering, University of Nevada, Reno, Nevada, Report No. CCEER-07-04, October 2007.

CCEER 07-05 Bahen, N. and Sanders, D., "Strut-and-Tie Modeling for Disturbed Regions in Structural Concrete Members with Emphasis on Deep Beams," Center for Civil Engineering Earthquake Research, Department of Civil Engineering, University of Nevada, Reno, Nevada, Report No. CCEER-07-05, December 2007.

CCEER 07-06 Choi, H., Saiidi, M. and Somerville, P., "Effects of Near-Fault Ground Motion and Fault-Rupture on the Seismic Response of Reinforced Concrete Bridges," Center for Civil Engineering Earthquake Research, Department of Civil Engineering, University of Nevada, Reno, Nevada, Report No. CCEER-07-06, December 2007.

CCEER 07-07 Ashour M. and Norris, G., "Report and User Manual on Strain Wedge Model Computer Program for Files and Large Diameter Shafts with LRFD Procedure," Center for Civil Engineering Earthquake Research, Department of Civil Engineering, University of Nevada, Reno, Nevada, Report No. CCEER-07-07, October 2007.

CCEER 08-01 Doyle, K. and Saiidi, M., "Seismic Response of Telescopic Pipe Pin Connections," Center for Civil Engineering Earthquake Research, Department of Civil Engineering, University of Nevada, Reno, Nevada, Report No. CCEER-08-01, February 2008.

CCEER 08-02 Taylor, M. and Sanders, D., "Seismic Time History Analysis and Instrumentation of the Galena Creek Bridge," Center for Civil Engineering Earthquake Research, Department of Civil Engineering, University of Nevada, Reno, Nevada, Report No. CCEER-08-02, April 2008.

CCEER 08-03 Abdel-Mohti, A. and Pekcan, G., "Seismic Response Assessment and Recommendations for the Design of Skewed Post-Tensioned Concrete Box-Girder Highway Bridges," Center for Civil Engineering Earthquake Research, Department of Civil and Environmental Engineering, University of Nevada, Reno, Nevada, Report No. CCEER-08-03, September 2008.

CCEER 08-04 Saiidi, M., Ghasemi, H. and Hook, J., "Long Term Bridge Performance Monitoring, Assessment & Management," Proceedings, FHWA/NSF Workshop on Future Directions," Center for Civil Engineering Earthquake Research, Department of Civil and Environmental Engineering, University of Nevada, Reno, Nevada, Report No. CCEER 08-04, September 2008.

CCEER 09-01 Brown, A., and Saiidi, M., "Investigation of Near-Fault Ground Motion Effects on Substandard Bridge Columns and Bents," Center for Civil Engineering Earthquake Research, Department of Civil and Environmental Engineering, University of Nevada, Reno, Nevada, Report No. CCEER-09-01, July 2009.

CCEER 09-02 Linke, C., Pekcan, G., and Itani, A., "Detailing of Seismically Resilient Special Truss Moment Frames," Center for Civil Engineering Earthquake Research, Department of Civil and

Environmental Engineering, University of Nevada, Reno, Nevada, Report No. CCEER-09-02, August 2009.

CCEER 09-03 Hillis, D., and Saiidi, M., "Design, Construction, and Nonlinear Dynamic Analysis of Three Bridge Bents Used in a Bridge System Test," Center for Civil Engineering Earthquake Research, Department of Civil and Environmental Engineering, University of Nevada, Reno, Nevada, Report No. CCEER-09-03, August 2009.

CCEER 09-04 Bahrami, H., Itani, A., and Buckle, I., "Guidelines for the Seismic Design of Ductile End Cross Frames in Steel Girder Bridge Superstructures," Center for Civil Engineering Earthquake Research, Department of Civil and Environmental Engineering, University of Nevada, Reno, Nevada, Report No. CCEER-09-04, September 2so009.

CCEER 10-01 Zaghi, A. E., and Saiidi, M., "Seismic Design of Pipe-Pin Connections in Concrete Bridges," Center for Civil Engineering Earthquake Research, Department of Civil and Environmental Engineering, University of Nevada, Reno, Nevada, Report No. CCEER-10-01, January 2010.

CCEER 10-02 Pooranampillai, S., Elfass, S., and Norris, G., "Laboratory Study to Assess Load Capacity Increase of Drilled Shafts through Post Grouting," Center for Civil Engineering Earthquake Research, Department of Civil and Environmental Engineering, University of Nevada, Reno, Nevada, Report No. CCEER-10-02, January 2010.

CCEER 10-03 Itani, A., Grubb, M., and Monzon, E, "Proposed Seismic Provisions and Commentary for Steel Plate Girder Superstructures," Center for Civil Engineering Earthquake Research, Department of Civil and Environmental Engineering, University of Nevada, Reno, Nevada, Report No. CCEER-10-03, June 2010.

CCEER 10-04 Cruz-Noguez, C., Saiidi, M., "Experimental and Analytical Seismic Studies of a Four-Span Bridge System with Innovative Materials," Center for Civil Engineering Earthquake Research, Department of Civil and Environmental Engineering, University of Nevada, Reno, Nevada, Report No. CCEER-10-04, September 2010.

CCEER 10-05 Vosooghi, A., Saiidi, M., "Post-Earthquake Evaluation and Emergency Repair of Damaged RC Bridge Columns Using CFRP Materials," Center for Civil Engineering Earthquake Research, Department of Civil and Environmental Engineering, University of Nevada, Reno, Nevada, Report No. CCEER-10-05, September 2010.

CCEER 10-06 Ayoub, M., Sanders, D., "Testing of Pile Extension Connections to Slab Bridges," Center for Civil Engineering Earthquake Research, Department of Civil and Environmental Engineering, University of Nevada, Reno, Nevada, Report No. CCEER-10-06, October 2010.

CCEER 10-07 Builes-Mejia, J. C. and Itani, A., "Stability of Bridge Column Rebar Cages during Construction," Center for Civil Engineering Earthquake Research, Department of Civil and Environmental Engineering, University of Nevada, Reno, Nevada, Report No. CCEER-10-07, November 2010.

CCEER 10-08 Monzon, E.V., "Seismic Performance of Steel Plate Girder Bridges with Integral Abutments," Center for Civil Engineering Earthquake Research, Department of Civil and Environmental Engineering, University of Nevada, Reno, Nevada, Report No. CCEER-10-08, November 2010.

CCEER 11-01 Motaref, S., Saiidi, M., and Sanders, D., "Seismic Response of Precast Bridge Columns with Energy Dissipating Joints," Center for Civil Engineering Earthquake Research, Department of Civil and Environmental Engineering, University of Nevada, Reno, Nevada, Report No. CCEER-11-01, May 2011.

CCEER 11-02 Harrison, N. and Sanders, D., "Preliminary Seismic Analysis and Design of Reinforced Concrete Bridge Columns for Curved Bridge Experiments," Center for Civil Engineering Earthquake Research, Department of Civil and Environmental Engineering, University of Nevada, Reno, Nevada, Report No. CCEER-11-02, May 2011.

CCEER 11-03 Vallejera, J. and Sanders, D., "Instrumentation and Monitoring the Galena Creek Bridge," Center for Civil Engineering Earthquake Research, Department of Civil and Environmental Engineering, University of Nevada, Reno, Nevada, Report No. CCEER-11-03, September 2011.

CCEER 11-04 Levi, M., Sanders, D., and Buckle, I., "Seismic Response of Columns in Horizontally Curved Bridges," Center for Civil Engineering Earthquake Research, Department of Civil and Environmental Engineering, University of Nevada, Reno, Nevada, Report No. CCEER-11-04, December 2011.

CCEER 12-01 Saiidi, M., "NSF International Workshop on Bridges of the Future – Wide Spread Implementation of Innovation," Center for Civil Engineering Earthquake Research, Department of Civil and Environmental Engineering, University of Nevada, Reno, Nevada, Report No. CCEER-12-01, January 2012.

CCEER 12-02 Larkin, A.S., Sanders, D., and Saiidi, M., "Unbonded Prestressed Columns for Earthquake Resistance," Center for Civil Engineering Earthquake Research, Department of Civil and Environmental Engineering, University of Nevada, Reno, Nevada, Report No. CCEER-12-02, January 2012.

CCEER 12-03 Arias-Acosta, J. G., Sanders, D., "Seismic Performance of Circular and Interlocking Spirals RC Bridge Columns under Bidirectional Shake Table Loading Part 1," Center for Civil Engineering Earthquake Research, Department of Civil and Environmental Engineering, University of Nevada, Reno, Nevada, Report No. CCEER-12-03, September 2012.

CCEER 12-04 Cukrov, M.E., Sanders, D., "Seismic Performance of Prestressed Pile-To-Bent Cap Connections," Center for Civil Engineering Earthquake Research, Department of Civil and Environmental Engineering, University of Nevada, Reno, Nevada, Report No. CCEER-12-04, September 2012.

CCEER 13-01 Carr, T. and Sanders, D., "Instrumentation and Dynamic Characterization of the Galena Creek Bridge," Center for Civil Engineering Earthquake Research, Department of Civil and Environmental Engineering, University of Nevada, Reno, Nevada, Report No. CCEER-13-01, January 2013.

CCEER 13-02 Vosooghi, A. and Buckle, I., "Evaluation of the Performance of a Conventional Four-Span Bridge During Shake Table Tests," Center for Civil Engineering Earthquake Research, Department of Civil and Environmental Engineering, University of Nevada, Reno, Nevada, Report No. CCEER-13-02, January 2013.

CCEER 13-03 Amirihormozaki, E. and Pekcan, G., "Analytical Fragility Curves for Horizontally Curved Steel Girder Highway Bridges," Center for Civil Engineering Earthquake Research, Department of Civil and Environmental Engineering, University of Nevada, Reno, Nevada, Report No. CCEER-13-03, February 2013.

CCEER 13-04 Almer, K. and Sanders, D., "Longitudinal Seismic Performance of Precast Bridge Girders Integrally Connected to a Cast-in-Place Bentcap," Center for Civil Engineering Earthquake Research, Department of Civil and Environmental Engineering, University of Nevada, Reno, Nevada, Report No. CCEER-13-04, April 2013.

CCEER 13-05 Monzon, E.V., Itani, A.I., and Buckle, I.G., "Seismic Modeling and Analysis of Curved Steel Plate Girder Bridges," Center for Civil Engineering Earthquake Research, Department of Civil and Environmental Engineering, University of Nevada, Reno, Nevada, Report No. CCEER-13-05, April 2013.

CCEER 13-06 Monzon, E.V., Buckle, I.G., and Itani, A.I., "Seismic Performance of Curved Steel Plate Girder Bridges with Seismic Isolation," Center for Civil Engineering Earthquake Research, Department of Civil and Environmental Engineering, University of Nevada, Reno, Nevada, Report No. CCEER-13-06, April 2013.

CCEER 13-07 Monzon, E.V., Buckle, I.G., and Itani, A.I., "Seismic Response of Isolated Bridge Superstructure to Incoherent Ground Motions," Center for Civil Engineering Earthquake Research, Department of Civil and Environmental Engineering, University of Nevada, Reno, Nevada, Report No. CCEER-13-07, April 2013.

CCEER 13-08 Haber, Z.B., Saiidi, M.S., and Sanders, D.H., "Precast Column-Footing Connections for Accelerated Bridge Construction in Seismic Zones," Center for Civil Engineering Earthquake Research, Department of Civil and Environmental Engineering, University of Nevada, Reno, Nevada, Report No. CCEER-13-08, April 2013.

CCEER 13-09 Ryan, K.L., Coria, C.B., and Dao, N.D., "Large Scale Earthquake Simulation of a Hybrid Lead Rubber Isolation System Designed under Nuclear Seismicity Considerations," Center for Civil Engineering Earthquake Research, Department of Civil and Environmental Engineering, University of Nevada, Reno, Nevada, Report No. CCEER-13-09, April 2013.

CCEER 13-10 Wibowo, H., Sanford, D.M., Buckle, I.G., and Sanders, D.H., "The Effect of Live Load on the Seismic Response of Bridges," Center for Civil Engineering Earthquake Research, Department of Civil and Environmental Engineering, University of Nevada, Reno, Nevada, Report No. CCEER-13-10, May 2013.

CCEER 13-11 Sanford, D.M., Wibowo, H., Buckle, I.G., and Sanders, D.H., "Preliminary Experimental Study on the Effect of Live Load on the Seismic Response of Highway Bridges," Center for Civil Engineering Earthquake Research, Department of Civil and Environmental Engineering, University of Nevada, Reno, Nevada, Report No. CCEER-13-11, May 2013.

CCEER 13-12 Saad, A.S., Sanders, D.H., and Buckle, I.G., "Assessment of Foundation Rocking Behavior in Reducing the Seismic Demand on Horizontally Curved Bridges," Center for Civil Engineering Earthquake Research, Department of Civil and Environmental Engineering, University of Nevada, Reno, Nevada, Report No. CCEER-13-12, June 2013.

CCEER 13-13 Ardakani, S.M.S. and Saiidi, M.S., "Design of Reinforced Concrete Bridge Columns for Near-Fault Earthquakes," Center for Civil Engineering Earthquake Research, Department of Civil and Environmental Engineering, University of Nevada, Reno, Nevada, Report No. CCEER-13-13, July 2013.

CCEER 13-14 Wei, C. and Buckle, I., "Seismic Analysis and Response of Highway Bridges with Hybrid Isolation," Center for Civil Engineering Earthquake Research, Department of Civil and Environmental Engineering, University of Nevada, Reno, Nevada, Report No. CCEER-13-14, August 2013.

CCEER 13-15 Wibowo, H., Buckle, I.G., and Sanders, D.H., "Experimental and Analytical Investigations on the Effects of Live Load on the Seismic Performance of a Highway Bridge," Center for Civil Engineering Earthquake Research, Department of Civil and Environmental Engineering, University of Nevada, Reno, Nevada, Report No. CCEER-13-15, August 2013.

CCEER 13-16 Itani, A.M., Monzon, E.V., Grubb, M., and Amirihormozaki, E. "Seismic Design and Nonlinear Evaluation of Steel I-Girder Bridges with Ductile End Cross-Frames," Center for Civil Engineering Earthquake Research, Department of Civil and Environmental Engineering, University of Nevada, Reno, Nevada, Report No. CCEER-13-16, September 2013.

CCEER 13-17 Kavianipour, F. and Saiidi, M.S., "Experimental and Analytical Seismic Studies of a Four-span Bridge System with Composite Piers," Center for Civil Engineering Earthquake Research, Department of Civil and Environmental Engineering, University of Nevada, Reno, Nevada, Report No. CCEER-13-17, September 2013.

CCEER 13-18 Mohebbi, A., Ryan, K., and Sanders, D., "Seismic Response of a Highway Bridge with Structural Fuses for Seismic Protection of Piers," Center for Civil Engineering Earthquake Research, Department of Civil and Environmental Engineering, University of Nevada, Reno, Nevada, Report No. CCEER-13-18, December 2013.

CCEER 13-19 Guzman Pujols, Jean C., Ryan, K.L., "Development of Generalized Fragility Functions for Seismic Induced Content Disruption," Center for Civil Engineering Earthquake Research, Department of Civil and Environmental Engineering, University of Nevada, Reno, Nevada, Report No. CCEER-13-19, December 2013.

CCEER 14-01 Salem, M. M. A., Pekcan, G., and Itani, A., "Seismic Response Control Of Structures Using Semi-Active and Passive Variable Stiffness Devices," Center for Civil Engineering Earthquake Research, Department of Civil and Environmental Engineering, University of Nevada, Reno, Nevada, Report No. CCEER-14-01, May 2014.

CCEER 14-02 Saini, A. and Saiidi, M., "Performance-Based Probabilistic Damage Control Approach for Seismic Design of Bridge Columns," Center For Civil Engineering Earthquake Research, Department Of Civil and Environmental Engineering, University of Nevada, Reno, Nevada, Report No. CCEER-14-02, May 2014.

CCEER 14-03 Saini, A. and Saiidi, M., "Post Earthquake Damage Repair of Various Reinforced Concrete Bridge Components," Center For Civil Engineering Earthquake Research, Department Of Civil and Environmental Engineering, University of Nevada, Reno, Nevada, Report No. CCEER-14-03, May 2014.

CCEER 14-04 Monzon, E.V., Itani, A.M., and Grubb, M.A., "Nonlinear Evaluation of the Proposed Seismic Design Procedure for Steel Bridges with Ductile End Cross Frames," Center For Civil Engineering Earthquake Research, Department Of Civil and Environmental Engineering, University of Nevada, Reno, Nevada, Report No. CCEER-14-04, July 2014.

CCEER 14-05 Nakashoji, B. and Saiidi, M.S., "Seismic Performance of Square Nickel-Titanium Reinforced ECC Columns with Headed Couplers," Center For Civil Engineering Earthquake Research, Department Of Civil and Environmental Engineering, University of Nevada, Reno, Nevada, Report No. CCEER-14-05, July 2014.

CCEER 14-06 Tazarv, M. and Saiidi, M.S., "Next Generation of Bridge Columns for Accelerated Bridge Construction in High Seismic Zones," Center For Civil Engineering Earthquake Research, Department Of Civil and Environmental Engineering, University of Nevada, Reno, Nevada, Report No. CCEER-14-06, August 2014.

CCEER 14-07 Mehrsoroush, A. and Saiidi, M.S., "Experimental and Analytical Seismic Studies of Bridge Piers with Innovative Pipe Pin Column-Footing Connections and Precast Cap Beams," Center For Civil Engineering Earthquake Research, Department Of Civil and Environmental Engineering, University of Nevada, Reno, Nevada, Report No. CCEER-14-07, December 2014.

CCEER 15-01 Dao, N.D. and Ryan, K.L., "Seismic Response of a Full-scale 5-story Steel Frame Building Isolated by Triple Pendulum Bearings under 3D Excitations," Center For Civil Engineering

Earthquake Research, Department Of Civil and Environmental Engineering, University of Nevada, Reno, Nevada, Report No. CCEER-15-01, January 2015.

CCEER 15-02 Allen, B.M. and Sanders, D.H., "Post-Tensioning Duct Air Pressure Testing Effects on Web Cracking," Center For Civil Engineering Earthquake Research, Department Of Civil and Environmental Engineering, University of Nevada, Reno, Nevada, Report No. CCEER-15-02, January 2015.

CCEER 15-03 Akl, A. and Saiidi, M.S., "Time-Dependent Deflection of In-Span Hinges in Prestressed Concrete Box Girder Bridges," Center For Civil Engineering Earthquake Research, Department Of Civil and Environmental Engineering, University of Nevada, Reno, Nevada, Report No. CCEER-15-03, May 2015.

CCEER 15-04 Zargar Shotorbani, H. and Ryan, K., "Analytical and Experimental Study of Gap Damper System to Limit Seismic Isolator Displacements in Extreme Earthquakes," Center For Civil Engineering Earthquake Research, Department Of Civil and Environmental Engineering, University of Nevada, Reno, Nevada, Report No. CCEER-15-04, June 2015.

CCEER 15-05 Wieser, J., Maragakis, E.M., and Buckle, I., "Experimental and Analytical Investigation of Seismic Bridge-Abutment Interaction in a Curved Highway Bridge," Center For Civil Engineering Earthquake Research, Department Of Civil and Environmental Engineering, University of Nevada, Reno, Nevada, Report No. CCEER-15-05, July 2015.

CCEER 15-06 Tazarv, M. and Saiidi, M.S., "Design and Construction of Precast Bent Caps with Pocket Connections for High Seismic Regions," Center For Civil Engineering Earthquake Research, Department Of Civil and Environmental Engineering, University of Nevada, Reno, Nevada, Report No. CCEER-15-06, August 2015.

CCEER 15-07 Tazarv, M. and Saiidi, M.S., "Design and Construction of Bridge Columns Incorporating Mechanical Bar Splices in Plastic Hinge Zones," Center For Civil Engineering Earthquake Research, Department Of Civil and Environmental Engineering, University of Nevada, Reno, Nevada, Report No. CCEER-15-07, August 2015.

CCEER 15-08 Sarraf Shirazi, R., Pekcan, G., and Itani, A.M., "Seismic Response and Analytical Fragility Functions for Curved Concrete Box-Girder Bridges," Center For Civil Engineering Earthquake Research, Department Of Civil and Environmental Engineering, University of Nevada, Reno, Nevada, Report No. CCEER-15-08, December 2015.

CCEER 15-09 Coria, C.B., Ryan, K.L., and Dao, N.D., "Response of Lead Rubber Bearings in a Hybrid Isolation System During a Large Scale Shaking Experiment of an Isolated Building," Center For Civil Engineering Earthquake Research, Department Of Civil and Environmental Engineering, University of Nevada, Reno, Nevada, Report No. CCEER-15-09, December 2015.

CCEER 16-01 Mehraein, M and Saiidi, M.S., "Seismic Performance of Bridge Column-Pile-Shaft Pin Connections for Application in Accelerated Bridge Construction," Center For Civil Engineering Earthquake Research, Department Of Civil and Environmental Engineering, University of Nevada, Reno, Nevada, Report No. CCEER-16-01, May 2016.

CCEER 16-02 Varela Fontecha, S. and Saiidi, M.S., "Resilient Earthquake-Resistant Bridges Designed For Disassembly," Center For Civil Engineering Earthquake Research, Department Of Civil and Environmental Engineering, University of Nevada, Reno, Nevada, Report No. CCEER-16-02, May 2016.

CCEER 16-03 Mantawy, I. M, and Sanders, D. H., "Assessment of an Earthquake Resilient Bridge with Pretensioned, Rocking Columns," Center For Civil Engineering Earthquake Research, Department

Of Civil and Environmental Engineering, University of Nevada, Reno, Nevada, Report No. CCEER-16-03, May 2016.

CCEER 16-04 Mohammed, M, Biasi, G., and Sanders, D., "Post-earthquake Assessment of Nevada Bridges using ShakeMap/ShakeCast," Center For Civil Engineering Earthquake Research, Department Of Civil and Environmental Engineering, University of Nevada, Reno, Nevada, Report No. CCEER-16-04, May 2016.

CCEER 16-05 Jones, J, Ryan, K., and Saiidi, M, "Toward Successful Implementation of Prefabricated Deck Panels to Accelerate the Bridge Construction Process," Center For Civil Engineering Earthquake Research, Department Of Civil and Environmental Engineering, University of Nevada, Reno, Nevada, Report No. CCEER-16-05, August 2016.

CCEER 16-06 Mehrsoroush, A. and Saiidi, M., "Probabilistic Seismic Damage Assessment for Sub-standard Bridge Columns," Center For Civil Engineering Earthquake Research, Department Of Civil and Environmental Engineering, University of Nevada, Reno, Nevada, Report No. CCEER-16-06, November 2016.

CCEER 16-07 Nielsen, T., Maree, A., and Sanders, D., "Experimental Investigation into the Long-Term Seismic Performance of Dry Storage Casks," Center For Civil Engineering Earthquake Research, Department Of Civil and Environmental Engineering, University of Nevada, Reno, Nevada, Report No. CCEER-16-07, December 2016.

CCEER 16-08 Wu, S., Buckle, I., and Itani, A., "Effect of Skew on Seismic Performance of Bridges with Seat-Type Abutments," Center For Civil Engineering Earthquake Research, Department Of Civil and Environmental Engineering, University of Nevada, Reno, Nevada, Report No. CCEER-16-08, December 2016.

CCEER 16-09 Mohammed, M., and Sanders, D., "Effect of Earthquake Duration on Reinforced Concrete Bridge Columns," Center For Civil Engineering Earthquake Research, Department Of Civil and Environmental Engineering, University of Nevada, Reno, Nevada, Report No. CCEER-16-09, December 2016.

CCEER 16-10 Guzman Pujols, J., and Ryan, K., "Slab Vibration and Horizontal-Vertical Coupling in the Seismic Response of Irregular Base-Isolated and Conventional Buildings," Center For Civil Engineering Earthquake Research, Department Of Civil and Environmental Engineering, University of Nevada, Reno, Nevada, Report No. CCEER-16-10, December 2016.

CCEER 17-01 White, L., Ryan, K., and Buckle, I., "Thermal Gradients in Southwestern United States and the Effect on Bridge Bearing Loads," Center For Civil Engineering Earthquake Research, Department Of Civil and Environmental Engineering, University of Nevada, Reno, Nevada, Report No. CCEER-17-01, May 2017.

CCEER 17-02 Mohebbi, A., Saiidi, M., and Itani, A., "Development and Seismic Evaluation of Pier Systems w/Pocket Connections, CFRP Tendons, and ECC/UHPC Columns," Center For Civil Engineering Earthquake Research, Department Of Civil and Environmental Engineering, University of Nevada, Reno, Nevada, Report No. CCEER-17-02, May 2017.

CCEER 17-03 Mehrsoroush, A., Saiidi, M., and Ryan, K., "Development of Earthquake-resistant Precast Pier Systems for Accelerated Bridge Construction in Nevada," Center For Civil Engineering Earthquake Research, Department Of Civil and Environmental Engineering, University of Nevada, Reno, Nevada, Report No. CCEER-17-03, June 2017.

CCEER 17-04 Abdollahi, B., Saiidi, M., Siddharthan, R., and Elfass, S., "Shake Table Studies on Soil-Abutment-Structure Interaction in Skewed Bridges," Center For Civil Engineering Earthquake Research,

Department Of Civil and Environmental Engineering, University of Nevada, Reno, Nevada, Report No. CCEER-17-04, July 2017.

CCEER 17-05 Shrestha, G., Itani, A., and Saiidi, M., "Seismic Performance of Precast Full-Depth Decks in Accelerated Bridge Construction," Center for Civil Engineering Earthquake Research, Department of Civil and Environmental Engineering, University of Nevada, Reno, Nevada, Report No. CCEER-17-05, September 2017.

CCEER 17-06 Wu, S., Buckle, I., and Ryan, K., "Large-Scale Experimental Verification of an Optically-Based Sensor System for Monitoring Structural Response," Center for Civil Engineering Earthquake Research, Department of Civil and Environmental Engineering, University of Nevada, Reno, Nevada, Report No. CCEER-17-06, October 2017.

CCEER 17-07 Nada, H., and Sanders, D., "Analytical Investigation into Bridge Column Innovations for Mitigating Earthquake Damage," Center For Civil Engineering Earthquake Research, Department Of Civil and Environmental Engineering, University of Nevada, Reno, Nevada, Report No. CCEER-17-07, October 2017.

CCEER 18-01 Maree, A. F., and Sanders, D., "Performance and Design of Anchorage Zones for Post-Tensioned Box Girder Bridges," Center for Civil Engineering Earthquake Research, Department of Civil and Environmental Engineering, University of Nevada, Reno, Nevada, Report No. CCEER-18-01, January 2018.

CCEER 18-02 Mostafa, K., and Sanders, D., "Improving the Long-Term Performance of Bridge Decks using Deck and Crack Sealers," Center for Civil Engineering Earthquake Research, Department of Civil and Environmental Engineering, University of Nevada, Reno, Nevada, Report No. CCEER-18-02, March 2018.

CCEER 18-03 Blount, S., Ryan, K., Henry, R., Lu, Y., and Elwood, K., "Evaluation of lower damage concepts for enhanced repairability of reinforced concrete walls," Center for Civil Engineering Earthquake Research, Department of Civil and Environmental Engineering, University of Nevada, Reno, Nevada, Report No. CCEER-18-03, June 2018.

CCEER 18-04 Mohebbi, A., Jordan, E., and Saiidi, M., "Exploratory Experimental Studies of Spliced Cam Shape Memory Alloy Bars for Seismic Application," Center for Civil Engineering Earthquake Research, Department Of Civil and Environmental Engineering, University of Nevada, Reno, Nevada, Report No. CCEER-18-04, September 2018.

CCEER 19-01 Saint Pierre, E., Elfass, S., Watters, R., Norris, G., and Ashour, M. "Improving Strain Wedge Model Capabilities in Analyzing Laterally Loaded Drilled Shafts in Cemented Soils," Center for Civil Engineering Earthquake Research, Department of Civil and Environmental Engineering, University of Nevada, Reno, Nevada, Report No. CCEER-19-01, March 2019.

CCEER 19-02 Benjumea, J., Saiidi, M., and Itani, A., "Experimental and Analytical Seismic Studies of a Two-Span Bridge System with Precast Concrete Elements and ABC Connections," Center for Civil Engineering Earthquake Research, Department of Civil and Environmental Engineering, University of Nevada, Reno, Nevada, Report No. CCEER-19-02, May 2019.

CCEER 19-03 Subedi, D., Moustafa, M., and Saiidi, M., "Non-Proprietary UHPC for Anchorage of Large Diameter Column Bars in Grouted Ducts," Center for Civil Engineering Earthquake Research, Department of Civil and Environmental Engineering, University of Nevada, Reno, Nevada, Report No. CCEER-19-03, May 2019.

CCEER 19-04 Shoushtari, E, D., Saiidi, M., Itani, A., and Moustafa, M., "Shake Table Studies of a Steel Girder Bridge System with ABC Connections," Center for Civil Engineering Earthquake Research, Department of Civil and Environmental Engineering, University of Nevada, Reno, Nevada, Report No. CCEER-19-04, June 2019.

CCEER 19-05 Wu, S., Miah, M., and McCallen, D., "Four Canonical Steel Moment Frame Buildings and Inter-Code Comparisons of Nonlinear Building Response," Center for Civil Engineering Earthquake Research, Department of Civil and Environmental Engineering, University of Nevada, Reno, Nevada, Report No. CCEER-19-05, September 2019.

CCEER 20-01 Schwartz, T., Saiidi, M., and Moustafa, M., "Simplifying Cast-in-Place Joint Design Using ABC Pocket Connection Details in High Seismic Regions," Center for Civil Engineering Earthquake Research, Department of Civil and Environmental Engineering, University of Nevada, Reno, Nevada, Report No. CCEER-20-01, January 2020.

CCEER 20-02 Shrestha, G., Saiidi, M., and Sanders, D., "Seismic Studies of Spliced Columns and Anchorage of Large Diameter Bars in Grouted Duct," Center for Civil Engineering Earthquake Research, Department of Civil and Environmental Engineering, University of Nevada, Reno, Nevada, Report No. CCEER-20-02, February 2020.

CCEER 20-03 Ozsahin, E. and Pekcan, G., "Torsional Ground Motion Effects on the Seismic Response of Continuous Box-girder Highway Bridges," Center for Civil Engineering Earthquake Research, Department of Civil and Environmental Engineering, University of Nevada, Reno, Nevada, Report No. CCEER-20-03, April 2020.

CCEER 20-04 Wu, S., Eckert, E., Huang, J., and McCallen, D., "Evaluation of the Domain Reduction Method Applied to Broad-Band, Near-Fault Earthquake Ground Motions with Inter-Code Comparisons," Center for Civil Engineering Earthquake Research, Department of Civil and Environmental Engineering, University of Nevada, Reno, Nevada, Report No. CCEER-20-04, June 2020.

CCEER 20-05 Jones, J., Saiidi, M., and Itani, A. "Experimental and Analytical Studies of a Two-Span Bridge System with Precast Elements Incorporating Rebar Hinge and Socket Connections," Center for Civil Engineering Earthquake Research, Department of Civil and Environmental Engineering, University of Nevada, Reno, Nevada, Report No. CCEER-20-05, August 2020.

CCEER 20-06 Camarena, C., Saiidi, M., and Moustafa, M. "Development and Seismic Evaluation of Cast-in-Place Emulating ABC Pocket Connections and SMA Reinforced Two-Way Column Hinges," Center for Civil Engineering Earthquake Research, Department of Civil and Environmental Engineering, University of Nevada, Reno, Nevada, Report No. CCEER-20-06, August 2020.

CCEER 20-07 Kenawy, M. and McCallen, D. "Regional-Scale Seismic Risk to Reinforced Concrete Buildings Based on Physics-Based Earthquake Ground Motion Simulations," Center for Civil Engineering Earthquake Research, Department of Civil and Environmental Engineering, University of Nevada, Reno, Nevada, Report No. CCEER-20-07, September 2020.